The sedimentary and stratigraphic record of external and internal factors affecting deep-water sedimentary systems

A thesis submitted to The University of Manchester for the degree of Doctor of Philosophy in the Faculty of Science and Engineering

2020

Euan Soutter

School of Natural Sciences

Department of Earth and Environmental Sciences

TABLE OF CONTENTS

LIST OF FIGURES

LIST OF TABLES

Total words (including references): 82,078

ABSTRACT

Deep-water sedimentary systems are the products of, and may record, the interaction of a range of external and internal factors. External factors, i.e., climate, eustasy, and tectonics, act to control sediment supply and accommodation space, while internal factors, such as flow dynamics and bedform deposition, act to control sediment distribution and character. The expression of the interplay between external and internal forces acting on deep-water sedimentary systems is archived in the stratigraphic record, however, deconvolving these in time and space remains challenging.

This study aims to enhance our understanding of the influence of external and internal factors on deep-water systems through a multi-scalar and multi-method approach. Outcrop data from the Eocene-Oligocene Alpine foreland and Cretaceous Greater Caucasus are compared with subsurface data from the Paleocene-Eocene North Sea Central Graben, with the results of these studies compared to simplified physical models of the topographic configurations of these basins.

Key insights derived from this study include: 1) onlap patterns in deep-water systems are controlled by a predictable interplay between external and internal factors, with 'external' onlap trends produced by progradation which is partially masked by 'internal' onlap trends produced by the character and evolution of the flows in space and time; 2) the isotopic record of deep-water systems can be used to assess the dominant external control on deposition within a basin and Earth's surface conditions during deposition; 3) deep-water deposition in the Alpine foreland was enhanced by increased aridity and lowered eustatic sea-levels associated with the Eocene – Oligocene climate transition and hinterland tectonism; 4) enhanced burial of organic carbon in deep-water systems during greenhouse-icehouse transitions may provide a positive feedback for cooling during these transitions; 5) far afield tectonic perturbations are recorded within the stratigraphy of deep-water basins, and can be used to reconstruct the timing of tectonic events; 6) deposition in deep-water systems affected by tectonic perturbations may initially be characterised by large-scale mass-transport, with progradation of submarine fans affected by the topography of this early mass-transport-dominated period; 7) deep-water systems characterised by contemporaneous carbonate and siliciclastic deposition have facies, facies associations and stacking patterns that differ from purely siliciclastic systems; 8) the orientation of basin floor topography, with respect to the sediment delivery system, exerts a fundamental control on the distribution and geometry of turbidity current deposits, and as a result controls the stratigraphic record of confined deep-water systems.

DECLARATION

University of Manchester PhD by published work Candidate Declaration

Candidate Name: Euan Lewis Soutter

Faculty: Science and Engineering

Thesis Title: The sedimentary and stratigraphic record of external and internal factors affecting deep-water sedimentary systems

I declare that the thesis has been composed by myself and that the work, other than that identified below, has not be submitted for any other degree or professional qualification. I confirm that the work submitted is my own, except where work which has formed part of jointly-authored publications has been included. My contribution and that of the other authors to this work has been explicitly indicated below. I confirm that appropriate credit has been given within this thesis where reference has been made to the work of others.

Author contributions

Chapter 3: **Soutter, E.L., Kane, I. A., Fuhrmann, A., Cumberpatch, Z. A., and Huuse, M., The stratigraphic evolution of onlap in siliciclastic deep-water systems: Autogenic modulation of allogenic signals**

Status:

Published in *Journal of Sedimentary Research*, Volume 49, 2019: Pages 890 – 917.

Author contributions:

1. Soutter, E.L: Main author. Responsible for data collection, processing, and analysis. Wrote manuscript.
2. Kane, I. A.: In-depth discussion, fieldwork assistance. Detailed manuscript reviews.
3. Fuhrmann, A.: Field assistance, discussion and manuscript review.
4. Cumberpatch, Z. A.: Field assistance, discussion and manuscript review.
5. Huuse, M.: Discussion and manuscript review.

Chapter 4: **Soutter, E.L., Kane, I.A., Martinez-Donate, A., Stacey, J., and Boyce, A., Enhanced deep-marine deposition across the Eocene-Oligocene climate transition: a feedback mechanism for global cooling**

*Status***:**

In prep.

Author contributions:

1. Soutter, E.L: Main author. Responsible for data collection, processing, and analysis. Wrote manuscript.
2. Kane, I. A.: In-depth discussion and manuscript reviews.
3. Martinez-Donate, A.: Field assistance, discussion and manuscript review.
4. Stacey, J.: Petrographic analysis of carbonates.
5. Boyce, A.: Isotope analysis discussion.

Chapter 5: Soutter, E.L., Kane, I.A., and Huuse, M., Giant submarine landslide triggered by Paleocene mantle plume activity in the North Atlantic.

Status:

Published in *Geology,* Volume 46, 2018: Pages 511-514.

Author contributions:

1. Soutter, E.L: Main author. Responsible for data collection, processing, and analysis. Wrote manuscript.
2. Kane, I. A.: In-depth discussion and manuscript reviews.
3. Huuse, M: In-depth discussion and manuscript reviews.

Chapter 6: Cumberpatch, Z.A., Soutter, E.L., Kane, I.A., and Casson, M., Evolution of a mixed siliciclastic-carbonate deep-marine system on an unstable margin: the Cretaceous of the Eastern Greater Caucasus, Azerbaijan

Status:

In review at *Basin Research*. Available on EarthArXiv (10.31223/osf.io/wsvu6):

Author contributions:

1. Cumberpatch, Z. A.: Co-author. Co-responsible for data collection, processing, and analysis. Co-wrote manuscript.
2. Soutter, E. L.: Co-author. Co-responsible for data collection, processing, and analysis. Co-wrote manuscript.
3. Kane, I. A.: In-depth discussion and manuscript reviews.
4. Casson, M: Provided subsurface analogue and manuscript reviews.

Chapter 7: Soutter, E.L., Bell, D., Cumberpatch, Z.A., Ferguson, R., Spychala, Y., Kane, I.A., and Eggenhuisen, J., Turbidity currents interacting with variable topography: physical models and geological implications.

Status:

In prep.

Author contributions:

1. Soutter, E. L.: Main author. Co-responsible for data collection. Responsible for data processing and analysis. Wrote manuscript.
2. Bell, D.: Co-responsible for data collection. Discussion and manuscript reviews.
3. Cumberpatch, Z. A.: Co-responsible for data collection. Discussion and manuscript reviews.
4. Ferguson, R.: Assistance with experiments, discussion and manuscript reviews.
5. Spychala, Y.: Assistance with experiments, discussion and manuscript reviews.
6. Kane, I. A.: Assistance with experiments, discussion and manuscript reviews.
7. Eggenhuisen, J.: Manuscript reviews.

COPYRIGHT STATEMENT

I. The author of this thesis (including any appendices and/or schedules to this thesis) owns certain copyright or related rights in it (the "Copyright") and s/he has given The University of Manchester certain rights to use such Copyright, including for administrative purposes.

II. Copies of this thesis, either in full or in extracts and whether in hard or electronic copy, may be made only in accordance with the Copyright, Designs and Patents Act 1988 (as amended) and regulations issued under it or, where appropriate, in accordance with licensing agreements which the University has from time to time. This page must form part of any such copies made.

III. The ownership of certain Copyright, patents, designs, trademarks and other intellectual property (the "Intellectual Property") and any reproductions of copyright works in the thesis, for example graphs and tables ("Reproductions"), which may be described in this thesis, may not be owned by the author and may be owned by third parties. Such Intellectual Property and Reproductions cannot and must not be made available for use without the prior written permission of the owner(s) of the relevant Intellectual Property and/or Reproductions.

IV. Further information on the conditions under which disclosure, publication and commercialisation of this thesis, the Copyright and any Intellectual Property and/or Reproductions described in it may take place is available in the University IP Policy (see http://documents.manchester.ac.uk/DocuInfo.aspx?DocID=2442 0), in any relevant Thesis restriction declarations deposited in the University Library, The University Library's regulations (see http://www.library.manchester.ac.uk/about/regulations/) and in The University's policy on Presentation of Theses.

ACKNOWLEDGEMENTS

I would like to thank my supervisors Ian Kane and Mads Huuse for their support throughout this project.

I would also like to thank my fellow students Dan, Ross, Zoë, David, Jack, Arka, Chris, Arne, Manu, Kevin, Ander, Rhys, Orrin, and Ashley, who have made my time at Manchester extremely enjoyable.

Finally, I would like to thank my parents Morag and Douglas, and my sister Rhona. Without their love and support I wouldn't be typing this today.

"I've got blisters on my fingers" – Ringo Starr

This work was funded by the Natural Environment Research Council Centres for Doctoral Training Oil and Gas grant number NE/M00578X/1.

CHAPTER 1: Rationale

Deep-water sedimentary systems form the largest sediment accumulations on Earth (e.g Curray and Moore, 1971; Clift et al. 2001). Understanding these systems is important because they are long-term sinks of climate-modulating organic carbon (e.g. Galy et al. 2007; Cartapanis et al. 2016), preferentially store anthropogenic pollutants (e.g. Kane and Clare, 2019), are reservoirs of economically-valuable hydrocarbons (e.g. Weimer and Link, 1991; Beaubouef et al. 2000), are important sites of carbon storage (e.g. Marshall et al. 2006), and form archives of events that affect the Earth's geosphere (e.g. Romans et al. 2016; Hessler and Fildani, 2019). Deep-water sedimentary systems are controlled by external and internal factors. External factors, such as eustasy, climate and tectonism, are external to the deep-water sedimentary system, and have been shown to control both ancient (e.g. Castlelltort et al. 2017; Sharman et al. 2017) and modern (e.g. Weber et al. 1997; Ducassou et al. 2009) deep-water systems. Internal factors, such as depositional topography, act to control the distribution and character of sediment in deep-water systems (e.g. Kneller, 1995; Sweet et al. 2019). Understanding the combined impacts of external and internal controls on deep-water basins and their stratigraphic record is consequently important for both palaeoclimatic and palaeogeographical reconstructions (e.g. Hessler and Fildani, 2019; Pickering et al. 2020). This study therefore aims to: 1) investigate how external factors affect the sedimentological and stratigraphic record of deep-water sedimentary systems, 2) investigate how internal factors, particularly basin topography and flow processes, affect deep-water sedimentary systems, and 3) investigate how the interplay between external and internal factors is recorded within the stratigraphic record of deep-water sedimentary systems.

These aims will be investigated through a series of case-studies, each of which addressing particular aspects of the overarching aims. The first case-study seeks to evaluate how basinal topography affects flow processes and deposits at outcrop, and how this may affect the stratigraphic record of sediment supply changes. The second case-study aims to use geochemical and outcrop data to resolve the external controls on sediment delivery to deep-marine basins. The third and fourth case-studies aim to assess how tectonic activity influences the stratigraphic evolution of deep-marine basins using subsurface and outcrop data. These case-studies also seek to evaluate the effect of basinal and depositional topography on the stratigraphic evolution of deep-marine basins. The final case study aims

to investigate the influence of confining topography orientation on turbidity current processes and deposit geometries using experimental models.

An additional rationale for this project lies in its approach, with existing investigations of deep-water sedimentary systems either relying on the incomplete record of their exhumed remains (e.g. Grundvåg et al. 2014; Prélat et al. 2009), relatively low-resolution seismic-data (e.g. Jackson et al. 2008; Deptuck et al. 2008), physical models that are often difficult to scale to natural conditions (e.g. Kneller, 1995; Amy et al. 2004; Hamilton et al. 2015) or relatively few direct measurements (e.g. Sumner et al. 2013; Clarke, 2016; Azpiroz-Zabala et al. 2017b). The wide spatio-temporal scope of these individual methods often renders their findings difficult to compare across scales, with phenomena identified through each of these methods rarely linked together within one study (e.g. Kneller, 1995; Amy et al. 2004; Bakke et al. 2014, Hage et al. 2018). This study therefore seeks to address this by incorporating these normally isolated methods into one integrated study, with the rationale being that common phenomena seen across separate methods, scales and localities are more likely to be pervasive in deep-water sedimentary systems.

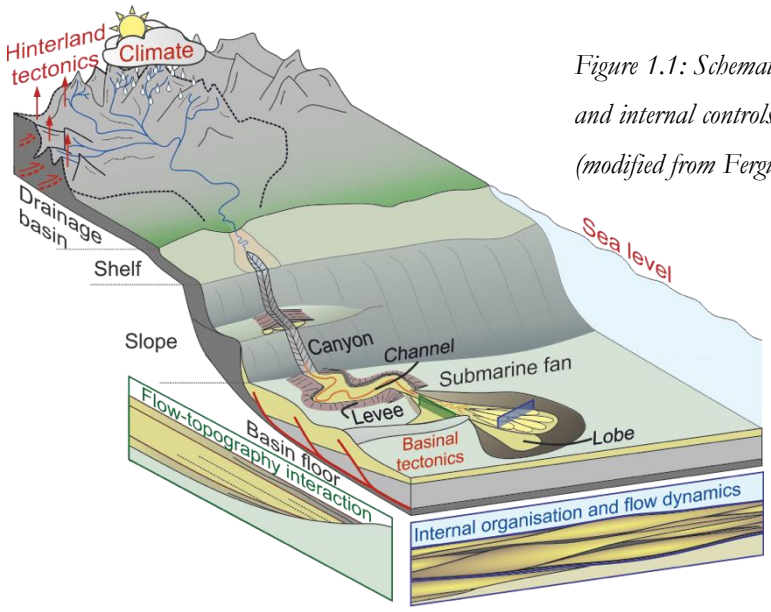

Figure 1.1: Schematic diagram of the external and internal controls studied within this thesis (modified from Ferguson et al. 2020).

1.1 *How does topography control the sedimentology and stratigraphic record of a confined deep-water basin margin?*

Basins that receive sediment-gravity-flows which are partially or completely confined by the margins of the basin are described as confined-deep-water basins (e.g. Gorsline and Emery, 1959; Lomas and Joseph, 2004). Confined deep-water basins are formed in a variety of different tectonic settings, such as fold-thrust belts (e.g. Morley and Leong, 2008; Vinnels et al. 2010) and rifted basins (e.g. Smith, 1995; Cullen et al. 2019), and

by a variety of different processes, such as salt diapirism (e.g. Oluboyo et al. 2014; Doughty-Jones et al. 2019) and mass-transport (Armitage et al. 2009; Alves, 2010). Flows that enter these basins deposit sediment which pinches-out and progressively onlaps the slope or basin margin (e.g. McCaffrey and Kneller, 2001; Gardiner, 2005), creating an onlap pattern as the basin fills.

Previous work has tended to characterize onlap in a binary fashion based on two end-member flow types (McCaffrey and Kneller, 2001; Pickering and Hilton, 1998; Smith and Joseph, 2004). Sediment gravity flows, however, encompass a wide variety of different flow types (e.g. Middleton and Hampton, 1973; Talling et al. 2012) and resultantly a wide variety of different onlap styles (e.g. Gardiner, 2006; Bakke et al. 2013). It is important to understand how the deposits of these different flow types onlap a slope because the onlap patterns they generate can be used as indicators of external factors affecting deep-water sedimentary systems, such as varying subsidence or sediment supply rates (e.g. Sylvester et al. 2015). If internal processes, such as flow type, influence onlap patterns more than is appreciated then onlap-based interpretations of these external processes may need to be reappraised. The chapter therefore seeks to understand: 1) how the basin-internal influences of topography and sediment-gravity-flow type affect onlap patterns, 2) if this influence is predictable through time, and 3) how onlap patterns may record the interplay between internal (autogenic) and external (allogenic) factors affecting deep-water deposition.

1.2 *Can you resolve the external controls on a deep-water sedimentary system?*

The three main external factors affecting deep-water sedimentary systems are eustatic sea-level, tectonism, and climate (e.g. Allen, 1997; Cantuneanu, 2020). It is often difficult, however, to disentangle the relative impacts of these processes on the stratigraphic record of a deep-water basin (e.g. Pickering and Bayliss, 2009; Sømme et al. 2009a; Romans et al. 2016). The ratio between the stable isotopes of carbon ^{12}C and ^{13}C ($\delta^{13}C$), are sensitive to climate and sea-level, and can be measured from hemipelagic deep-water successions (e.g. Jenkyns, 1996; Mitchell et al. 1996; Saltzman and Thomas, 2012). The $\delta^{13}C$ record of these successions therefore provides a way to disentangle the effects of sea-level, climate and tectonism on deep-marine deposition, and has previously been utilised successfully to decipher controls on deep-marine deposition in the exhumed Pyrenean foreland (Castelltort et al. 2017). Application of this method to analogous basins has so far not been performed, and resultantly the exportability of this method is uncertain.

The Grès d'Annot of the Alpine foreland basin is analogous to the Pyrenean strata studied by Castelltort et al. (2017), representing a deep-marine succession that displays periods of enhanced and decreased deposition attributed to sea-level, climate and tectonism (Callec et al. 2004; Puigdefàbregas et al. 2004; Euzen et al. 2004). The relative impacts of these processes, however, has not been tested. Understanding the relative influence of these controls could provide insights into 1) Corsica-Sardinian tectonism and foreland basin sedimentation, and 2) the relative impact of tectonically-modulated sea-level, generated by subsidence in front of the orogenic belt, and eustatic sea-level, on foreland basin sedimentation.

Biostratigraphic data also indicates that the Grès d'Annot was deposited during the Eocene-Oligocene transition (EOT) (Du Fornel et al. 2004; Euzen et al. 2004). The EOT signifies the transition from Paleogene greenhouse to Oligocene-Recent icehouse conditions, and has been well-constrained globally (e.g. Prothero and Berggren, 2014). Most EOT studies tend to focus on quantifying temperature (e.g. Eldrett et al. 2009; Liu et al. 2009) or sea-level (Katz et al. 2008; Miller et al. 2008) changes, with few studies assessing how the EOT affected marine sedimentary systems (e.g. Schlanger and Premoli Silva, 1986), and how this in turn may have modulated the EOT. The primary research questions addressed in this chapter are therefore: 1) can the $\delta^{13}C$ record of a deep-marine system resolve the external factors affecting deposition in that system?, 2) is the period of major global climatic change associated with the Eocene-Oligocene transition recorded within the sedimentological and stratigraphic record of deep-water basins? and, 3) could the (internal) depositional response have had a feedback effect on the external event that caused it?

1.3 *What is the response of a deep-water sedimentary system to tectonic activity?*

Tectonic activity, such as uplift (e.g. Métivier et al. 1999; Sømme et al. 2019) or earthquakes (Gorsline et al. 2000; Noda et al. 2008), has been shown to affect deep-water sedimentary systems, and is often manifested by mass-transport (e.g. Masson et al. 2006; Wu et al. 2019) and/or submarine fan progradation (e.g. Clift et al. 2001; McNeill et al. 2017; Pickering et al. 2020). These studies, however, are typically limited by incomplete exposure or seismic coverage of ancient systems, a lack of subsurface lithology data, or accurate constraints on tectonic event timing or cause. The Paleocene interval of the Central North Sea basin represents a unique setting in which these limitations are partially

mitigated against by extensive subsurface data and well-constrained tectono-stratigraphic chronology (e.g. Den Hartog Jager et al. 1993; Mudge et al. 2015).

Previous work has shown that tectonism caused by impingement of the proto-Icelandic mantle plume and the opening of the North Atlantic during the early Paleocene affected deep-water systems in the North Sea (e.g. White and Lovell, 1997; Mudge and Jones, 2004). These studies, however, provide little information on the deep-water depositional processes recording the transition to a new tectonic regime, and how this evolves spatially and temporally as the sedimentary system adjusts to its new regime. This knowledge gap has prevented application of this well-constrained interval to analogous exhumed or subsurface basins with less data availability. Stratigraphic predictions and tectonic reconstructions of these poorly-constrained basins consequently have the potential to be greatly improved by filling this gap, with case-studies of well-constrained analogues providing a more accurate basis for interpretation in these poorly-constrained basins. The primary research questions of the chapter are therefore: 1) what is the sedimentological and stratigraphic record of tectonic activity in a deep-water basin? And, 2) how does the depositional response to tectonism evolve through time?

1.4 ***What is the stratigraphic evolution of a mixed deep-water system on an unstable margin?***

Mixed siliciclastic-carbonate deep-water systems (mixed-systems) are those in which both siliciclastic and carbonate sediment gravity flows are deposited contemporaneously in the same basin (e.g. Mount, 1984; Moscardelli et al. 2019). These systems are less-well studied than their siliciclastic counterparts, therefore little is known about the applicability of siliciclastic depositional processes (e.g. Mulder and Alexander, 2001; Talling et al. 2012), facies associations (e.g. Mutti, 1992; Spychala et al. 2017) and stacking patterns (e.g. Deptuck et al. 2008; Prélat et al. 2009) to these systems. This chapter seeks to address this by investigating a Cretaceous mixed-system deposited in the Buduq Trough of the Greater Caucasus, Azerbaijan. The particular research questions are: 1) what are the depositional processes operating in mixed systems?, 2) what are the facies associations and depositional elements of mixed systems?, and 3) how do contemporaneous siliciclastic and carbonate submarine fans interact?

The Buduq Trough at this time was also highly unstable due to far-field tectonic activity, and is consequently characterised by extensive mass-transport deposition (Bochud,

2011). The effect of this tectonism on the sedimentological and stratigraphic evolution of the deep-water Buduq Trough, however, has not been studied in detail. Mass-transport topography has been also been shown to have affected deep-marine depositional patterns in ancient systems in the subsurface (e.g. Alves, 2010; Ortiz-Karpf et al. 2015, 2016) and at outcrop (e.g. Armitage et al. 2009; Fallgatter et al. 2017; Brooks et al. 2018). This chapter therefore also aims to further investigate 1) the effect that mass-transport deposition may have had on depositional patterns in the Buduq Trough, 2) how this may be resolved at outcrop and in the subsurface, and 3) whether the depositional response to tectonic activity changed through time. The rationale of this Chapter is therefore closely aligned with Chapter 6.

1.5 *What effect does topographic orientation have on confined turbidity currents?*

The influence of confining topography orientation on deep-water sedimentation is typically inferred from the deposits that sediment gravity flows leave behind, which are generally incompletely revealed due to poor exposure (e.g. Feletti, 2002; Smith et al. 2004b) or low seismic resolution (e.g. Gee et al. 2001; Bakke et al. 2013). Resultantly, there is little data on the generic depositional patterns that may be expected with varying orientations of confining topography. This knowledge gap is problematic because many palaeogeographic or structural reconstructions of deep-water basins are dependent on using the stratigraphic record of the flows that entered them as proxies for the basin shape (e.g. Sinclair, 1994; 2000; Pinter et al. 2017). If the effect of topographic orientation on this record is unknown then these reconstructions may be incorrect. This lack of knowledge will also affect how researchers interpret the external controls on deep-water systems, as it is may be unknown how the basin shape affected the transfer and preservation of the depositional signals from external events.

Physical models of turbidity currents interacting with topography at varying orientations have been used to address this knowledge gap, however they are usually performed under experimental conditions that limit scaling to natural conditions, such as using flows with unrealistic sediment compositions or flume tanks with non-erodable substrates (e.g. Alexander and Morris, 2004; Abhari et al. 2018). The research questions posed are therefore: 1) what is the effect of topographic orientation on scalable turbidity current velocities, erosion, and deposition? 2) can physical models explain features seen in exhumed or subsurface confined deep-water systems? and 3) how does basinal topography affect the transfer of external signals in deep-water systems?

CHAPTER 2: Deep-water sedimentary systems

2.1 *Introduction*

Understanding of the depositional processes operating in the deep-sea began with the bathymetric identification of submarine channels at the mouth of the Hudson River, Western North America (Dana, 1863) and the Rhone River in Lake Geneva, Switzerland (Forel, 1885). It was suggested by Forel (1885) that the Lake Geneva channel was carved by the subaqueous continuation of the Rhone River. As exploration and data coverage of the deep-sea increased other examples of channels and canyons along continental margins were identified (Spencer, 1903), such as the Congo Canyon (Fig. 2.1) (Buchanan, 1887; 1888) and the Laurentian Canyon (Spencer, 1889), with Daly (1936) suggesting in '*Origin of Submarine "Canyons."*' that these canyons were eroded by gravity-driven subaqueous flows of suspended sediment, which he called 'turbidity currents'.

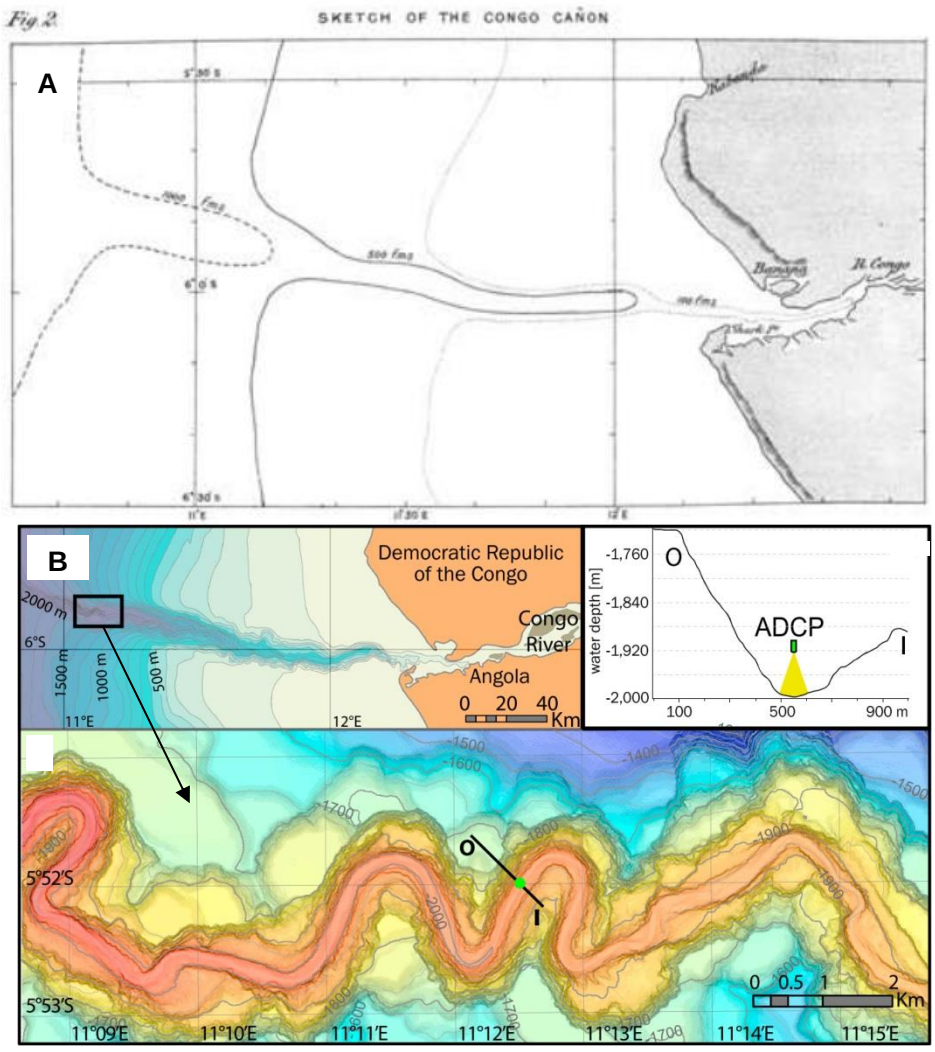

Figure 2.1: A) Sketch of the Congo Canyon from Buchanan (1888). B) Present-day resolution of the Congo Canyon (Aspirez-Zabala et al. 2017a).

An understanding of how these turbidity currents may be preserved in the rock record began with the interpretation of graded deposits on the seafloor (Bramelette and Bradley, 1940) and within reservoirs ('black blizzards' of Bell (1942)) as being deposited by turbulent flows. Ancient sand-rich and graded beds within otherwise fine-grained marine sequences were then interpreted based on these observations and experimental models to have been formed by turbulent flows moving sediment into deep-water (Kuenen and Migliorini, 1950; Natland and Kuenen, 1951; Bouma, 1962, 1964; Harnes and Fahnestock, 1965). Damaged submarine infrastructure provided the first indirect measurements of these flows in nature (e.g. Heezen and Ewing, 1952; Mulder et al., 1997), with direct measurements of turbulent flows now recorded from various locations across the globe (e.g. Sumner et al. 2013; Talling et al. 2013; Azpiroz-Zabala et al. 2017ab; Paull et al. 2018; Clare et al. 2019; Maier et al. 2019). The exact nature and variety of these flows, and the geomorphology they build, however, remains a topic of intense research (e.g. Talling et al. 2012; Howlett et al. 2019; Picot et al. 2019; Maier et al. 2019; McHargue et al. 2019; Fonnesu et al. 2020; Heerema et al. 2020). The following sections will summarise what is presently known about sediment gravity flow (SGF) processes, their deposits and the geomorphic elements they produce.

2.2 ***Flow processes***

Sediment is transported to deep-water (below storm wave-base) by sediment gravity flows (SGFs) (Fig. 2.2) (Daly, 1936; Kuenen and Migliorini, 1950; Middleton and Hampton, 1973; Lowe, 1982; Mulder and Alexander, 2001; Talling et al. 2012). SGFs form due to the action of gravity on the density contrast between sediment-laden fluid and ambient fluid (seawater or freshwater) (e.g. Middleton and Hampton, 1973; Lowe, 1979). A spectrum of SGF types has been identified and differentiated based on their particle support mechanism (Fig. 2.2), which Mulder and Alexander (2001) describe as being controlled by some combination of matrix strength, buoyancy, pore pressure, grain-to-grain interaction, turbulence and bed support. Two end-member flow types are commonly differentiated: turbulent (Bouma, 1962; Kuenen and Migliorini, 1950; Garcia, 1994; Kneller and Branney, 1995; Kneller and McCaffrey, 1999; Lamb et al. 2004; Eggenhuisen et al. 2017) or laminar (Hampton, 1972; Nardin et al. 1979; Sohn, 2000; Ilstad et al. 2004; Baas et al. 2009; Inverson et al. 1997, 2010; Jackson, 2011), with transitional flows (e.g. Baas and Best, 2002; Baas et al. 2009; Sumner et al. 2009) bridging the gap between these two end-members (Fig. 2.2).

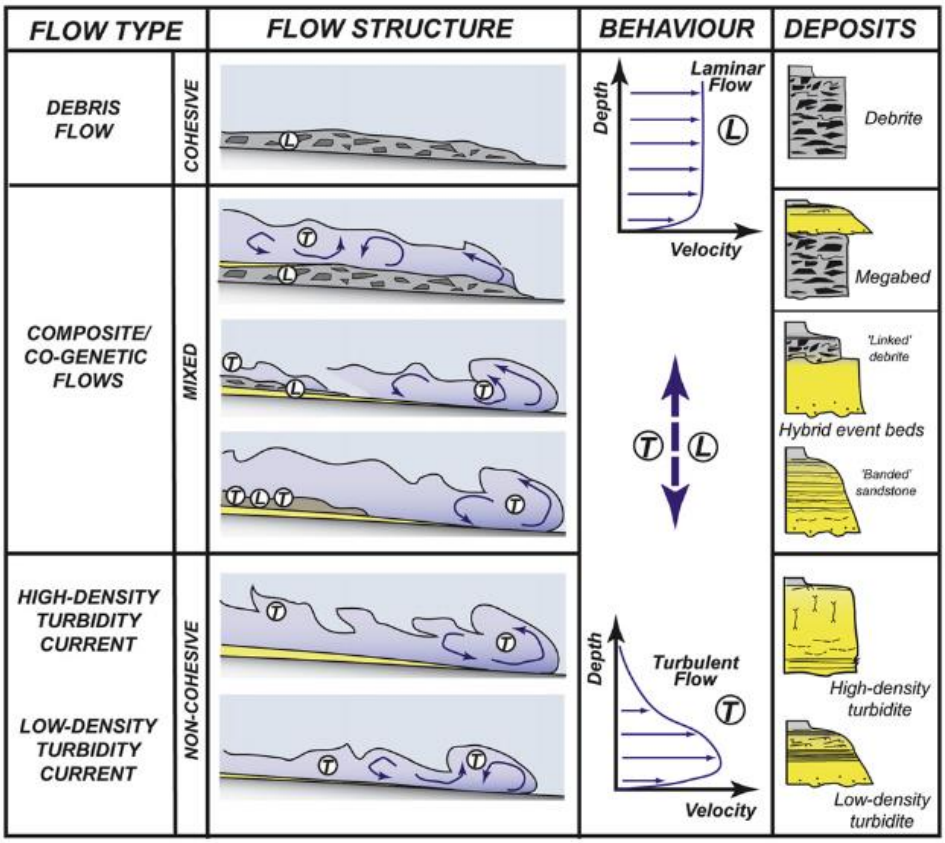

Figure 2.2: Variation in SGF type, structure, velocity and resultant deposit (Haughton et al. 2009).

Turbulent flows

SGFs, or regions of individual SGFs, can be described as turbulent when the downward-directed force of gravitational settling competes with the upward-directed force of turbulence, resulting in the partial or complete suspension of sediment (e.g. Middleton, 1967; Middleton and Hampton, 1973; Lowe, 1982; Middleton, 1993; Mulder and Alexander, 2001; Baas et al. 2005; Talling et al. 2012). Turbulent sediment gravity flows have a general structure comprising a head, body and tail (Fig. 2.3), as the head of the flow interacts with and entrains the ambient fluid, the mean velocity and sediment concentration is highest in the body of the flow and decreases toward the tail (e.g. Middleton, 1967; Kneller and Buckee, 2000). Therefore, during the passage of an individual turbulent flow over a fixed point, velocities will increase with the arrival of the head, will reach their maximum during the passage of the flow body behind the head and will wane during the passage of the body and tail (e.g. Kuenen and Migliorini, 1950; Middleton and Hampton, 1973; Kneller and Buckee, 2000). The velocity maximum marks the separation between a lower 'wall-region', where turbulence is created by bottom shear, and upper 'jet-region', where turbulence is created in the free shear zone and ambient fluid is entrained (Altinakar

et al. 1996). Numerous intra-flow velocity and concentration variations are over-printed on this more general pattern (e.g. Baas et al. 2005) (Fig. 2.3), with turbulent flows and their structure remaining an active area of research (e.g. Luchi et al. 2018; Paull et al. 2018; Eggenhuisen et al. 2019; Maier et al. 2019; Pohl et al, 2019a; Heerema et al. 2020). It has been shown recently through direct measurements, for example, that naturally-occurring turbulent sediment gravity flows may actually be fastest at the head of the flow within a high-concentration fore-running basal layer (Aspiroz-Zabala et al. 2017).

In general, turbulent flows will continue to flow down-slope until they either 'subside' by a reduction in the density contrast between the flow and the ambient fluid through ambient fluid entrainment and/or deposition of sediment from the flow (e.g. Parker et al. 1986; Middleton, 1993; Mulder and Alexander, 2001; Talling et al. 2012), or 'ignite' through erosion and incorporation of sediment as they flow, allowing them to maintain excess densities and run-out for longer distances (e.g. Parker et al. 1986; Fukushima et al. 1985; Middleton, 1993; Heerema et al. 2020).

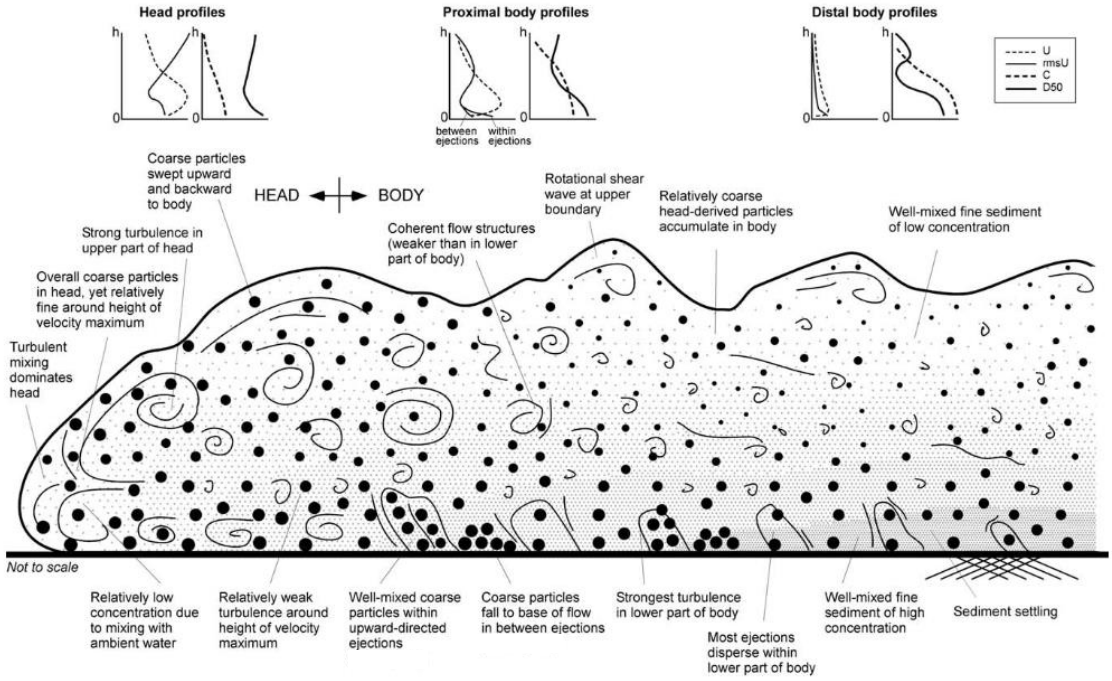

Figure 2.3: Schematic diagram showing the key features of a turbulent flow from Baas et al. (2005). U = downstream velocity, rmsU = root-mean-squared values of downstream velocity, C = suspended sediment concentration, D50 = median grain size.

Turbulent flows can be sub-divided based on their sediment concentration into low-density and high-density flows (e.g. Lowe, 1982; Kneller and Branney, 1995). Low-density flows have lower sediment concentrations and are entirely supported by fluid

turbulence (e.g. Baas et al. 2011). High-density flows have higher sediment concentrations, which suppresses turbulence close to the bed (Lowe, 1982; Talling et al. 2005). High-density flows are therefore supported by a combination of fluid turbulence and grain-to-grain interaction (Mulder and Alexander, 2001).

Laminar flows

SGFs characterised by laminar flow conditions, often called debris flows, are those in which turbulence is suppressed and sediment is supported by a matrix of high yield-strength fluid and fine sediment (i.e. mud) (e.g. Vanoni, 1946; Hampton, 1972; Middleton and Hampton, 1973; Nardin et al. 1979; Coussot and Meunier, 1996; Wang and Plate, 1996; Sohn, 2000; Ilstad et al. 2004; Baas et al. 2009; Inverson et al. 1997, 2010). Laminar flow conditions typically arise when electrostatic bonds between clay minerals cause the suppression of turbulence, resulting in non-Newtonian flow (e.g. Wang and Larsen, 1994; Coussot and Meunier, 1996). The high yield strength of this water-clay fluid phase (matrix) supports the flow (e.g. Coussot and Meunier, 1996), compared with the dominantly fluidal support of a turbulent flow and grain-grain support of a grain flow (Middleton and Hampton, 1973), with the cohesive matrix of laminar flows preventing ambient fluid entrainment and dilution (Mulder and Alexander, 2001). Laminar conditions may also arise in cohesionless (i.e. mud-poor) flows if grain concentrations are high enough for grains to interlock and give the flow frictional strength (Shanmugam and Moiola, 1995; Amy et al. 2005).

When the shear stress, or 'driving gravity stress' (Middleton and Hampton, 1973), applied to the flow cannot overcome the yield or frictional strength of the flow then en-masse deposition of the flow will occur (Lowe, 1982; Postma, 1986; Amy et al. 2005). Debris flows may rheologically transform through dilution to form turbulent flows (Hampton, 1972; Fallgatter et al. 2017), and vice versa (Haughton et al. 2003; Talling et al. 2007a; Hodgson et al. 2009; Fonnesu et al. 2018).

Transitional flows

Transitional flows are those in which sediment is transported through a continuum of processes between fully turbulent and fully laminar (e.g. Wang and Plate, 1996; Baas and Best, 2002; Sumner et al. 2009; Baas et al. 2009), and typically arises when fully turbulent flows increase their relative concentration of mud as they flow down-dip (Fig. 2.4), either

by deposition of coarse grains up-dip and/or erosion and entrainment of mud (e.g. Marr et al., 2001; Haughton et al., 2003; Kane and Pontén, 2012).

Transitional flows are manifested by strong turbulence near the bed, and weak or no turbulence within a laminar later immediately above the bed and in the upper parts of the flow (Baas et al. 2009; Sumner et al. 2009), and can be sub-divided into low- and high-density transitional flows (Baas and Best, 2002; Baas et al. 2002). Low-density transitional flows (or 'turbulence-enhanced transitional flows') exhibit enhanced near-bed turbulence and reduced turbulence in the upper region of the flow when compared with fully turbulent low-density flows (Baas and Best, 2002; Baas et al. 2009) (Fig. 2.4). Cohesive forces become more important as concentration increases, with a low-turbulence plug flow layer developing in the upper region of the flow and expanding downwards with increasing concentration, thus increasing the near-bed turbulence intensity (Baas et al. 2009). High-density transitional flows (or 'upper transitional plug flows') are therefore characterised by a thick plug flow region, and flow as a low-turbulence 'rigid fluid mass' over a shear layer with reducing turbulent intensity (Baas and Best, 2002; Baas et al. 2009) (Fig. 2.4). As transitional flows become increasingly concentrated in clay shear at the flow base becomes increasingly unable to break the clay bonds, resulting in the development of fully laminar flow conditions (Wang and Plate, 1996; Baas et al. 2009).

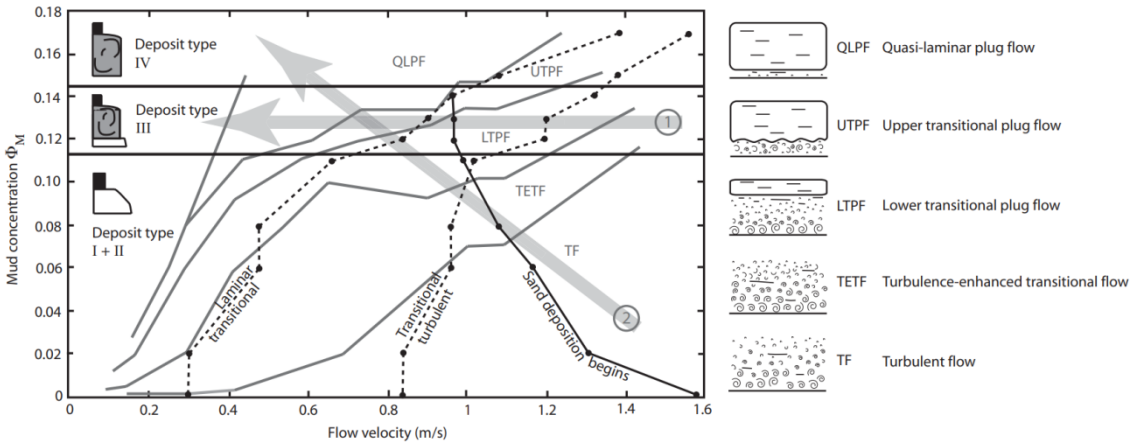

Figure 2.4: Experimental relationship between flow velocity, flow structure, mud concentration, and the resultant deposit (from Baas et al. 2009; Sumner et al. 2009). Arrows show trajectory of flows that would deposit a linked turbidite-debrite (Sumner et al. 2009).

2.3 ***Flow deposits***

Low-density turbidites

Low-density turbidites (LDTs) are deposited from low-concentration flows (<< 10 % sediment-volume) in which sediment within the flow was supported by fluid turbulence throughout its height (Mulder and Alexander, 2001; Baas et al. 2011). Preferential settling of larger grains within these flows results in a vertical density stratification profile (*sensu* Bagnold, 1962), with coarser-grains at the base of the flow and finer-grains dispersed homogenously throughout the flow (e.g. Garcia, 1994; Baas et al. 2005; Tiltston et al. 2015; Eggenhuisen et al. 2019). This results in incremental layer-by-layer deposition as the flow wanes, shear velocities decrease and progressively finer grains are deposited (Kneller and Branney, 1995; Talling et al. 2005), forming a normally-graded LDT ('Bouma Tb-e' of Fig 2.5A; 2.6). Low-density turbidites are characterised by tractional structures, such as ripples, which are diagnostic of near-bed turbulence (Baas et al. 2011; Talling et al. 2012) (Fig. 2.5A; 2.6). Near-bead turbulence is also manifested in the form of flutes often present on LDT bed bases (e.g. Kuenen, 1957), which record differential erosion during the passage of the high-velocity flow head and body (e.g. Elliot, 2000), and are frequently used to indicate paleoflow (e.g. Glennie, 1963; Kneller, 1991).

LDTs are typically thin (< 40 cm) (Ricci Lucchi, 1967; Talling, 2001) and commonly observed in distal or marginal environments as flows become more dilute during water entrainment and loss of sediment down-slope or away from the flow axis (e.g. Walker, 1967, Mutti, 1977; Hiscott et al. 1997; Boulesteix et al. 2019a). LDTs are also often associated with channelised deposition, where the upper and finer portions of a flow spill over confining channels (e.g. Mutti, 1977; Pirmez and Imran, 2003; Hansen et al. 2015; Jobe et al. 2017; Eggenhisen et al. 2019), forming levees (e.g. Normark et al., 1983; Kane and Hodgson, 2011). Sand content and LDT thickness will decrease distally away from the channel and within the levee in this setting (Skene et al. 2002; Kane et al., 2007).

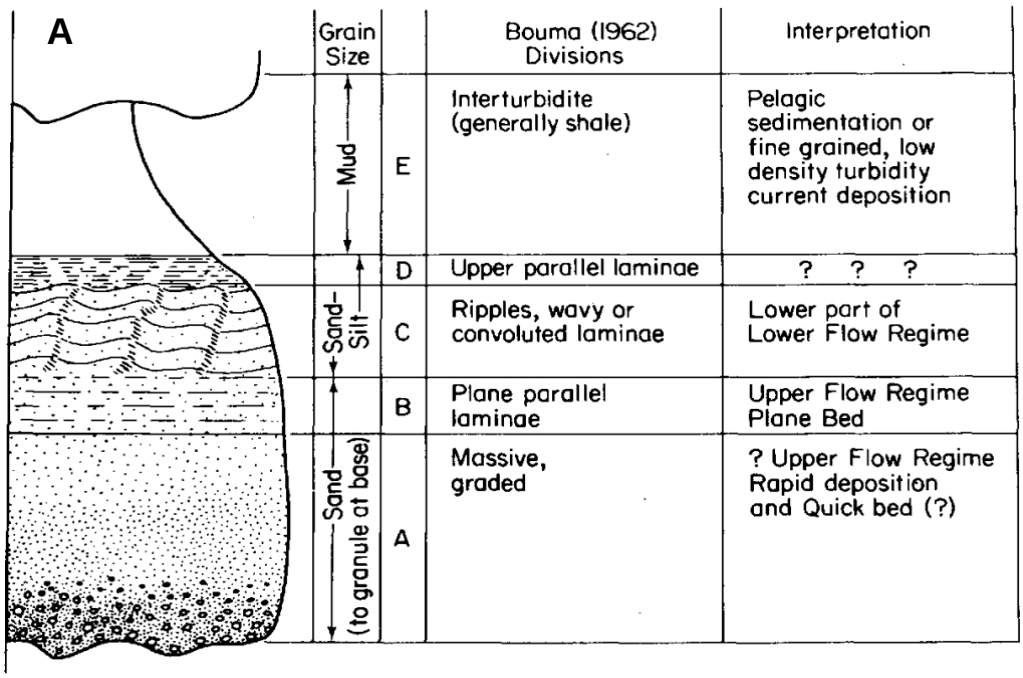

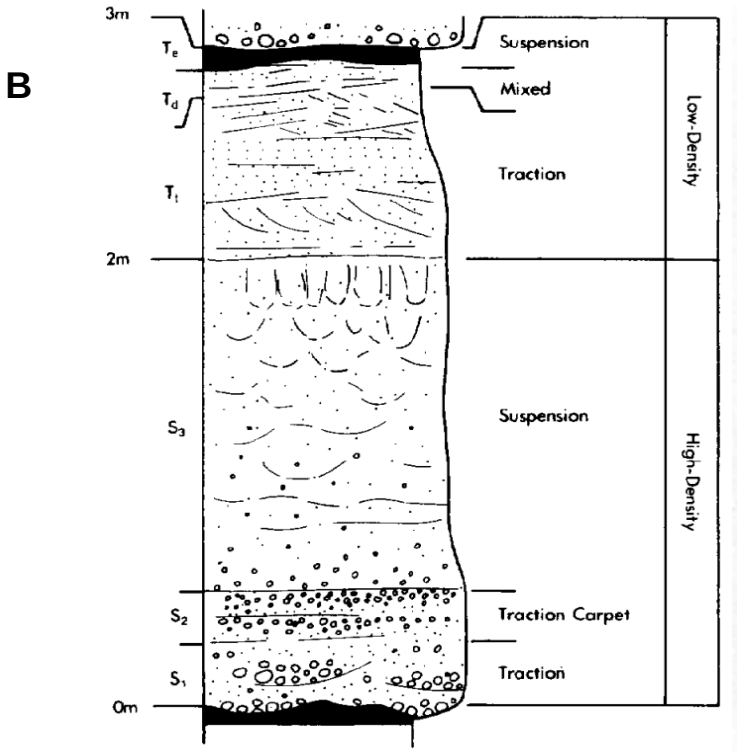

Figure 2.5: A) The Bouma sequence (Bouma, 1962) forms the first idealised model for deposition from a waning turbidite (Middleton and Hampton, 1973) B) The early idealised model for a high-density turbidite from Lowe (1982).

High-density turbidites

High-density turbidites (HDTs) are the depositional products of flows with high sediment concentrations (> ~10 % sediment-volume) and consequently high densities (e.g Mulder and Alexander, 2001). When these flows lose their capacity for transport (e.g. Hiscott et al. 1994), they rapidly deposit the entire grain size range of their sediment load, causing the suppression of near-bed turbulence, which prevents the formation of tractional bedforms (Baas et al. 2011; Talling et al. 2012). Grains in this turbulence-supressed lower region are supported by grain-grain interaction and hindered settling (e.g. Bagnold et al. 1962; Mulder and Alexander, 1972), and therefore have a poorly-defined flow-deposit boundary (Kneller and Branney, 1995). Sheared and truncated fluid-escape structures may also be preserved within HDTs, indicating pore water escape from a loosely packed and rapidly aggrading bed that was being sheared by the over-riding flow or still undergoing downslope gravity-driven transport (e.g. Lowe, 1982, Kneller and Branney, 1995).

HDTs therefore tend to be relatively thick, poorly-sorted, ungraded and structureless (Middleton and Hampton, 1973; Talling, 2012), with normal grading within the upper divisions sometimes present when the flow has evolved from a highly-concentrated lower region and less-concentrated upper/trailing region (Lowe, 1982; Postma, 1986) (Fig. 2.5B; 2.7), which may be manifested by an abrupt grain-size break (e.g. Talling et al. 2012; Stevenson et al. 2015) (Fig. 2.6). HDTs are difficult to distinguish from sand-rich debrites due to their often structureless appearance and lack of architectural constraint, which hinders identification of deposit pinchouts, causing some debate (e.g. Shanmugam, 1996; Talling et al. 2003; Amy et al., 2005).

Internal structures can be preserved in HDTs through the formation of 'traction carpets' (e.g. Dzulynsky and Sanders, 1962) (Fig. 2.5B), which result from grain-flow-like deposition of highly-concentrated layers transported through shear by the overriding flow (Lowe, 1982; Sohn, 1997). 'Spaced stratification' forms through progressive aggradation of these layers, which may result in inverse grading (Hiscott and Middleton, 1980; Sohn, 1997). Internal erosion surfaces and scour fills may also be preserved within HDTs as aggraded sediment is periodically scoured and filled by the surges within the overlying flow (e.g. Lowe, 1982).

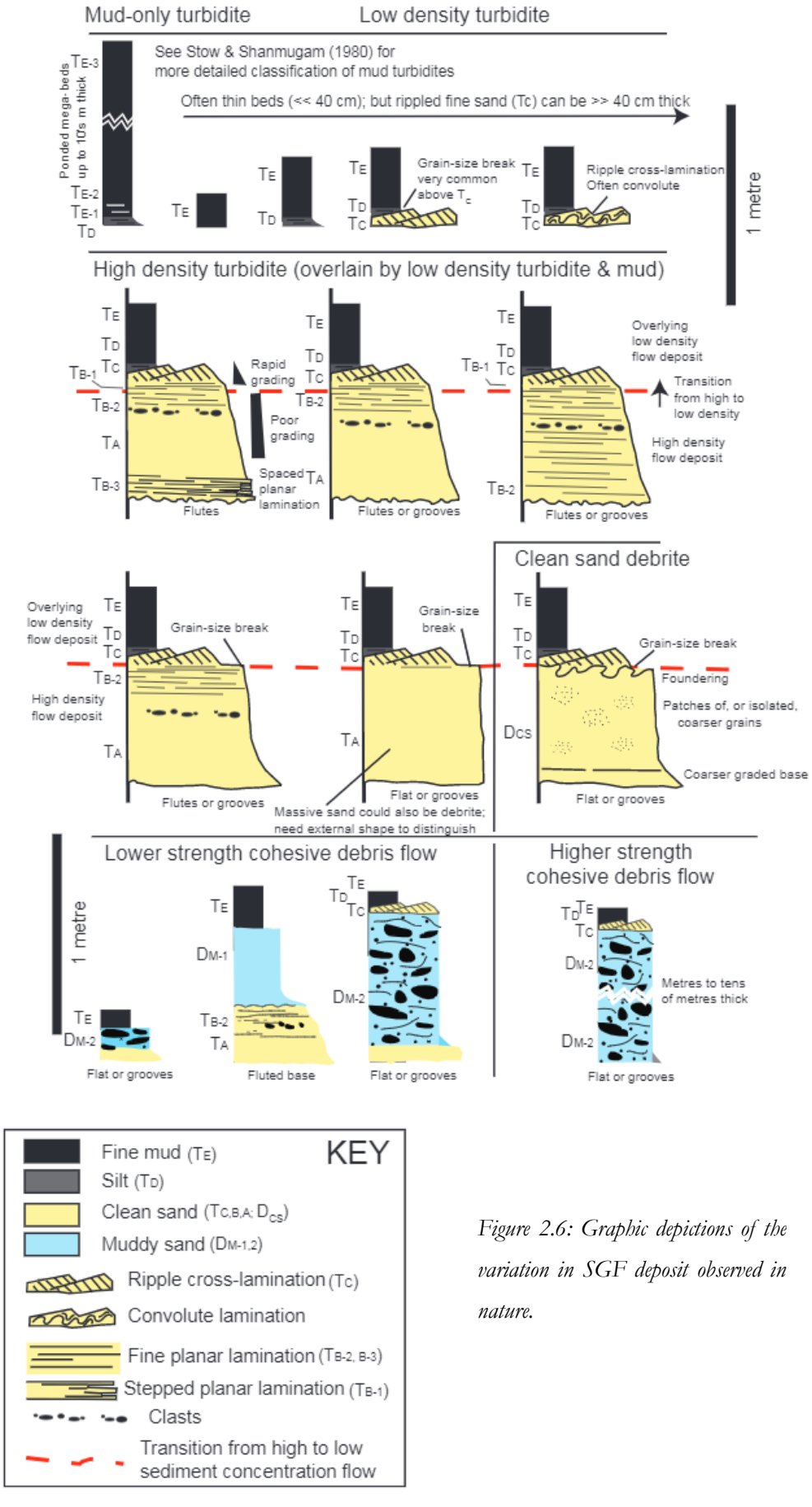

Figure 2.6: Graphic depictions of the variation in SGF deposit observed in nature.

HDTs are more likely to be deposited in proximal areas where high-energy flows capable of transporting high volumes of sediment are most prevalent, or at points of rapid deceleration e.g. at a reduction in slope angle or decreased confinement (Middleton and Hampton, 1973). HDTs are therefore characteristic of both channels axis (Hubbard et al. 2016; Jobe et al. 2017; Bell et al, 2018a) and lobe axis (Hodgson et al. 2006; Grundvåg et al. 2010; Bell et al. 2018a; Hansen et al. 2019) deposition.

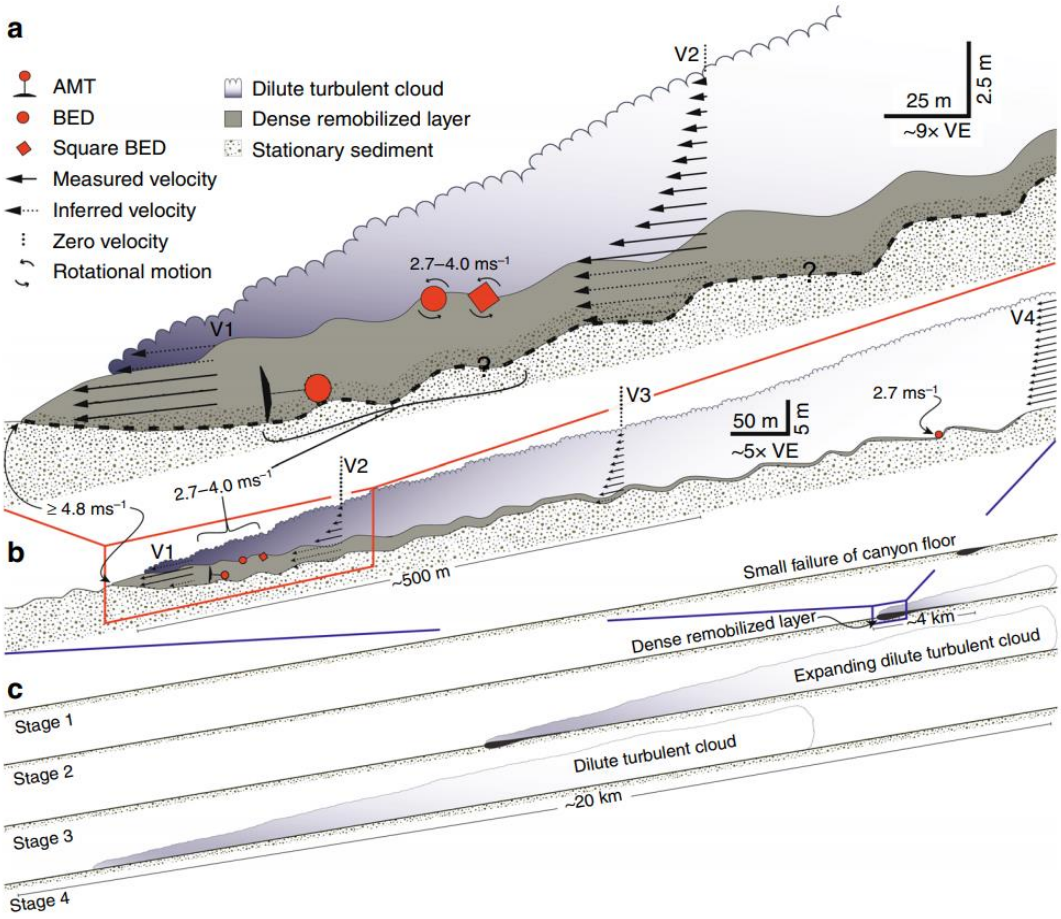

Figure 2.7: Synthesis of direct measurements from turbidity currents in the Monterey Canyon (Paull et al. 2018 The dense basal layers identified may produce the high-density turbidites seen in the rock record.

Debrites

Debrites are the depositional products of debris flows, and differ from turbidites because they 'freeze' as they decelerate and deposit en-masse (e.g. Middleton and Hampton, 1973). Debrites are typically identified as ungraded mud-rich deposits with floating clasts that pinch-out abruptly at their edges (Talling et al. 2013). Debrite thickness and clast-size depends on the yield strength of the parent debris flow, with high-strength debrites characterised by thick deposits capable of transporting km-scale clasts (e.g.

Hodgson et al. 2019), and low-strength deposits characterised by thinner debrites capable of transporting sand-grade clasts (Talling et al. 2013) (Fig. 2.6). The cohesive nature of debris flows makes them prone to deformation during transport (e.g. Jackson et al. 2011). This often results in the preservation of deformational structures, such as folding (e.g. Sobesiak et al. 2016) and faulting (e.g. Bull et al. 2009), within debrites.

Transitional flow deposits

Deposits may record flow behaviour intermediate between fully turbulent and fully laminar, or 'transitional' (Talling et al. 2004; Baas and Best, 2008; Baas et al. 2009; Sumner et al. 2009; Kane and Pontén 2012). This occurs when turbulent flows become enriched in mud as they flow down-slope through progressive deposition of coarser sediment or erosion and incorporation of mud (e.g. Haughton, 2003; Kane and Pontén 2012), causing the development of turbulence-enhanced near-bed layer and turbulence-suppressed upper layer within the flow (e.g. Baas et al. 2009) (Fig. 2.8).

Deposition from these flows records the longitudinal evolution of increasing mud concentration and density stratification within the flow, with a clean basal sand deposited

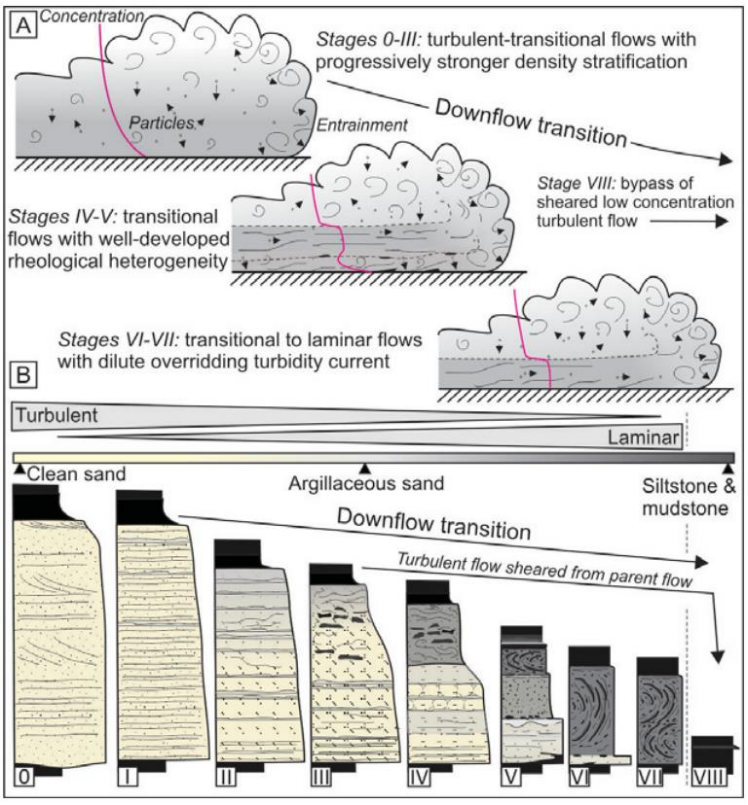

Figure 2.8: Model for the longitudinal rheological transformation of a turbulent flow and resultant deposits (Kane and Pontén, 2012).

by a lower turbulence-enhanced layer giving way to an increasingly thick debritic layer

down-dip as the plug-flow expands (Sumner et al. 2009; Kane and Pontén, 2012) (Fig. 2.8). Shearing by this over-riding plug-flow during aggradation may cause the development of shear fabrics within TFDs, and prevents the development of bedforms (Kane and Pontén, 2012). TFDs have been recognised in many deep-water systems, such as the North Sea (Lowe and Guy, 2000), East Carpathians (Sylvester and Lowe, 2004), and Gulf of Mexico (Kane and Pontén, 2012), and are typically associated with deposition in distal (Kane and Pontén, 2012) (Fig. 2.8) or topographically-confined (Lowe and Guy, 2000) environments where mud concentrations are able to rise.

Hybrid beds

Flows that transform from turbulent to laminar through increases in mud concentration may also deposit beds with more distinct divisions between deposits formed from turbulent and laminar flow, forming composite deposits known as 'hybrid beds'

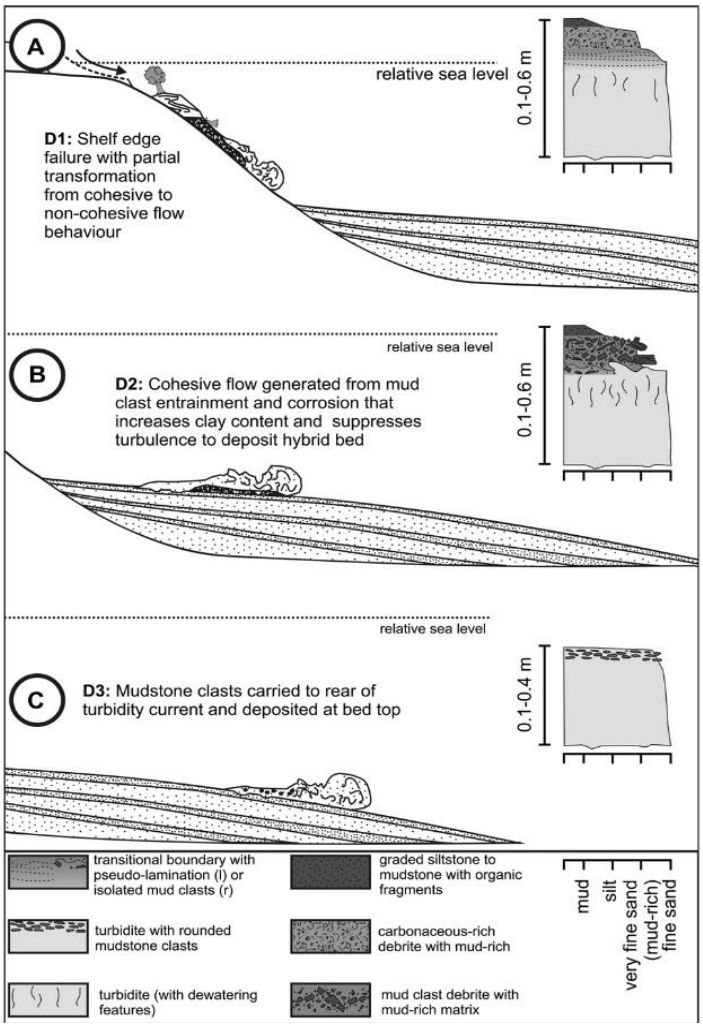

Figure 2.9: Mechanism for the emplacement of different types of exhumed hybrid bed identified in the Karoo Basin, South Africa (from Hodgson, 2009).

(Haughton et al. 2003, 2009; Talling et al. 2004; Davis et al. 2009; Hodgson, 2009; Baas et

al. 2011; Fonnesu et al. 2015, 2018; Patacci et al. 2014; Southern et al. 2015; Muller et al. 2017) (Fig. 2.9). Hybrid beds are typically observed as single event beds comprising a turbidite capped by, or associated with, a debrite (Talling et al., 2004; Jackson et al., 2009; Haughton et al., 2009). The upper debrite is sometimes termed a 'linked-debrite' (Haughton et al., 2003; Sumner et al. 2009 Jackson et al., 2009). Hybrid beds are thought to form through similar processes as TFDs, with numerous mechanisms for their emplacement proposed (e.g. Sumner et al. 2009; Talling et al. 2004) (Fig. 2.9), such as: incorporation of mud and rheological transformation during transport (e.g. Haughton et al. 2003; Hodgson, 2009; Kane et al. 2017), shearing and dilution of debris flows generating co-genetic turbulent flows (e.g. Fallgater et al. 2017), and settling of sand grains through low-strength debris flows (e.g. Marr et al. 2001).

Hybrid beds are typically differentiated from TFDs based the more defined separation between component depositional processes, with an often distinct boundary between the deposit of turbulent flow and the deposit of laminar flow seen within hybrid beds (e.g. Haughton et al. 2003; 2009). The boundary between these deposits, however, often records transitional flow conditions (e.g. Haughton et al. 2003; 2009) and there is a complicated stratigraphic relationship between the flow phases (Fonnesu et al. 2015), making an interpretation of flow process from deposit particularly difficult within hybrid beds and transitional flows.

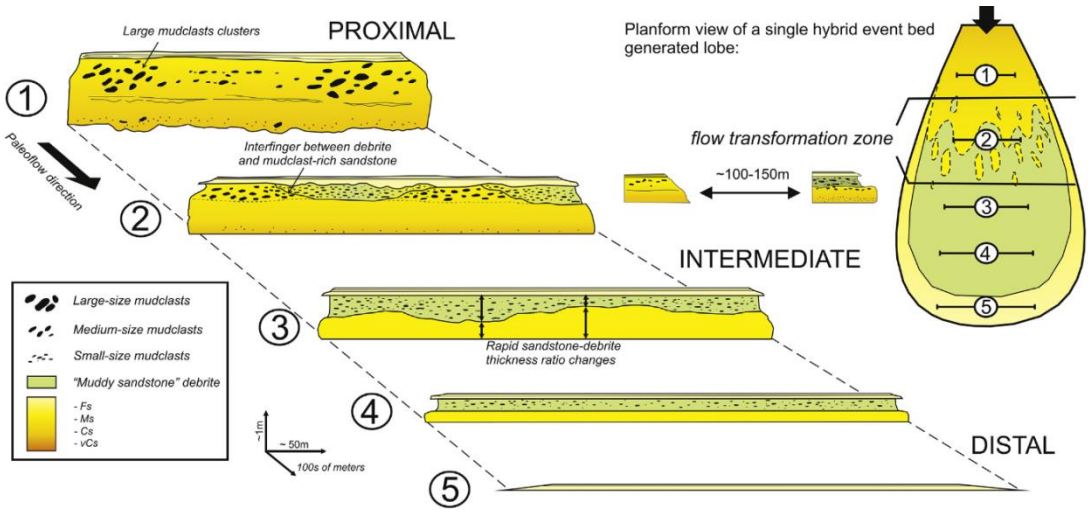

Figure 2.10: Schematic diagram showing the longitudinal evolution of hybrid beds on a lobe (from Fonnesu et al. 2015).

Hybrid bed deposition typically requires long run-out distances to allow flow segregation and elevated mud concentrations, and is therefore often found in the distal

extents of deep-water systems (Davis et al. 2009; Hodgson et al., 2009; Pyles and Jenette, 2009; Spychala et al. 2017) (Fig. 2.10). It has also been observed that flow deceleration due to basinal topography (Tinterri and Magalhaes, 2011; Patacci et al., 2014; Southern et al. 2015) and enhanced erosion at channel-lobe transitions (e.g. Mueller et al. 2017) may cause the deposition of relatively proximal hybrid beds, which complicates the interpretation of these deposits as purely distal facies.

Mass-transport

Large-scale slope failure can cause the deposition of large masses of lithified and unlithified sediment hundreds of kilometres into the basin (Hampton et al., 1996; Locat and Lee, 2002; Moscardelli and Wood, 2008), forming some of the largest depositional events on Earth (Talling et al. 2007a; Georgiopoulou et al. 2010; Calvès et al. 2015) (Fig. 2.11). The deposits of these failures are generally referred to as submarine landslides (Hampton et al. 2006; Masson et al. 2006) or mass-transport deposits (MTDs), and can vary from debrites, slides, to slumps and relatively dilute flows, depending on source material and the degree of disaggregation (Nardin et al., 1979). MTDs are also associated the formation of large scours, or 'megascours' (e.g Moscardelli et al. 2006), at their base (Fig. 2.11C) and the transport of large allochthonous clasts, or 'megaclasts' (e.g. Jackson, 2011; Hodgson et al. 2019), into deep-water (Fig. 2.11B). MTDs are therefore associated with deposits of widely varying lithology and depositional relief (Bryn et al. 2005; Kneller et al. 2016; Fallgatter et al. 2018). In seafloor and subsurface data it is generally not possible to recognize individual event deposits reliably, for this reason 'mass-transport complex' (MTC) is often used to depositional bodies interpreted as being emplaced by mass-transport on seismic data (Weimer and Shipp, 2004; Moscardelli and Wood, 2008).

Mass-transport occurs in many depositional environments, including: submarine canyons (Carlson and Karl, 1988), volcanic ridges (Moore et al., 1989), lakes (Schnellmann et al. 2005), fjords (Prior et al., 1982) and open continental margins (Calves et al., 2015), and can triggered by tectonic activity (e.g. Ortiz-Karpf et al. 2016), volcanic activity (e.g. Chadwick Jr et al. 2012), excess pore pressures (Urlaub et al. 2018) and glacial advance (Bryn et al. 2005).

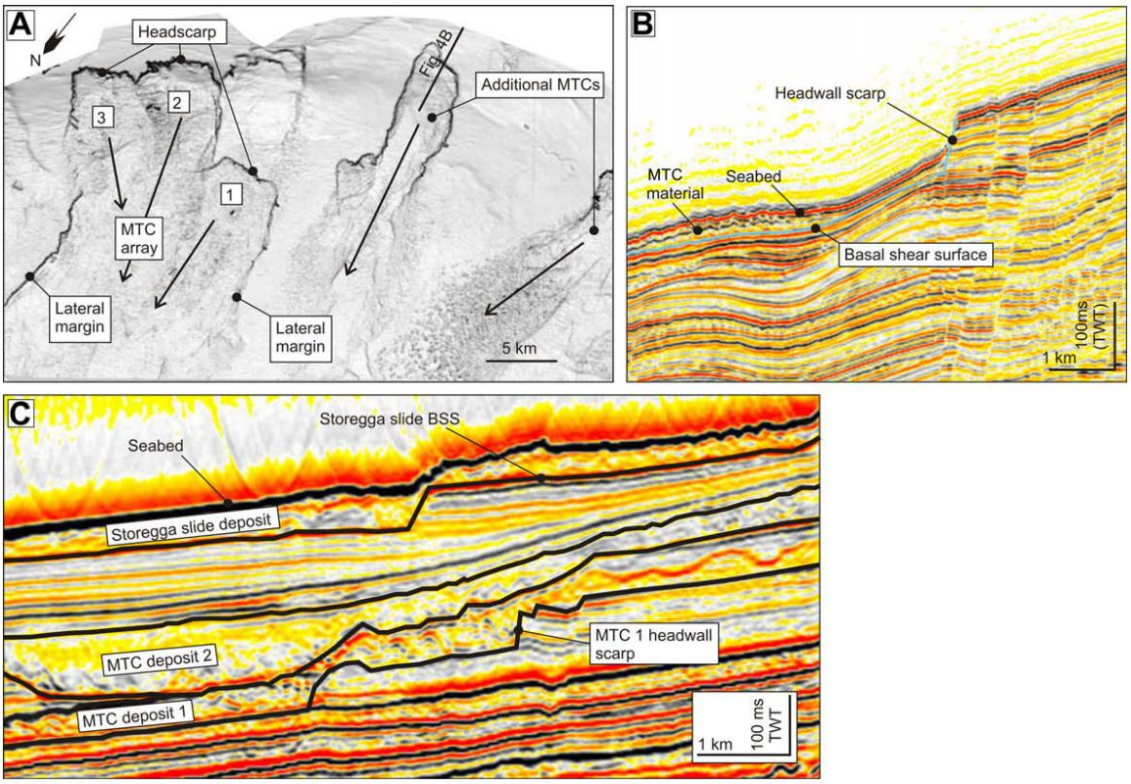

Figure 2.11: Examples of the depositional features typically associated with mass-transport complexes, such as headscarps (A,B), megaclasts (A lower left), and significant basal erosion (C). From Bull et al. (2009).

2.4 *Geomorphic elements of deep-water systems*

Modern and ancient deep-water systems are linked by common geomorphic elements that evolve in response to SGF erosion and deposition through time (e.g. Walker, 1967, 1978; Normark, 1978; Normark et al. 1979; Deptuck et al. 2007; Prather et al. 2012). These elements can be broadly sub-divided into canyons, channels, channel-lobe transition zones, and lobes.

Canyons

Submarine canyons are major conduits for the delivery of sediment from shallow to deep-water and have been identified in the modern (e.g. Spencer, 1903; Covault et al. 2011, 2012; Harris and Whiteway, 2011) and ancient (e.g. Von der Borch et al. 1985; Morris et al. 1988) as erosional and predominantly linear features that are incised into the slope or shelf (Fig. 2.12). Submarine canyons are formed by a combination of submarine erosion beneath successive SGFs, retrogressive slope failure, and subaerial erosion during low sea-levels (e.g. Daly et al. 1936; Farre et al. 1983; Pratson and Coakley, 1996; Talling, 1998; Popescu et al. 2004; Krastel et al 2001), and can be hundreds of kilometres in length, tens of kilometres wide, and several kilometres deep (Harris and Whiteway, 2011). Canyons are either: 1) shelf-incised and directly connected to a river, 2) shelf-incised and not directly connected to a river, or 3) slope-incised ('blind'), with shelf-incised canyons more common on active continental margins and continental margins supplied with high volumes of sediment (Harris and Whiteway, 2011) (Fig. 2.12).

Modern submarine canyons are composed of an axis or axial channel, which when sampled on the seafloor is coarse-grained, and a steep finer-grained margin prone to slope failure (Paull et al. 2005). Decametre-long crescentic bedforms are also evident in canyon axes, with direct measurements within the Monterey Canyon axis indicating they are formed by periodic SGFs (Paull et al. 2010). When exhumed, canyon fills are characterised by coarse-grained HDTs and barforms in a canyon axis confined by a slump-dominated inner-canyon margin (Anderson et al. 2006). Flows that enter submarine canyons are often not of high enough magnitude to flow through the entirety of the canyon (Howell and Normark, 1982), with only rare high-magnitude events passing through the canyon, eroding the canyon floor, and depositing further down-slope (e.g. Jobe et al. 2018).

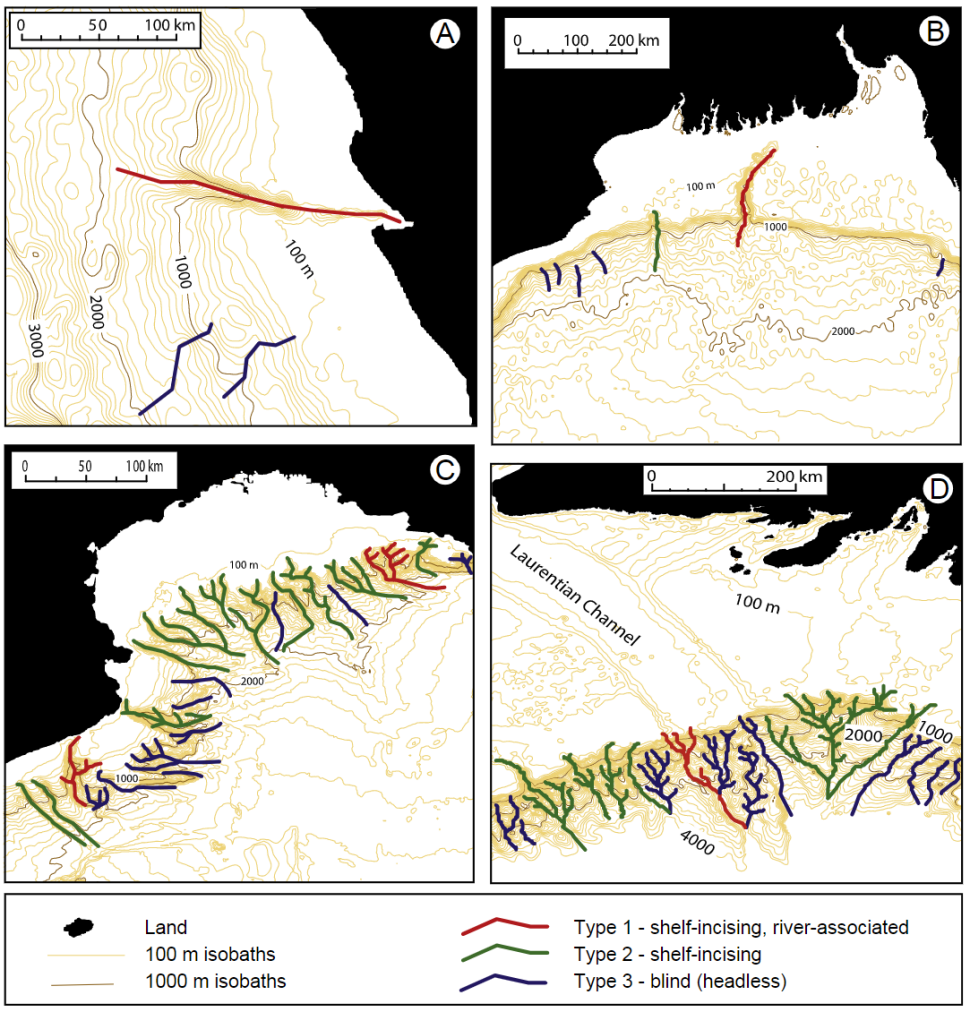

Figure 2.12: Examples of the different types of submarine canyon seen globally. A) Congo Canyon, B) Swatch-No-Ground Canyon, Bay of Bengal, C) Gulf of Lion, D) Eastern Canada (Harris and Whiteway, 2011).

Channels

Submarine channels are erosional or depositional features on the seafloor that are capable of transporting vast quantities of sediment down-dip (e.g. Menard, 1955; Normark et al. 1983; Mutti and Normark, 1987; Clark and Pickering, 1996; Peakall et al. 2000; Abreu et al. 2003; Deptuck et al. 2007; Straub et al. 2008; Kane et al. 2010; 2011; Mayall et al. 2010; Hodgson et al. 2011; Sylvester et al. 2011; Figueiredo et al. 2013; Hubbard et al. 2014; Hansen et al. 2015; Jobe et al. 2017; McArthur et al. 2019; Kneller et al. 2019) and often evolve from canyons up-dip (e.g. Normark, 1978; Covault et al. 2011, 2012) (Fig. 2.13). Submarine channels tend to initiate during a period of erosion and bypass (Elliott, 2000; Fildani et al. 2013; Stevenson et al. 2015), becoming increasingly entrenched on the slope through repeated phases of incision (Sylvester et al. 2011; Hodgson et al. 2016) (Fig. 2.14). Sedimentation within submarine channels is typically characterised by an early phase both

of lateral channel fill migration (e.g. Covault et al. 2016) and repeated erosion (e.g. Hage et al. 2018; Englert et al. 2018; Vendettuoli et al. 2019) (Fig. 2.14).

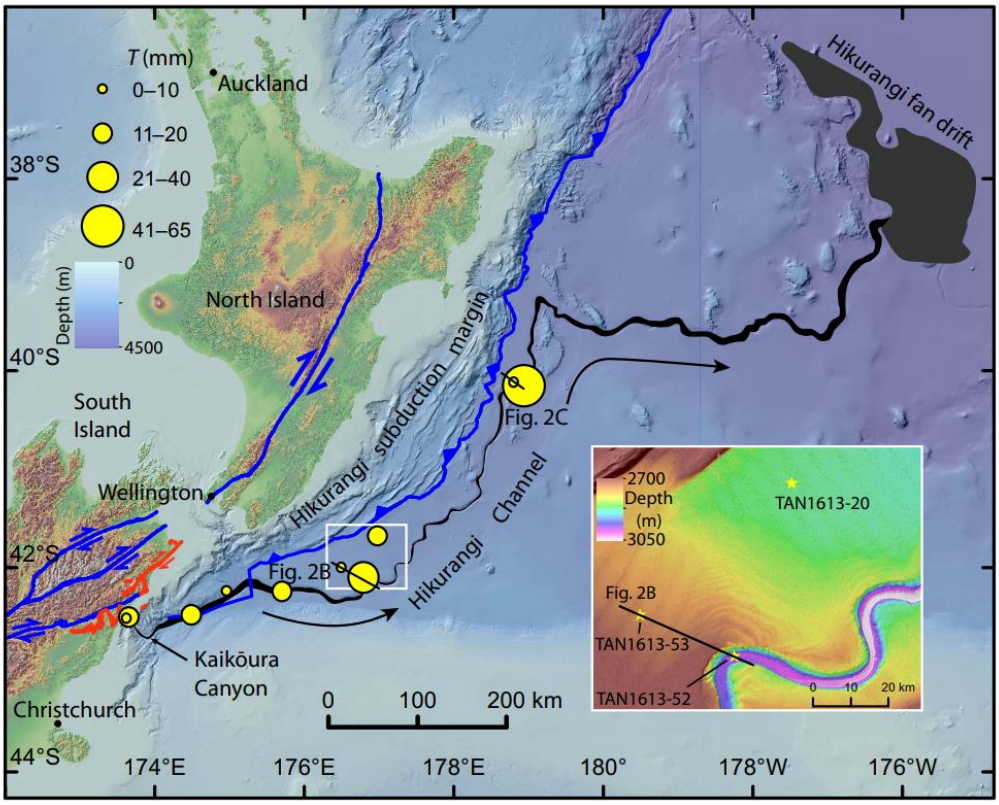

Figure 2.13: The 1500 km-long Hikurangi Channel offshore New Zealand. This Channel has was shown to transfer sediment destabilised during seismic events, and is fed by > 10 submarine canyons (Mountjoy et al. 2018).

As aggradation rates increase channel-fills begin to migrate vertically (e.g; McHargue et al. 2011; Covault et al. 2016) (Fig. 2.14), with channel sinuosity also tending to increase through time (Kane et al. 2008; Peakall et al. 2010; Sylvester et al. 2011, Maier et al. 2013). Aggradation within channels occurs in response to a change in flow properties (Kneller, 2003), driven by sediment supply or sea-level changes (e.g. Mutti and Normark, 1991; Kneller, 2003; Syvlester et al. 2011), or a decreased slope angle (e.g. Kneller, 2003; Sylvester et al. 2011; McHargue et al., 2011). Aggradation will continue until the accommodation space within the channel is filled and avulsion occurs (e.g. Clark and Pickering, 1996; Maier et al. 2013;) or deformation re-routes flows (e.g. Sylvester et al. 2011), resulting in channel abandonment (e.g. Figueiredo et al. 2013).

The large variation in channels identified in the subsurface and at outcrop has led the development of hierarchical models that attempt to normalise descriptions across different deep-water systems (e.g. Campbell, 1967; Sprague et al., 2002; 2005; Campion et al., 2003; McHargue et al., 2011; Maier et al. 2013). The primary architectural component is the channel element (McHargue et al., 2011; Macauley and Hubbard, 2013) or storey (Sprague et al. 2003), with genetically related channel elements stacking together to form an individual channel complex (McHargue et al. 2011). Genetically-related complexes form a channel complex set (Campion et al., 2003; McHargue et al., 2011).

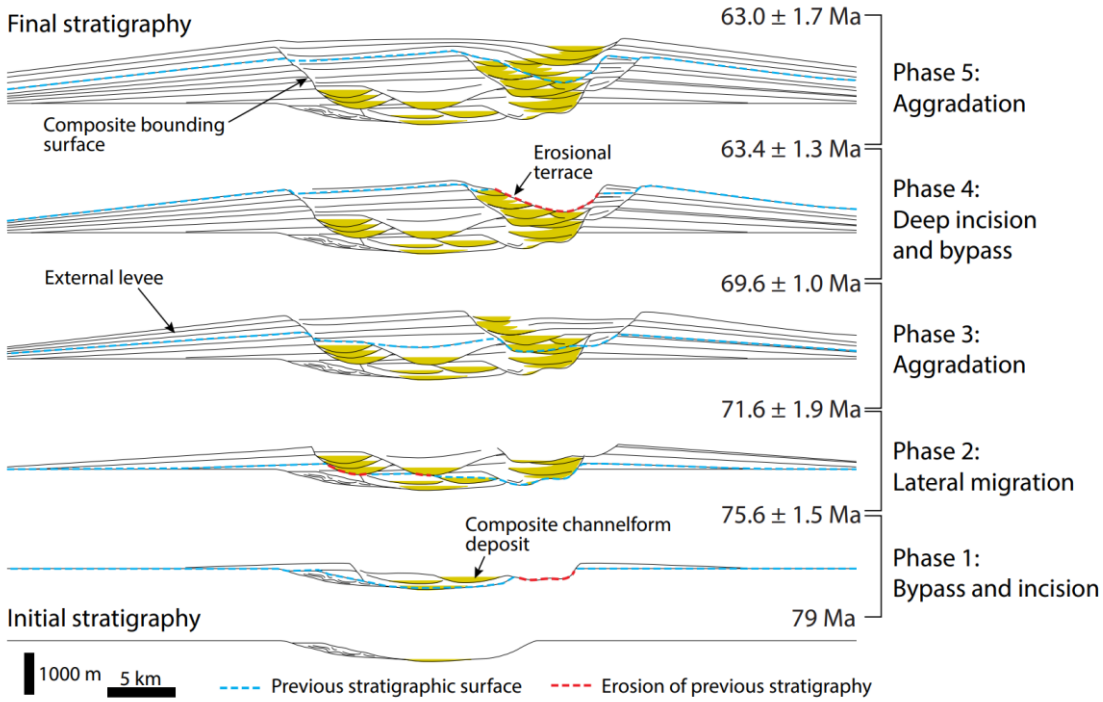

Figure 2.14: Evolution of a Late Cretaceous channel system constrained using outcrop and detrital zircon data (Englert et al. 2019).

Channel complex sets are composed of a channel-belt with an axis and margin (e.g. Kneller et al. 2019). Channel belt margins consist of geomorphic elements such as terraces and internal levees (Kane and Hodgson, 2011; Kane et al. 2011; Hansen et al. 2017; Kneller et al. 2019). Channel complex sets are confined by either an external levee, formed by repeated overspill of channelized flows (e.g. Normark et al. 1983; Kane and Hodgson, 2011), or an erosion surface (Kneller et al. 2019). In general, a submarine channel system is composed of one or more complex sets that can be tied to a sequence stratigraphic framework, with multiple complex sets typically representing a 3rd order sea-level cycle (1 – 10 My) and a single complex set representing higher-order cycles (< 1 My) (McHargue et al., 2011).

Channel-lobe transition zones

When flows exiting channels lose confinement or encounter a break in slope they form a geomorphic element called a channel-lobe transition zone (CLTZ), which marks the region between well-defined channels and lobes (e.g. Palanques et al. 1995; Wynn et al. 2002; Hofstra et al. 2015; Stevenson et al. 2015; Carvajal et al. 2017; Maier et al. 2018; Brooks et al. 2018; Pohl, 2020). Modern CLTZs can vary in downstream size from a few kilometres (Normark et al. 1979) to greater than 100 km (Kenyon and Millington, 1995; Morris et al. 1998), and tend to be characterised by bypass and erosion (e.g. Garcia and Parker, 1989; Wynn et al. 2002; Brooks et al. 2018), which has been attributed to enhanced turbulence as rapidly decelerating flows undergo a hydraulic jump (Garcia and Parker, 1989; Kenyon et al. 1995; Dorrel et al. 2016) or flow 'relaxation' as flows thin upon loss channel of confinement, resulting in a lowering of the velocity maximum (Pohl et al. 2019a).

Deposition in CLTZs is often manifested by large (10s m to 1000s m) depositional features, such as sediment waves and scour-fills (e.g. Wynn et al. 2002; Palanques et al. 1995; Fildani and Normark, 2004; Hofstra et al. 2015; Pemberton et al. 2016). CLTZs are typically poorly preserved as they are subject to repeated periods of erosion and aggradation as flow axes laterally migrate at mouth of feeder channels (e.g. Hofstra et al. 2018), thus CLTZs tend to require channel avulsion or enhanced aggradation to be preserved (Pemberton et al. 2016; Brooks et al. 2018).

Lobes

Lobes are lobate depositional bodies formed at the distal extents of deep-water systems (e.g. Normark, 1978; Normark et al. 1979, 1983; Mutti, 1992; Postma et al. 1993; Deptuck et al. 2008; Prélat et al. 2009, 2010, 2011; Grundvåg et al. 2014; Marini et al. 2015; Spychala et al. 2016, 2017; Kane et al. 2017; Dodd et al. 2018; Rabouille et al. 2019; McHargue et al. 2019) (Fig. 2.15). Lobe deposition occurs in response to flows spreading radially and decelerating as they exit the confines of a channel (e.g. Normark, 1978; Mutti, 1992; Kane et al. 2017). Lobes typically thicken from the mouth of the channel and through the CLTZ to an apex (e.g. Brooks et al. 2018) via flow relaxation and bypass upon loss of channel confinement (Pohl et al. 2019a), with thinning and fining occurring laterally and distally (Deptuck et al. 2008; Spychala et al. 2017; Hansen et al. 2018) (Fig. 2.16). This depositional pattern generates positive relief on the seafloor, resulting in compensational

stacking of successive lobes (e.g. Groenenburg et al. 2010; Straub et al. 2012; Jobe et al. 2017) (Fig. 2.16B).

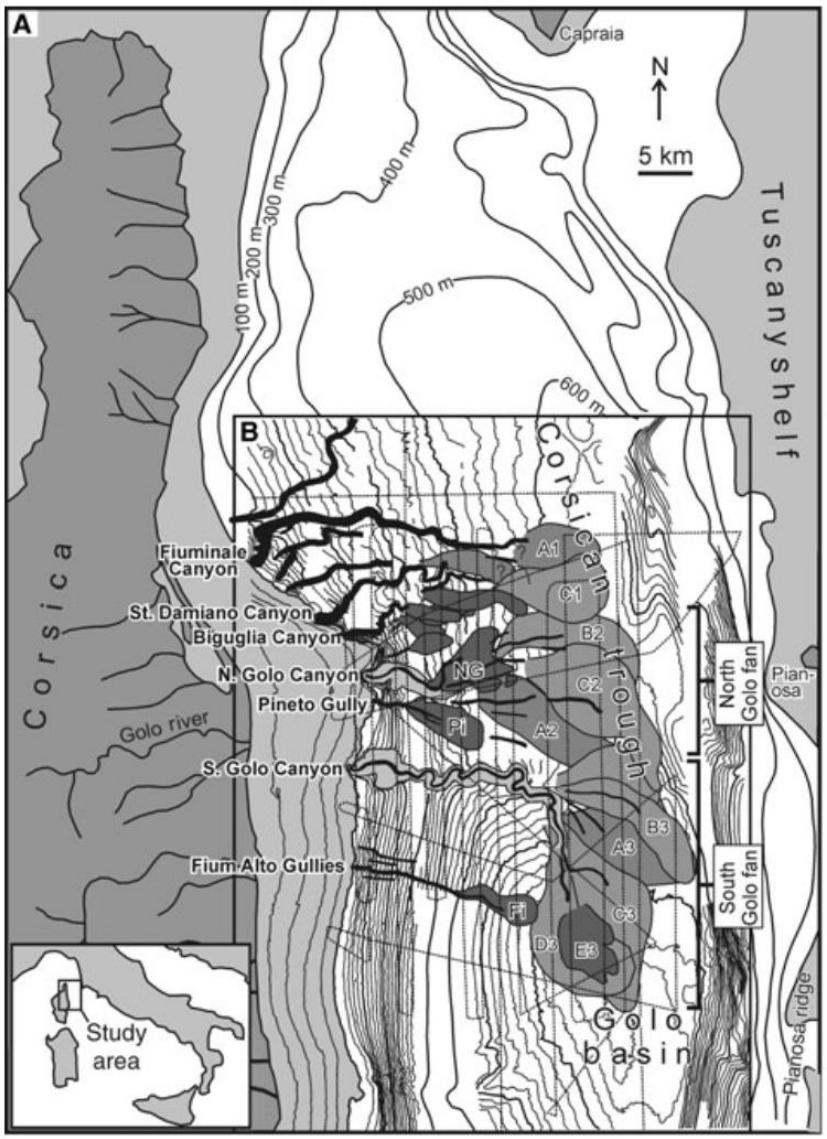

Figure 2.15: Submarine lobes deposited in Corsican Trough mapped using seismic data by Deptuck et al. (2008). Each lobe is fed by a canyon-channel system, with the lobes building to form the North and South Golo fan.

Lobes can be divided into sub-environments based on the proximal-distal and proximal-lateral evolution of the flows that build them (e.g. Walker, 1967; Mutti, 1977; 1992; Chen and Hiscott, 1999; Grundvåg et al. 2014; Spychala et al. 2015, 2017; Kane et al. 2017; Bell et al. 2018ab; Fonnesu et al. 2018; Hansen et al. 2019), with high- and medium-density turbidites of the lobe axis and off-axis transitioning down-dip to transitional flow deposits, hybrid beds and low-density turbidites of the lobe fringe (e.g. Walker, 1967; Haughton, 2003; Kane and Ponten, 2012; Spychala et al. 2017; 2019; Boulesteix et al. 2019ab) (Fig. 2.17). Hybrid beds are preferentially developed in the frontal lobe fringe as

flows within the axis of lobes are more erosive, and therefore more capable of incorporating mud and rheologically transforming (Spychala et al. 2017), and because muddy dense flows have more momentum, thus show reduced radial spreading in a downstream direction (Fig. 2.17).

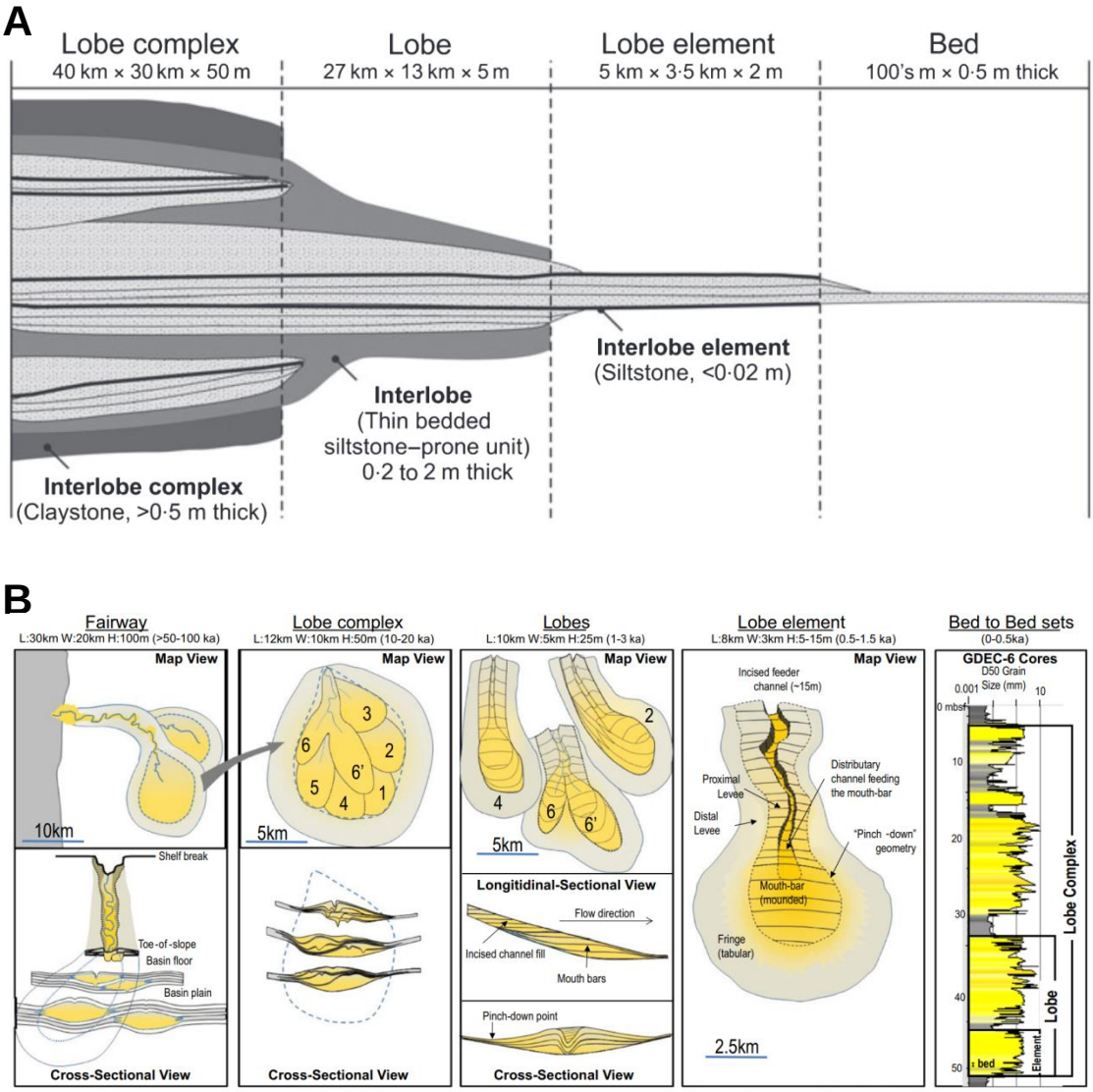

Figure 2.16: The outcrop-derived (B) hierarchy of submarine lobe systems from Prélat et al. (2009), applied to subsurface Quaternary lobes offshore Corsica by Sweet et al (2019).

As with channels, a hierarchical framework can be applied to lobes (e.g. Pyles et al. 2007; Prélat et al. 2009; Deptuck et al. 2008; Straub and Pyles, 2012; Sweet et al. 2019) (Fig. 2.16). Different lobe elements were identified in a Pleistocene submarine fan through seismic interpretation by Gervais et al. (2006), however this study lacked lithological constraint. Deptuck et al. (2008) integrated core with seismic observations, which addressed some of these uncertainties, and added terms such as proximal isolated lobes

(PILs) and composite mid-fan lobes (CMLs) to the nomenclature. Much of the most recent key work on lobe architecture and hierarchy has been derived from the well exposed deep-water sediments of the Karoo Basin, South Africa (e.g. Prélat et al., 2009; 2010; 2013; Hodgson, 2009; Kane et al. 2017; Spychala et al. 2017), with stacks of individual event-beds interpreted to form a lobe element (Fig. 2.16A). Lobe elements in turn stack to form lobes, with a sequence of genetically related lobes making up a lobe complex (Prélat et al. 2009). Similar hierarchies have since been described in modern lobe systems (e.g. Sweet et al. 2019) (Fig. 2.16B).

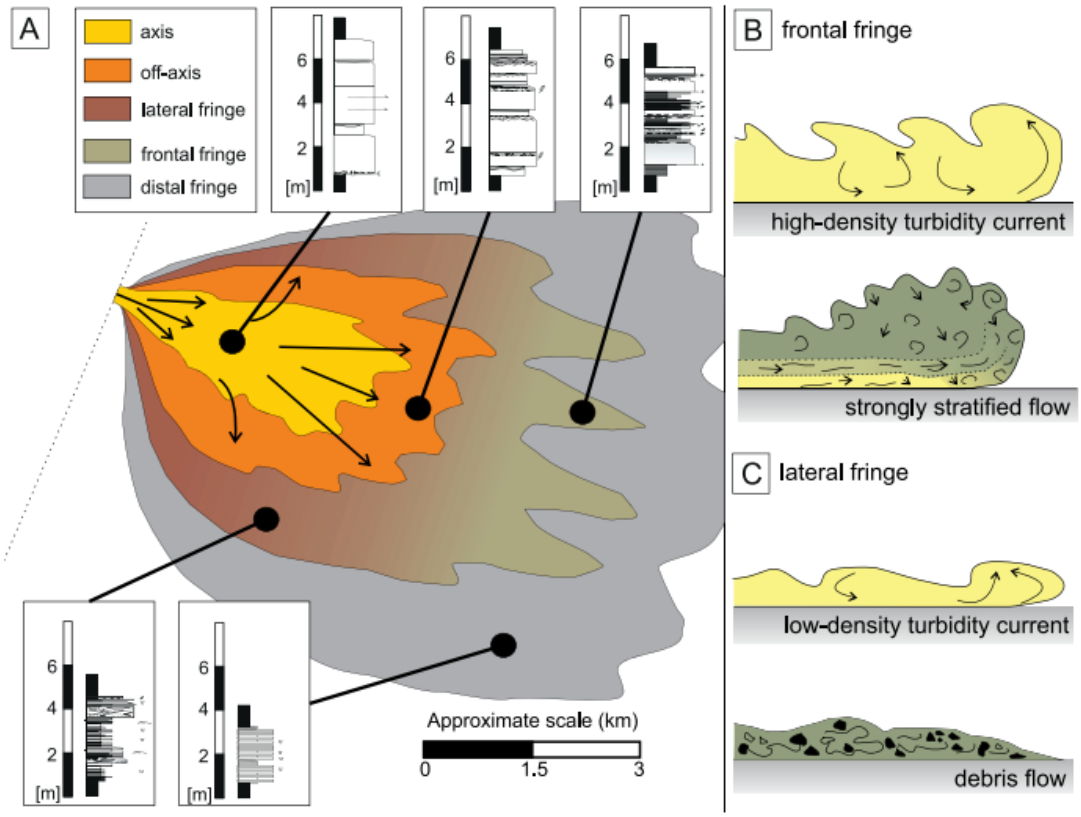

Figure 2.17: Facies associations related to submarine lobe sub-environments. These associations reflect the longitudinal evolution of flows across a lobe. B, C) Flow process change from the frontal fringe to the distal fringe (Spychala et al. 2017).

Differentiation between these hierarchical elements has been defined using the thickness of bounding and fine-grained 'interlobes' (Prélat et al. 2009), with interlobe thicknesses positively correlating with position in the hierarchy. An interlobe element, for example is < 2 cm thick, while an interlobe is up to 2 m thick (Fig. 2.16A). From this Prélat et al. (2009) suggested a changing depositional control up-hierarchy, with lobe elements tending to be controlled by autogenic compensation and lobe complexes controlled by allogenic sediment supply shut-off. Recent work by Boulesteix et al. (2019ab) has shown

that interlobes are composed of mm-scale event beds, and are the distal or lateral extents of lobes.

2.5 *Topographic controls on deep-water sedimentary systems*

One of the earliest observations of SGFs being affected by topography was noted by Menard (1957), who showed through seafloor bathymetry data, or "echograms", from the Baja California Seamount Province that topography on the seafloor was steering canyon-sourced sediment gravity flows. Gorsline and Emery (1959) then used bathymetry and core data to show that seafloor topography may partition the seafloor into a series of confined sub- or minibasins that are sequentially filled from proximal to distal by successive flows (Fig. 2.18). This early model can be regarded as one of the first models for the stratigraphic evolution of a confined basin. The following sections will discuss some of the features of SGF interaction with topography and the stratigraphic evolution of confined basins since these early models were proposed.

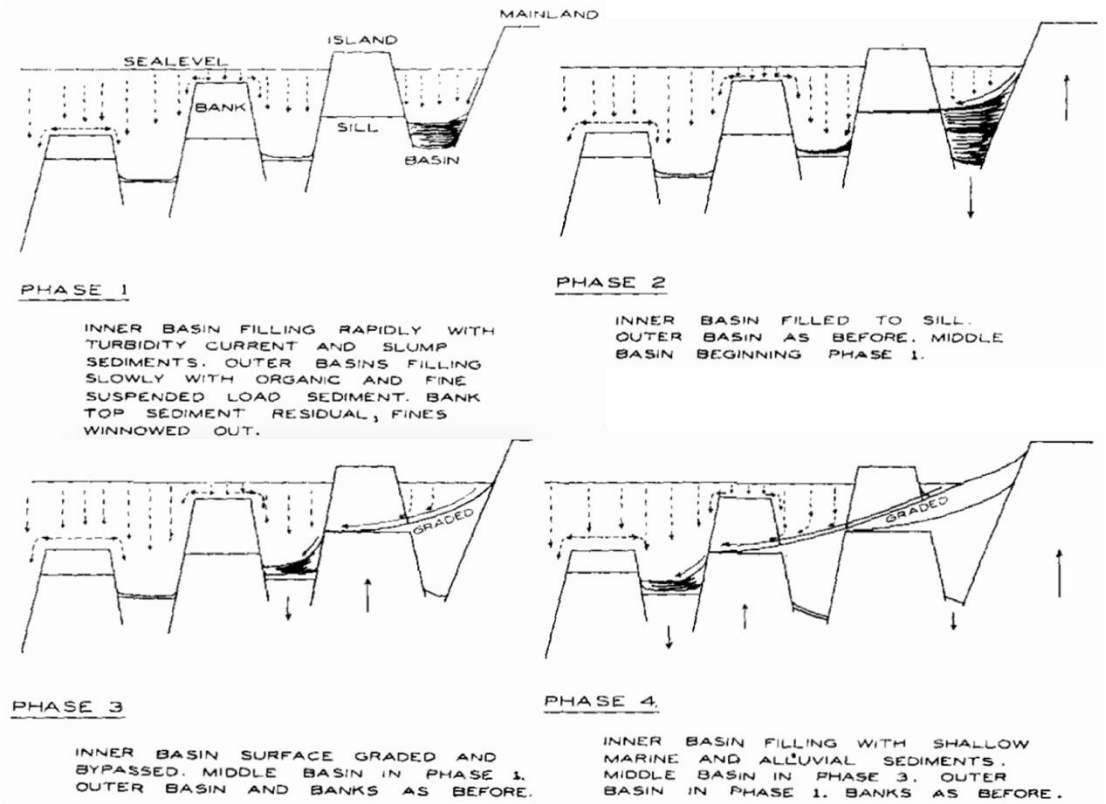

Figure 2.18: An early model for depositional evolution of confined basins from offshore California (Gorsline and Emery, 1959). Fault-bound basins fill proximally until they reach the basin spill-point (a low within the confining bank or 'sill') and are able deposit into more distal down-dip basins.

Why are sediment gravity flows affected by topography?

Sediment gravity flows are driven down-slope by the force of gravity acting upon them (e.g. Daly, 1936). The shape of this slope dictates the direction and speed of these flows, which will affect the location and character of their deposits (e.g. Kneller, 1995). The deposits of SGFs can therefore be used to infer the shape of the topography that the flow interacted with, and the nature of flows themselves. SGFs are attributed to a spectrum of different flow processes (e.g. Middleton and Hampton, 1973; Mulder and Alexander, 2001; Talling et al. 2015), accordingly their response to topography will be different. Kneller and McCaffrey (1999) suggested that the basal and denser part of an individual flow will respond differently to topography than the upper and more dilute part of the same flow, which will affect deposition adjacent to topography; this was described using the internal Froude number (F_i):

$$F_i = U/(Nh)$$

where U is the depth-averaged velocity, h a charactestic length scale (e.g. thickness of current or height of topography) and N is the buoyancy frequency, which is positively correlated with the density of the flow. When F_i is small, dividing streamlines will exist within a flow. Above the streamline, kinetic energy is sufficient to allow the flow to run up and over an obstacle, below the streamline the flow will be deflected around the obstacle. It therefore follows that the high-density flows, or high-density regions of flows (with higher *N* values), will be more affected by topography than lower-density flows or lower-density regions of flows (with lower *N* values). Deposits from these flows, or an individual stratified flow, will consequently be differentially distributed around topography, resulting in deep-water facies distributions that may be indicative of topographic interaction.

Topographically-influenced facies

Flow interaction with topography has been shown to result in a range of facies variations that are characteristic of deposition adjacent to slopes (Pickering and Hiscott, 1985; Sinclair, 1994; Kneller and McCaffrey, 1999; McCaffrey and Kneller, 2001; Felletti, 2002; Al Ja'Aidi et al. 2004; Lomas and Joseph, 2004; Bersezio et al. 2005; Pyles and Jennette, 2009; Stevenson and Peakall, 2010; Bakke et al. 2013; Patacci et al. 2014; Spychala et al. 2016, Southern et al. 2017; Cunha et al. 2017; Tinterri et al. 2017; Bell et al. 2018a). Topographic interaction, for example, has used to explain the deposition of thick, sand-rich turbidites adjacent to paleo-slopes (e.g. Alexander and Morris, 1994; Kneller and McCaffrey, 1995; Puigdefàbregas et al. 2004; Bersezio et al. 2005; Stevenson and Peakall,

2010; Tinterri and Magalhaes, 2011) through processes such as: 1) rapid flow deceleration and aggradation (e.g. Kneller, 1995; Bersezio et al. 2005), 2) rapid flow deceleration and hydraulic jump formation (Alexander and Morris, 1994; Spinewine et al. 2009), and 3) rapid aggradation, density contrast reduction, and 'lofting' of the flow (Stevenson and Peakall, 2010).

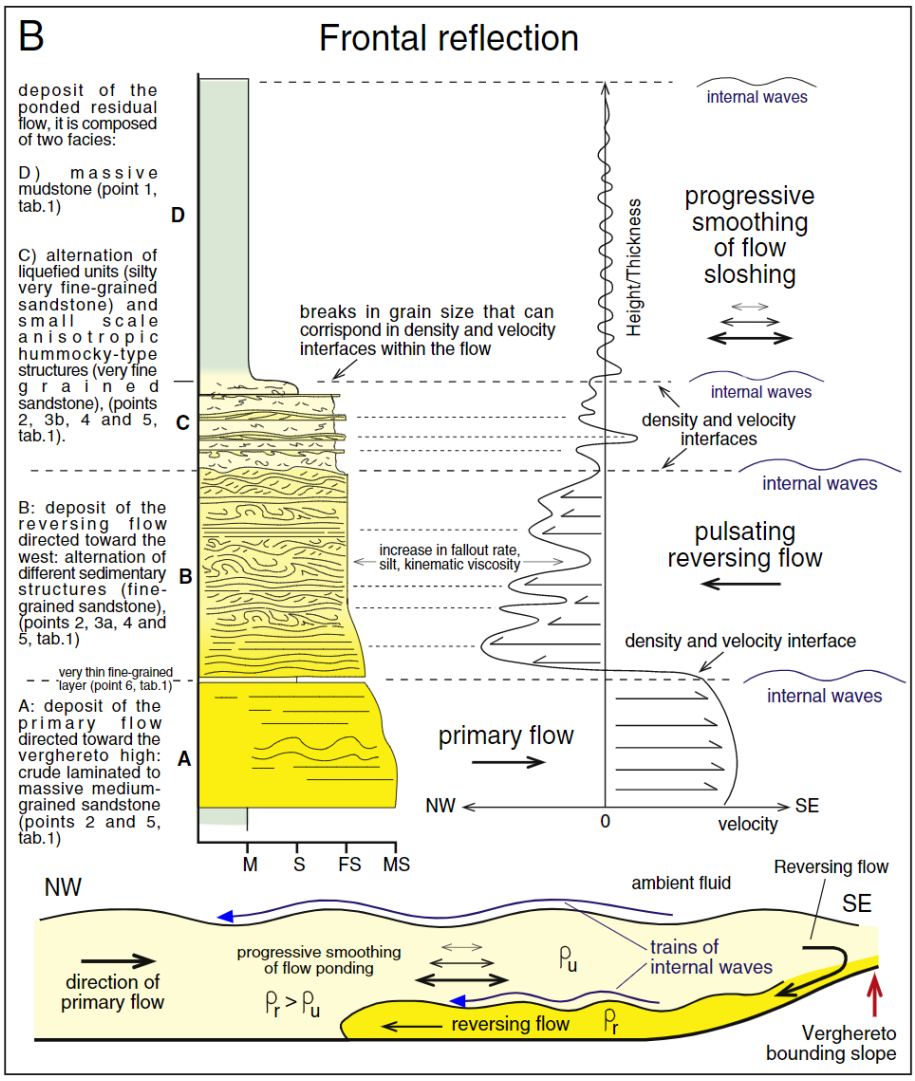

Figure 2.19: Example of the reflected facies that may be produced as turbulent flow ineracts with topography (Tinterri et al. 2016).

Topographic interaction may also cause flow deflection (Fig. 2.19), which can result in 1) remobilisation and re-deposition of sand deposited higher on the slope at the foot of the slope (e.g. McCaffrey and Kneller, 2001; Puigdefàbregas et al. 2004), 2) run-up and collapse of the high-velocity base of a flow into its more dilute cloud (Haughton, 1994; Hodgson and Haughton, 2004), 3) pulsing and repetition of turbidite divisions (i.e. Bouma divisions) (e.g. Edwards et al. 1994), or 4) along-slope flow acceleration or constriction,

resulting in enhanced bypass and erosion (e.g. Kneller, 1995; Kneller and McCaffrey, 1999; Jobe et al. 2017).

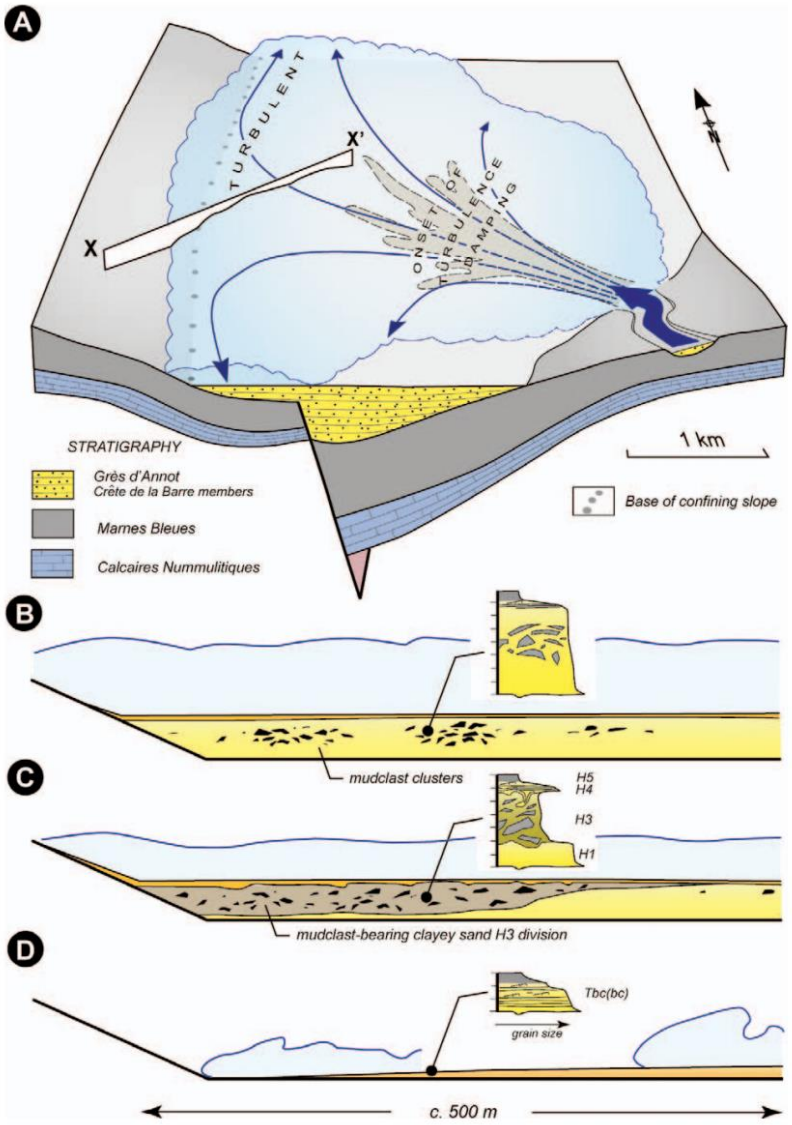

Figure 2.20: Model for hybrid bed development adjacent to topography based on outcrop data from SE France (Patacci et al. 2014)

Topographic interaction may also result in laminae-scale soft-sediment deformation (e.g. Tinterri, 2016) and complex tractional structures (e.g. Pickering and Hiscott, 1985) as flows deflect off counter-slope and re-work their aggrading deposit (Allen, 1985; Pantin and Leeder, 1987; Muck and Underwood; 1990; Patacci et al. 2015; Bell et al. 2018a) (Fig. 2.19). This re-working can also result in paleocurrent divergence adjacent to topography, which can be used to reconstruct the shape of the topography (Pickering and Hiscott, 1985; Marjanac, 1990; Kneller et al. 1991; Sinclair, 1994; Marini et al. 2015).

High-aggradation rates adjacent to topography and consequent loss of sand-grade sediment has also been shown to enrich flows in mud, resulting in short length-scale (10s – 100 m) rheological flow transformation and hybrid bed deposition (Lowe and Guy, 2000; Patacci et al. 2014; Barker et al. 2008; Southern et al. 2015; Southern et al. 2017; Bell et al. 2018b) (Fig. 2.20), which may affect depositional architectures adjacent to slopes (Bell et al. 2018b). Hybrid beds have also been hypothesized to form next to topography due to incoming flows inducing slope failure and the emplacement of a debrite within an aggrading turbidite (McCaffrey and Kneller, 2001), with thicker debrites indicating proximity to the slope.

Onlap geometries

Onlap is defined by Mitchum (1977) as "a base-discordant relation in which initially horizontal strata terminate progressively against an initially inclined surface, or in which initially inclined strata terminate progressively updip against a surface of greater initial inclination". Further to this Mitchum (1977) differentiates proximal onlap against a surface dipping towards the source of sediment and distal onlap as dipping away from the source of sediment.

McCaffrey and Kneller (2001) suggest that the controlling factor on turbidite onlap geometry is parent flow magnitude (discharge rate per unit width); large flows will thicken at topography (type A) while smaller flows will thin (type B). Smith and Joseph (2004) use different criteria to describe onlap types; Class 1 onlaps display no coeval slope aggradation, resulting in 'pure' or abrupt onlap against the primary onlap surface, or type A of McCaffrey and Kneller (2001). Class 2 onlap occurs when higher rates of slope aggradation result in each successive turbidite being deposited on a younger, or secondary, onlap surface, resulting in a 'feathered' onlap. The onlap surface in this situation will follow a steep trajectory if slope aggradation rates are high, giving a false impression of the geometry of the basin margin (Smith and Joseph, 2004).

Pickering and Hilton (1998) describe the geometry of turbidite onlap using two end members; type 1 and type 2. Type 1 onlap is broadly consistent with the pure onlap of Smith and Joseph (2004). Type 2 onlap is differentiated by significant draping of turbidites over the onlap surface, and is similar to class 2 of Smith and Joseph (2004).

Bakke et al (2013) integrated their own subsurface and outcrop observations with observations from other studies (McCaffrey and Kneller, 2001; Gardiner, 2006; Patacci, 2010) to propose six different styles of seismically-resolvable deep-water onlap: simple onlap, draping onlap, bed thickening, advancing pinch-out, convergent pinch-out and converging thickening (Fig. 2.21). Preferential formation of each of these onlap styles is controlled by various factors, such as: flow concentration, flow magnitude, slope angle and slope stability (Bakke et al. 2013).

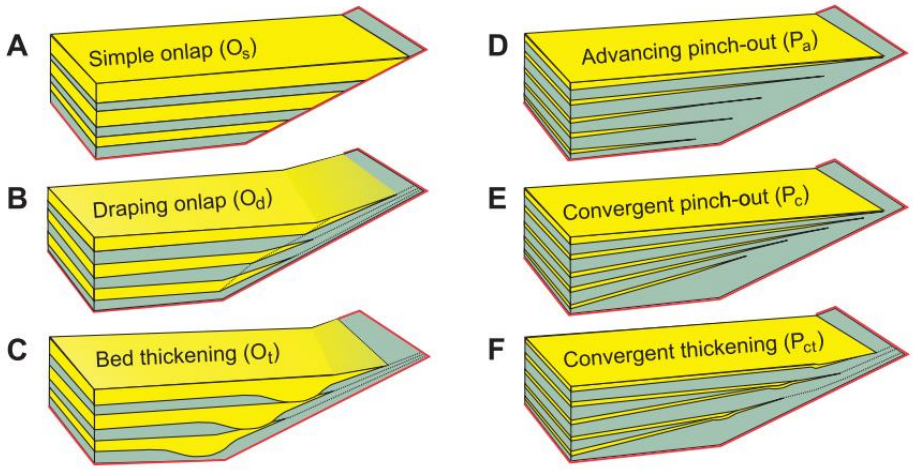

Figure 2.21: Different onlap styles described by Bakke et al. (2013).

Stratigraphic evolution of confined basins

Confined basins are those in which SGF routing and depositional patterns are controlled by the topography of the basin (e.g. Gorsline and Emery, 1959; Van Andel and Komar, 1969; Ricci Lucchi and Valmori, 1980; Hiscott et al. 1986; McGee et al. 1994; Winker, 1996; Gervais et al. 2004; Lomas and Joseph, 2004; Bersezio et al. 2005; Covault and Romans, 2009; Marini et al. 2015; 2016a; Cunha et al. 2017; Dodd et al. 2018). Southern et al. (2015) classified confined systems based on whether they are unconfined and uncontained (UU), confined and uncontained (CU) or confined and contained (CC) (Fig. 2.22). Confined flows are affected by topography, while contained flows are entirely encircled and retained within a depositional low (Southern et al., 2015). Contained deposition is analogous to flow 'ponding' (*sensu* Van Andel and Komar, 1969), which is typically used to describe flows entirely confined by their basin margins.

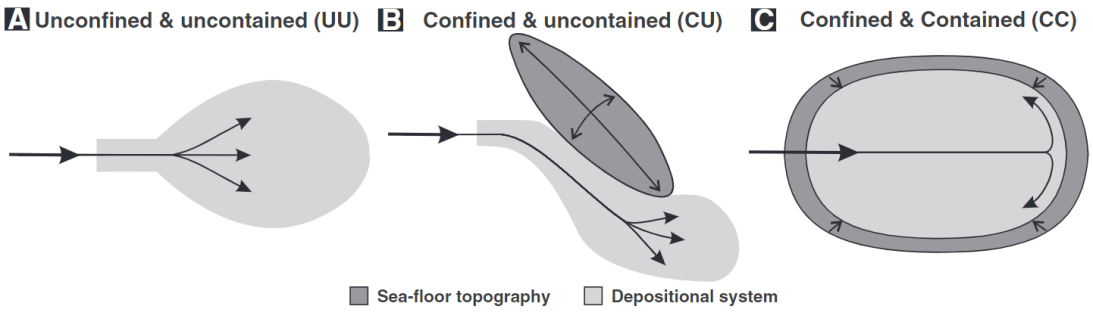

Figure 2.22: Different types of confinement that a deep-water system, or individual SGF, may be characterised by (from Southern et al. 2015).

Ponded flows generate limited positive relief as the full sediment load is trapped within the basin, thus developing a 'flat-topped cloud' that spreads over the whole basin (Marini et al. 2015), which results in 'sheet-like' deposition and simple vertical stacking patterns (e.g. Pickering and Hiscott, 1985; Haughton, 1994; Talling et al. 2007b). When relative confinement is reduced stacking patterns become more complex as beds are able to thin distally, and thus stack with varying degrees of compensation (e.g. Marini et al. 2015; Bell et al. 2018b; Liu et al. 2018).

Relative confinement has also been inferred through the stratigraphic trend of the mud-to-sand ratio within individual event beds (e.g. Felletti, 2002; Sinclair and Cowie, 2003; Bersezio et al. 2005; Marini et al., 2015), with the absence of a mud-cap indicating that the confining topographical relief was not sufficient to prevent bypass of the finer, upper region of the flow (e.g. Haughton, 1994), resulting in 'flow stripping' (e.g. Sinclair

and Tomasso, 2002; Sinclair and Cowie, 2003; Toniolo et al. 2006; Patacci et al. 2015). Thick mud-caps may indicate flows were fully confined by their basin margins (e.g. Haughton, 1994; Marini et al. 2015).

Integration of outcrop (e.g. Sinclair, 1994) and subsurface (e.g. Prather et al. 1998; Prather, 2000) data led Sinclair and Tomasso (2002) to describe a generic depositional model for the fill of a confined basin with four aggradational stages (Fig. 2.23): 1) flow ponding, where flows are entirely confined by the basin margins 2) flow stripping, where the upper parts of flows are able to 'escape' the basin, 3) flow bypass, where the majority of the incoming flow is able to deposit down-dip and 4) blanketing or abandonment. Numerical modelling by Wang et al. (2016) has shown, contrary to Sinclair and Tomasso (2002), that confined minibasins tend to fill retrogradationally, with deposition concentrated in the basin centre and counter slope due to a hydraulic jump as incoming flows decelerate upon impact with the basin floor. Similar retrogradational stacking patterns were described from outcrop by Amy et al. (2007).

Smith (2004) regarded the fill-spill model as an end-member depositional style for confined basins, with the other end member termed being a 'connected tortuous corridor'. In the tortuous corridor model flows are laterally confined down-dip, but not frontally confined, and follow a 'tortuous' topographically-controlled path down-dip. This style of deposition has since been observed on the modern seafloor (Bourget et al. 2011), the subsurface (e.g. Hay and Prather, 2015) and at outcrop (e.g. Vinnels et al. 2010; Pinter et al. 2018).

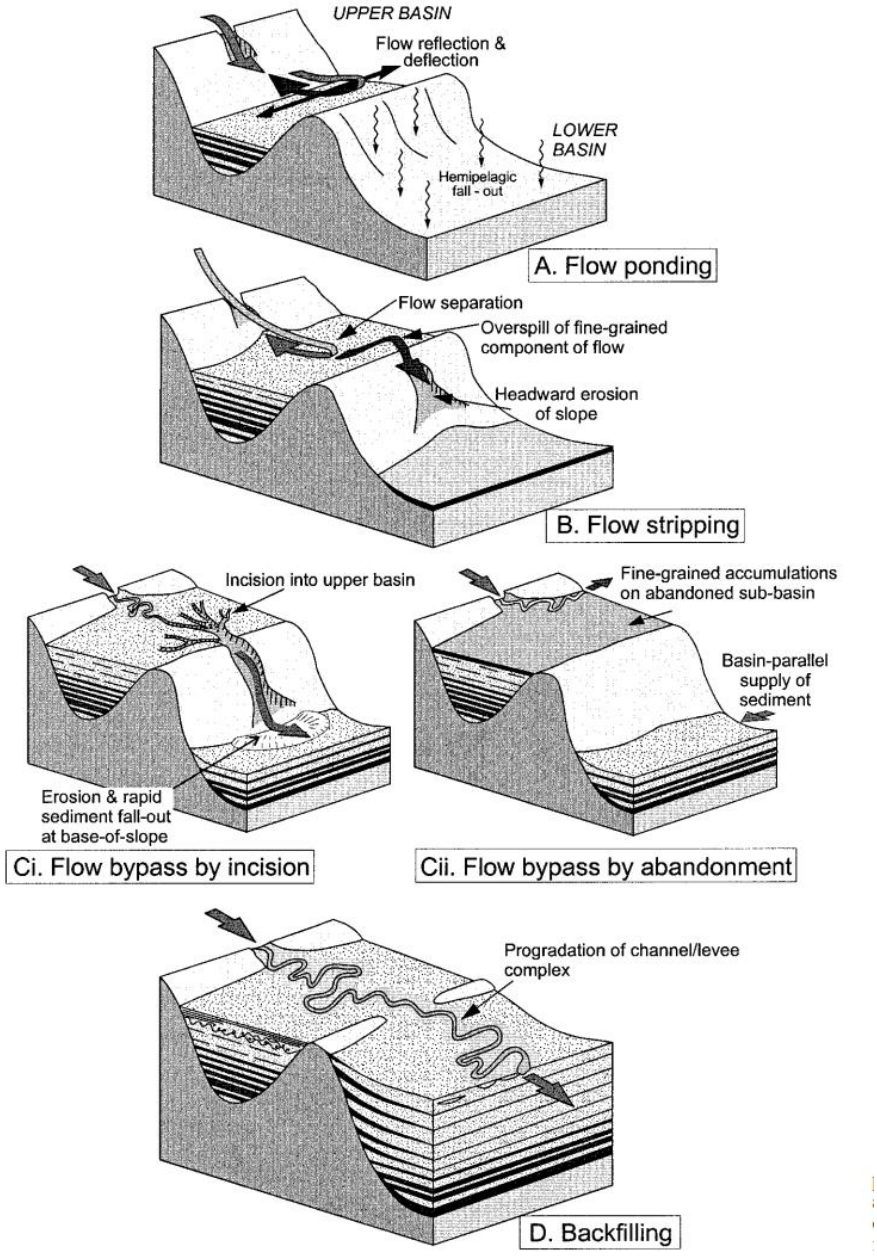

Figure 2.23: The fill-spill model for the stratigraphic evolution of a confined basin from Sinclair and Tomasso (2002).

2.6 *External controls on deep-water sedimentary systems*

The three main external, or allogenic, controls on sedimentary systems are climate, tectonism, and eustatic sea-level, which act together to control sediment supply and accommodation space (e.g. Vail et al. 1977; Muto and Steel, 1997; Miall, 2014; Castelltort et al. 2017; Cantuneanu, 2020). Depositional signals formed by modifying the relative impact of these controls are stored in the stratigraphic record of sedimentary basins (e.g. Castelltort and Driessche, 2003; Allen, 2008; Simpson and Castelltort, 2012; Coulthard and Van de Wiel, 2013; Romans et al. 2016; Toby et al. 2019). Deep-water sedimentary systems represent the ultimate sink of these signals and are therefore important in reconstructing climatic, tectonic or eustatic conditions through time (Fig. 2.24) (e.g. Allen, 1997; Sømme et al. 2009a; Covault et al. 2010; Romans et al. 2016; Castelltort et al. 2017; Hessler and Fildani, 2019). While external controls are often highly interwoven (e.g Dadson et al. 2003; Allen, 2008; Bourget et al. 2010; Hessler and Fildani, 2019), such as cooler climates causing glaciation and lower eustatic sea-levels (e.g. Miller et al. 2005; Katz, 2008), the aim of the following sections is to give examples of how particular external factors have been shown to affect deep-water systems.

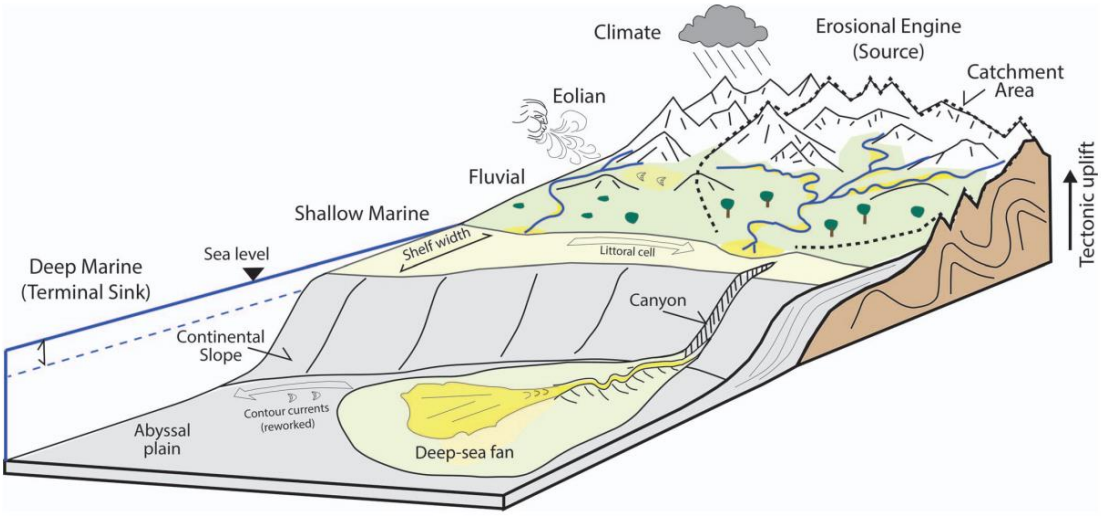

Figure 2.24 The key factors affecting sediment routing to deep-water environments (from Clark et al. 2017; Hessler and Fildani, 2019)

Climate

Climate has been shown to be intimately linked to deep-water sedimentary systems in a variety of different locations (e.g. Hessler and Fildani, 2019). Holocene submarine fans offshore California, for example, have been shown to grow in response to higher

precipitation and fluvial discharge associated with increased El Niño magnitude and frequency (e.g. Romans et al. 2009; Covault et al. 2010). Holocene humid-arid cycles related to the West African monsoon have also been shown to affect channel avulsion patterns in the Congo fan (Picot et al. 2019) (Fig. 2.25). Similarly, it has been found that monsoonal cycles in Asia have controlled sedimentation in the Bengal Fan (e.g. Weber et al. 2003; Fournier et al. 2017). Increased precipitation and run-off related to orbital cycles has also been related to increased deep-water sedimentation in exhumed Miocene systems in Greece (Postma et al. 1993) and exhumed Eocene systems in Spain (Catalejo and Pickering, 2014).

Global temperatures also effect deep-water sedimentation, with cooler climates and associated glaciations during the Pleistocene altering onshore drainage networks (Reece et al. 2011; Fildani et al. 2018) and increasing hinterland erosion rates (e.g. Gulick et al. 2015), thus increasing sediment supply to deep-water systems. De-glaciation has also been shown to increase discharge to fluvial systems through meltwater run-off, which consequently increases sediment delivery to deep-water systems, such as the Mississippi fan in the Gulf of Mexico (Mason et al. 2017) and the Tufts fan in the NW Pacific (Brunner et al. 2009; Normark and Reid, 2003).

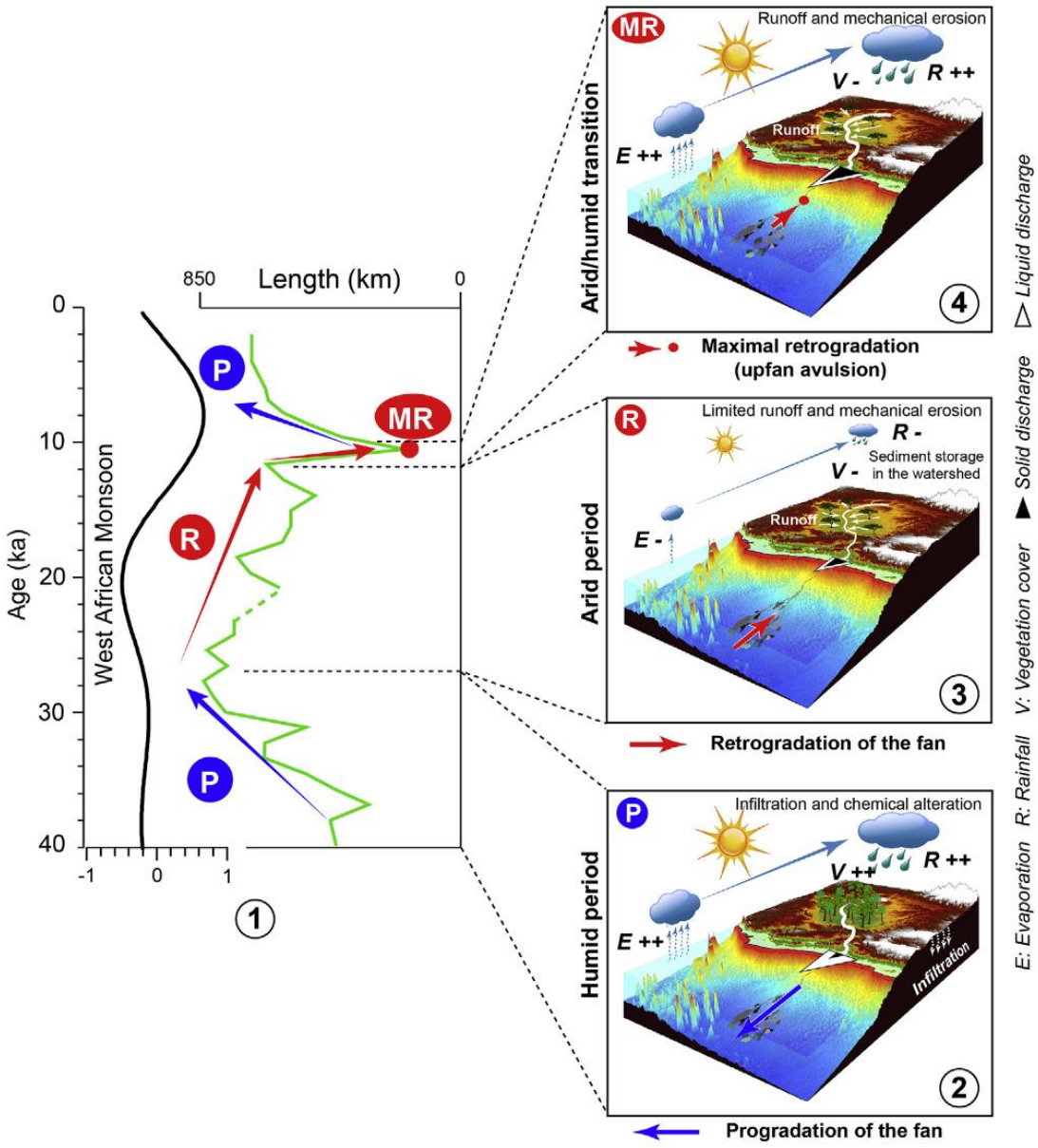

Figure 2.25: The Congo Fan is an example of a predominantly climate-controlled deep-water system (from Picot et al. 2019), with humid periods causing enhanced run-off and sediment supply to deep-water. P = progradation, R = retrogradation, MR = maximum retrogradation.

Tectonism

Much like climate, tectonism can control deep-water sedimentation in a variety of ways, from orogenic uplift and erosion (e.g. Clift et al. 2008; Castelltort et al. 2017) to seismic activity and slope failure (e.g. Bao et al. 2018; Mountjoy et al. 2018), which can be used to assess the earthquake recurrence intervals (e.g. Nelson et al. 2012). Deep-water systems connected to Himalayas, for example, have been shown to be closely-related to the growth of the mountain belt (Fig. 2.26), with sediment supply to the Indus and Bengal

Fans related to up to 55 million years of Himalayan evolution (Milliman and Syvitski, 1992; France-Lanord et al. 1993; Einsele et al. 1996; Métivier et al. 1999, Clift et al. 2001; 2011; Pickering et al. 2020).

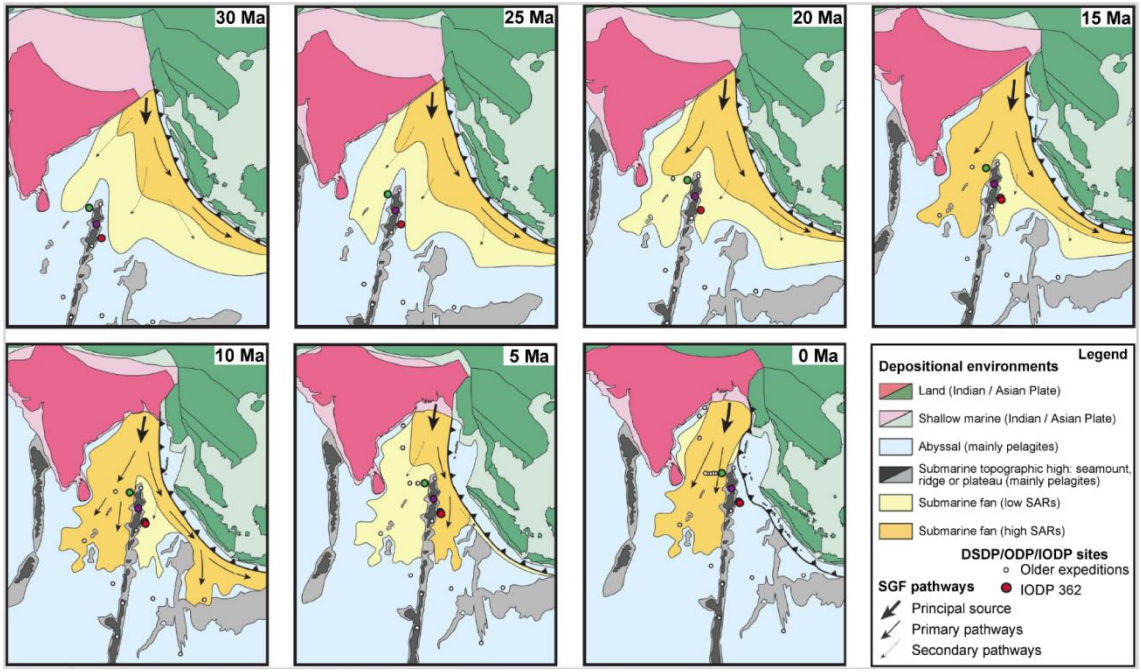

Figure 2.26: An example of the tectonic influence on submarine fan growth from the Bengal-Nicobar Fan, which is heavily-influenced by the Sunda subduction margin encroaching from the east (Pickering et al. 2020)

Tectonism related to plate collision has also been shown to result in increased rates of deep-water deposition in the Eocene Pyrenean foreland (Pickering and Corregidor, 2005; Pickering and Bayliss, 2009; Castelltort et al. 2017), the present-day Japanese Trench (Bao et al. 2018) and Izu peninsula (Ito, 1985), and the Colombian Sinú fold-belt (Kolla and Buffler, 1984; Alfaro and Holz, 2014; Ortiz-Karpf et al. 2015; 2016). Tectonism with associated volcanism can also promote deposition in deep-water systems through magmatic underplating and uplift (e.g. White and Lovell, 1997; Williams and Gostin, 2000), and a supply of volcaniclastic sediment from active volcanoes (Farquharson et al. 1984; Saint-Ange et al. 2007; Shumaker et al. 2018). The steep slopes and narrow shelves that tend to characterise these tectonically-active settings will also promote deep-water deposition by both increasing sediment supply rates and the ability of sediment to be transferred to deeper-water (e.g. Stow et al. 1983; Milliman and Syvitski, 1992; Reading and Richard, 1994; Covault et al. 2007, 2011; Harris and Whiteway, 2011).

Tectonic activity has also been shown to reduce sediment supply to deep-water systems by diverting onshore drainage systems away from continental margins (e.g. Marsaglia et al. 2011). It has also been demonstrated that tectonically-forced changes to drainage patterns in North America played a significant role in modulating sediment supply to the deep-water Gulf of Mexico during the Early Cenozoic (Sharman et al. 2017) (Fig. 2.27).

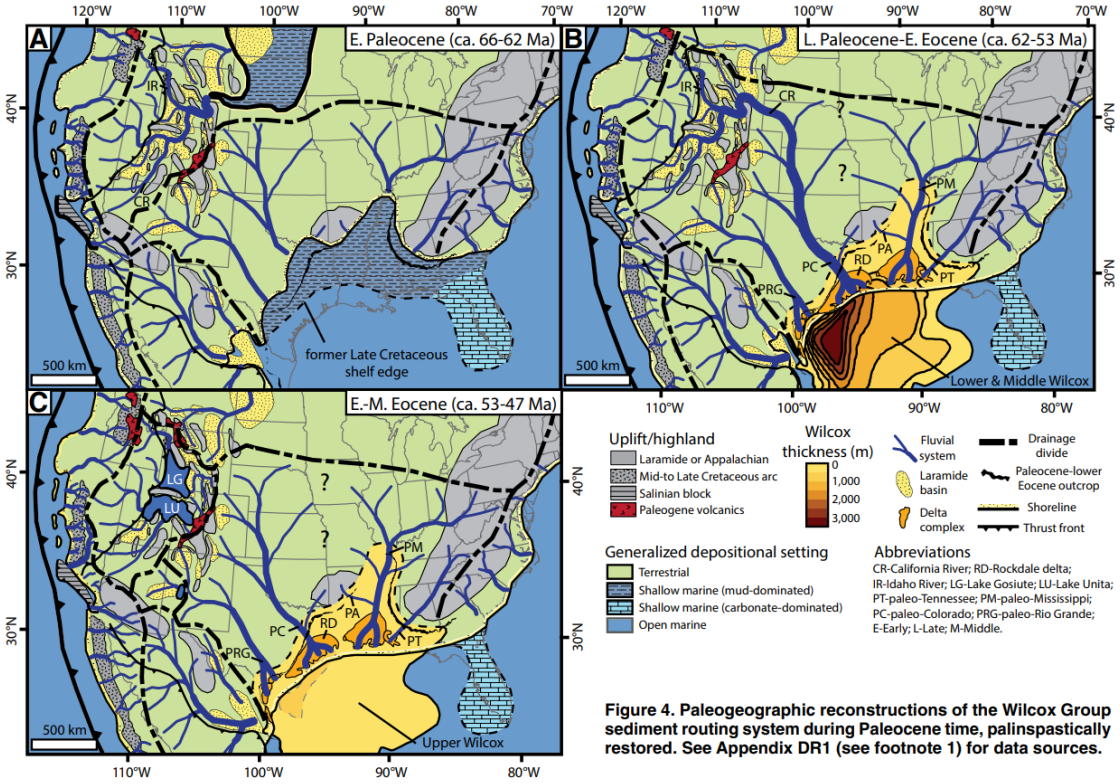

Figure 2.27: Tectonically-forced changes in drainage pattern during the Cenozoic have caused sedimentation within the Gulf of Mexico to drastically increase (Sharman et al. 2017).

Eustasy

Low eustatic sea-levels, or 'lowstands', are suggested to increase sediment delivery to deep-water systems by allowing rivers and deltas to reach the shelf-edge and deposit sediment directly into deep-water (*sensu* Vail et al. 1977; Posamentier et al. 1988; van Wagoner et al. 1990). Lowstands have been shown to increase sediment delivery to many deep-water systems, such as the Quaternary Amazon Fan (e.g. Manley and Flood, 1988; Flood and Piper, 1997; Schlünz et al. 1999), the Quaternary Indus Fan (e.g. Prins et al. 2000 Bourget et al. 2013), the Quaternary Danube Fan (Popescu et al. 2001), the Quaternary Golo Fan (Sweet et al. 2019), Miocene fans offshore China (Pickering et al. 2013), Eocene fans in the Pyrenean foreland (e.g. Castelltort et al. 2017) and the Cenozoic Gulf of Mexico

(Galloway, 2001). Most of these studies describe systems on passive margins (e.g. the Amazon and Indus Fans) deposited during icehouse periods characterised by large sea-level fluctuations (e.g. the Quaternary), as these are the conditions during which low eustatic sea-levels are believed to have the greatest influence of deposition (e.g. Pitman, 1978; Sømme et al. 2009b).

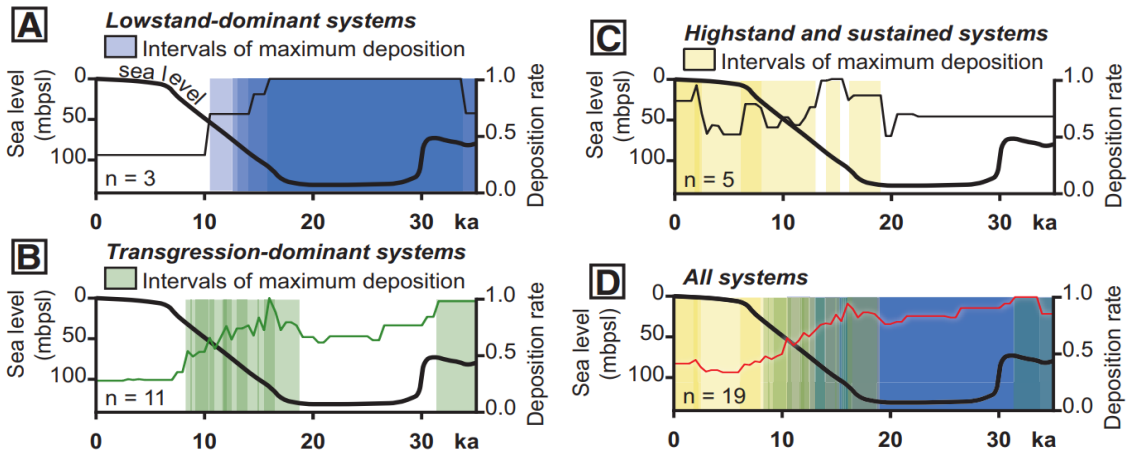

Figure 2.28: Holocene fans are preferentially active during all periods of sea-level fall and rise (solid black line). Low sea-levels are therefore not always correlated with increased deep-marine deposition. Deposition rate is shown by the finer line (Covault and Graham, 2010).

The lowstand model is therefore not ubiquitous in deep-water settings, with periods of increased deep-water sedimentation found to be associated with all sea-level stands (e.g. Covault and Graham 2010) (Fig. 2.28). The Mississippi deep-water system, for example, received significant volumes of sediment during rising sea-levels as canyons that were incised landward during lowstands remained active during higher sea-levels (Kolla and Perlmutter, 1993). Rising sea-levels have also been shown to remobilize and redeposit Late Quaternary shelf sediments into deeper water (Pierau, 2010), with Allin et al. (2018) suggesting that high rates of sea-level change, whether rising or falling, increase the likelihood of canyons 'flushing' their sediment down-slope. Similar findings were made by Trincardi et al. (2003), who hypothesized that rapid Late Quaternary sea-level rise enhanced pore pressures within drowned shelf-margin sediments of the Tyrrhenian Sea, resulting in slope failure and mass-transport. Remobilization of carbonate platforms and deposition in deep-water has also been shown to occur preferentially during rising sea-levels ('highstand shedding) (e.g. Droxler and Schlager, 1985; Schlager et al. 1994). Other external controls, such as high sediment supply (e.g. Carvajal and Steel, 2006), narrow shelves (e.g. Stow et al. 1983; Covault et al. 2011), steep canyon gradients (e.g. Weber, et al. 1997), and ocean

currents (e.g. Covault et al. 2007; Cantuneanu, 2020), will modulate the impact of eustasy on deep-water systems.

CHAPTER 3: The stratigraphic evolution of onlap in siliciclastic deep-water systems: autogenic modulation of allogenic signals

Euan L. Soutter[1], Ian A. Kane[1], Arne Fuhrmann[1], Zoë A. Cumberpatch[1] and Mads Huuse[1]

[1]Department of Earth and Environmental Sciences, University of Manchester, Manchester, M13 9PL, U.K.

3.1 *Abstract*

Seafloor topography affects the sediment gravity flows that interact with it. Understanding this interaction is critical for accurate predictions of sediment distribution, paleogeography, and structural reconstructions of deep-water basins. The effects of seafloor topography can be seen from the bed scale, through facies transitions toward intra-basinal slopes, to the basin scale, where onlap patterns reveal the spatial evolution of deep-water systems. Basin-margin onlap patterns are typically attributed to allogenic factors, such as sediment supply signals or subsidence rates, with few studies emphasizing the importance of predictable spatio-temporal autogenic flow evolution. This study aims to assess the autogenic controls on onlap by documenting onlap styles in the confined Eocene-to-Oligocene deep-marine Annot Basin of SE France. Measured sections, coupled with architectural observations, mapping, and paleogeographical interpretations, are used to categorize onlap styles and place them within a generic stratigraphic model. These observations are compared with a simple numerical model. The integrated stratigraphic model predicts that during progradation of a deep-water system into a confined basin successive onlap terminations will be partially controlled by the effect of increasing flow concentration. Initially thin-bedded low-density turbidites of the distal lobe fringe are deposited and drape basinal topography. As the system progrades these beds become overlain by hybrid beds and other deposits of higher-concentration flows developed in the proximal lobe fringe. This transition is therefore marked by intra-formational onlap against the underlying and lower-concentration lobe fringe that drapes the topography. Continued progradation results in deposition of lower-concentration deposits in the lobe off-axis, resulting in either further intra-formational onlap against the lobe fringe or onlap directly against the hemipelagic basin margin. Basinal relief is gradually reduced as axial and higher-volume flows become more prevalent during progradation, causing the basin to become a bypass zone for sediment routed down-dip. This study presents an autogenic mechanism for generating complex onlap trends without the need to invoke allogenic processes. This has implications

for sequence-stratigraphic interpretations, basin subsidence history, and forward modeling of confined deep-water basins.

3.2 *Introduction*

Deep-water submarine fans are amongst the largest sedimentary bodies on Earth and comprise terrigenous sediment shed from the adjacent continental shelf and slope (e.g., Piper et al., 1999; Talling et al., 2007; Prélat et al., 2010; Clare et al., 2014). They offer a record of Earth's climate and sediment transport history, form valuable hydrocarbon reservoirs, aquifers, and are sites of mineral accumulation (e.g., Weimer and Link, 1991; Hodgson, 2009; Sømme et al., 2011; Bell et al., 2018a). Sediment-gravity-flow evolution across unconfined deep-water settings results in a fairly uniform radial spreading and deceleration of flows, causing the development of elongate to lobate sedimentary bodies with predictable facies transitions (e.g., Baas, 2004; Hodgson et al., 2009; Spychala et al., 2017), which are generically known as 'lobes'.

Sediment gravity flows encountering seafloor topography in confined-basin settings form a range of onlap geometries that are often associated with complicated sedimentary facies (Fig. 3.1) (e.g., Kneller, 1991; Haughton, 1994; Wynn et al. 2000; McCaffrey and Kneller, 2001; Smith, 2004a; Smith 2004b; Amy et al., 2004; Gervais et al. 2004; Lomas and Joseph, 2004; Smith and Joseph, 2004; Puigdefàbregas et al., 2004; Gardiner, 2006; Mayall et al. 2010; Tinterri et al. 2016; Hansen et al. 2019). The effect of seafloor topography on sediment gravity flows, their deposits, and onlap styles has been studied through outcrop data (e.g., Kneller et al. 1991; Sinclair, 1994; Bakke et al., 2013), subsurface data (e.g., Prather et al., 1998; 2012; Covault and Romans, 2009; Bakke et al., 2013), and numerical models (e.g., Smith, 2004b; Kubo, 2004; Gardiner, 2006; Sylvester et al., 2015) and physical models (e.g., Kneller, 1995; Kneller and McCaffrey; 1995; Amy et al., 2004; Brunt et al., 2004; Kubo, 2004). Seafloor topography is generated by a variety of geological processes, such as: pre-depositional tectonic deformation (e.g., Jackson et al. 2008; Kilhams et al. 2012), syn-depositional tectonic deformation (e.g., Wilson et al., 1992; Haughton, 2000; Grecula et al., 2003; Hodgson and Haughton, 2004; Tomasso and Sinclair, 2004; Kane et al. 2010; Salles et al., 2014), mass transport deposit relief (e.g. Armitage et al., 2009; Ortiz-Karpf et al., 2015; 2016; Kneller et al., 2016; Soutter et al., 2018) and salt diapirism (e.g., Hodgson et al., 1992; Kane et al. 2012; Prather et al. 2012; Oluboyo et al. 2014; Doughty-Jones et al., 2017). Improved prediction of the distribution of sediment gravity flow

deposits around seafloor topography is therefore critical for both paleogeographic reconstructions (e.g., Pinter et al., 2017) and stratigraphic hydrocarbon or CO_2 trap risking (e.g., McCaffrey and Kneller, 2001).

The onlap geometry (3D shape of an event bed or sequence of related event beds at pinch-out) and facies (internal sedimentary characteristics of an event bed at pinch-out) (Fig. 3.1A), herein termed onlap termination, are controlled by: 1) flow magnitude, duration, velocity, thickness, concentration, and sediment composition; 2) the gradient and incidence angle of the counter-slope; and 3) seafloor composition and induration. Typically, high-concentration flows and steep counter-slopes cause abrupt terminations, whereas low-concentration flows and shallow counter-slopes cause draped terminations (Fig. 3.1) (Smith and Joseph, 2004; Bakke et al. 2013). Flows with a high mud content may also be more prone to varying degrees of rheological transformation approaching counter-slopes, resulting in complicated facies distributions at confining basin margins (Fig. 3.1) (Barker et al., 2008; Patacci et al., 2014; Southern et al., 2015).

Recent field-based studies on the spatial and temporal evolution of unconfined

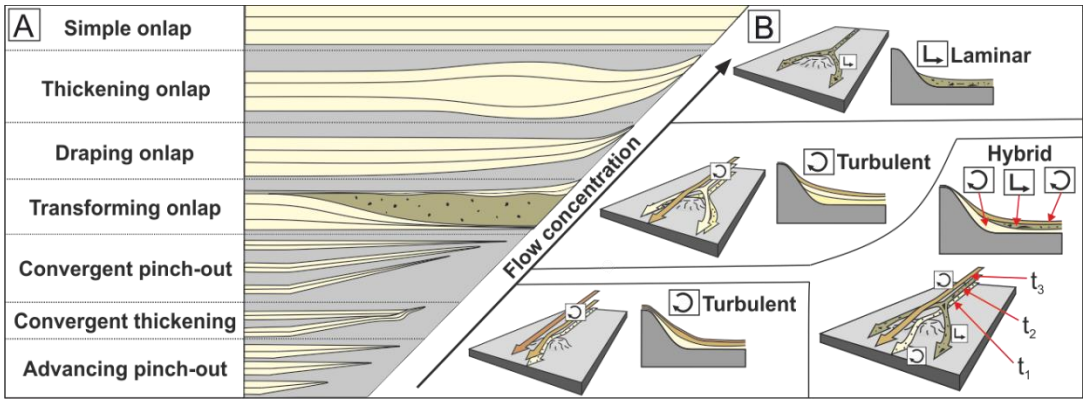

Figure 3.1: A) Examples of onlap termination styles (modified from Al-Jaidi et al. 2004; Bakke et al. 2013; Patacci et al. 2014). B) Generalized relationship between flow concentration and onlap geometry (modified from Bakke et al. 2013). t = time.

submarine lobes have used the longitudinal evolution of flows and their associated facies to establish criteria for differentiating lobe sub-environments at the bed scale (e.g., Prélat et al. 2009; Grundvag et al. 2014; Spychala et al. 2017). The applicability of these facies associations to confined lobes and the complex system-scale stacking patterns that they may produce is only recently being investigated (e.g., Marini et al. 2015; Spychala et al. 2015, 2017; Bell et al. 2018b; Fonnesu et al. 2018; Liu et al. 2018). Previous flow-dependant onlap models mainly focussed on end-member geometries (e.g., McCaffrey and Kneller,

2001; Smith, 2004b; Smith and Joseph, 2004). As yet there is no generic model to account for how the wide variety of deposits resulting from the longitudinal evolution of sediment gravity flows will manifest themselves at onlap surfaces through the fill of a confined basin.

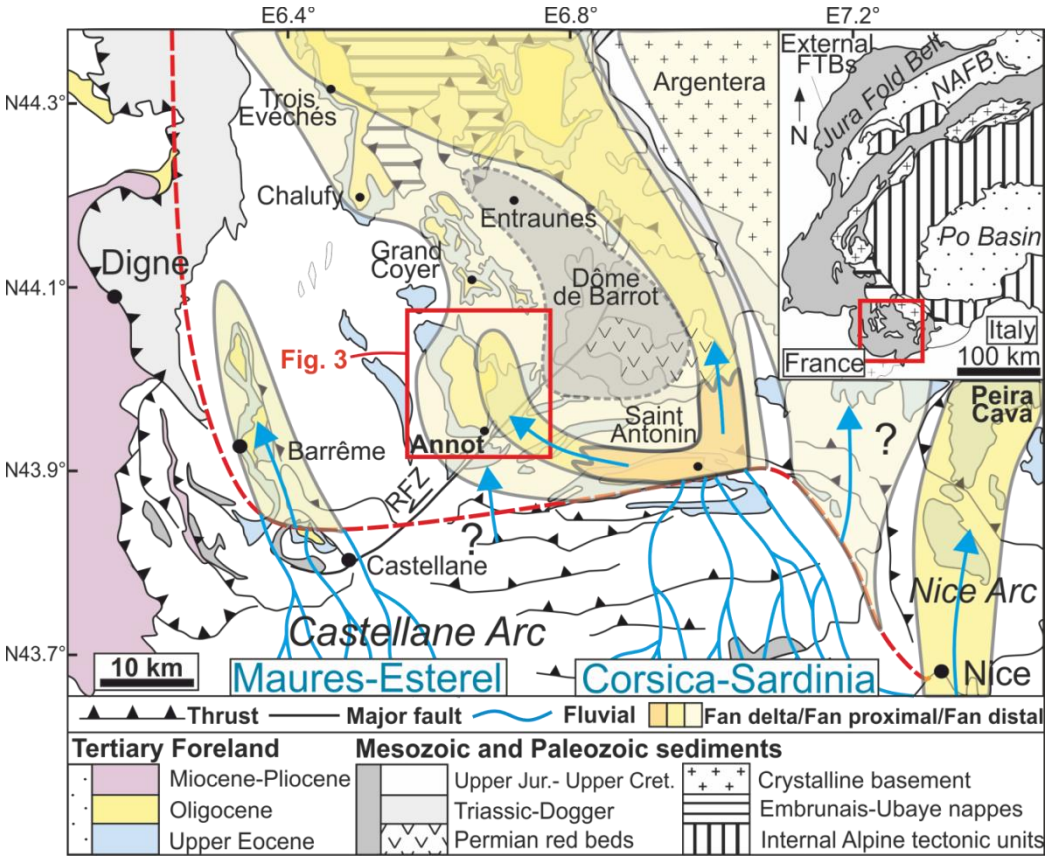

Figure 3.2: Location and geological setting of the Cenozoic foreland basin of the Western Alps. The generalized Late Eocene paleogeography is overlaid (modified from Joseph and Lomas, 2004 and Salles et al. 2014) and shows the Annot Basin (red box) situated in a clastic deep-marine environment.. Rea line indicates boundary between terrestrial and marine environments. RFZ, Rouaine Fault Zone. Blue arrows indicate paleoflow, and blue lines indicate schematic fluvial systems.

This study uses the well-constrained Cenozoic Annot Basin of SE France to integrate bed-scale and basin-scale onlap observations into a generically applicable depositional model. The aims of this study are to: i) reappraise the Annot Basin stratigraphy with respect to specific deep-water sub-environments, with particular emphasis on the poorly studied eastern exposures of the basin, ii) document lateral facies changes within beds approaching the basin margin and relate these facies changes to longitudinal flow evolution, iii) assess how the longitudinal evolution of confined flows impacts onlap geometry and stacking patterns, and iv) integrate these observations into a generic model for the evolution of onlap in deep-water basins.

3.3 *Annot Basin*

Basin structure

The 160-km-long and 80-km-wide (Clark and Stanbrook, 2001) Cenozoic foreland basin of the western Alps formed due to SW-directed collision of the Adria and European plates, and subsequent loading of the European plate by the Alpine orogenic wedge (Figs. 3.2, 3.3) (e.g., Ford et al., 1999). This orogenic deformation is represented in the foreland-

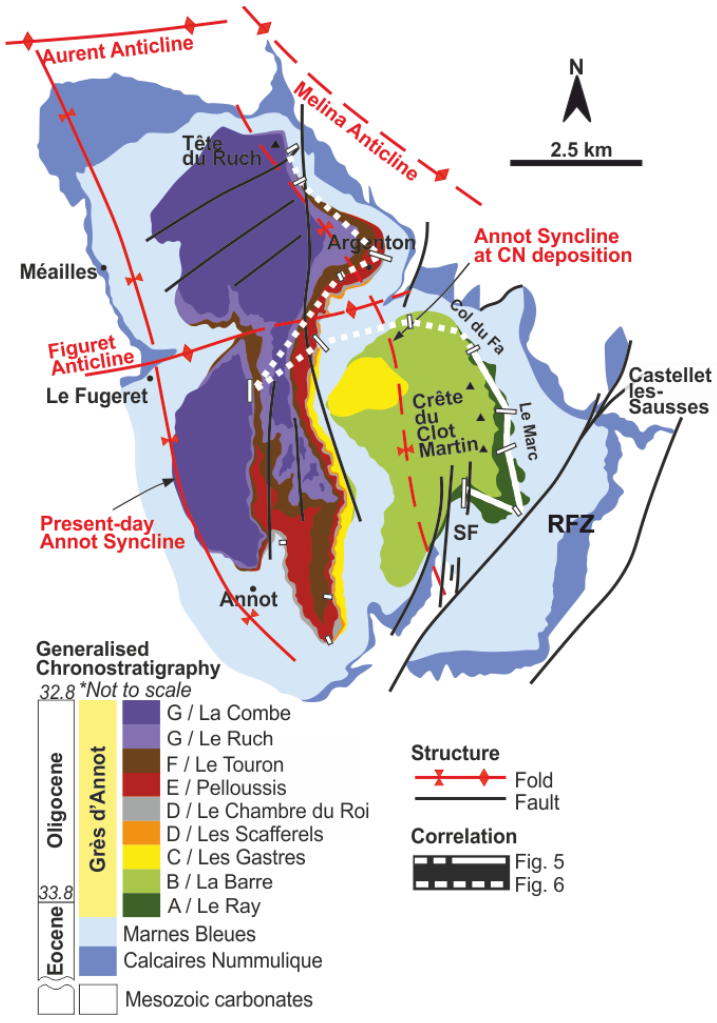

Figure 3.3: Structure, chronostratigraphy, and geological map of the Annot Basin (modified from Puigdefàbregas et al., 2004; Du Fornel et al. 2004; Salles et al. 2014). The various anticlines confine deposition across the Basin. The clastic sequence has been divided into members based on aerial and outcrop mapping (modified from Puigdefàbregas et al., 2004; Salles et al., 2014). An attempt has been made to reconcile the member subdivisions used by Puigdefàbregas et al. (2004) and Salles et al. (2014). White boxes indicate logged localities. White lines indicate correlation panels in Fig. 5 and Fig. 6. RFZ, Rouaine Fault Zone; BF, Braux Fault. Black dashed lines indicate exhumed syn-sedimentary fault escarpments.

basin stratigraphy by a progressive younging to the southwest (e.g. Ford et al., 1999; Du Fornel et al. 2004). Sediment deposition in the basin was affected by complicated basinal topography (e.g., Joseph and Lomas, 2004), which formed due to Late Cretaceous northward-directed Pyrenean compression that was subsequently overprinted by Cenozoic SW-directed Alpine compression (Fig. 3.3) (e.g., Apps et al., 2004). This resulted in NW-SE-oriented synclinal sub-basins with E-W anticlinal sills. The synclines are interpreted as the surface expression of underlying Alpine thrust-fault-propagation folds (Fig. 3.3) (e.g., Elliott et al. 1985; Apps, 1987; Ravenne et al. 1987).

The Annot sub-basin, herein termed the Annot Basin, is one of the exhumed synclinal Cenozoic depocenters in the Alpine foreland basin, representing the proximal end of the deep-marine Annot-Grand Coyer-Chalufy chain of sub-basins (Figs. 3.2, 3.3) (see Joseph and Lomas, 2004, for review). The Annot Basin is bounded to the south by the SW-NE Rouaine Fault Zone, which acted as an entry point for sediment gravity flows into the basin (e.g., Salles et al. 2014) (Figs. 3.2, 3.3). The SW-NE Braux normal fault is related to this fault zone and created local bathymetric relief during the Late Eocene (e.g., Tomasso and Sinclair, 2004) (Figs 3.3, 3.4). The western and eastern margins of the basin are defined by fault-propagation anticlines created by Mesozoic blind thrusts (Figs. 3.3, 3.4) (e.g., Apps, 1987). The eastern margin is formed by the Melina anticline, or "kink zone" (Apps, 1987), and the western margin by the Puy du Rent anticline (Fig. 3.3; 4B). These anticlines were developing during deposition of the Annot turbidites, causing syn-depositional rotation of the basin depocenter towards the west (Fig. 3.3) (e.g., Salles et al., 2014).

E-W-oriented Pyreneo-Provençale structures also affect the Annot Basin structure, with the northern extent of the basin formed by the Aurent anticline (Fig. 3.3). This structure forms a gently southward-dipping terminal slope (e.g., McCaffrey and Kneller, 2004). More minor basin-floor relief may have been formed by the E-W Fugeret anticline, which lies between the Rouiane fault zone and the Aurent anticline (Fig. 3.3) (Salles et al., 2014). These E-W-oriented structures show little evidence of major syn-depositional movement due to compressional deformation being dominantly driven by the SW-directed Alpine orogeny during the Eocene and Oligocene.

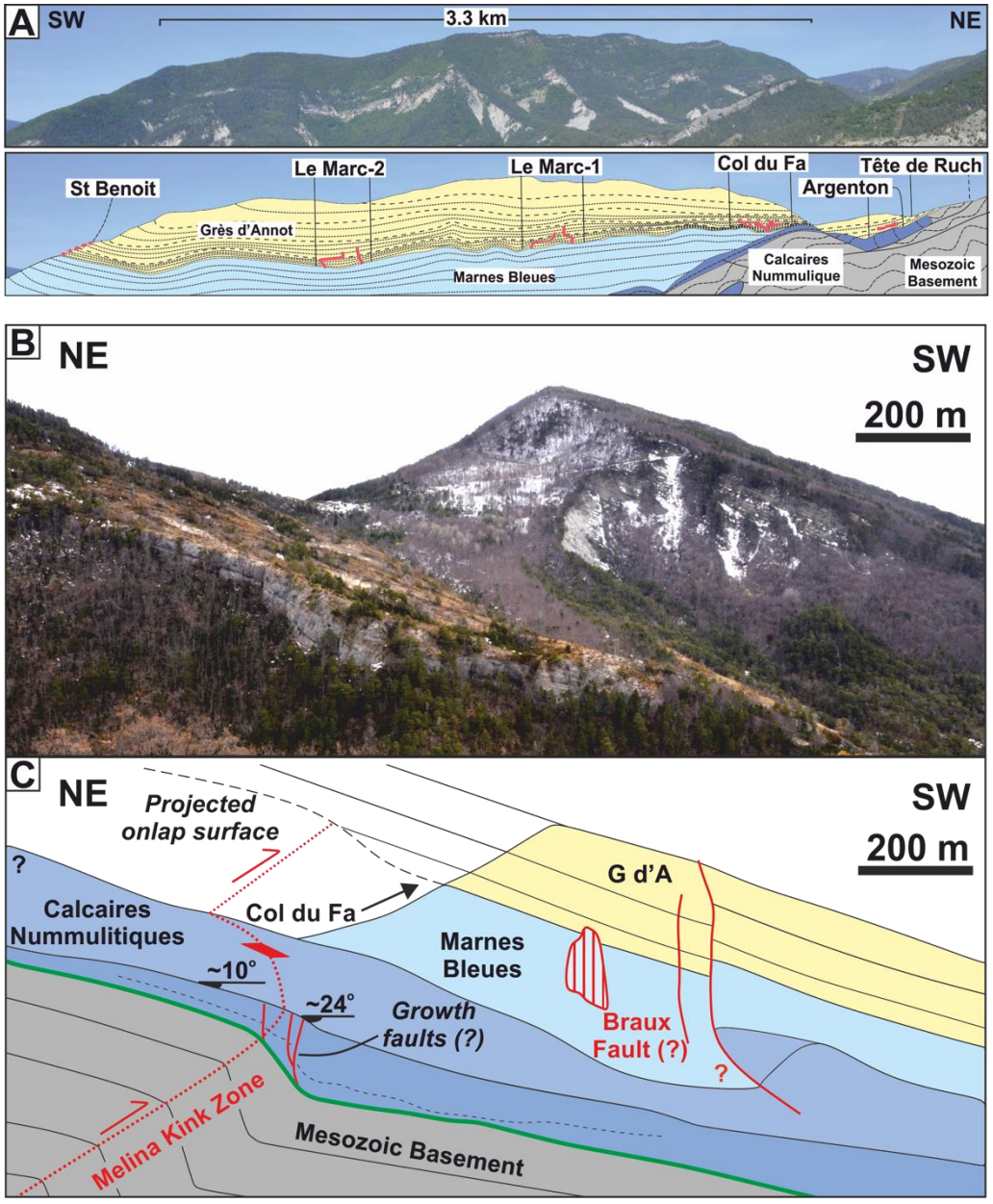

Figure 3.4: A) Dip and B) strike field sketches of the stratigraphy and structure of the Annot Basin. Logged localities are shown as red traverses in part A.

Stratigraphic evolution

The Annot Basin has the same transgressive Cenozoic foreland-basin stratigraphy as is seen across the western Alps (Figs. 3.2, 3.3) (e.g., Sinclair, 1997), with Oligocene shallow-marine limestones of the Calcaires Nummulitique overlain by deep-marine marls of the Marnes Bleues. The Marnes Bleues records the deepening of the basin, with foraminifera suggesting water depths of ~ 100 m at the base of the succession, to ~ 800 m by the end of deposition (Mougin, 1978). Supply of siliciclastic sediment began abruptly in the Late Eocene (35.2 Ma) as the Corsica-Sardinia massifs were uplifted via subduction-related back-thrusting towards to the south (Fig. 3.2) (e.g., Stanley and Mutti, 1968; Apps, 1987). This resulted in a depositional shift from the marls of the underlying Marnes Bleues, into south-to-north dispersing clastic sediment gravity flows of the Grès d'Annot. An upwards coarsening trend in the Grès d'Annot suggests progradation of the clastic system, most-likely related to fan-delta advance (Fig. 3.3) (e.g., Puigdefàbregas et al., 2004).

During early clastic deposition the Annot Basin was located on the western side of a distal submarine fan extending over the foreland basin, with flows entering the basin from syncline-bounded fan deltas to the south (Fig. 3.2) (e.g., Stanley, 1980; Sinclair, 2000; Joseph and Lomas, 2004) and being dispersed northwards through relay ramps in the Rouaine Fault Zone (Fig. 3.3) (Joseph and Lomas, 2004; Salles et al., 2014). This early deposition is represented in the Annot Basin by low-density turbidites, often referred to as the Marnes Brunes Inferiérures (e.g., Stanbrook and Clark, 2004), which form the distal equivalent of the Grès d'Annot. The lowermost Grès d'Annot member, termed Le Ray (Puigdefàbregas, 2004) or the A Member (Du Fornel et al., 2004), onlaps both the underlying Marnes Brunes and Marnes Bleues slope (Fig. 3.3). Early flows were confined by the Braux Fault to the west, a combination of the Braux Fault and the Fugeret anticline to the north, and the Melina anticline to the northeast (Salles et al., 2014). The sediment entry point shifted throughout deposition of the Grès d'Annot, with a more easterly Late Eocene entry point suggested for these early flows, as evidenced by an up-stratigraphy rotation of paleocurrents from NE- to NW-directed (McCaffrey and Kneller, 2004; Salles et al., 2014). Alternatively, this may be an apparent repositioning of the sediment entry point as the basin depocenter itself migrated gradually westward due to Alpine compression (Salles et al., 2011; 2014). This deformation is believed to have been continuous throughout the fill of the basin; however, the apparent rate of deformation is suppressed in the Grès d'Annot due to the higher depositional rates associated with

gravity-flow deposition (Apps et al. 2004). The remaining Grès d'Annot members were confined by the major Melina (east), Puy du Rent (west) and Aurent anticlines (north) as the topography of the Braux Fault and Fugeret Anticline was healed relatively early in the Oligocene (Fig. 3.3) (Salles et al., 2014).

The basin gradually filled throughout the early Oligocene, with contemporaneous deposition occurring in the parallel Grand Coyer sub-basin to the northeast (Salles et al., 2014). Once the basin was largely filled, the Aurent Anticline ceased to terminally confine flows, and flows bypassed the Annot Basin into the Grand Coyer and Chalufy sub-basins (Fig. 2) (e.g., Apps, 2004; Salles et al., 2014). Few channel fills are seen within the Grès d'Annot succession, and the depositional architecture is interpreted as being predominantly sheet-like (Apps, 1987).

3.4 ***Data and methods***

The dataset comprises 50 (581 m cumulatively) sedimentary logs collected along sections predominantly oriented oblique to depositional-dip along the eastern margin of the Annot Basin (Figs. 3.3, 3.4A, 3.5) (Appendix A). Logs were collected at 1:10 scale, and individual beds were walked out at outcrop where possible (100s of metres) (Figs. 3.6, 3.7). Higher resolution 1:2 scale logs were collected from some beds approaching onlap to better capture facies transitions near the slope. Logs within thin-bedded facies were collected at a 1:5 scale to allow accurate representation of their thicknesses and structures. Samples of individual facies and individual beds were collected in order to quantitatively constrain lateral grain-size and matrix changes. 104 paleocurrent measurements were collected (Fig. 3.5), with 2D paleocurrent measurements qualitatively noted.

Margin correlation

Sedimentological contacts between the discrete members of the Grès d'Annot from the geological maps of Puigdefàbregas et al. (2004), Du Fornel et al. (2004), and Salles et al. (2014) were ground-truthed and compared to observations made by this study (Fig. 3.3). The observations of stratigraphic contacts made during this study most closely agree with those made by Puigdefàbregas et al. (2004); therefore their geological map was used for placement of sedimentary logs within members and for the intra-member correlation of sedimentary logs (Figs. 3.5, 3.6). This allows facies transitions across the basin to be assessed both spatially and temporally. Where member boundaries are unclear due to the

resolution of the geological map (as boundaries converge at pinchout) the top of individual members is defined by either abrupt facies changes, commonly an abrupt coarsening and thickening of event beds, or lateral relationships and correlations (Fig. 3.5). An attempt has been made to reconcile the nomenclature used by Puigdefàbregas et al. (2004) and Salles et al. (2014) to enable comparisons to be made between the two (Fig. 3.3).

Detailed correlations of the Le Ray member are based on the identification of key surfaces, such as onlap surfaces, and walking out of individual beds (Fig. 3.6). Where beds could not be walked out, units were correlated based on the methodology of Prélat et al. (2009) for the identification of the hierarchical elements that builds lobes, e.g., beds, lobe elements, and lobes. This methodology uses the thicknesses of fine-grained intervals and vertical facies transitions as indicators of lobe evolution.

Figure 3.5: Dip-oblique correlation panel along the eastern margin of the Annot Basin. No horizontal scale. Localities and panel orientation are shown in Fig. 3. Members have been correlated based on published maps and lithological observations. Paleocurrent data are associated with one sedimentary log or series of logs from one locality. The vertical thickness represents the exposed stratigraphy along the correlated margin (see Fig. 3 for location) and does not represent the accommodation of the entire basin, which had a westward-migrating depocenter. This migration is represented in the eastern exposures by decreasing member thicknesses through time. It should also be noted that due to the oblique nature of the correlation the margin position is a representation of the relative confinement at the member scale and does not indicate onlap angle.

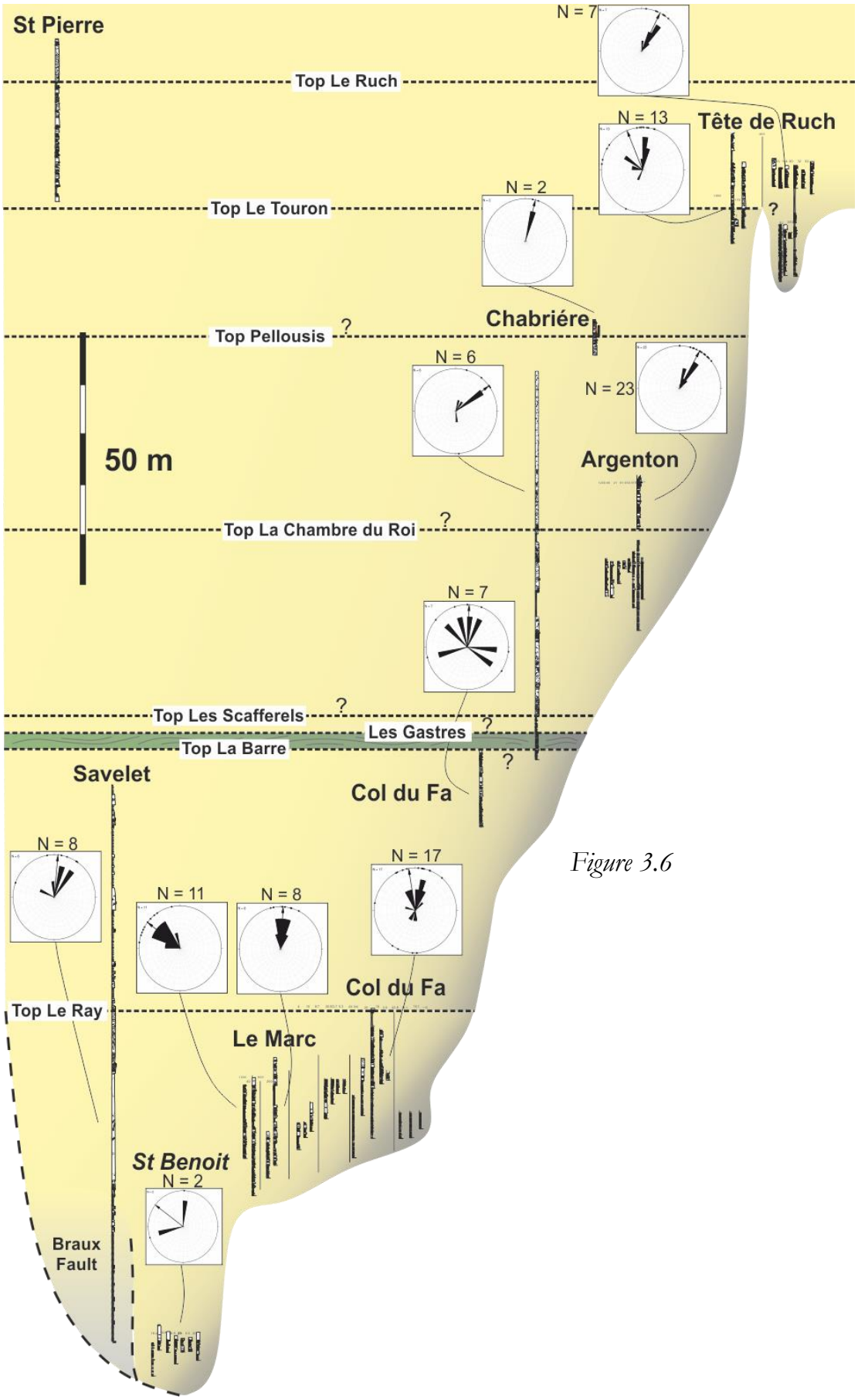
St Pierre
N = 7
Top Le Ruch
N = 13
Tête de Ruch
N = 2
Top Le Touron
?
Chabriére
Top Pellousis
?
N = 6
N = 23
50 m
Argenton
Top La Chambre du Roi
?
N = 7
Top Les Scafferels
?
Les Gastres
?
Top La Barre
?
Savelet
Col du Fa
N = 8
N = 17
N = 11
N = 8
Col du Fa
Top Le Ray
Le Marc
St Benoit
N = 2
Braux
Fault

Figure 3.6

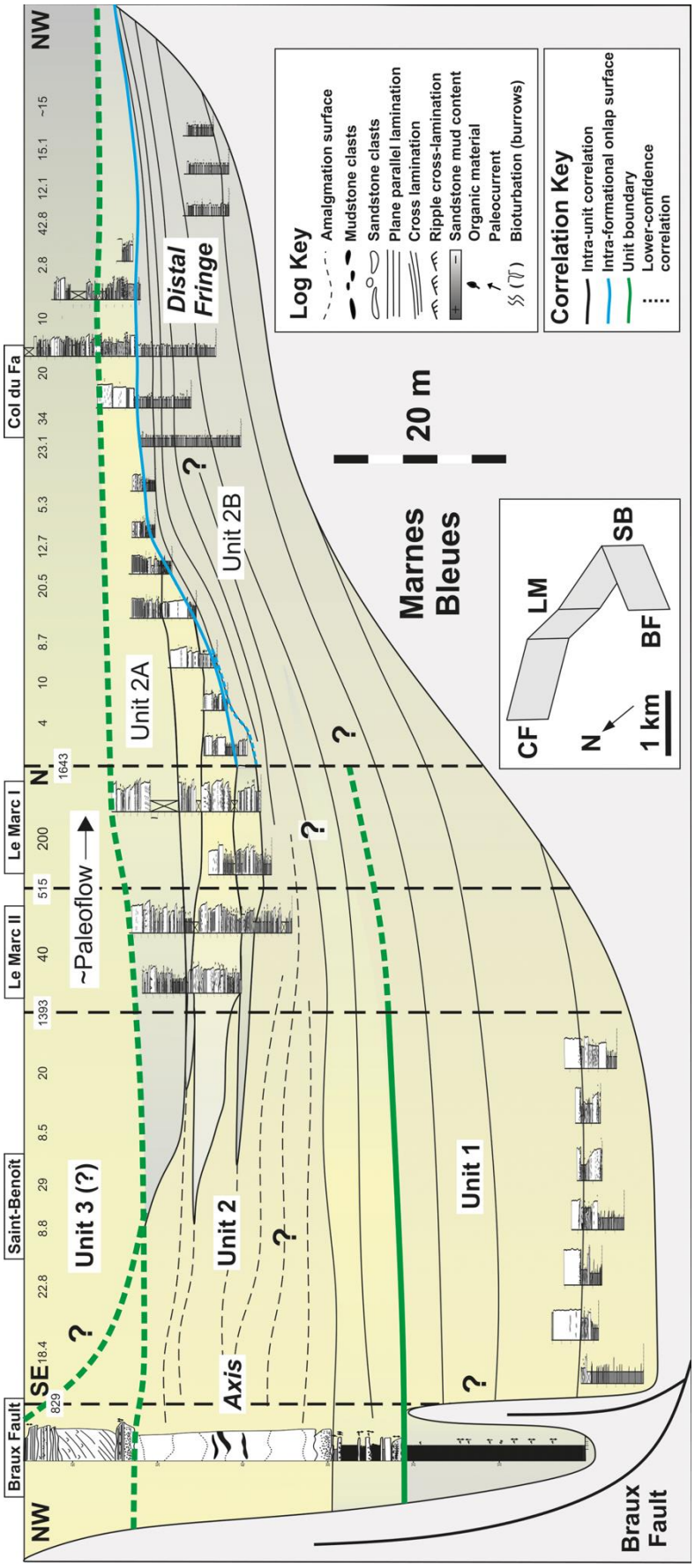

Figure 3.7: Correlation panel for the Le Ray member in the Annot Basin. Paleoflow is from the left to right (south to north). Inset shows 3D orientation of panel. BF, Braux Fault; SB, Saint-Benoît; LM, Le Marc; CF, Col du Fa. Distances between logs shown in metres between logs.

3.5 ***Results***

Facies associations

Facies associations (FA) have been interpreted based on the dominant lithofacies (LF) and depositional features of a given succession (Table 1). The dominant lithofacies has been described and interpreted within each facies association in order to justify their placement in that sub-environment. The lobe sub-environments of Spychala et al. (2017) are used because they best fit the observations made in this study (Figs. 3.8, 3.9). The onlap geometry of each lithofacies, and therefore the inferred onlap geometry of the facies association in which that lithofacies dominantly occurs, is summarized in Table 1. Facies associations are presented in the following section from proximal to distal positions on the lobe, in descending stratigraphic order and, broadly, in descending order of thickness.

FA 1 Lobe-axis

Observations: Facies association 1 is composed dominantly of one lithofacies: thick-bedded (0.5 - 2 m) sandstones (LF 1A) (Figs. 3.10A, B, E), with thin-bedded (0.01 m - 0.5 m) sandstones (LF 1B) and medium-bedded sandstones (0.1 - 0.8 m) (LF 3) commonly associated. LF 1B is composed of medium- to cobble-grade (most typically coarse-grained), poorly sorted, massive sandstones (Fig. 3.10B) and is less prevalent than LF 1A. Individual beds have erosional bases, often with groove, flute, and tool marks, and irregular tops. Beds are often lenticular, thickening and thinning from < 10 cm before pinching out over tens of meters. The beds often occur within successions of medium-bedded sandstones (LF 2) below packages of LF 1.

Lithofacies	Description	Interpretation	Facies Association	Onlap Geometry
Thick-bedded sandstone (LF 1)	Forms 1 - 20 m amalgamated packages or 0.5 - 2 m beds, Medium - granule grain size. Flat or erosional bed bases and flat bed tops. Mostly structreless with some planar laminae. Often contains mud clasts (<5 cm) and soft-sediment deformation, e.g. flames and dishes.	Rapid aggradation beneath a highly concentrated flow. Planar-spaced laminae indicate traction-carpet deposition (*sensu* Lowe, 1982).	Lobe axis (FA 1) Lobe off-axis	Abrupt termination High-density flows deposit abruptly at counter-slope due to loss of capacity, compared to lower-concentration flows with otherwise similar flow properties (e.g. Hiscott, 1994). The slope may be draped by deposition from the overriding and dilute tail of the same flow.
Medium-bedded sandstone (LF 2)	0.1 - 0.8 m beds. Fine - coarse grain size. Flat or weakly erosional bed bases and flat or convolute bed tops. Flutes and grooves on bed bases. Sporadic granules sometimes present and associated with structureless lower bed divisions. Mostly normally graded with planar and convolute laminae. Ripples at bed tops.	Presence of flutes, normal grading, and tractional structures indicates deposition from a dilute turbidity current. These beds are interpreted as medium-density turbidites due to their often structureless basal divisions and thicknesses greater than 10 cm.	Lobe off-axis (FA 2) Lobe axis Proximal fringe	Abrupt to draped termination More capable of surmounting topography than higher-density flows because they are more able to maintain turbulent energy while flowing up the counter-slope (e.g., Bakke et al., 2013; Eggenhuisen et al. 2017). Wide variety of sediment concentrations in these flows causes drape to extend from meters to tens of meters up the slope.
Hybrid beds (LF 3)	0.1 - 1.2 m bipartite or tripartite beds. Lower medium-coarse sandstones (division 1) overlain sharply or loaded by argillaceous sandstones (division 2). Argillaceous sandstones often have a sheared fabric. Cleaner, often finer, and tractionally reworked sandstone sometimes present capping these divisions with a sharp or foundered base (division 3). Decimeter scale organic material sometimes present in middle division.	Beds containing deposits of both turbulent and transitional/ laminar flows interpreted as hybrid beds (*sensu* Haughton et al. 2009). Flow transformation occurs through increasing concentration of fines during run-out (e.g., Kane et al. 2017) or through forced deceleration (Barker et al. 2008; Patacci et al. 2014).	Proximal fringe (FA 3) Lobe off-axis Distal fringe Lobe axis	Abrupt to draped termination Debritic or argillaceous middle divisions are highly concentrated so terminate abruptly. Draping of the middle division may occur if the slope is shallow enough to allow run-up of the debritic middle division. The turbulent lower part of the flow may drape the slope and amalgamate with the overlying sandstone or deposit abruptly if high-density.
Thin-bedded sandstone (LF 4)	0.01 - 0.1 m siltstones and fine sandstones. Parallel and convolute laminae, normal grading. Flutes rarely preserved. Ripples occasionally show opposing paleoflow directions.	Fine grain size, thin event beds, and abundance of tractional structures indicates that these beds were deposited by low-density/concentration turbidity current and are therefore interpreted as low-density turbidites.	Distal fringe (FA 4) Proximal fringe Lobe off-axis	Draped termination Low-concentration flows are less affected by changes in slope angle and are thus able to surmount basin topography and drape topography for substantial distances up the counter-slope (e.g., Muck and Underwood, 1990). Low-density turbidites are therefore able to dominate much of the sediment thickness on the upper parts of the confining slope.

Table 3.1: Key lithofacies, facies associations, and onlap geometries seen in the Grès d'Annot of the Annot Basin.

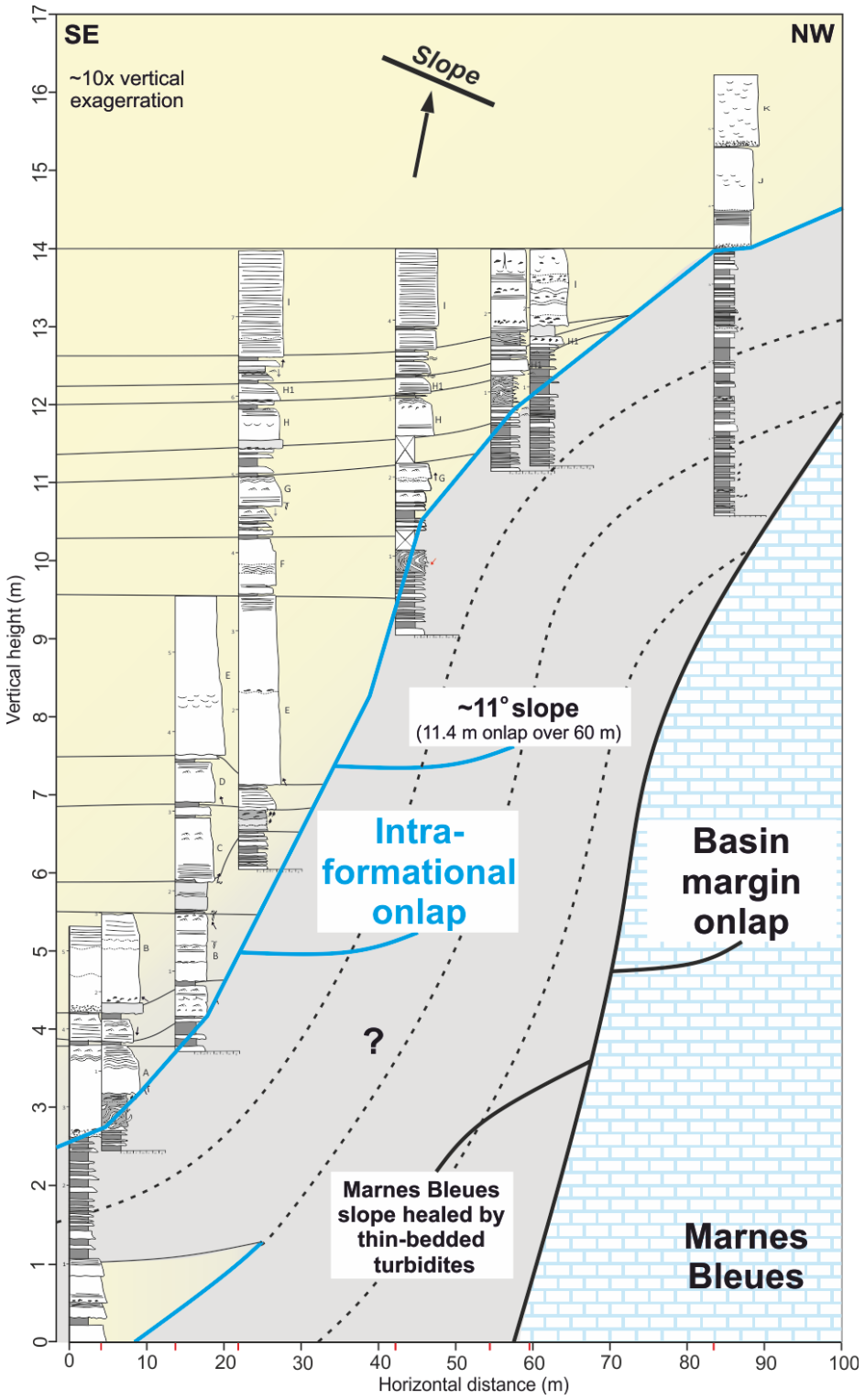

Figure 3.8: Correlation panel from the Col du Fa outcrop. The thinner-bedded low-density turbidites drape and heal the topography of the Marnes Bleues basin margin onlap surface, while the higher-density and thicker-bedded turbidites initially onlap against these distal deposits, forming an intra-formational onlap surface. Red lines on the horizontal axis indicate exact log position. Log key on Fig. 6.

The thick-bedded LF 1A sandstones are medium-grained to granular sandstones with bed bases that are flat (at exposure scale) or erosional (Figs. 3.7, 3.11B). Flat bases are most prominent when overlying mudstones, while erosional bases are most commonly expressed as amalgamation surfaces (Fig. 3.9B, C, D). Both bedding-parallel and erosional bases are associated with decimeters of deformation in the underlying beds. This deformation obscures the primary depositional characteristics of the underlying beds, making interpretation of the deformed beds difficult. Bed bases with steeper dips than the bed top are observed at pinch-out of these beds (Fig. 3.11B), with bed bases steepening towards the pinch-out. Amalgamation surfaces are identified by mudstone-clast-rich rugose horizons, abrupt grain-size breaks, and truncated trace-fossil burrows. Bed tops are flat and exhibit little depositional relief. Beds are typically structureless, with rarely preserved faint parallel lamination and tractional structures, and ungraded, though some beds show weak normal grading (Figs. 3.7, 3.9B, C, D).

Interpretations: The presence of erosional bed bases with tool marks and grooves indicates that LF 1A beds were deposited by high-concentration flows that initially carried large clasts and other detritus at the base of the flow. Superimposed flute marks, normal grading, and tractional structures are indicative of evolution to a less concentrated, more turbulent flow. The rarity of tractional structures and commonly massive and poorly sorted beds, however, indicates that these beds were deposited rapidly (*sensu* Lowe, 1982). This is most likely due to a reduction in flow capacity (*sensu* Hiscott, 1994), preventing the formation of grading and the preservation of bedforms. These turbidites are therefore interpreted as high-density turbidites (*sensu* Lowe, 1982). The presence of deformation structures beneath these flows has been attributed to high shear stresses acting on the seabed (e.g. Clark and Stanbrook, 2001; Puigdefàbregas et al. 2004). These laterally extensive (up to 1 km where outcrop allows) high-density turbidites, which are commonly amalgamated, are interpreted to be analogous to lobe axis deposits observed elsewhere (e.g., Prélat et al. 2009).

The coarse grain size and thin-bedded nature of LF 1B suggests that these beds were deposited as a coarse-grained lag in a bypass-dominated part of the system. The lenticular geometry suggests that either i) flow energy, and therefore bypass potential, was not homogeneous laterally within the flow or ii) erosion by later flows or waxing of the flow (Kane et al., 2009), scoured the bed top (Fig. 3.10B). Because this lithofacies is

confined stratigraphically to sequences underlying thick-bedded and amalgamated sandstones of similar grain sizes, they are inferred to be laterally related. These lags are interpreted to represent a mostly bypassing equivalent of the thick-bedded sandstones in the lobe axis.

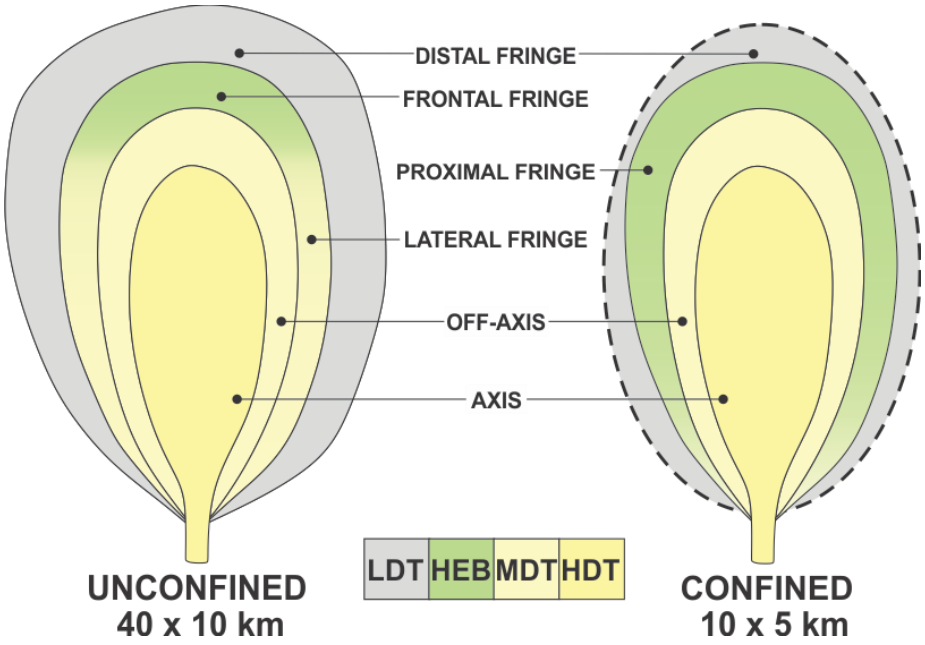

Figure 3.9: A) Nomenclature comparison between unconfined lobe sub-environments (Spychala et al. 2017) and B) confined lobe sub-environments. The only difference is that hybrid beds are more prevalent in lateral positions in confined systems due to rapid flow deceleration and transformation at basin margins. LDT = low-density turbidite; HEB = hybrid (event) bed; MDT = medium-density turbidite; HDT = high-density turbidite. Unconfined and confined lobe dimensions are from Prelat et al. (2010).

FA 2: Lobe off-axis

Observations: Facies association 2 is composed primarily of normally graded medium-bedded (0.1 - 0.8 m) fine- to medium-grained sandstones (LF 2) with flat to slightly erosional bed bases and flat bed tops (Figs 3.7, 3.10A, 3.12). Flutes and grooves are often seen at bed bases. Ripples at bed tops commonly show opposing paleoflow directions to those measured from flutes and grooves on individual event beds (Fig. 3.5). Beds pinch out abruptly towards the basin margin, and often can be traced away from the onlap surface to a parent thick-bedded sandstone (Fig. 3.7). In the uppermost stratigraphy of the basin, LF 2 commonly has highly irregular bed tops with abundant tractional

structures, such as climbing ripples and convolute lamination (Figs. 3.10E, 3.12). These beds are termed LF 2B.

Interpretations: The presence of flutes, normal grading, and tractional structures indicate that the LF 2 beds were deposited by waning, turbulent flows which were able to rework the aggrading deposit (Bouma, 1962). This suggests that these flows were more dilute than the parent flows of the thick-bedded sandstones (LF 1). These medium-bedded sandstones are therefore interpreted as medium-density turbidites and are differentiated from low-density turbidites by bed thicknesses being greater than 10 cm and a coarser grain size. These medium-density turbidites also have a thicker massive interval at their base compared to low-density turbidites. Opposing paleocurrent directions within event beds is characteristic of flows encountering topography (e.g., Kneller et al., 1991), indicating that many of these beds were deposited close to a basin margin. Coarser, denser parts of the flow may be more strongly influenced by topography than the upper more dilute part of the same flow (Bakke et al., 2013).

The finer, better sorted and thinner-bedded nature of this lithofacies compared to thick-bedded sandstones indicates that these beds were deposited beyond the axis of the lobe (off-axis) (Prélat et al. 2009; Bell et al., 2018a) (Fig. 3.8). LF 2B is interpreted as representing flows that were deposited close to the basin margin or possibly within slump scars on the basin margin. Bypassing flows deflected by the margin or trapped in scars caused complicated oscillatory-flow patterns to develop which deformed the aggrading deposits (Pickering and Hiscott, 1985; Tinterri et al. 2016; Cunha et al. 2017). An example of this can be seen at Tête de Ruch, where this facies dominates a ~ 10 m thick scar fill (Puigdefàbregas et al. 2004) and is overlain by thin beds showing simple uniformly directed ripples and plane-parallel lamination (Figs. 3.5, 3.11C). These thin beds were deposited over the scar fill where flows were relatively unconfined, allowing more uniform and waning flow deposition to dominate.

Figure 3.10: Sedimentary logs with facies and paleogeographical interpretations. Each member contains elements of each lobe sub-environment; however, there is an increasing prevalence of higher-density deposits upwards through stratigraphy. This pattern is interpreted as representing overall lobe progradation. Colored bars next to logs represent facies on sub-environment key.

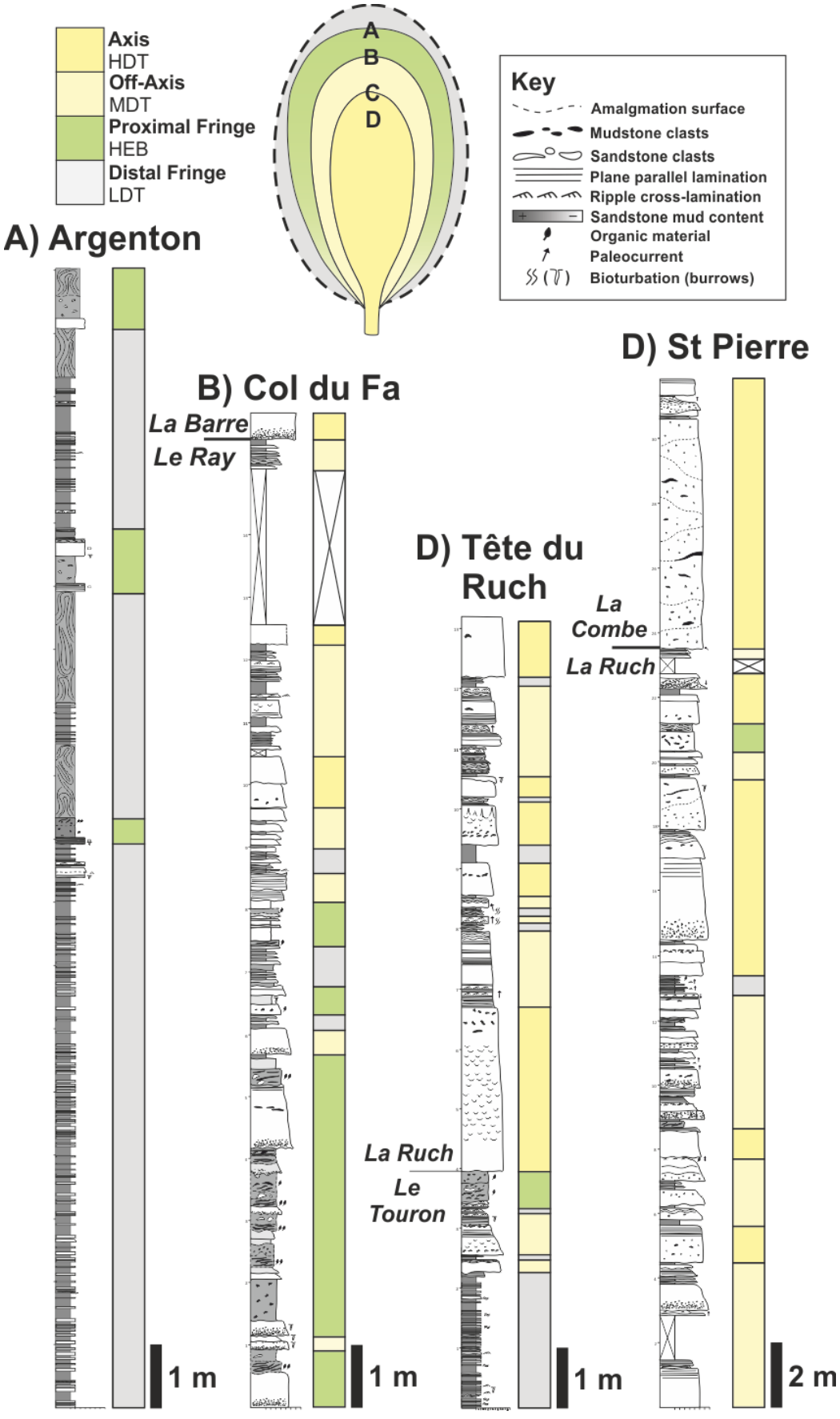
Axis
HDT
Off-Axis
MDT
Proximal Fringe
HEB
Distal Fringe
LDT
A
B
C
D
Key
Amalgmation surface
Mudstone clasts
Sandstone clasts
Plane parallel lamination
Ripple cross-lamination
Sandstone mud content
Organic material
Paleocurrent
Bioturbation (burrows)
A) Argenton
B) Col du Fa
La Barre
Le Ray
D) Tête du Ruch
La Ruch
Le Touron
D) St Pierre
La Combe
La Ruch
1 m
1 m
1 m
2 m

FA 3: Proximal fringe

Observations: Facies association 3 is dominated by medium- to thick- bedded (0.1 m - 1.2 m) bipartite or tripartite event beds (LF 3) (Figs. 3.9, 3.11C, D, G). These beds are composed of a lower division of medium- to thick-bedded sandstone (LF 1 and LF 2) with an irregular top which is loaded and/or eroded into by an overlying argillaceous sandstone (Fig. 3.10D). The middle division is an argillaceous sandstone, poorly sorted and often deformed, which appears as a sheared fabric (Fig. 3.10D). The argillaceous sandstone can either contain clasts of the underlying sandstone or be clast-poor. Organic matter (< 70 cm in length) may be present in this bed, with organic-rich sandstones typically thicker than the more argillaceous sandstones. Elongate organic matter is usually aligned with its long axis approximately parallel to paleoflow recorded on the bed base (Fig. 3.10C).

Argillaceous sandstones, which are rich in cleaner sandstone clasts, commonly occur where the lower, cleaner sandstone is coarser-grained; thus most sandstone clasts seen tend be coarse-grained than the argillaceous matrix. This deposit can show variable sand-to-mud ratios. Higher sand contents within this middle division are associated with increased prevalence of lamination, with centimeter-scale layering (mud-concentrated laminae) sometimes evident, and higher mud contents associated with more sheared and poorly sorted deposits. Both of these divisions may contain coarse-sand to granule-size quartz grains supported within the matrix.

Overlying this argillaceous sandstone, medium-bedded, often muddy sandstone may occur, although it is sometimes difficult to assess whether this sandstone is part of the underlying event bed or represents a separate event bed (Fig. 3.10D). This sandstone has an irregular base and can show loading and foundering into the underlying argillaceous sandstone (Fig. 3.10D). The bed top is typically flat or mounded. Approaching basin margins these beds can be seen to transition laterally from thick-bedded sandstones (Fig. 3.13A, B).

The middle division of the bed may pinch out between the underlying and overlying sandstones, which then amalgamate at the onlap surface (Fig. 3.13C), forming a complicated and often muddy pinch-out (Fig. 3.14). Stratigraphically this lithofacies dominantly occurs following the thin-bed-dominated sequence and underlying the medium- to thick-bedded sandstones (Fig. 3.9).

Interpretations: The basal and upper sandstones within these bipartite or tripartite event beds are interpreted as either high-density or medium-density turbidites. The

massive, poorly sorted, and mud-rich nature of the division encased by these turbidites is interpreted as being caused by en-masse deposition of a laminar and cohesive flow (e.g., Middleton and Hampton, 1973; Mulder and Alexander, 2001). This bed division is therefore interpreted as a debrite. The irregular contact seen between these divisions has been attributed to complex short-wavelength soft-sediment deformation and erosion (e.g., Fonnesu et al. 2015). Where the overlying turbidite is relatively thick it is difficult to differentiate between a debritic or deformed (see LF 1 basal deformation) origin for the middle division, particularly when the overlying turbidite has foundered into the underlying division (e.g., Fonnesu et al. 2015). Where the middle sandstone division is slightly cleaner, with lamination and/or layering, the sandstone is interpreted as having been deposited by flows transitional between laminar and turbulent and therefore termed a transitional-flow deposit (Baas et al., 2011; Kane and Pontén, 2012). These tripartite event beds therefore contain deposits of both turbulent and laminar flow regimes and are subsequently interpreted as hybrid beds (*sensu* Haughton et al., 2003; 2009).

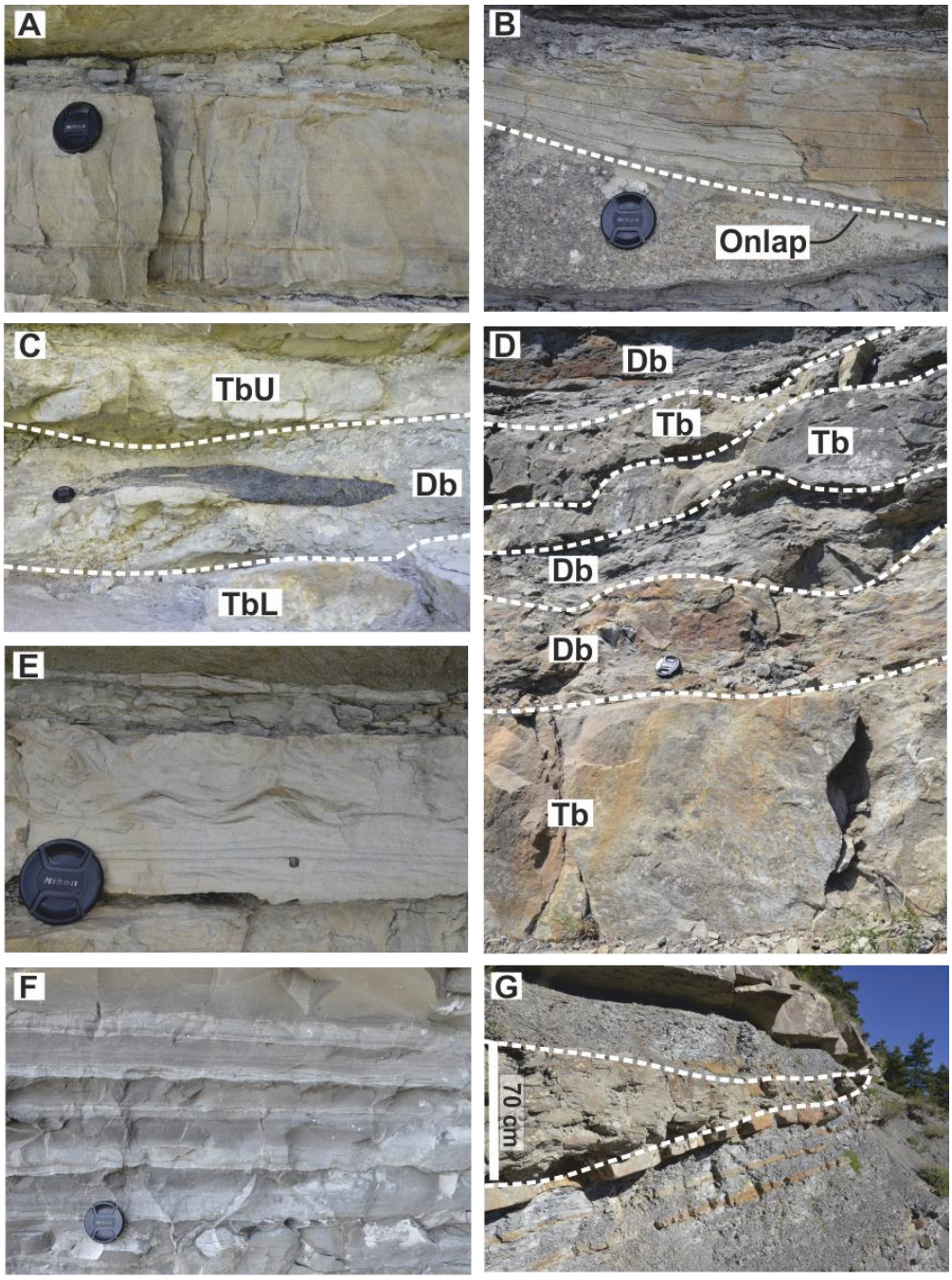

Figure 3.11 A) Medium-density turbidite (MDT) at Col du Fa. B) Low-density turbidite (LDT) onlapping a gravel lag deposit at Tête du Ruch (Lower). C) Organic material in the debritic division of a hybrid bed at Le Marc. D) Pinch-out amalgamation zone at Col du Fa. Debritic (Db) and turbiditic (Tb) sections can be identified and correlate with thick- and medium-bedded turbidites up-dip. It is difficult to differentiate groups of event-beds in these slope proximal units. E) Highly tractionally r-worked LDT. F) Typical thin-bedded LDT facies. G) Slumped thin-bedded turbidites at Argenton. Fold hinges indicate failure perpendicular to the slope.

It is suggested that the more organic-rich linked debrites, with decimeter clasts of terrestrial debris, are derived from flows which originated from events in the hinterland that carried significant amounts of terrestrial debris into the marine environment (see also Hodgson, 2009). These beds are therefore deposits from particularly high-magnitude flows; this may explain their greater average thickness compared with the more argillaceous hybrid-beds. It is also possible that the organic material was staged for significant periods of time on the shelf, making terrestrial debris a poor indicator of flow magnitude. The close association of terrestrial debris and coarse grain sizes in these relatively distal environments, however, indicates that these beds were the result of high-magnitude or "outsize" flows that were capable of significant substrate erosion (Fonnesu et al. 2018). Incorporation and disaggregation of this eroded substrate will have primed these flows for

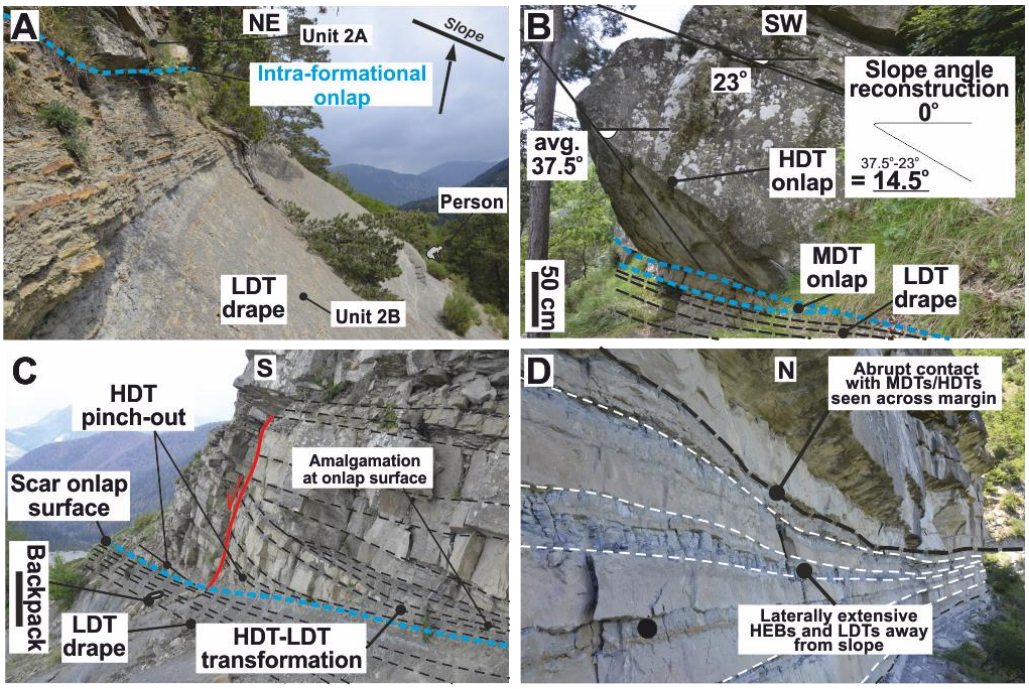

Figure 3.12: A) Contact between the thin beds and high-density turbidites at Col du Fa. The high-density turbidites onlap against the low-density turbidite slope drape at an incidence angle almost perpendicular to the slope (arrow is paleoflow). B) Example of a high-density turbidite with a wedged base onlapping the underlying slope drape. Restoring the bed top to horizontal allows a rough estimate of the paleo-slope angle. C) Scar fill at Tête de Ruch (upper). The higher-density flows either onlap the scar drape abruptly or transform to low-density turbidites up the counter-slope. D) Laterally continuous hybrid beds at Le Marc. These beds are interpreted to have been deposited away from the basin margin and cohesively transformed through distal run-out. 7 cm camera lens (black circle) for scale.

rheological transformation (Kane et al. 2017; Fonnesu et al. 2018). LF 1 can be seen to transform into these hybrid beds over tens of meters approaching the slope, further

indicating that these beds were highly erosive and prone to rheological transformation, even in proximal positions, due to forced deceleration against the basin margin (e.g., Patacci et al. 2014). The presence of large amounts of erodible and muddy draping substrate on the basin margin will aid in short-length-scale flow transformation in these high-magnitude flows (Fig. 3.14) (e.g., Fonnesu et al. 2018).

It is possible that the debritic division of these beds represents high-concentration turbidity currents hitting the counter-slope, causing intra-basinal slope instability and failure. The turbidity current will then have aggraded around this failure, represented depositionally by a sandwiched debrite (e.g., McCaffrey and Kneller, 2001). It is difficult to differentiate between a flow-transformation or slope-failure origin for the co-genetic debrite at outcrop; however, the presence of large organic clasts within an identified debritic division may favor a flow-transformation origin.

Because these beds dominantly underlie the thicker-bedded and more sandy turbidites of FA 1 and 2, they are interpreted as being depositionally adjacent (*sensu* Walther, 1894) (Figs. 3.8, 3.9). An abundance of hybrid beds indicates a more distal lobe sub-environment compared with the axis and off-axis deposits of FA 1 and FA 2 (e.g., Hodgson, 2009; Jackson et al. 2009; Kane et al., 2017; Fonnesu et al. 2018). This sub-environment is termed the lobe fringe. FA 3 is therefore interpreted as being analogous to lobe-fringe deposition seen in unconfined systems (e.g., Spychala et al. 2017). The lobe fringe can be further subdivided into a lateral and frontal fringe, with the lateral fringe having a lower proportion of hybrid beds compared to the frontal fringe (Spychala et al. 2017). In confined settings this definition is complicated because flow deceleration against lateral slopes cause flow transformations and subsequent enrichment of hybrid beds in the lateral fringe (Figs. 3.8, 3.15, 3.16, 3.17). This relationship is also evident in the Late Cretaceous Britannia Sandstones of the North Sea, where flows underwent rheological transformation against a lateral slope (Lowe and Guy, 2000; Barker et al. 2008). This study thus uses the general term proximal fringe because the frontal and lateral fringe are expected to be similar due to the counter-slope causing a prevalence of hybrid beds in both settings (Figs. 3.8, 3.14, 3.17).

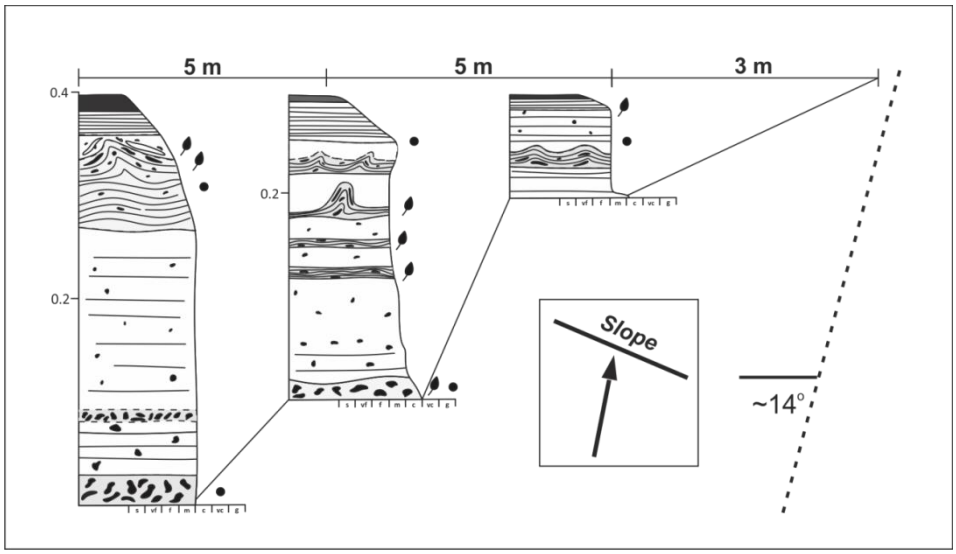

Figure 3.13: High-resolution log of one medium-density turbidite approaching onlap at Col du Fa showing the short length-scale variability seen in these beds.

It should also be noted that particularly erosive flows in the lobe axis and off-axis also generate hybrid beds at the onlap surface (e.g., Patacci et al. 2014; Fonnesu et al. 2018). This can make lobe-sub-environment interpretation challenging when adjacent to a steep basin margin because much of the succession may be margin-affected over short length scales (tens of metres) (Fig. 3.14) and therefore not represent their primary lobe-scale paleogeographic position (e.g., Southern et al. 2015). This is enhanced in tectonically active basins where flow types can be highly variable (e.g., Mutti et al. 2009). Facies back-stripping may therefore need to be attempted to assess the lobe-scale sub-environment (Fig. 3.16). These short-length-scale margin effects and attempts at back-stripping are summarized in Figure 3.16 and 3.17.

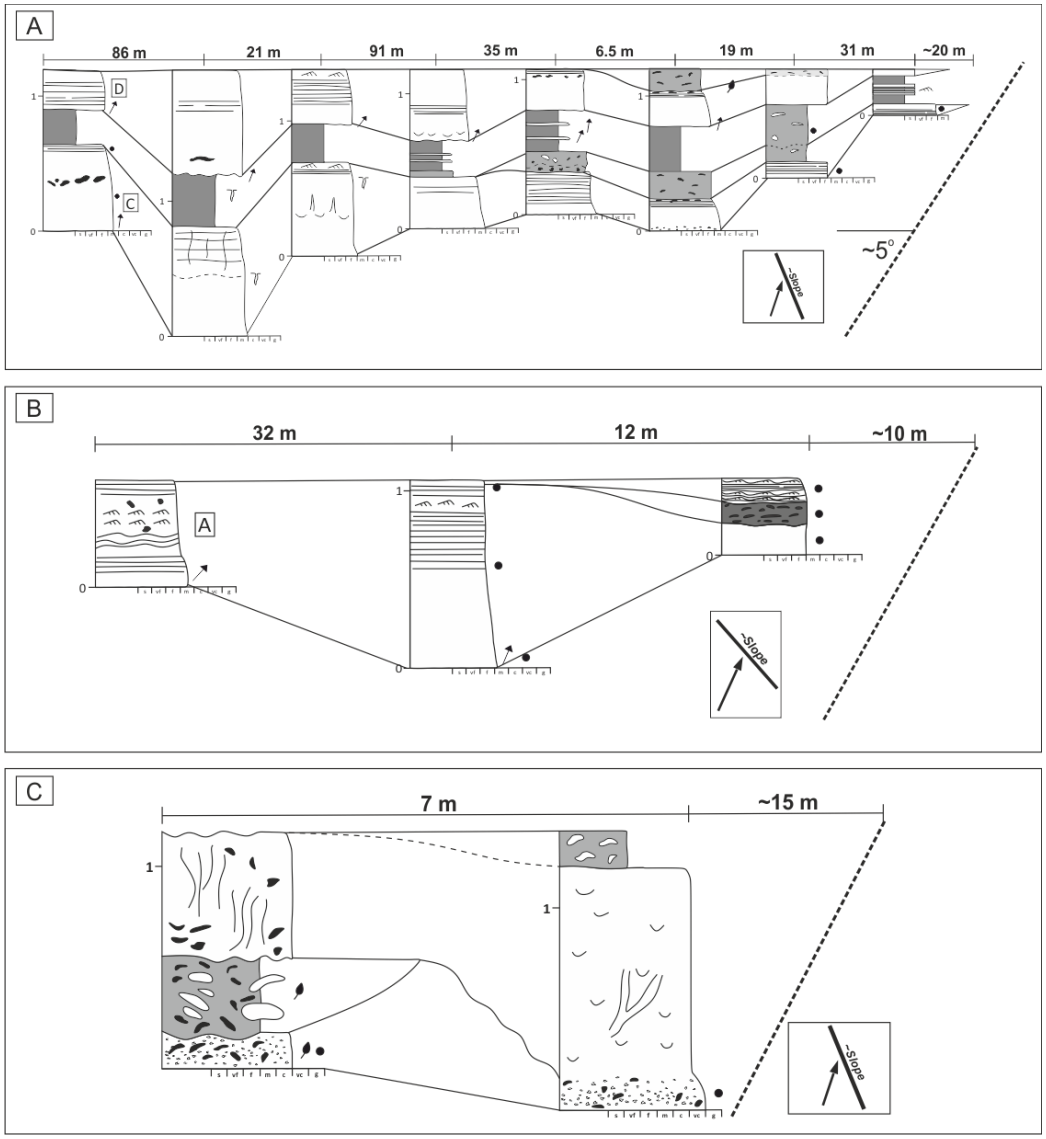

Figure 3.14: A) Hybrid-bed evolution approaching topography at Argenton. B) Hybrid evolution at Tête de Ruch (lower) C) Hybrid-bed evolution at the Tête de Ruch (upper). The complex interaction between the debritic and turbiditic intervals are suggested to result from either differential interaction with the slope between rheologically distinct flow phases or erosion at the onlap surface. Letters in blacked boxes = correlated bed label. Log key on Fig. 6.

FA 4: Distal fringe

Observations: Facies association 4 is dominated by thin-bedded (0.01 – 0.1 m) siltstones to fine-grained sandstones (LF 4) that form laterally continuous event beds (Figs. 3.7, 3.11A, 3.14). Parallel and convolute lamination is common (Fig. 3.10F). Beds are normally graded, with ripples common on bed tops (Fig. 3.10F). Ripples may show multiple and opposing paleocurrent directions within single beds. Beds tend to pinch out

over tens to hundreds of meters towards the basin margin (Fig. 3.15), with amalgamation of event beds sometimes observed towards the onlap surface, causing local bed thickness increases in a regional thinning trend. Slumping and folding of beds (LF 5) is evident in this FA, particularly immediately underlying the abrupt transition to dominantly medium- and thick-bedded sandstone sequences (Fig. 10G). Fold-axis measurements indicate that deformation was both oblique and perpendicular to paleo-slopes. Stratigraphically, these beds immediately overlie the Marnes Bleues, forming a distinct sequence that significantly drapes the Marnes Bleues slope (11A). This lithofacies becomes less common up stratigraphy (Fig. 3.9).

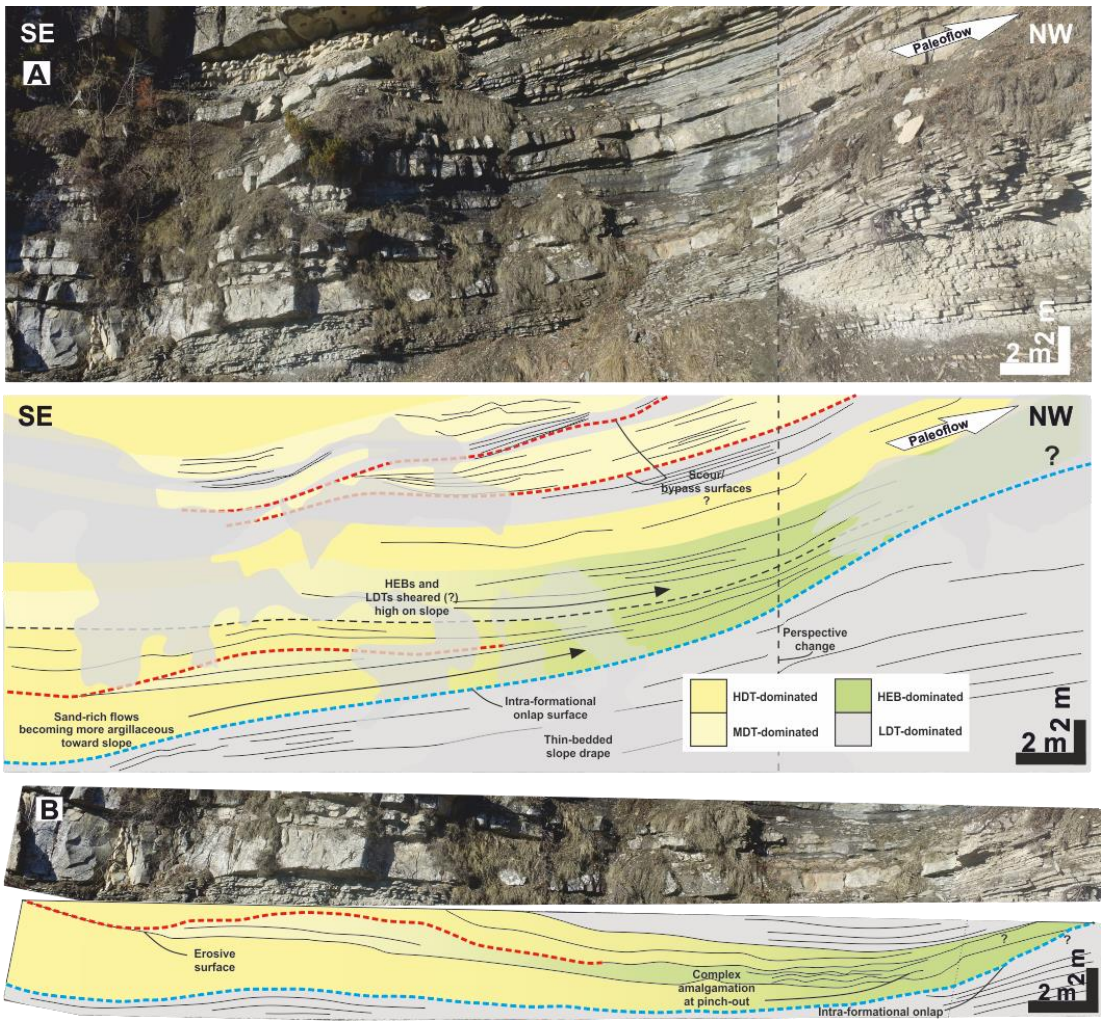

Figure 3.15: Outcrop sketch from the Col du Fa locality. A) Low-density turbidites drape the slope and are onlapped by hybrid beds and higher-density turbidites. B) Flow transformation can be seen to occur in the proximal fringe deposits over 10 - 15 m approaching the onlap surface to the NW, resulting in complex amalgamation zones at pinch-out (see Fig. 10D for pinch-out detail).

Interpretations: The fine grain-size, abundance of tractional structures, and dominance of thin beds within LF 4 indicates deposition from dilute, low-density turbidity currents (*sensu* Lowe, 1982). The narrow grain-size range (dominantly silt) of these slope-draping beds is numerically predicted because of the quadratic decrease in settling velocity of silt and mud and the consequent increase in likelihood of flow inflation far above the initial flow depth in silt- and mud-rich flows (Dorrell et al. 2019). Because these beds are able to drape the existing relief they are suggested to have healed much of the initial relief present on the Marnes Bleues slopes (Figs. 3.7, 3.11A). Slumping in these successions (LF 5) is interpreted to represent slope failure on the steep basin margins (Fig. 3.10G). Progressive deformation and seismicity along the Alpine thrust front is suggested as the primary reason for slope failure (Fig. 3.2). Failure scars may contribute to some of the heterogeneity seen within the overlying medium- and thick-bedded sandstones by creating a rugose topography high on the slope (Fig. 3.11C).

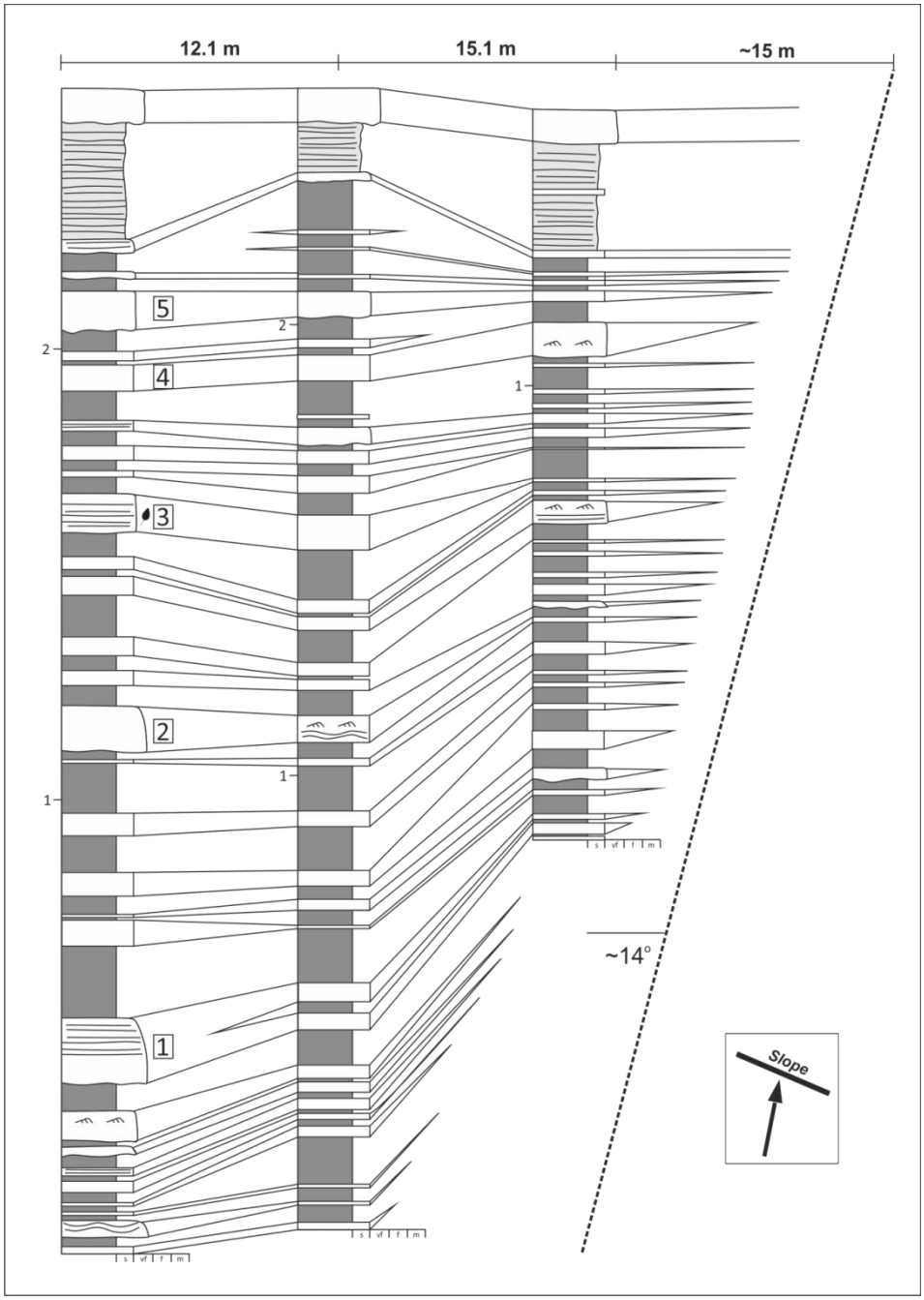

Figure 3.16: Example of correlated low-density turbidites approaching the Col du Fa basin margin. Very little facies variation is seen in these beds and thinning rates are lower than those seen within thicker-bedded turbidites approaching the basin margin.

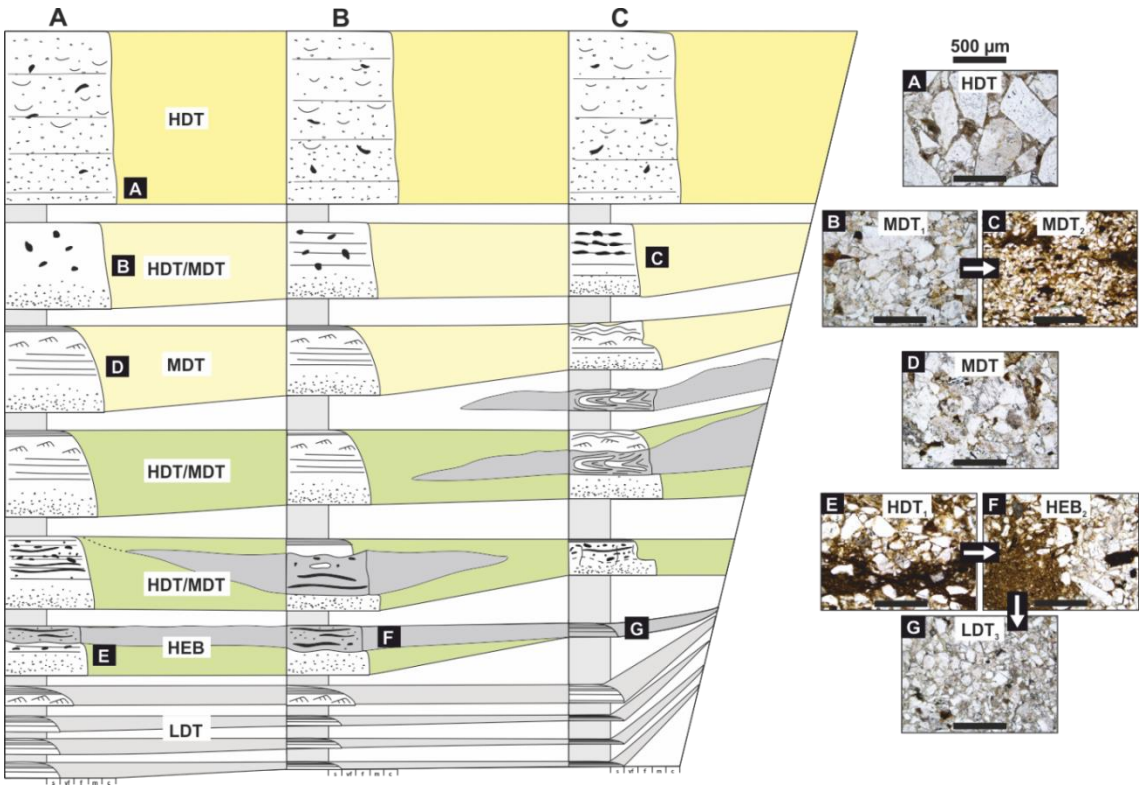

Figure 3.17: Summary logs showing facies transition approaching pinch-out toward basin margins for given lobe sub-environments and their dominant facies. The right-hand petrographic images are taken from representative beds in the Annot Basin approaching onlap. The corresponding letter (white text in black box) on the logs indicates the point in the bed where the sample was taken. Onlap to right.

The lateral continuity, fine grain-size and thin-bedded character of the thin beds is consistent with both levee deposition and lobe-fringe deposition. Because of the few long-lived channels identified and the low stratigraphic position of these beds in a prograding lobe (Fig. 3.9), they are not interpreted to be levee deposits, but are instead attributed to the distal fringe of a submarine lobe on the basin floor (e.g., Boulesteix et al. 2019a, b) (Fig. 3.8), which caused termination of Marnes Bleues carbonate deposition. This is supported by the published paleogeographic position of the lowermost Grès d'Annot (Fig. 3.2) (Apps et al., 2004; Joseph and Lomas, 2004; Salles et al., 2014). The relative lack of hybrid beds in the LF5 sequence also supports a distal lobe fringe interpretation (Figs. 3.8, 3.9A, 3.13) (Spychala et al., 2017).

Stacking patterns

Confined basins have previously been associated with sheet-like deposition, where incoming flows are entirely confined by the basin margins, resulting in tabular stratigraphy with little or no autogenic compensational stacking (e.g., Sinclair and Tomasso, 2002). Numerical studies (Dorrell et al. 2018), subsurface studies (e.g., Beaubouef and Friedmann, 2000), and outcrop studies (e.g., Spychala et al. 2016; Bell et al. 2018b; Liu et al. 2018), however, have shown the stacking-pattern complexity that may arise in basins that display variable degrees of confinement. This study uses data from the lowermost member of the Grès d'Annot, the Le Ray member (Figs 3.5, 3.6), to build on these studies. Le Ray (Puigdefàbregas et al., 2004), or member A (Du Fornel et al. 2004), is suggested to have been fully confined by the basin margins during its deposition (Callec, 2004; Salles et al. 2014) through onlap mapping and thinning trends.

Unit 1: This unit comprises a sequence of thin-bedded low-density turbidites (LF 4) overlain abruptly by medium- and thick-bedded high-density turbidites (LF 1 and 2). These thick-bedded sandstones correlate with a thick sequence of thin-bedded turbidites ~ 800 m to the NW adjacent to the Braux Fault footwall (Figs 3.3, 3.6). This transition is caused either by flow over-spill across the paleobathymetry of the Braux Fault or draping of the lower-density part of the flow up the Braux Fault topography. Correlation of this unit toward the NE is hindered by lack of exposure; however, it is possible that the distal Unit 1 correlates with some of the early Unit 2B deposition (Fig. 3.6).

Unit 2: Proximal Unit 2 is characterized by a thick 33 m amalgamated sandstone body interpreted as being deposited by high-concentration turbidity currents. Indicators of erosion, such as scours and decimeter-scale mud-clasts, indicate that this was a region of significant bypass (e.g., Stevenson et al. 2015) and is interpreted to represent the lobe axis (FA 1) through Le Ray deposition. Down-dip this unit has been subdivided into Unit 2A and 2B based on facies and stacking. Unit 2B is composed of thin-bedded turbidites that drape the frontal confinement of the early Annot Basin and stack aggradationally (Fig. 3.11A). This confinement was caused by a combination of the basin closure due to the NW-SE Melina anticline, the E-W Fuguret anticline, and the NE-SW Braux Fault (Fig. 3.3). Unit 2A represents an abrupt transition into thicker-bedded sandstones that pinch out against the underlying Unit 2B. These sandstones can be subdivided into various lobes based on the correlation of intervening packages comprising low-density turbidites (LF 4)

overlain by hybrid beds (LF 3), medium-density turbidites (LF 2), and amalgamated high-density turbidites (LF 1), which are interpreted to represent the sequential stacking of distal-fringe (FA 4), proximal-fringe (FA 3), off-axis (FA 2), and axis deposits (FA 1). These lobes represent the depositional products of the bypassing flows from the proximal thick sandstone body, forming the lobe axis.

The axis of each of these lobes steps farther into the basin, suggesting allogenic progradation, which likely occurred in response to increasing sediment flux from the uplifting Corsica-Sardinia hinterland toward the south (e.g., Apps et al. 1987; Euzen et al. 2004). This pattern is not uniform, however, and a degree of compensational stacking is clearly visible, with the axes of successive lobes (represented by amalgamated high-density turbidites) overlying the fringes of underlying lobes, which represented lows on the seafloor (e.g. Deptuck et al. 2008; Prélat et al. 2009). These stacked lobes could also represent lobe "fingers" that were focussed between the lows of the previous axial deposits (e.g., Groenenberg et al. 2010). In this case the apparent basinward stepping of the Le Ray lobes may be autogenically-driven, as flows are focussed between the lows and build passively into the basin. This explanation may operate in tandem with allogenic progradation, particularly during early deposition, due to the prevalence of these finger-like geometries in the basal stratigraphy of lobe complexes (e.g., Prélat et al. 2009; Groenenberg et al. 2010). These indicators of compensational stacking are at odds with the prevailing suggestion that basins generically described as "confined" can be assumed to have a sheet-like architecture, and fit with the recent work indicating that lobes deposited within basins with varying degrees of confinement are characterized by more complicated stratigraphic relationships (e.g., Marini et al. 2015; Bell et al. 2018b; Liu et al. 2018).

The presence of thick and coarse sandstones in distal positions has also been described in subsurface datasets of submarine lobes and lobe elements and has been attributed to flow stripping of the upper dilute parts of flows over the basin's confining topography, leaving behind the coarser parts of the flow (e.g., Marini et al. 2016a,b; Jobe et al. 2017). This process may also contribute to the preservation of the thick and abruptly terminating sandstones within Unit 2A of the Le Ray member.

Unit 3: This unit has been differentiated because it cannot be reliably correlated to another unit. It is possible that Unit 3 represents the distal expression of the upper parts of

Unit 2, however the lack of exposure between the proximal and distal parts of the upper Le Ray prevents reliable correlation.

Alternative Interpretations: The observed intra-formational onlap against the low-density fringe (Unit 2B) at the Col du Fa locality is likely caused by the inferred proximity of the basin margin. An alternative explanation for this stratigraphic relationship may be the presence of a large erosional feature, such as a scour, at the Col du Fa margin. Such scours are interpreted higher in the basin stratigraphy at Tête du Ruch (e.g., Puigdefàbregas et al. 2004), and show the same intra-formational onlap relationship (Fig. 3.11C). Decameter-thick scour fills are also suggested to be present in the Grès d'Annot at Peira Cava (Lee et al. 2004). The scour would have created accommodation space to be filled by the incoming flows, resulting in the onlap geometries described by this study. Exposure limits further analysis of this problem, however, a scour interpretation is not believed to affect the underlying principles of this study as the low-density turbidites still drape the scour and are onlapped by the later higher-density turbidites.

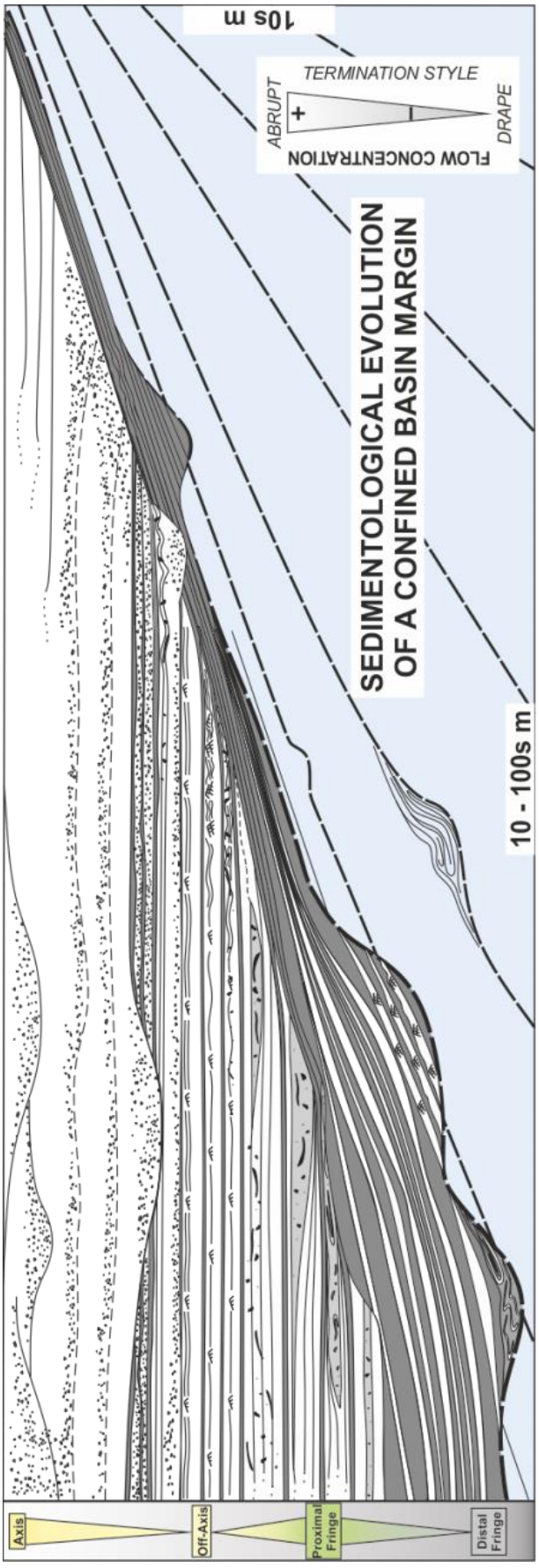

Figure 3.18: Synthesis of faces evolutions seen in the Grès d'Annot towards the basin margins and their stratigraphic position. Flow concentration at the point of sedimentation largely controls the style of the onlap termination. Lobe sub-environments are often obscured adjacent to onlap surfaces due to topographic interaction between the flow and the slope, but can be back-stripped. Flow concentration key indicates onlap pattern produced by flows of varying concentrations.

Another explanation for the observed intra-formational onlap may be that the low-density fringe (Unit 2B) was tilted (e.g., Salles et al. 2014) and subsequently onlapped by higher-density flows when the basin was relatively static or depositional rates were higher, resulting in the wedge-shaped geometry observed (Apps et al. 2004). Unit 2B may therefore represent the distal extents of early Le Ray (i.e., Unit 1), while the onlapping Unit 2A is either more proximal and late-stage Le Ray or early La Barre (i.e., Unit 3) (Figs. 3.3, 3.5). Differential compaction between the basin center and the basin margin may have also acted to enhance the tilting effect (Sinclair, 1994). The inability to walk out individual units between outcrop localities again makes further analysis of this problem difficult. If tectonism or differential compaction is the reason for the observed relationship, then run-up of the low-density turbidites that characterize Unit 2B would have acted to exaggerate the intra-formational onlap that was caused by tilting, and the underlying principles of this study are maintained. Unit 1 would therefore be analogous to the ponded aprons identified in intra-slope basins of the Gulf of Mexico, while Unit 2 would similar to a perched apron (Prather et al. 2017).

3.6 *Turbidity-current run-up and onlap geometry*

Sediment gravity flows are able to deposit high on confining slopes through flow run-up and/or inflation (e.g., Muck and Underwood, 1990; Lamb et al. 2008; Dorrell et al. 2019). The distance a turbidity current runs up topography is termed the run-up height (*H*) and, in its simplest form (following Straub et al. 2008), can be represented by the ratio between kinetic and potential energy within a flow,

(1) $$H = h + \frac{\rho_c U^2}{(\rho_c - \rho_a) 2g}$$

Where h = flow thickness, U = flow velocity, ρ_c= bulk density of the flow (composed of quartz at 2650 kg m^{-3}), ρ_a = density of the ambient water (seawater at 1020 kg m^{-3}), g = acceleration due to gravity (9.81 m s^{-1}). In order to assign a single value for sediment concentration there is an assumption that there is no density stratification within the flow. A 30-m-deep channel-form at Chambre du Roi (Sinclair, 2000) has been used as the basis for estimating minimum flow height. This is slightly arbitrary but serves the purpose of this thought-experiment. In order to correct for channel-related superelevation, this flow height has been multiplied by 1.3 (see Mohrig and Buttles, 2007), giving a h value of 39 m. This height represents the minimum height of the flow at the lobe apex, disregards compaction, and is assumed constant. It should be noted that due to a lack of flow height proxies preserved at outcrop this value is used purely to demonstrate the underlying principles of the model, i.e., the model does not attempt to fully reconstruct the turbidity currents entering the Annot Basin. The depth-averaged flow velocities used range from 5 m s^{-1} to 0.5 m s^{-1}. The upper limit of 5 m s^{-1} is derived from the maximum flow velocities (4 - 6 m s^{-1}) reached by sand-rich flows in the Monterey Canyon (Symons et al. 2017), while the lower limit of 0.5 m s^{-1} is derived from average measurements of finer-grained flows in the Congo Canyon (Azpiroz-Zabala et al. 2017b).

The Annot system is sand-rich; therefore the faster Monterey flows are likely the most analogous, at least close to the input. Flow velocity will decrease with decreasing concentration, making the use of a constant velocity problematic. This is suggested to be less important for small and confined basins, such as the Annot Basin, where flows may be prevented from significant velocity decay between the axis and pinch-out. If velocities do decay significantly, then plotting single velocity values through the height of an individual flow will be required; for example, the 5 ms^{-1} and 10% concentration basal part of a hypothetical flow will run-up 9.2 m above the flow height, while its 1 ms^{-1} and 0.1%

concentration tail will run-up 32 m above the flow height. This decameter scale difference may explain the ~ 15 m of slope drape at Col du Fa (Figs. 3.6, 3.8). This parameter is further complicated by the possible presence of low-velocity dense basal layers within highly-concentrated stratified flows (e.g., Stevenson et al. 2018). Turbulence is suppressed in these basal layers; this reduces velocity and run-up heights, resulting in the increased likelihood of an abrupt pinch-out of the sand-rich basal layer and bypass of the upper and low-concentration parts of the flow. The wedged high-density turbidites identified at onlap by this study (Fig. 3.11B) may be the depositional products of such basal layers.

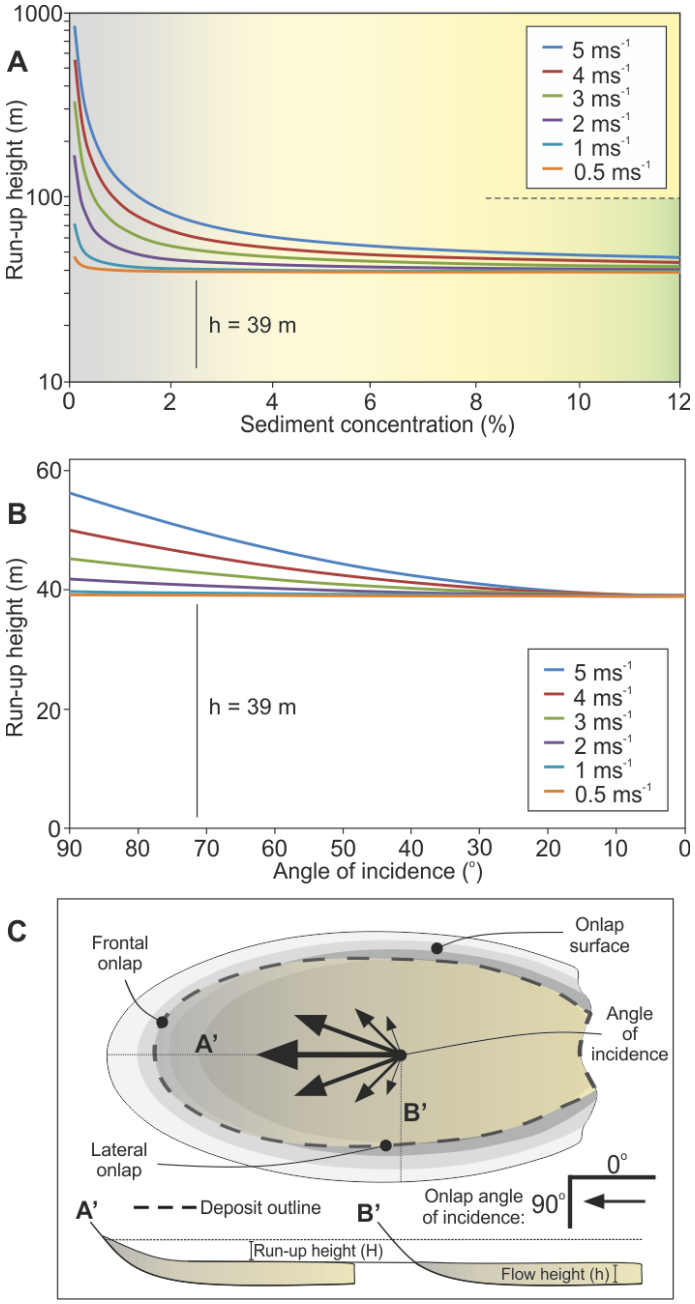

Figure 3.19: A) Run-up height versus flow sediment concentration for flows of varying velocities. Flows with high concentrations are less able to run up topography than low-concentration flows if all other parameters are equal. B) Run-up height versus the angle of incidence between the flow and the slope for flows of varying velocities. Lower angles of incidence cause higher run-up of flows. C) Schematic diagram showing the relationship between frontal and lateral onlap (modified from Al A'Jaidi et al. 2004).

By varying flow concentration in equation (1), a clear trend is developed, with lower sediment concentrations resulting in greater run-up heights (Fig. 3.18A). In prograding lobe systems turbidity currents with lower sediment concentrations (well below 10%), forming low- or medium-density turbidites, are typically found in the distal or basal stratigraphy and flows with higher sediment concentrations (> 10%), forming high-density turbidites, are typically found in the proximal or upper stratigraphy (e.g., Hodgson et al. 2006, 2009; this study). This therefore suggests that earliest turbulent flows into a receiving basin should have the greatest run-up heights, assuming all of these flows are of similar thickness, with run-up heights decreasing through time as flows become more concentrated (Fig. 3.18A). It should be noted that the effect of increasing concentration through time will be counteracted by increasing velocities, as discussed previously. Suspended-sediment concentrations of > ~ 8% have been shown to suppress the generation of current ripples and cause transformation from turbulent to transitional flow, where flows decelerate sufficiently, forming transitional or hybrid-flow deposits (Baas et al. 2011). This concentration (> ~ 8%) has therefore informed the placement of hybrid beds along the x-axis of the run-up height trend (Fig. 3.18A), giving hybrid beds a similar run-up potential as high-density turbidites. It should be noted that Baas et al. (2011) emphasize that this value is dependent on flow velocity, grain size, and sediment composition, and that the dimensionless Reynolds number is a much better predictor of flow phase. The results of this analysis fit with facies-dependant thinning rates compiled from 18 outcrop studies by Tőkés and Patacci (2018), with hybrid-beds having 1.3 to 2.8 times higher thinning rates than turbidites. Data collected in this study also support the compiled data of Tőkés and Patacci (2018), with thinner-bedded turbidites having lower thinning rates than thicker-bedded turbidites and consequently draping topography (Figs. 3.6, 3.7, 3.15). Similar thinning trends have been reported from levee sandstones (DeVries and Lindholm. 1994).

Lateral vs. Frontal Onlap

To assess the run-up variation between frontal and lateral onlap the velocity of the modeled flow (at 5% concentration) was varied according to the incidence angle of the flow with the slope. It is assumed that the flow velocity will be at its maximum (5 m s^{-1} in this case) in the principal direction of travel, or an angle of incidence of 90° with respect to the slope, and that the flow velocity will fall to 0 ms^{-1} perpendicular to its axis at an angle of incidence of 0°, i.e., when the flow is running perpendicular to the topography. In reality there will still be some lateral velocity; however, for the purposes of this simple analysis it is assumed that this is negligible. The fastest flows occur at an angle of incidence of 90° or perpendicular to the slope (Fig. 3.18B). These flows therefore run farther up the counter-slope. Deposits of these flows would pinch out higher up the frontal slope than the lateral slope (Fig. 3.18B, C). In the 5 ms^{-1} case, for example, the difference in run-up height between the frontal and lateral part of the flow is 17 m. The difference will be increased in lower-density flows and reduced in slower flows.

3.7 *Discussion*

Stratigraphic Evolution of Onlap

Based on the similarity between facies transitions and associations seen in this confined basin and those in unconfined or weakly confined submarine lobes (Figs. 3.8, 3.9) (e.g., Hodgson, 2009; Spychala et al., 2016, 2017), and the onlap termination styles shown by this study to be produced by the parent flows of these facies (Figs. 3.16, 3.17), a predictable stratigraphic evolution of onlap at confined basin margins is proposed (Fig. 3.19).

Distal Fringe.--Initially, onlap terminations will be characterized by draping of the slope as low-density turbidites of the lobe fringe are deposited (Figs. 3.17, 3.19). This low-density turbidite drape is likely to be composed predominantly of silt or mud, because fine-grained flows are much more capable of flow inflation and deposition high on the slope (Dorrell et al. 2018). It is also suggested that much of the poorly-exposed hemipelagic sediment in deep-marine basins is composed of millimeter-scale and centimeter-scale event beds (Fig. 3.10F) (Boulesteix et al. 2019a, b), and consequently represents the distal lobe fringe. Lobe-fringe deposition is therefore likely to be more widespread than previously appreciated (Boulesteix et al. 2019b; Spychala et al. 2019) and results in the healing of

substantial amounts of basinal topography, forming a dominantly aggradational sequence of thin beds on the basin margin (Figs. 3.11A, 3.17, 3.19).

Proximal Fringe: Hybrid beds and low-density turbidites of the proximal lobe fringe are then deposited into the basin as the system progrades (Fig. 3.19). These hybrid flows are more concentrated and will therefore have lower flow efficiencies when they encounter the slope, so will be unable to deposit as far up the slope as the underlying low-density turbidites of the distal lobe fringe (Figs. 3.17, 3.18A). This will cause abrupt intra-formational onlap of these higher-concentration flows against the underlying lobe- fringe deposits (Fig. 3.19). In the Annot Basin this is represented by proximal-fringe deposits wedging out against the underlying distal-fringe deposits (Figs. 3.11A, 3.15). The abruptness and complex 3D geometry of these terminations is enhanced by the combined

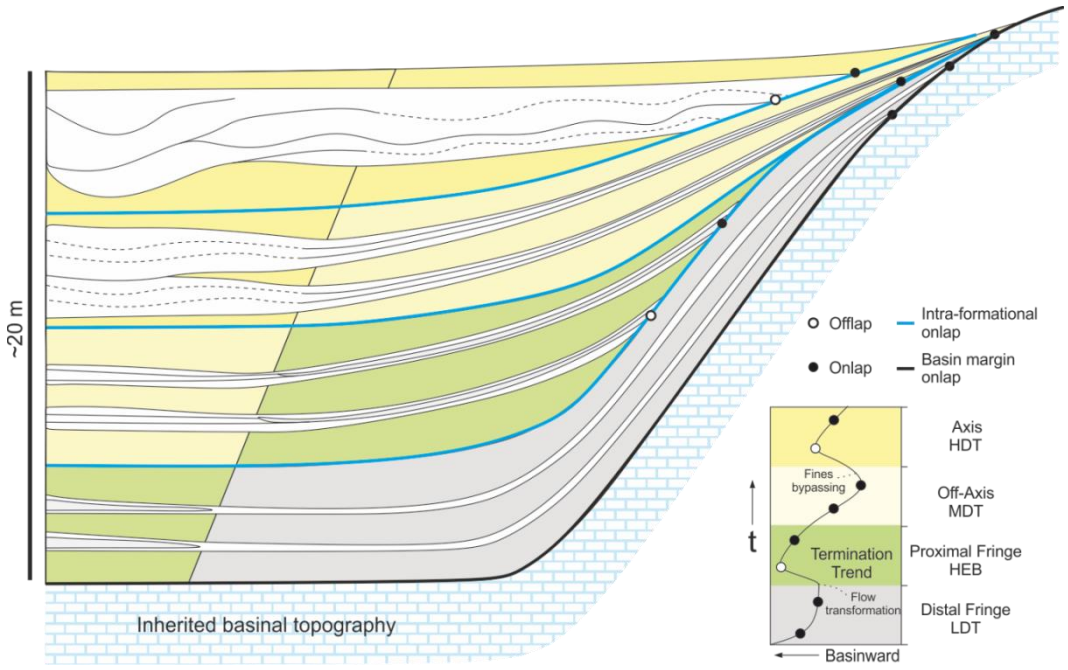

Figure 3.20: Model for the stratigraphic evolution of flow terminations in a static confined deep-water basin. It is suggested that the pattern of termination trends may be used to predict the termination style expected at a given point on the onlap surface. Flow transformation, which increases flow concentration, can result in offlap. Similarly, bypass of the upper parts of axial flows results in offlap of the deposits of the highly concentrated basal layers of these flows against the underlying deposits. Concurrent hemipelagic deposition has been ignored for simplicity.

potential for hybrid-bed development through long-run-out cohesive flow transformation (e.g., Haughton et al. 2009), slope-induced flow transformation (e.g., Barker et al. 2008; Patacci et al. 2014; Bell et al. 2018b), and flow-induced slope failures (e.g., McCaffrey and Kneller, 2001) (Fig. 3.16). This depositional pattern will be seen in cross sections as a

progressive migration of termination points towards the basin center (offlap) (Fig. 3.19) or a reduction in distance between successive onlapping termination points towards the basin margin. Sylvester et al. (2015) generated similar onlap trends using a geometric approach with subsidence and sediment supply as the variables.

Off-Axis: As progradation continues, these hybrid-bed-prone proximal-fringe deposits will become overlain by deposits of more proximal flows which have not decelerated to the same degree and hence are more turbulent and of lower concentration, but sand-rich (Figs. 3.17, 3.19). The off-axis deposits will be able to drape the slope more effectively than the underlying hybrid beds owing to their lower sediment concentrations (Fig. 3.19). This will result in progressive termination of their deposits higher up on the slope and either intra-formational onlap against the now thinner veneer of the low-density fringe or onlap directly against the hemipelagic basin margin (Figs. 3.17, 3.19, 3.20, 3.21).

Axis: As higher-concentration flows begin to dominate, intra-formational onlap may occur against the underlying fringe or off-axis deposits that were able to run up the hemipelagic slope (Fig. 3.19). The highly concentrated basal layers of these flows will be preserved as abruptly onlapping high-density turbidites, with the low-density tail of the flow bypassed down-dip. These axial flows will also be more erosive and able to incorporate mud-rich substrate, resulting in an increasing likelihood of intra-formational onlap through short-length-scale rheological flow transformation and consequent higher thinning rates adjacent to the basin margin (Fig. 3.14). The scours formed by these erosive events close to onlap will promote further autocyclic modulation of stacking patterns adjacent to the basin margin (e.g., Eggenhuisen et al. 2011). This relationship will also be exaggerated in coarser-grained systems because higher concentration flows will be less able to deposit farther up the slope, particularly at lateral margins if these high-concentration flows are narrower (Al-Jaidi et al. 2004).

A critical point in the basin fill will then be reached when these deposits heal the confining topography sufficiently to allow bypass of the coarser components of flows over the confining slope, forming a stepped, instead of a ponded, basin (Prather et al. 2017). Until this level is reached the finer-grained parts of the flows were stripped, thus increasing the sand proportion in the up-dip basin (Prather et al. 2017). This transition is represented toward the sill of the Annot Basin, where proximal lobe-axis deposits bypass down-dip to

the Grand Coyer minibasin (Fig. 3.2), where this stratigraphic evolution repeats in the next confined depocenter.

In the case that the topography is sufficient so as not to be healed by the underlying deposits, the lobe-axis deposits will continue to onlap against the underlying deposits until the accommodation is healed sufficiently to allow the axial deposits to onlap against the hemipelagic basin margin or completely fill the basinal relief and behave as essentially unconfined deposits, resulting in downlapping terminations (Fig. 3.19). Apparent unconfinement in a vertical section may also occur if allogenic progradation (e.g., increasing sediment flux) does not keep pace with topographic healing. This will result in the axial sandstones rarely onlapping directly against the constantly retreating basin margin and instead depositing away from the slope and on the basin floor (e.g., Kneller and McCaffrey, 1999).

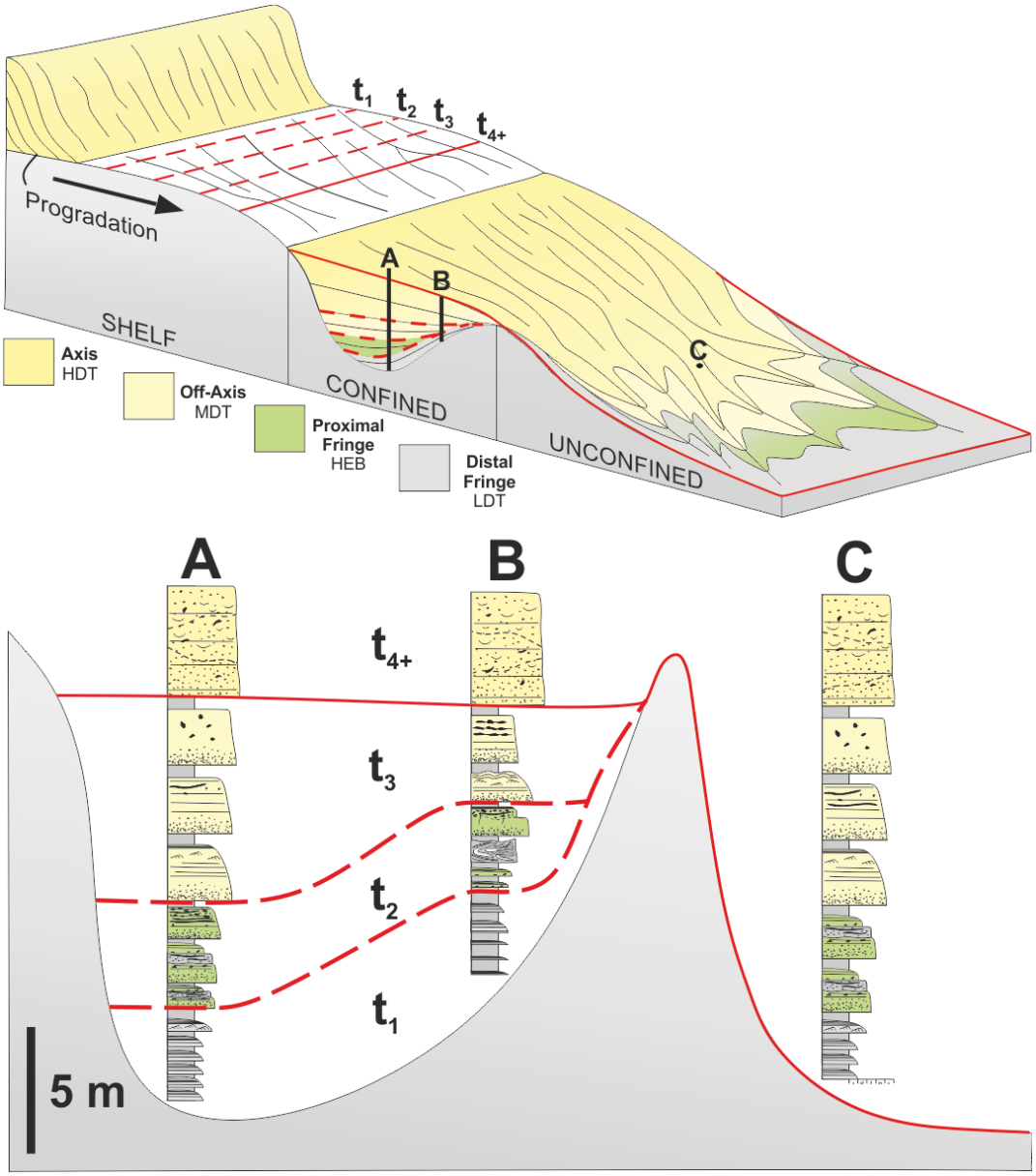

Figure 3.21: Model for the progradation of a clastic system into an intra-slope minibasin. Representative logs (A, B, and C) of the various sub-environments are indicated.

Applicability and Limitations

Syn-Depositional Deformation: This general stratigraphic evolution applies most readily to static basins with little syn-depositional deformation, where onlap trends are not modified by changes in subsidence or depocenter migration (Figs. 3.19, 3.21). The Annot Basin was subject to syn-depositional movement of the depocenter (e.g., Salles et al., 2014); however stratigraphic units of the basin fill show the same conceptual evolution as hypothesized for a static basin (Fig. 3.6), with the only difference being that the onlap is exaggerated on the tilted eastern exposures because of the increasing slope angle during

deposition (Fig. 3.11A) (Salles et al. 2014). In salt-deformed basins, where syn-depositional subsidence can be rapid, this onlap evolution will be also be exaggerated. The general model for onlap evolution (Fig. 3.19) may therefore broadly apply to actively deforming basins (Fig. 3.21). It may be difficult, however, to differentiate between allogenic onlap patterns caused by syn-depositional subsidence or sediment flux (e.g., Sylvester et al., 2015) and those caused by autogenic variations in flow properties (Fig. 3.21). Care therefore needs to be taken when reconstructing tectonic histories from onlap trends alone, especially in datasets without lithological control.

Onlap Incidence Angle: Frontal onlap causes greater turbidity current run-up than lateral onlap (Fig. 3.18B, C). This in turn makes the model presented here more applicable for dip sections against a confining slope. This is further reinforced by the Le Ray dip-oblique correlation (Fig. 3.6), which is interpreted to record the stratigraphic evolution of onlap described. The lack of a significant thin-bedded slope drape at the lateral onlap of Grès d'Annot at Chalufy (e.g., Puigdefàbregas et al. 2004; Smith and Joseph, 2004) may be an example of the importance of incidence angle, with run-up decreased against the lateral slope (Fig. 3.18B, C).

A minor thin-bedded slope drape does exist at Chalufy, however, and intra-formational onlap does occur against these thin beds (e.g., Bakke et al. 2013). This relationship may occur against lateral margins because flows become increasingly elongate with increasing sediment concentrations (Al-Jaidi et al. 2004). In strike sections this will result in a similar onlap termination pattern, with thicker and lower-concentration flows of the lobe fringe depositing higher on the lateral slope than higher-concentration flows of the lobe axis, which are elongated in the dip direction and more prone to bypass down-dip. This relationship may therefore apply to both strike and dip exposures; however, greater understanding of frontal vs. lateral onlap in exposed or subsurface deep-water systems is required for further analysis.

The lack of a substantial thin-bedded drape at Chalufy may also be caused by its relatively distal position compared to the Annot Basin (Fig. 3.2), resulting in lower-velocity and lower-concentration flows being unable to maintain enough energy during their longer passage down the slope to deposit significant thicknesses of sediment high on the confining slopes (Fig. 3.20).

Hierarchical Scale: The onlap patterns observed in this study are seen mainly on the scale of tens of meters, similar to typical lobe or possibly lobe-complex dimensions (Prélat et al. 2009). Above the spatio-temporal scale of lobe complexes the morphology of the depositional element is less likely to be the result of autogenic processes acting on individual events and more likely to be controlled by allogenic factors, such as the interplay of basin subsidence and sediment supply (see stratigraphic interval scale of Sheets et al. 2002; Jobe et al. 2017) (Fig. 3.21). It should be noted that in confined basins established morphometric ranges for unconfined depositional element thicknesses break down due to variable degrees of confinement across systems (Prélat et al. 2010). The lobe-scale applicability of the model is therefore purely a hierarchical observation because lobe thicknesses will vary across systems.

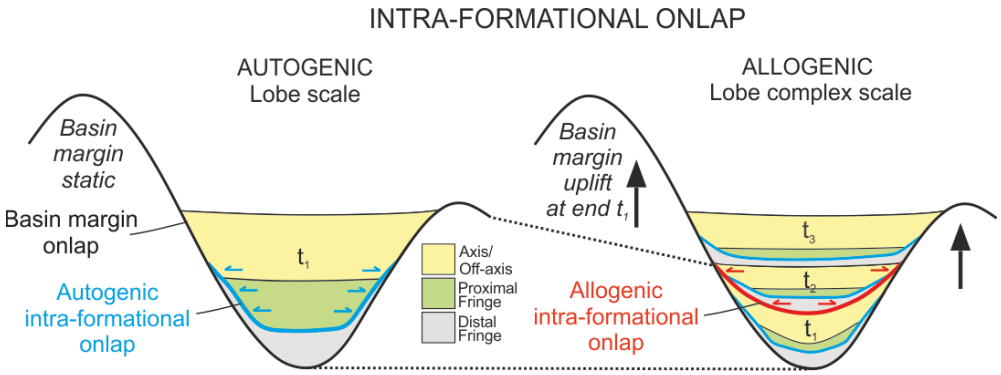

Figure 3.22: Types of intra-formational onlap that can be recognized in confined deep-water basins (modified from Sinclair and Tomasso, 2002). A distinction is made between autogenic onlap, caused by longitudinal flow evolution over shorter timescales, and allogenic onlap, caused by tectonic subsidence over longer timescales. Autogenic processes will create short-length-scale heterogeneities in larger-scale and allogenically controlled sequences.

Stratigraphic Position: Lobe progradation is unlikely to be constant; fluctuations in sediment supply, relative sea-level or changes in routing may result in small-scale backstepping. This backstepping creates discrete boundaries between successive members in the Annot Basin (Callec, 2004; Euzen et al. 2004) (Figs. 3.3, 3.5). These fluctuations will result in a non-uniform evolution of flow concentration during progradation, however on the basin-scale the overall trend of increasing flow concentration and subsequent onlap style will be maintained, with higher-density flows becoming more prevalent in the basin through progradation. These observations make the model most applicable to the early fill

of confined deep-water systems, where confinement is greatest and distal thin-bedded turbidites will be most prevalent.

Low-density and thin-bedded turbidites also tend to form thinner successions than high-density and thick-bedded turbidites. This is because sediment volume and sedimentation rates are greater in higher-density flows and because differential compaction more heavily affects finer-grained successions. This has implications for the evolution of onlap because the distal lobe fringe will be thinner than the lobe axis. As a result, the intra-formational onlap against the underlying fringe will be much more difficult to detect through time as the draping low-density turbidites gradually become thinner as the basin fills, eventually resulting in the higher-density flows onlapping directly against the hemipelagic basin margin (Fig. 3.17). This relationship is seen in the Le Ray member (Fig. 3.6), where the thin-bedded fringe is gradually surmounted by later flows.

Other Variables: This conceptual model aims to describe in simple terms the effect that autogenic flow evolution may have on onlap patterns in confined basins. Variables such as a waxing-waning sediment supply, hemipelagic aggradation rates, and the dominant grain size of the system are not discussed fully; however they will act to alter the autogenic processes that affect onlap and should be explored in future studies.

3.8 *Conclusion*

Understanding flow interaction with, and bed termination against, confining topography is critical for reconstructing the structural and sedimentological evolution of deep-water basins. This study presents a review of onlap styles in deep-water settings based on detailed field investigations and compares these results against those from a simple numerical model. Onlap terminations are shown to evolve in a predictable way through the progradation of a submarine lobe succession, with different lobe sub-environments identified at the basin margin through the migration of successive termination points and facies trends.

Initially termination points migrate towards the basin margins as low-density turbidites significantly drape the inherited basinal topography. Progressively higher-magnitude flows with greater sediment concentrations of the hybrid-bed-rich proximal fan fringe onlap these underlying deposits, causing the development of an intra-formational onlap surface that is characterized by either a basinward shift in termination points or a

reduced distance between successive termination points towards the basin margin. Hybrid beds are also shown to constitute significant thicknesses of the proximal fringe in confined systems through long run-out transformation, slope-induced transformation, and intra-basinal slope instability. Progradation of the lobe off-axis over the proximal fringe will cause further intra-formational onlap as the lower-concentration off-axis deposits drape the slope. Onlap against the fringe drape will continue until it is surmounted and onlap occurs directly against the hemipelagic basin margin. Intra-formational onlap may also occur in the lobe axis through abrupt onlap of these high-concentration deposits against the underlying lower-concentration fringe or off-axis deposits.

These sedimentological processes act to modulate the allogenic signals present in the Grès d'Annot of the Annot Basin, with onlap patterns controlled by both allogenic processes, through tectonic deformation and increasing sediment supply, and autogenic processes, through the interaction between longitudinal flow evolution and confining basin margins. Depositional hierarchy is also shown to be important when interpreting onlap patterns, with autogenic processes more important at the lobe scale and allogenic processes more important at the lobe-complex scale.

CHAPTER 4: Enhanced deep-marine deposition across the Eocene-Oligocene climate transition: a feedback mechanism for global cooling

Euan L. Soutter[1], Ian A. Kane[1], Ander Martínez-Doñate[1], and Adrian Boyce[2]

[1]Department of Earth and Environmental Sciences, University of Manchester, Manchester, M13 9PL, U.K.

[2]Scottish Universities Environmental Research Centre, Glasgow, U.K.

4.1 *Abstract*

Submarine fans are the largest sediment accumulations on Earth and are sites of burial for gigatons of terrigenous sediment and organic carbon. Sequestration of organic carbon into deep-marine sediments removes carbon dioxide from the oceans and atmosphere, and thus affects global climate. A major global climatic cooling event occurred during the Eocene-Oligocene transition (EOT) and was characterised by a series of abrupt cooling steps and eustatic sea-level falls related to solar insolation minima and Antarctic ice sheet growth. New stable carbon isotope data from the Alpine foreland basin show that these cooling events and sea-level falls coincide with increased rates of terrigenous sediment supply to deep-marine environments and the growth of submarine fans. Enhanced burial of terrigenous organic carbon associated with this growth is inferred to have acted as a positive feedback to the EOT cooling events, aiding the transition from Paleogene greenhouse to current icehouse conditions. Rising sea-levels in the future may reverse this process, resulting in reduced organic carbon burial in deep-marine environments and increased global warming. Sequestration of organic carbon in submarine fans is suggested to be an under-appreciated modulator of Earth's climate, with submarine fan growth intimately linked to global climatic events. This study also provides insight into how external influences are recorded in the stratigraphic record of the Alpine foreland basin, and constrains the Oligocene chronostratigraphy of the basin.

4.2 *Introduction*

The Eocene-Oligocene climate transition (EOT) between ~34 and ~33 Ma occurred in response to the opening of oceanic gateways in the Southern Oceans (Kennett, 1977), decreased atmospheric CO_2 (Pearson et al. 2009) and favourable orbital cycles (Ladant et al. 2014) (Fig. 4.1). The EOT resulted in the establishment of major Antarctic ice sheets (Liu et a. 2009) and the transition from Paleogene greenhouse to current icehouse conditions (Wade et al. 2012). The EOT occurred through a series of global cooling 'steps' that correspond to positive $\delta^{18}O$ excursions and eustatic sea-level falls of up to 105 m (Katz et al. 2008). This 'stepwise transition' has been attributed to the wide variety of EOT forcings and the intricacy of the feedbacks between them (Katz et al. 2008; Pearson et al., 2008).

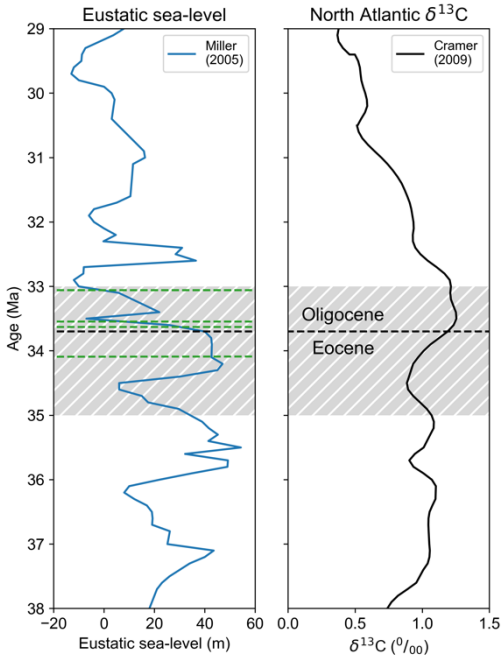

Figure 4.1: Sea-level (Miller et al. 2005) curve for the Eocene and Oligocene. Hatched interval represents the approximate extents of the Eocene-Oligocene transition (Miller et al. 2008), black dashed line represents Eocene-Oligocene boundary (Katz et al. 2008) and green dashed lines represent oxygen-isotope 'steps' that correspond to eustatic sea-level falls (Katz et al. 2008).

Submarine fans are built from the deposits of sediment-laden gravity-driven flows that transport gigatons of terrigenous sediment and organic carbon per year to deep-marine environments (e.g. Curray and Moore, 1971; Ingersoll et al. 2001). The Bengal Fan, for example, has been responsible for the burial of 15% of the Earth's organic carbon flux over the last 15 Myr (Galy et al. 2007). Submarine fan growth has been shown to occur during low (e.g. Posamentier et al. 1988, Van Wagoner et al. 1990) and high (e.g. Weber et al. 1997; Burgess and Hovius, 1998; Carvajal and Steel, 2006; Covault et al. 2007) sea levels, and may be driven by tectonic (Puigdefàbregas and Souquet, 1986; Pickering and Bayliss,

2009; Castelltort et al. 2017; Bao et al. 2018) and climatic processes (Weber et al. 2003; Ducassou et al. 2009; Jorry et al. 2010). The stable isotope of carbon ($\delta^{13}C$) has been used as a proxy for assessing sea-level control on deep-marine deposition (e.g. Jenkyns, 1996; Mitchell et al. 1996; Castelltort et al. 2017). Positive $\delta^{13}C$ excursions are considered to correspond to high sea-levels, flooded shelves, high biological productivity and burial of ^{12}C while negative $\delta^{13}C$ excursions correspond to low-sea levels, exposed continental shelves, lower productivity and greater run-off (Jenkyns et al. 1996; Castelltort et al. 2017). By constructing a $\delta^{13}C$ curve through a deep-marine sequence of a known age it is therefore potentially possible to relate periods of enhanced or decreased sedimentation to eustatic and climatic trends (Castelltort et al. 2017).

The Grès d'Annot represents an exhumed siliciclastic deep-marine succession deposited within the Alpine foreland basin during the EOT (Fig. 4.2) (Joseph and Lomas, 2004). The Grès d'Annot records a common deep-marine stratigraphic pattern of fine-grained intervals interspersed with coarser-grained intervals. In the Alpine foreland basin this cyclicity has been attributed to both sea-level and tectonism (Apps, 1987; Callec, 2004; Euzen et al. 2004; Puigdefàbregas et al. 2004); however, the relative impact of these processes has not been tested. This study therefore aims to investigate 1) the causes of

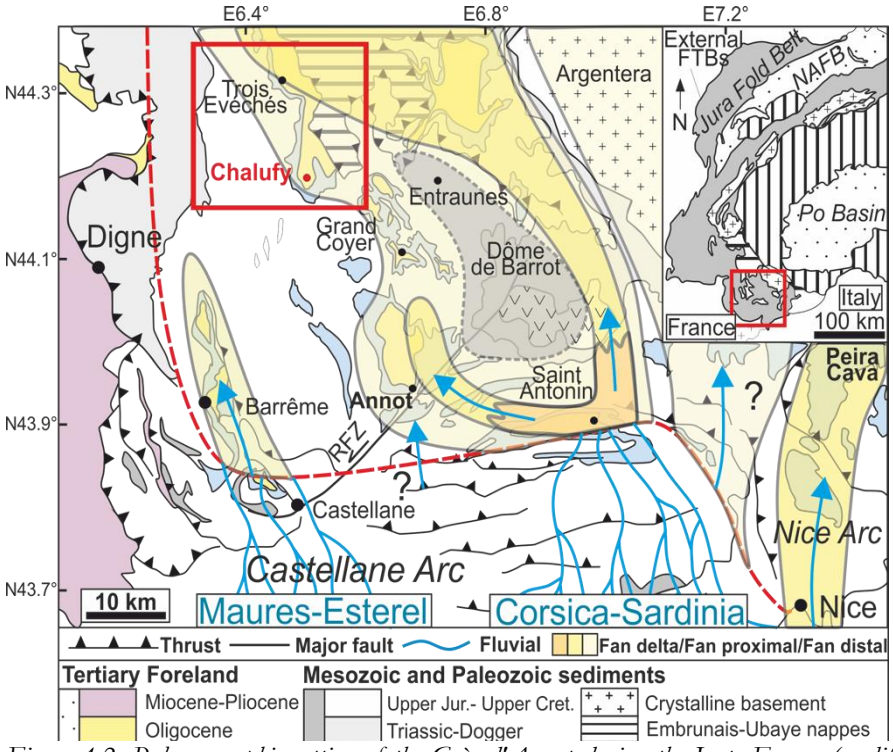

Figure 4.2: Paleogeographic setting of the Grès d'Annot during the Late Eocene (modified from Joseph and Lomas, 2004). The studied exposure is located at the distal extent of the SW Alpine foreland basin submarine fan.

lithological cyclicity in the Grès d'Annot, and 2) whether this relationship is related to the EOT climatic regime.

4.3 *Study area: Chalufy*

One of the most well-studied Grès d'Annot exposures is located at the Montagne de Chalufy and represents a relatively distal part of the Grès d'Annot submarine fan system (Fig. 4.2; Fig. 4.3). The exposure comprises onlap of three prominent coarse-grained Grès d'Annot intervals against an older marl paleo-slope (Du Fornel, 2003; Puigdefàbregas, 2004; Bakke et al. 2013). The coarse-grained intervals are interpreted as high-density turbidites deposited within confined submarine fan lobes deposited on the basin floor. These coarse-grained intervals are bound by finer-grained intervals, which are interpreted as low-density turbidites interbedded with thin hemipelagic mudstones that were deposited at the distal extents of coarse-grained lobes or distributary channels on the basin floor (Fig. 4.3; Appendix B). One of these coarse-grained channels can be correlated northwards from within the uppermost fine-grained interval, where it erodes downwards through an underlying coarse-grained interval (Joseph et al., 2000).

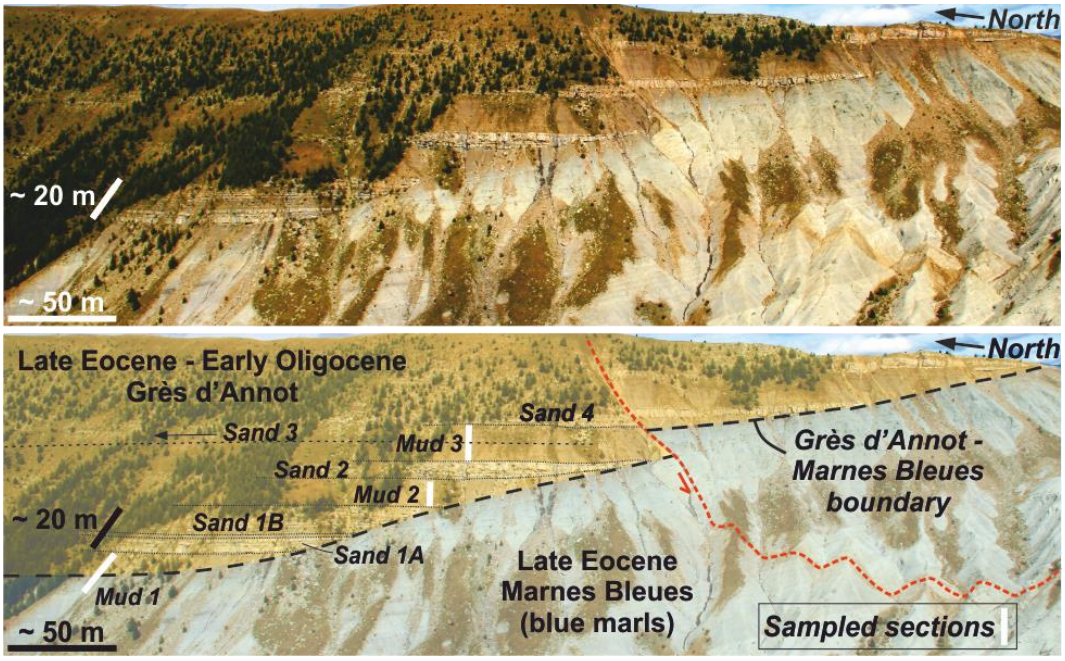

Figure 4.3: The measured section at Chalufy and stratigraphic context.

Foraminiferal dating indicates that the base of the Grès d'Annot exposed at Chalufy was deposited at a maximum of 34.2 Ma (NP20/NP21), with the top of the Grès d'Annot being deposited at a maximum of 32.8 Ma (NP21/22) or 32 Ma (top P18) (Fig.

4.3) (Du Fornel et al. 2004; Euzen et al. 2004). The base of P18 occurs prior to the first coarse-grained interval (Fig. 4.3; 4.3) (Du Fornel et al. 2004).

4.4 *Data and methods*

The dataset comprises one continuous measured section from the base to the top of Grès d'Annot exposure at the Chalufy exposure (Fig. 4.2; 4.2; Appendix B), with 111 samples recovered from three fine-grained intervals within this section (Fig. 4.4; Appendix B). The samples were collected at 50 cm intervals, from > 30 cm below the exposed surface and only within hemipelagic sections, thus avoiding potential influxes of allochthonous material. The samples were crushed and their bulk carbonate $\delta^{13}C$ and $\delta^{18}O$ values measured using mass-spectrometry, with 9 repeated measurements of section representative samples yielding a mean measurement error of ± 0.30 for $\delta^{13}C$ (Fig. 4.4) and ± 0.06 for $\delta^{18}O$. Carbon and oxygen isotopes are presented against the V-PDB and V-SMOW standards, respectively.

The resulting three isotopic curves, representing each fine-grained interval, were placed within bounding age constraints derived from micropaleontological zonation of the study area (foraminiferal P-zones of Du Fornel et al. 2004). Lack of micropaleontological resolution led to the time occupied by each curve within these palaeontological constraints to be assessed through correlation with time-equivalent and the geographically-closest data compilations; the North Atlantic $\delta^{13}C$ curve (Cramer et al. 2008) and eustatic sea-level curve of the New Jersey passive margin (Miller, 2005; Kominz et al. 2008), following the methodology of Castelltort et al. (2017). Selected samples distributed at regular heights from within the fine-grained sections have also undergone X-ray diffraction (XRD), total organic carbon (TOC) and petrographic analysis in order to assess the potential for mixed-carbonate-source error or diagenetic overprinting.

4.5 *Results*

Diagenetic overprinting

XRD of selected samples within each interval indicates total organic carbon (TOC) contents of < 0.7 % and a calcite to organic matter ratio of > 7:1, reducing the likelihood of diagenetic contamination from organic carbon (Saltzmann and Thomas, 2012). Oxygen isotopes ($\delta^{18}O$) are not used for paleo-environmental interpretation as $\delta^{18}O$ is prone to

diagenetic overprinting, with the extremely low $\delta^{18}O$ values produced by this study indicating interaction with warm subsurface waters (e.g. Saltzmann and Thomas, 2012). This can be used to assess the diagenetic effect on δ13C, with cross-plotting of $\delta^{13}C$ and $\delta^{18}O$ from each interval showing no co-variance (mean $R^2 = < 0.06$), indicating a lack of $\delta^{13}C$ diagenetic overprinting (Appendix B) (Marshall, 1991).

Carbon isotopes

The identification of benthic foraminifera in petrographic analysis of the samples (Appendix B), and the occurrence of dateable benthic foraminifera within the Chalufy section (Du Fornel et al. 2004) indicates that the bulk $\delta^{13}C$ measurements primarily record the signature of this fauna. The bulk $\delta^{13}C$ data shows a broadly increasing spread with increasing height in the section (1σ = 0.50 ‰, 0.44 ‰, 0.86 ‰, 0.97 ‰ for each sequential fine-grained interval), with a mean standard deviation of 0.89 ‰ (Fig. 4.4; Appendix B). Mean $\delta^{13}C$ values are 1.97 ‰ more negative than time-equivalent open oceanic values. Moving-average curves (the running mean of a sliding window of five data-points within lower fine-grained interval and ten data-points within the middle and upper fine-grained intervals) shows poor correlation between the Chalufy $\delta^{13}C$ curve and the oceanic $\delta^{13}C$ curve, with the positive global $\delta^{13}C$ excursion seen at the EOT (Cramer et al. 2008) not observed within this data (Fig. 4.5). The noise, more negative values, signal amplification and global disparity is attributed to: 1) microscopic turbidites or calcite-filled fractures within the hemipelagic sections, which create allochtonous noise with a dominantly autochthonous signal (Appendix B). Similar noise was seen by Melchin and Holmden (2006) in bulk $\delta^{13}C$ samples of potentially remobilised carbonates; 2) the relatively proximal position of the basin which may have resulted in the oxidation of light organic ^{12}C delivered by rivers (Jenkyns, 1996; Voigt and Hilbrecht, 1997); 3) the restricted nature of the basin preventing rapid exchange with the global carbon reservoir (Saltzmann and Thomas, 2012). This restriction may have resulted in a dominance of the 'local' signal over the relatively short timescale studied (< 2.5 my).

The averaged $\delta^{13}C$ curves of the two sandstone-bounded fine-grained intervals correlate well with time-equivalent sections of the global eustatic curve, with 5-point-average polynomial regressions yielding R^2 values of 0.55 (middle) and 0.74 (upper), and a 10-point-average yielding R^2 values of 0.81 (middle) and 0.88 (upper) (Fig. 4.5). The fine-

grained intervals correlate with eustatic sea-level highstands, with the ends of the curves (sands 1A, 1B and 4) correlating with sea-level lowstands, which are themselves related to global Oligocene cooling events (Miller et al. 2008; Katz et al. 2008). The lack of equivalent sea-level-related excursions on the global $\delta^{13}C$ curve is likely related to a buffering of the sea-level signal by other oceanographic or atmospheric processes in open oceanic and distal environments, and to the amplification of the sea-level signal in the proximal and restricted Alpine foreland basin.

The correlative surface of the coarse-grained channelized interval exposed to the north (sand 3) intersects mid-way through the third fine-grained interval (Joseph et al. 2000), and therefore correlates with a sea-level highstand. The exact depositional duration of this channel is uncertain due to the correlative surface representing a sustained period of bypass and erosion through the channel (e.g. Englert et al. 2019), however it must have been abandoned prior to deposition of fine-grained interval overlying the correlative surface as this interval overlies the channel to the north (Joseph, 2000), thus likely represents channel abandonment.

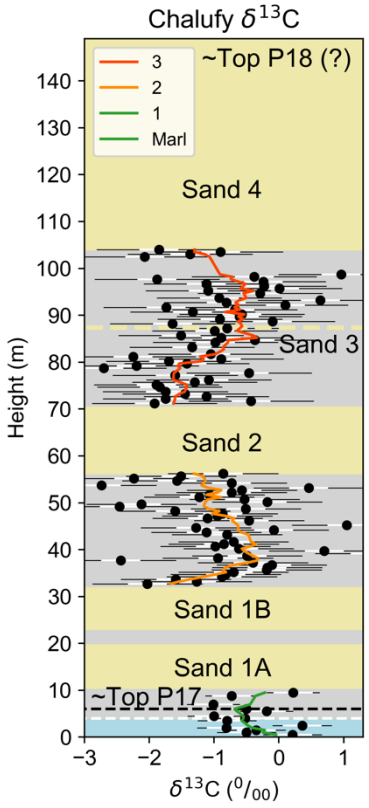

Figure 4.4: δ13C measurements for each fine-grained interval sampled and their bounding P Zones (Du Fornel, 2004). Data spread increases with height as the submarine fan grows and autochthonous material become more prevalent. Coloured line represents a 5-pt moving average for lower interval and 10-pt. moving average for middle and upper interval. Yellow = sand, grey = mud and silt, blue = marl. White line is an uncertain age break, and dashed yellow line correlates with the top of the channelised sand 3 preserved to the north. White error bar is the mean of the difference between 9 representative repeat measurements. Black error bar is one standard deviation.

The lower and upper boundaries of the marl and first fine-grained interval are uncertain due to their relatively low thicknesses and uncertainty surrounding how much time is occupied between the marl onlap surface and Grès d'Annot deposition, with the marginal position of the Chalufy section resulting in early thin-bedded turbidites deposited within the deepest part of the basin not being recorded (e.g. Du Fornel et al. 2004). The overall higher $\delta^{13}C$ values and biostratigraphic constraint within the first fine-grained interval (P17 boundary), however, indicate that these sections correspond to the highstand between ~34.2 and ~33.7 Ma.

4.6 *Discussion*

Eocene – Oligocene Transition

Globally-recognised EOT cooling events and associated sea-level falls correspond to periods of coarse-grained deep-marine deposition and submarine fan growth within the Alpine foreland basin (Fig. 4.5), with the first phases of growth correlating with a cooling and eustatic lowstand around EOT-2 and Oi-1 (50 – 105 m fall) and the second phase of growth correlating with a eustatic lowstand around Oi-1a (40 – 50 m fall) (Katz et al, 2008; Houden et al. 2012). The fourth phase of growth correlates with a eustatic lowstand at ~32 Ma, which could be a precursor to Oi-1b at ~31.7 Ma (Miller et al. 2008), or an orbital cycle (Zachos et al. 1996). Shallower marine erosion surfaces in Alabama (Miller et al. 2008) and deposition of calcareous turbidites adjacent to Pacific atolls (Schlanger and Silva, 1986) have also been correlated to early Oligocene $\delta^{18}O$ excursions and sea-level falls, highlighting the global depositional signature of these events.

Low sea-levels tend to enhance siliciclastic deep-marine deposition as rivers are able to traverse shallow contintental shelves and deliver sediment directly to deeper waters (e.g. Posamentier et al. 1988). Oxidisation of organic material eroded from soils and vegetation on land, and transported by rivers, is anticipated to have enhanced negative $\delta^{13}C$ excursions (Saltzmann and Thomas, 2012); during times of lowered sea-level, a large proportion of this organic material will have been transported by sediment-gravity-flows and buried on the seafloor, as is evidenced by the common occurrence of wood and plant debris preserved within Grès d'Annot turbidites (Stanley, 1986; MacArthur et al. 2016; Soutter et al. 2019), and the gigatons of organic carbon buried in submarine fans today (Galy et a. 2007). Organic carbon burial in deep-marine environments has also been shown to be 50 % higher during lowstands (Cartapanis et al., 2016), with the Amazon Fan accounting for >

13% of the global organic carbon burial rate during the Last Glacial Maximum (Schlünz et al. 1999; Cartapanis et al., 2016) and submarine fans in Central Japan showing an increased burial of terrigenous organic matter during Mio-Pleistocene lowstands (Omura and Hoyanagi, 2004). The present-day Congo fan, which is directly connected to its source-river and therefore analogous to a lowstand fan, stores 19% of all South Atlantic organic carbon, despite covering only < 0.01% of the total surface area of the South Atlantic (Rabouille et al. 2019), with most of the organic carbon stored in the distal lobes of the fan (Stetten et al. 2015). It is likely that similar submarine fan growth and consequent burial of organic carbon occurred during Oligocene lowstands.

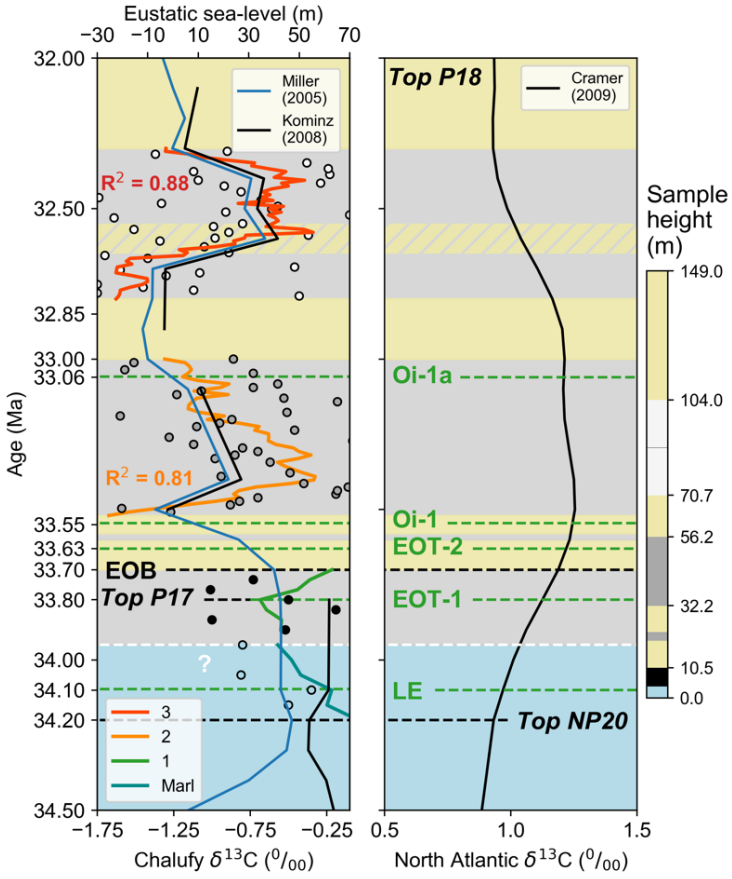

Figure 4.5: Correlation between A) lithology, the δ13C record of Chalufy (scale clipped to highlight trends), and eustatic sea-level (Miller, 2005; Kominz et al. 2008) B) open oceanic δ13C (Cramer, 2009), and EOT cooling events (green dashed lines) (Miller, 2008; Katz et al. 2008). LE = Late Eocene; EOT = Eocene-Oligocene Transition; EOT-1 = EOT Event 1 =, EOT-2 = EOT Event 2, Oi – 1 = Oligocene Event 1, Oi – 1a = Oligocene Event 2. Yellow = sand, grey = mud and silt, blue = marl. Ages tied to chronology of Berggren et al. (1995). White dashed line indicates time uncertainty across boundary.

The cooler (Eldrett et al. 2009) and more arid (Fan et al. 2020) northern latitude climates associated with these events will also have enhanced sediment delivery to the deep sea, with lower vegetation cover, or 'de-greening' (Caves et al. 2016), during cooler periods increasing hinterland erosion rates and run-off. Vegetation recovery during warm interglacials will have reduced erosion rates and run-off during EOT interglacials, resulting in positive $\delta^{13}C$ excursions and submarine fan retreat.

It is therefore suggested that falling CO_2 levels and cooling across the EOT (DeConto and Pollard, 2003; Zachos and Kump, 2005; Pearson et al. 2009) was enhanced by the burial and sequestration of organic carbon in deep-marine basins during cool and arid periods and associated low eustatic sea-levels. The transition from greenhouse to icehouse conditions in the Cenozoic, and related evolutionary and environmental consequences (e.g. Prothero and Berggren, 2014), was consequently modulated by the growth of submarine fans. It also suggested that future rising sea-levels are likely to reverse this process, with less burial of organic carbon in submarine fans and accelerated global warming.

Influence of hinterland tectonics

The only coarse-grained interval that does not correlate with an EOT event is sand 3, which was deposited during eustatic sea-level highstand between ~32.7 and ~32.4 Ma (Fig. 4.5), and represents a major period of aggradation within the shallow marine Alpine foreland (Euzen, et al. 2004) and channelization within the deep-water Alpine foreland (Joseph et al. 2000). The lack of global climatic or eustatic events related to this period of coarse-grained deposition indicates that sediment supply was enhanced to deep-water by a more 'local', or basin-specific, event. The most likely local forcing for this increased sediment supply is tectonic uplift and erosion of the Corsica-Sardinia hinterland, which was closely linked to the basin by steep drainage systems (e.g. Joseph and Lomas, 2004) and was being tectonically deformed at this time (e.g. Euzen et al. 2004; Advokaat et al. 2014). This transient increase in sediment supply will have competed with the accommodation increase associated with eustatic highstand, thus driving the major period of aggradation recorded on the shelf (Euzen et al. 2004) and the maintenance of coarse-grained deep-water deposition during highstand (e.g. Carvajal and Steel, 2006).

Implications for Alpine foreland basin stratigraphy

Key exposures in the Alpine foreland basin have been correlated litho- and biostratigraphically from the shelf to the deep basin, with the Chalufy exposures representing the distal extents of the correlation (Fig. 4.6) (Du Fornel, 2003; Du Fornel et al. 2004; Euzen et al. 2004). Relatively low biostratigraphic resolution, however, has made precise chronostratigraphic surfaces difficult to define (Fig. 4.6). The existing commonly used window for Grès d'Annot deposition is between ~34.2 Ma and ~32.8 Ma (Euzen et al, 2004; Salles et al. 2014), with the sequences resolved by this study deposited between ~33.8 and ~32.8 Ma (Du Fornel, 2003). This study indicates, however, that the Grès d'Annot deposition continued until at least 32.3 Ma (base of uppermost sand), thus extending the depositional window by ~500 ka (Fig. 4.6). Deposition likely continued well after 32.3 Ma, as the top of members F and G are not resolved by this dataset. This study also refines the previously unknown chronostratigraphy of members C, D, and E, with 100 – 200 kyr cycles of progradation within these members occurring at ~33.6 Ma, ~33.0 Ma, ~32.6 Ma and ~32.3 Ma, respectively (Fig. 4.6).

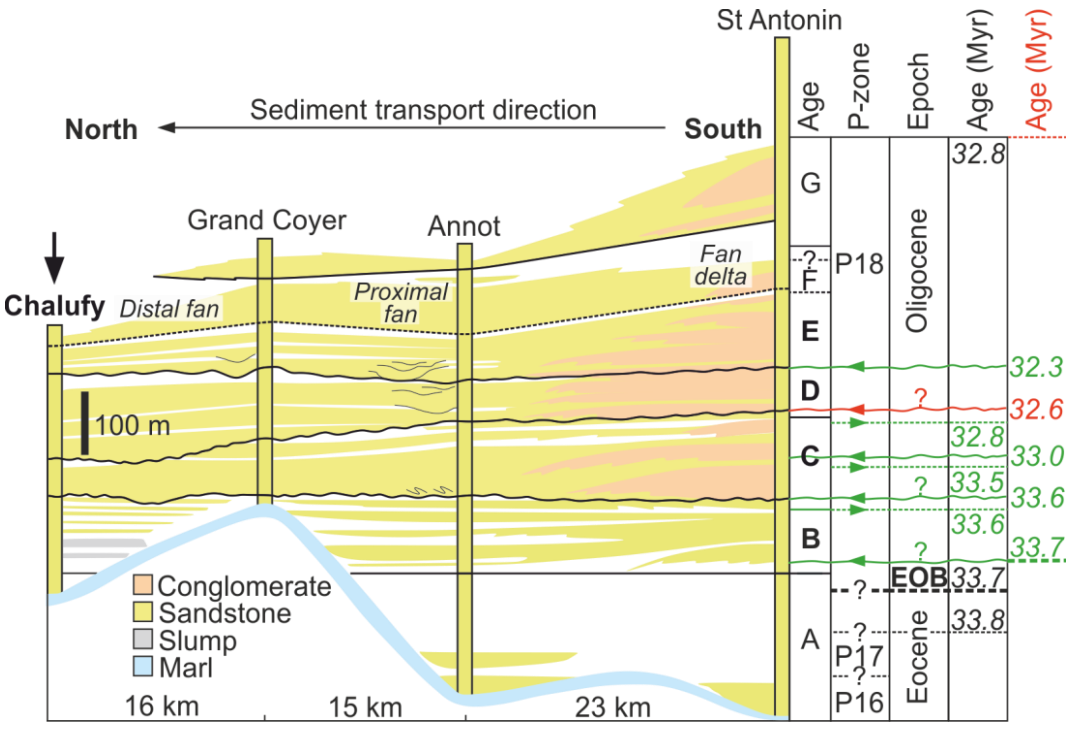

Figure 4.6: Correlation from proximal to distal within the Alpine foreland basin. Coloured lines indicate refined age relationships, with green lines indicating EOT-related forcings and red lines indicating tectonic forcings (modified from du Fornel et al. 2004).

These refined correlations may also have paleogeographical implications, indicating that coarse-grained flows were entirely confined to proximal basins during the Late Eocene, thus preventing coarse-grained deposition in the distal Chalufy sub-basin. Coarse-

grained deposition did not begin in the Chalufy sub-basin until the earliest Oligocene (~33.7-33.6 Ma) (Fig. 4.6; DR2), concurrent with connection of the proximal Grand Coyer and Annot sub-basins (Fig. 4.6) (Salles et al. 2004). These results are agreement with the 'fill-spill' stratigraphic evolution initially proposed for the Alpine foreland sub-basins (Sinclair and Tomasso, 2002). This study, however, indicates that the primary driver of this evolution was EOT-related eustatic and climatic events, with only one period of submarine progradation occurring during highstand at ~32.6 Ma, and therefore inferred to be tectonic in origin (e.g. Castelltort et al. 2017). In the absence of these external eustatic-climatic events sediment supply will have been reduced to the deep-water foreland. Consequently, these basins may have remained under-filled throughout the Oligocene as SW-propagating flexural subsidence from the growing Alps deepened the basins (e.g. Ford et al. 1999) and reduced sediment supply to deep-water.

4.7 ***Conclusion***

Deep-marine submarine fans are the most significant depositional sites for terrigenous sediment on Earth and are important sinks of organic carbon. Understanding the controls on this deposition is therefore critical for predicting sedimentation patterns and organic matter burial in the past and future. Stable carbon isotope and sedimentological data from the deep-marine Alpine foreland basin indicates that the combined effect of cooler climates and eustatic sea-level fall associated with the transition from Paleogene greenhouse conditions to current icehouse conditions resulted in increased sediment supply rates, submarine fan growth, and therefore enhanced burial of terrigenous sediment and organic matter in deep-marine environments. Withdrawal of organic carbon from the ocean-atmosphere system would have reduced atmospheric CO_2 and accelerated cooling across the Eocene-Oligocene transition. Future rising sea-levels are expected to reduce organic carbon burial in submarine fans, increase atmospheric CO_2 and accelerate global warming.

CHAPTER 5: Giant submarine landslide triggered by Paleocene mantle plume activity in the North Atlantic

Euan L. Soutter[1], Ian A. Kane[2] and Mads Huuse[1]

[1]Department of Earth and Environmental Sciences, University of Manchester, Manchester, M13 9PL, U.K.

5.1 *Abstract*

The 290 km long 'Halibut Slide' is the world's largest epicontinental submarine landslide. Between 64 and 62 Ma, plume-related uplift in the North Atlantic caused reactivation of major intra-plate faults. This reactivation caused instability of Cretaceous chalk slopes across the North Sea Basin, triggering the Halibut Slide (HS). Megascours, up to 1 km wide, 150 m deep and 70 km long, indicate slope failure from an intra-shelf high east of mainland Scotland and subsequent flow down a ~1.1° slope. Megascours were gouged by cuboid chalk blocks, up to 1 km wide and 170 m high, some of which out-ran the main slide body by up to 10 km. The Halibut Slide has a decompacted volume of ~850 km^3 and a basal slide surface extending over ~7000 km^2. Subsequent clastic sediment input points and dispersal pathways were controlled by the underlying Slide topography for ~10 Myr. The discovery of this major submarine landslide provides new insights into the response of sedimentary systems to regional and deeply rooted tectonic events, and the initiation of long term sediment routing patterns.

5.2 *Introduction*

Submarine landslides are the largest mass-movements known on Earth and are important seascape modifiers, creating some of the largest single-event deposits known (e.g. Calves et al., 2015). Submarine landslides can generate tsunamis (e.g. Dawson et al., 1988), damage submarine infrastructure (Mulder et al., 1994) and modify post-failure sediment distribution (Ortiz-Karpf et al., 2015). Understanding the formation and behaviour of large submarine landslides is therefore important for both geohazard assessment and hydrocarbon reservoir prediction (Clare et al., 2018).

Using an extensive basin-scale 3D seismic reflection dataset, integrated with core and wireline log data, this study aims to: 1) document and characterize the Halibut Slide, and 2) interpret slide genesis with reference to major basinal processes, principally mantle-upwelling and associated tectonic adjustments.

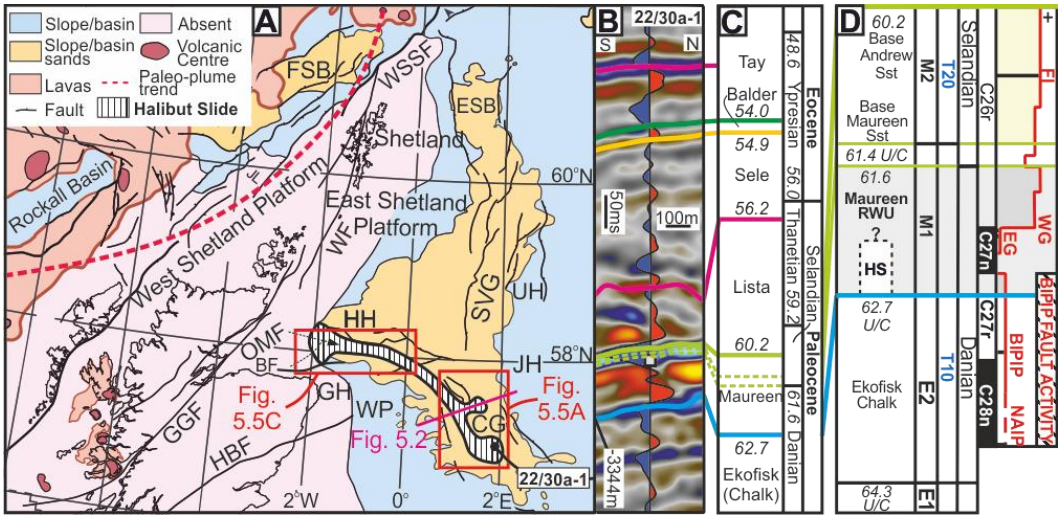

Figure 5.1: Paleocene paleogeography of the North Atlantic and the present-day extent of Cenozoic volcanism. The uplift caused by this volcanism caused Paleogene deposition in the North Sea and adjacent basins (modified from Ahmadi et al., 2003 and Mudge, 2015). The trend of the plume during the Late Paleocene is also indicated, showing the North Sea Basin at its SE margin (modified from Hartley et al., 2011). B, C: Seismic reflectors (B) and corresponding stratigraphic interval (C) (Absolute ages from Mudge (2015)). The Halibut Slide is represented by Top Maureen within well 22/30a-1; white box indicates logged core position. D: The relationship between mantle plume activity and clastic (yellow) or remobilised chalk (gray) deposition in the early Paleocene of the North Sea. Absolute ages from Mudge (2015). Solid red line shows North Atlantic volcanic activity from White and Lovell (1997). Dashed red line and black solid lines show earliest volcanic activity from Wilkinson et al. (2016) (no relative volcanic activity level is implied by dashed line), fault activity from Cooper et al. (2012). All dates tied to the magnetic chronology of Gradstein et al. (2012). BF, Banff Fault; CG, Central Graben; ESB, East Shetland Basin; FSB, Faroe–Shetland Basin; GGF, Great Glen Fault; GH, Grampian High; HBF, Highland Boundary Fault; HH, Halibut Horst; JH, Jaeren High; OMF, Outer Moray Firth; SVG, South Viking Graben; UH, Utsira High; WF, Walls Fault; WP, Western Platform; WSSF, West Shetland Spine Fault.

5.3 ***Data and methods***

This study utilises the full-offset pre-stack Kirchoff time migrated Central North Sea PGS MegaSurvey Plus 3D seismic dataset complemented by the post-stack time migrated merged PGS MegaSurvey covering the Moray Firth (Fig. 5.1). Vertical seismic resolution within the Paleocene interval is 25-33 m (given an interval velocity of ~3 to 4 km s^{-1} and a

dominant frequency ~30 Hz) with a bin spacing of 12.5 x 12.5 m in the Megasurvey Plus. A sub-sampled 50 x 50 m line spacing was used for analysing the MegaSurvey. Both surveys have a 4 ms sample rate and are processed to zero phase, with a downward increase in acoustic impedance represented by a trough (blue reflection). Conversions between thickness in two-way time (TWT) and depth were performed using a sonic-log derived average interval velocity of 4.3 km s^{-1} (range between 3.1 - 5 km s^{-1}) for the Halibut Slide.

Seismic picks were tied stratigraphically to wells (Fig. 5.1B). Synthetic seismograms were extracted from a database of 975 wells available within the study area to give further confidence in the picks and were combined with wireline log (primarily gamma-ray and sonic) and core data for interpretation of lithology (Fig. 5.1). A 12 m cored section was logged from the Halibut Slide within well 22/30a-1 (Appendix C).

The seismic data were interpreted by systematic horizon picking followed by horizon interpolation and iteration, allowing the regional Paleocene bounding surfaces of Top Chalk and Top Sele to be mapped (Fig. 5.1; 5.2; 5.3). The top of the Halibut Slide was identified, tracked and interpolated (Fig. 5.4). Surface attributes, such as variance and root mean square (RMS) amplitude, were then used to identify the extent of the slide. Horizon slicing between the bounding surfaces was used to assess the internal characteristics of the Halibut Slide and interpret depositional cycles within the overlying Paleocene section (after Kilhams et al., 2015) (Fig. 5.1; 5.2; 5.3). These horizon slices and bounding surfaces were used for spectral decomposition, allowing both the internal and external geomorphology of the slide to be better imaged (Fig. 5.5A, D, E).

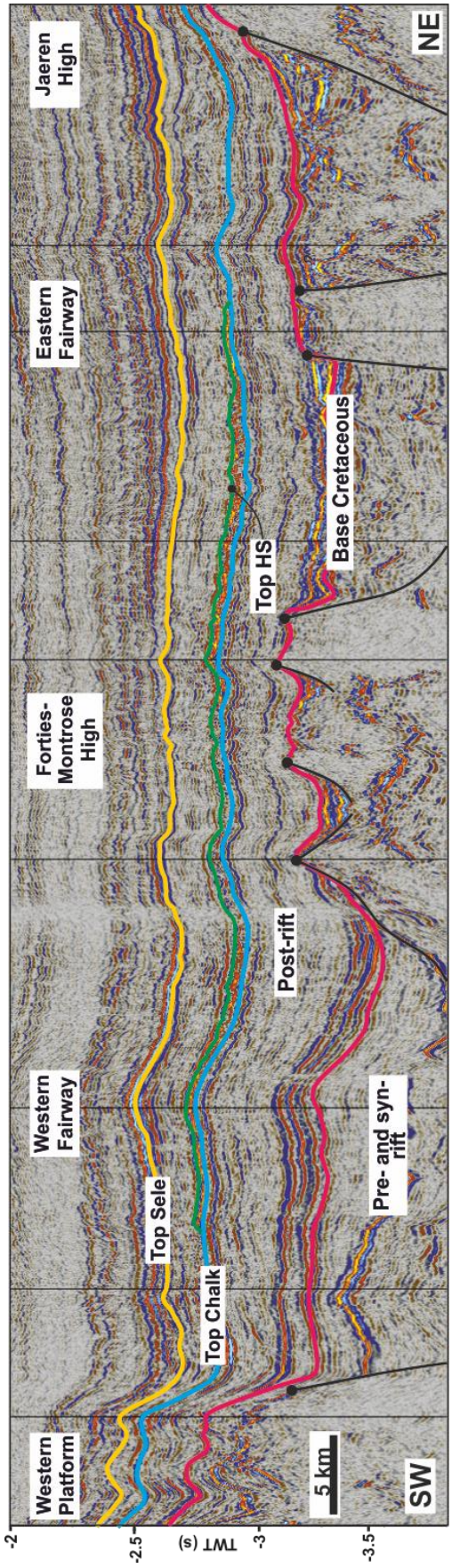

Figure 5.2: Strike-oriented seismic section showing the key structural and stratigraphic features of the North Sea Central Graben. The interval of interest lies between Top Chalk and Top Sele, which forms the bounding surfaces of the Paleocene. The Western Platform, Forties-Montrose High and Jaeren High are Mesozoic structures that act to partition the Central Graben basin floor into confined western and eastern fairways for incoming sediment gravity flows. Base Cretaceous surface approximate.

5.4 *Geological setting*

The central North Sea Basin comprises a Cenozoic sag basin overlying a failed Mesozoic rift (Fig. 5.2). Paleocene sedimentation was initiated due to uplift and subsequent SE-tilting of the northern UK landmass (Den Hartog Jager et al., 1993) associated with rifting and magmatic underplating in the North Atlantic around ~62 Ma (White and Lovell, 1997). The Moray Firth paleo-shelf is estimated to have undergone up to 390 m of uplift and erosion during the Paleocene (Nadin and Kusznir, 1996). Late Cretaceous to early Cenozoic fault re-activation within the Moray Firth has also been linked to North Atlantic tectonism (e.g. Underhill, 1991). Aeromagnetic data showing offset dyke swarms across the WSW-ENE trending fault zones that crosscut Northern Ireland and Scotland combined with dating of igneous centres and dyke swarms in Northern Ireland showed that these crustal-scale strike-slip faults were active in the early Paleocene between 64 and 62 Ma (Cooper et al. 2012). Paleocene sand-rich intervals within the Maureen, Lista and Sele Formations of the Central North Sea Basin have been related to episodic hinterland uplift caused by plume activity in the North Atlantic (White and Lovell, 1997; Mudge and Jones, 2004). The oldest of these intervals, the 'Maureen Reworked Unit' (MRU), overlies the Intra-Danian unconformity at 62.7 Ma (Mudge, 2015). The MRU is concurrent with some of the earliest volcanism in the North Atlantic, such as the British-Irish Paleogene Igneous Province at 63.2 ± 0.6 Ma (Wilkinson et al., 2016).

5.5 *Results*

Regional thickness observations

Regional thickness maps of the individual formations that make up the Paleocene interval show that deposition was focussed down the eastern and western corridors of the basin, with thinning occurring toward the SE (Fig. 5.3). These corridors are defined by pre-existing Mesozoic structuration (Fig. 5.2). The Maureen Formation is characterised in its eastern corridor by a thick and well-defined body extending from the NW, where it is less defined, to the SE, where it pinches out abruptly (Fig. 5.3A). This body is termed the Halibut Slide (HS). Deposition throughout the Paleocene and early Eocene appears to thin

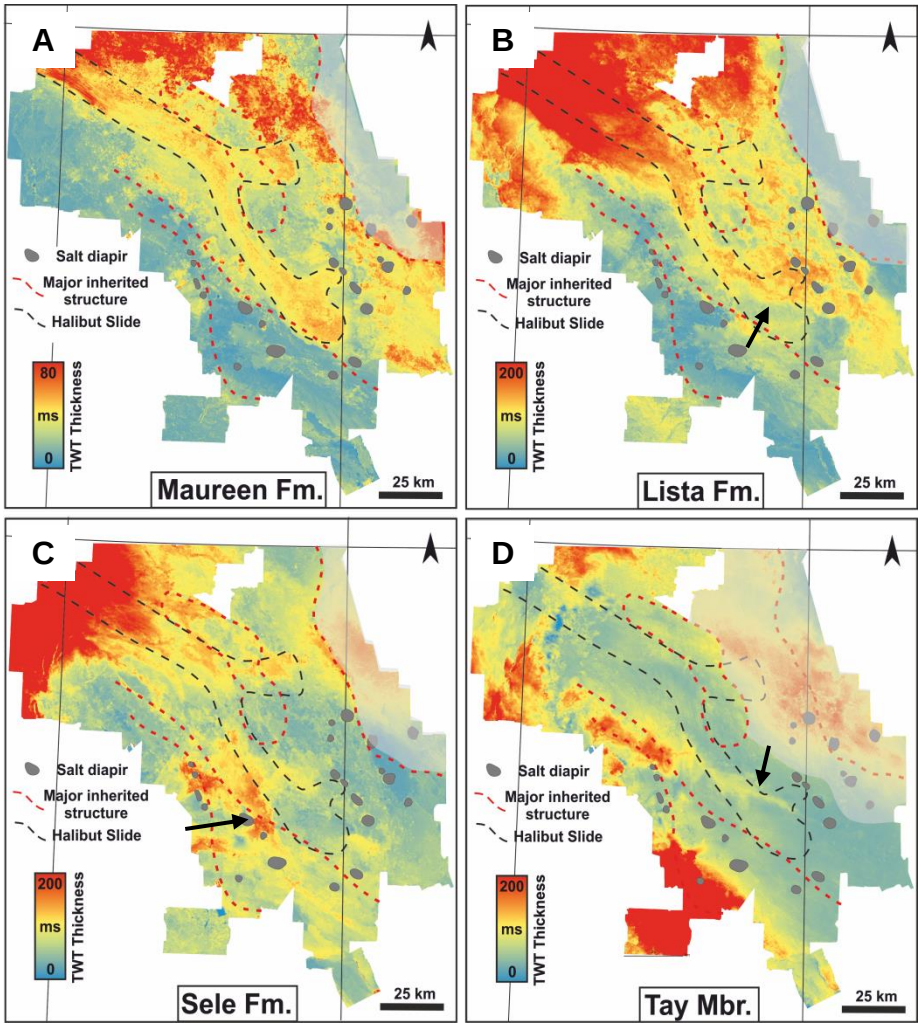

Figure 5.3: The effect of the Halibut Slide (approximate position in black dashed outline) on subsequent Paleocene sand-rich cycles (black arrow points to depositional effect of thickening adjacent to or thinning over distal toe of Slide). The topography of the Halibut Slide is almost entirely healed by the Eocene, with the Tay fan only showing subtle thinning and pinch-out within the Slide body (D). The distal toe of the slide appears to have had the greatest effect on subsequent cycles (black arrows), possibly due to the ponding and thickening of chalk megaclasts in this area, coupled with its distal position within the clastic system. The thickness map were generated following the horizon slicing method used regionally for the Paleocene by Kilhams et al. (2015). Areas with poor thickness estimates due to interpolation are shaded grey (e.g. the Jaeren High).

over the distal extent of the HS (Fig. 5.3B, C, D). Regions of thickened sedimentation also occur adjacent to the HS, particularly in the Lista Formation, where deposition appears to be steered by the distal extent of the HS, and in the Sele Formation, where SW-NE trending fairways abut and thicken at the margin of the HS (Fig. 5.3C). Thickened deposition also occurs in response to salt-diapir-related topography and remnant rift topography in the SW (Fig. 5.3C, D).

Halibut Slide observations

The Halibut Slide (HS) exhibits a maximum of ~170 m of mounded relief above the Top Chalk surface (Fig. 5.1; 5.4) and forms a continuous hard-reflection, with overlying reflections onlapping the mound (Fig. 5.5A). Within the HS, reflections are discontinuous

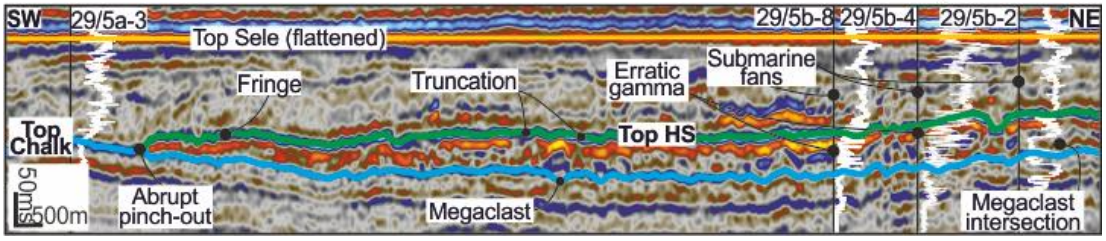

Figure 5.4: Flattened and interpreted seismic section through the Halibut Slide (location on Fig. 3E). Well intersections indicate dog legs in seismic line. The section has been flattened to mitigate the effects of post-depositional deformation. Megaclasts can be identified based on seismic reflection shape and amplitude. Gamma ray signatures are typically discontinuous within the Slide because of its poorly sorted composition (Gamma values decreases right-to-left).

and dim, with some isolated bright reflections (Fig. 5.4). Below the HS, the Top Chalk reflection is also discontinuous and frequently shows truncation and dimmed amplitudes. The mapped slide deposit maintains a relatively consistent thickness, thinning from around 170 m to 100 m over 170 km, before abruptly pinching-out over a distance of 10 km down-dip at the intra-basinal Erskine Ridge (Fig. 5.1; 5.5A, B). Megascours cut into the Top Chalk surface are up to 1 km wide, up to 150 m deep and extend for around 80 km down-dip within a 20 km wide scour 'belt' that defines the inferred lateral limits of the basal slide surface. The orientations of the most prominent megascours (Fig. 5.5C) indicate that the main failure event may have been sourced from the Grampian High, offshore NE Scotland (Fig. 5.1). Unfortunately, the headwall cannot be observed due to post-failure erosion of the Top Chalk surface (Fig. 5.5C). The Halibut Slide was heavily influenced

down-dip by existing seafloor topography, such as the northerly confining Halibut Horst, which the Slide has been named after. The measured length of the basal slide surface (290 km) is thus the minimum length of the slide. The majority of the slide volume extends

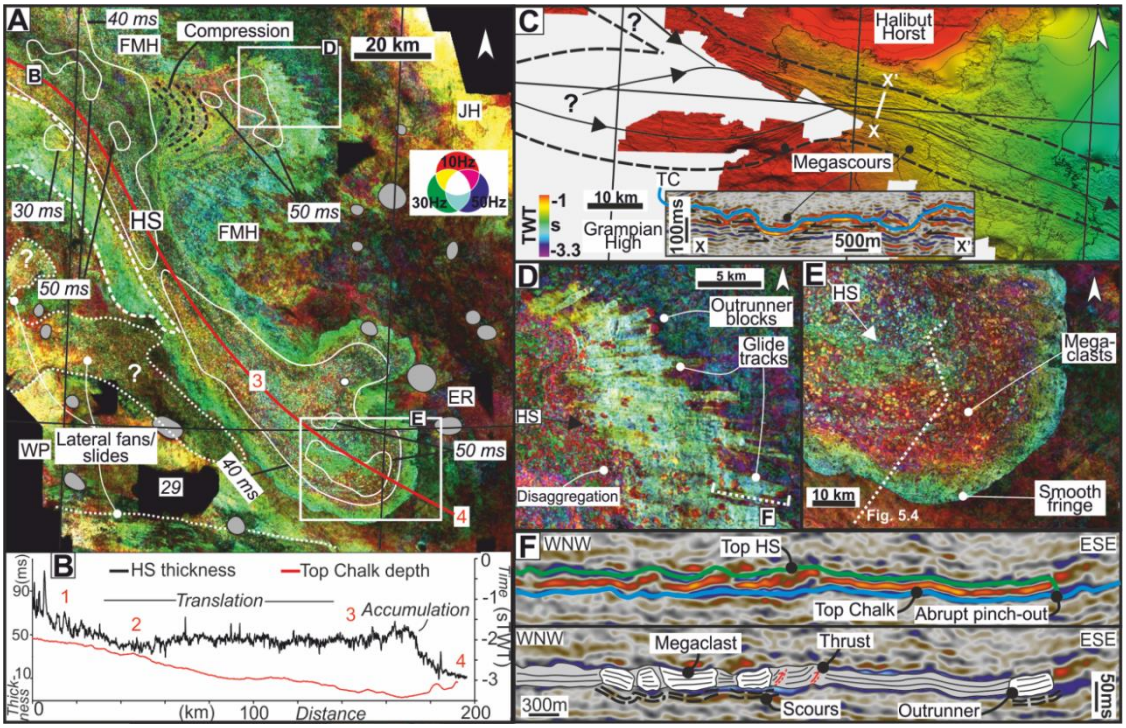

Figure 5.5: A: Spectral decomposition of a horizon slice within the HS. The lateral fan can be seen pinching out against the HS relief (dashed white line), along with numerous other MTCs along the south-western basin margin. White dot shows location of well 22/30a-1. Numbers in white squares refer to UK Continental Shelf Quadrant numbers. B: Thickness down the axis of the mapped Halibut Slide (extends 55km up-dip from fig. 4). Megascours affect the slide thickness up-dip (1) before consistent translation down-dip. The distal flow terminus forms a thickened accumulation zone (3), rich in megaclasts, before abrupt pinch-out down-dip (4). Interpolation of the surface through the steep and abrupt toewall causes the TWT thickness to stay slightly above 0 ms at pinch-out. C: Time structure of Top Chalk (Fig. 1) surface showing the megascour belt from the Outer Moray Firth. X-X': seismic section showing truncation (black arrows) of chalk reflectors against the megascours on the Top Chalk surface indicating significant erosion. D: Spectral decomposition of a horizon slice within the splayed Halibut Slide showing outrunner blocks forming scoured glide tracks and disaggregation and expansion of the flow as it decelerates into the western depocenter. E: Spectral decomposition of a horizon slice within the Halibut Slide showing a ponding of megaclasts at the frontally confined (Fig. 3B) Slide toewall. The continuous pale blue response represents the slide fringe. F: Down-dip seismic cross-section through the HS sub-body showing megaclasts and outrunner blocks. Both post-depositional extensional and syn-depositional compressional structures are seen within the HS. ER, Erskine Ridge; FMH, Forties-Montrose High; HBF, Highland Boundary Fault; HS, Halibut Slide; JH, Jaeren High; TC, Top Chalk; WP, Western Platform. Grey circles indicate salt diapirs.

from 200 km to 290 km down-dip on the basal slide surface, although uncertainty exists due to poorer seismic resolution within the up-dip survey.

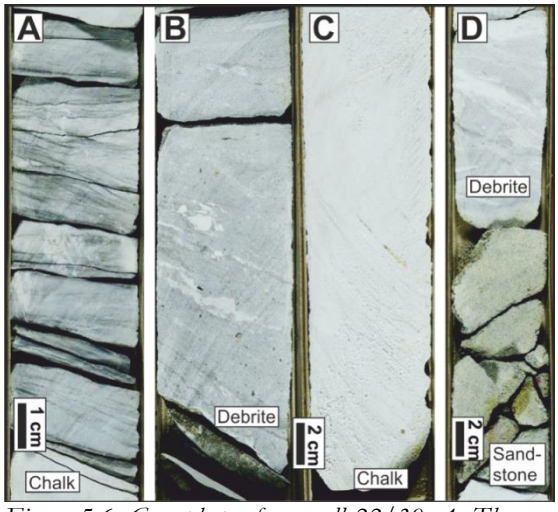

Figure 5.6: Core photos from well 22/30a-1. The core shows that the Halibut Slide is composed of allochtonous chalk (A, C), chalk-rich debrites (B, D) and some minor sandstones (D).

Spectral decomposition and colour blending of 10 Hz, 30 Hz and 50 Hz seismic frequencies (Fig. 5.5A; Appendix C) shows a clear bright body trending from the shelf toward the deep basin along a narrow corridor (~30 km wide). End Danian paleobathymetric reconstructions indicate the slope of this corridor was inclined at ~1.1° (Joy, 1992). This bright corridor is terminated by a 30 x 30 km lobate body in the deep basin (Fig. 5.5A, E). Bright specks within the HS range in width and length from ~50 m to over 1 km (average ~500 m) and are up to 160 m thick. Along the length of the HS the spectral decomposition signature partitions a relatively continuous response from the southern part of the body to a speckled response in the north (Fig. 5.5A). A similar speckled and lobate feature is evident more proximally, trending E-W (Fig. 5.5A), at a saddle-shaped low within the centre of the Mesozoic Forties-Montrose High (FMH) (Fig. 5.1, 5.5A, D). The specks have the same dimensions as those described within the Halibut Slide, suggesting a common origin. Lineations radiating from the FMH 'low' extend beyond the FMH speckled body and differentiate it from the distal HS which is characterized by a laterally continuous terminal boundary (Fig. 5.5D, F). Internally the FMH sub-body is similar to the Halibut Slide, with a bright top reflection and a chaotic body (Fig. 5.7). The FHM also shows up-dip inclined internal surfaces (Fig. 5.7).

The Halibut Slide is composed of chalk megaclasts within a mud-rich matrix, as indicated by logged core data (Fig. 5.1; 5.6, Appendix C), wireline logs (Fig. 5.4) and petrophysically derived carbonate and porosity distributions (Kilhams et al., 2015).

In total, the Halibut Slide has a length of at least 290 km and a minimum depositional extent of 200 km. The main slide body has an average width of ~30 km and average thickness of ~97 m, with the ~35 km long splayed slide having an average width of ~20 km and average thickness of ~80 m. In total this equates to a compacted volume of ~640 km^3. If we assume the chalk was compacted to ~150 m (maximum scour depth) and that the majority of the slide volume is dominated by chalk (megaclasts) then the decompacted volume is estimated at ~1450 km^3, based on a chalk porosity drop from 0.6 at 150 m to 0.1 at 3000 m (Mallon and Swarbrick, 2002).

Halibut Slide interpretation

Based on its geometry, internal seismic character, and the megascours, we interpret this feature as a large submarine landslide (herein termed a 'slide') deposited by variable sediment transport mechanisms, including sliding, debris flows, and probably associated turbidity currents. The allochtonous chalk within the Halibut Slide is suggested to have been either derived from the shelfal headwall or incorporated as the Slide gouged and eroded the sea-bed down-dip, as evidenced by the up to 150 m of chalk removal within the megascours (Fig. 5.5C). It is proposed that the radial sub-body of the HS described at the Forties-Montrose High (FMH) was formed by flow splitting as part of the HS escaped the lateral confinement of the FMH through its saddle-like depression (Fig. 5.5A). The splayed slide experienced acceleration into the depression and confinement at its margins, before flow expansion and deceleration as it moved past the FMH confines and into the low of the eastern depocentre (Fig. 5.5A, D; Appendix C). The inclined surfaces within the FMH sub-body are attributed to imbrication as the flow was compressed during deceleration (e.g. Frey-Martínez et al., 2006), indicating that the flow was cohesive during transport (Fig. 5.7). The radiating lineations that spread laterally from the axis of the MS are interpreted as erosional scours caused by megaclasts gouging the substrate (Fig. 5.5D). Out-running megaclasts seen at the ends of megascours support this interpretation (Fig. 5.5D; F; Appendix C). The diverging pattern of the scours reflects flow deceleration as the splayed slide became unconfined and began to disaggregate (Fig. 5.5A, D).

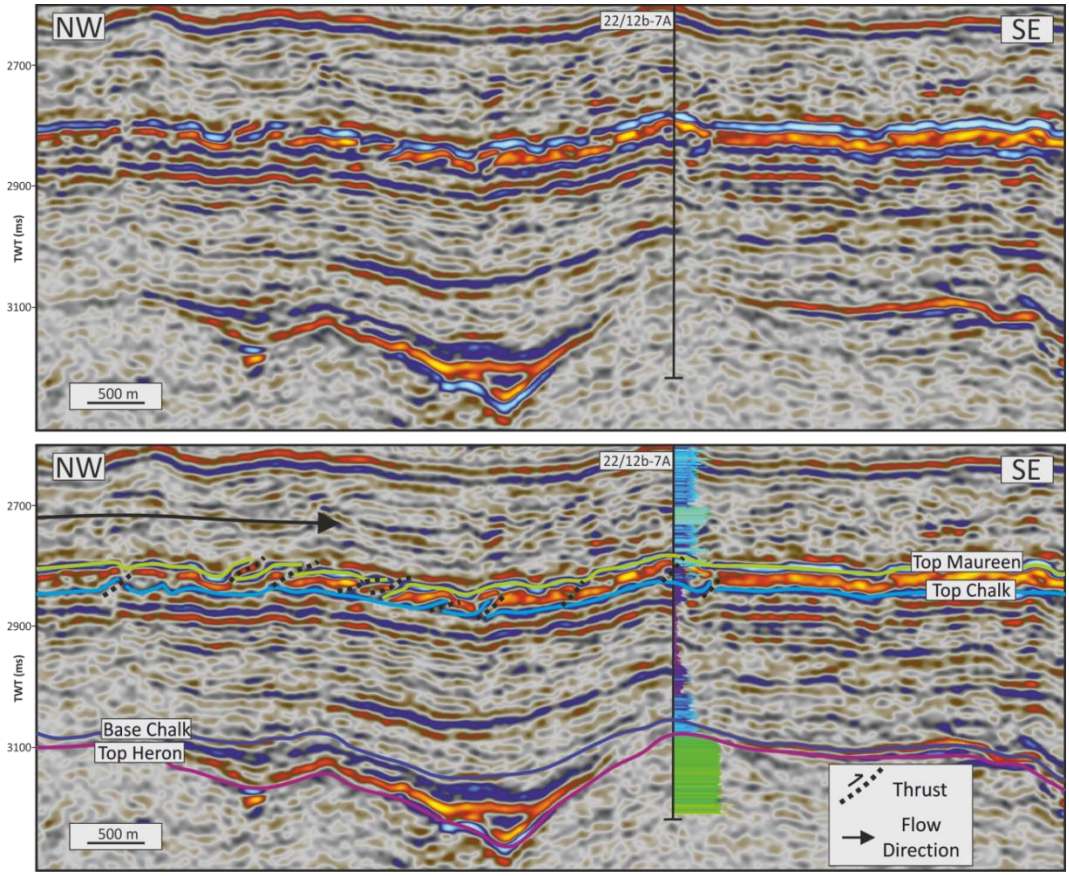

Figure 5.7: Uninterpreted (A) and interpreted (B) section through the splayed portion of the Halibut Slide. Internal thrusting and imbrication is evident within the splay as its cohesive mass decelerated during run-out. Location on Appendix C; Fig 11.6.

5.6 ***Discussion and conclusion***

The Halibut Slide is the largest epicontinental submarine landslide known on Earth and one of the most significant stratigraphic events within the geological history of the North Sea Basin. Paleocene plume-related uplift affecting the Scottish mainland and the Moray Firth (Nadin and Kusznir, 1996) caused tectonic rejuvenation and SE-ward tilting of the western basin margin around 63 Ma. Between 64 to 62 Ma, far-field compression due to a combination of plume-related uplift and the Alpine orogeny caused reactivation and accumulation of up to 1 km of slip along major crustal scale SW-NE trending strike-slip faults that crosscut Ireland and Scotland and entered the North Sea around the flanks of the Moray Firth (Fig. 5.1) (cf Underhill, 1991; Cooper et al. 2012). The Halibut Slide headwall region is located adjacent to these faults, lying ~50 km east of the Great Glen Fault Zone and 100 km north of the Highland Boundary Fault Zone (Figs 5.1; 5.5; 5.8). These fault zones would have moved many times to accumulate 1 km of slip between 64

Ma to 62 Ma (cf Wells & Coppersmith 1994; Cooper et al. 2012). It is therefore suggested that the combination of far-afield stresses and local reactivation of major tectonic lineaments primed the North Sea Basin margin for catastrophic slope failure, resulting in the emplacement of the Halibut Slide.

Other potential mechanisms contributing to plume-related slide initiation at this time include increased pore pressures associated with elevated heat flow, the hydrostatic effects of elevating the chalk aquifer above sea-level and loading of the slope by prograding clastic systems (Fig. 5.8). These mechanisms are believed to be less important due to the distal position of the basin compared with the main thermal anomaly, the relatively minor uplift accumulated during the earliest plume impingement and the time lag between initial uplift and clastic progradation. The slide represents the largest single depositional event within this period of major tectonic upheaval in the North Sea Basin, heralding the onset of subsequent Paleogene siliciclastic sediment supply. Sediment routing and deposition of the Paleogene deep-marine siliciclastic systems was controlled by the underlying Halibut Slide topography for ~10 Myr (Fig. 5.3). The discovery of the Halibut Slide demonstrates the close relationship between major mantle and lithospheric processes and the sedimentary history of the North Sea Basin.

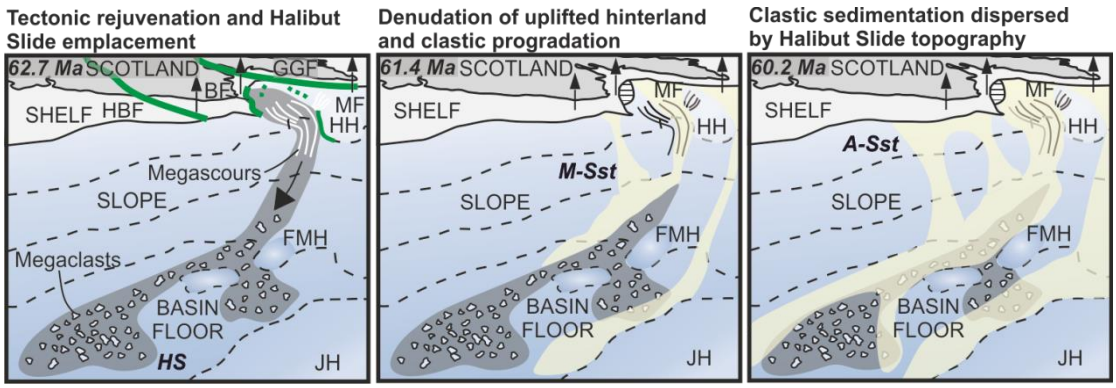

Figure 5.8: Depositional model for the emplacement of the Halibut Slide. The effect the Slide has on subsequent clastic sedimentation is also shown (based on data from DR 6). Absolute ages from Mudge (2015). Green lineaments indicate fault reactivation. Arrows indicate uplift. A-Sst, Andrew Sandstone; BF, Banff Fault; FMH, Forties-Montrose High; GGF, Great Glen Fault; HBF, Highland Boundary Fault; HH, Halibut Horst; HS, Halibut Slide; JH, Jaeren High; MF, Moray Firth; M-Sst, Maureen Sandstone;

CHAPTER 6: Evolution of a mixed siliciclastic-carbonate system on an unstable margin: the Cretaceous of the Eastern Greater Caucasus, Azerbaijan

Euan L. Soutter[1], Zoë A. Cumberpatch[1], Ian A. Kane[1] and Max Casson[1]

[1]Department of Earth and Environmental Sciences, University of Manchester, Manchester, M13 9PL, U.K.

6.1 *Abstract*

Mixed siliciclastic-carbonate deep-marine systems, herein termed 'mixed systems', are less well documented than their siliciclastic-dominated counterparts, but may be common globally and misinterpreted as transient transition zones between carbonate and siliciclastic deposition. The well-exposed Upper Cretaceous mixed-system of the Buduq Trough, Eastern Greater Caucasus (EGC), Azerbaijan, provides an opportunity to study the interaction between contemporaneous siliciclastic and carbonate deep-marine deposition. The Buduq Trough represents a sub-basin formed within the larger unstable post-rift margin of the EGC. Qualitative and quantitative facies analysis reveals that Upper Cretaceous stratigraphy of the Buduq Trough comprises a Cenomanian-Turonian siliciclastic submarine channel complex, which abruptly transitions into a Coniacian-Maastrichtian mixed-lobe succession. The Cenomanian – Turonian channels are shown to be entrenched in lows on the palaeo-seafloor, with the sequence entirely absent 10 km toward the west, where a Lower Cretaceous submarine landslide complex is suggested to have acted as a topographic barrier to deposition. By the Campanian this topography was largely healed, allowing deposition of the mixed-lobe succession across the Buduq Trough. Evidence for topography remains recorded through opposing palaeocurrents and frequent submarine landslides. The overall sequence is interpreted to represent abrupt Cenomanian-Turonian siliciclastic progradation, followed by ~Coniacian retrogradation, before a more gradual progradation in the Santonian-Maastrichtian. This deep-marine siliciclastic system interfingers with a calcareous system from the Coniacian onwards. These mixed lobe systems are different to siliciclastic-dominated systems in that they contain both siliciclastic and calcareous depositional elements, making classification of distal and proximal difficult using conventional terminology and complicating palaeogeographic interpretations. Modulation and remobilisation also occurs between the two contemporaneous systems, making stacking patterns difficult to decipher. The Buduq Trough is analogous in many

ways to offshore The Gambia, NW Africa, and could be a suitable analogue for mixed deep-marine systems globally.

6.2 *Introduction*

Mixed siliciclastic-carbonate systems

Sedimentary successions characterised by contemporaneous deposition of both siliciclastic and carbonate lithologies, herein termed 'mixed-systems', have been identified from the Cambrian (Osleger and Montañez, 1996) to the Quaternary (Dunbar & Dickens, 2003; Tucker, 2003). Mixed systems are formed by a variety of depositional processes (e.g. Mount, 1984; Chiarella et al. 2017) and are consequently recognised in a variety of depositional environments, such as: shoreface (Zonneveld et al. 1997), lagoonal (Mitchell et al. 2001), shelfal (Mount, 1984; Zeller et al. 2015), slope (Gawthorpe, 1986) and deep-water (Ditty et al. 1997; Yose & Heller, 1989; Bell et al. 2018; Moscardelli et al. 2019). Mixed-systems deposited in deep-marine (below storm-wave base) are usually formed by material shed from a shallower carbonate-producing shelf that periodically received terrigenous sediment (Fig. 1) (Mount, 1984; Dunbar & Dickens, 2003; Crevello & Schlager, 1980). This material is then re-deposited in deep-marine by a spectrum of sediment gravity flows types, from turbidity currents to submarine landslides (Dorsey & Kidwell, 1999; Miller & Heller, 1994; Tassy et al. 2015; Moscardelli et al. 2019).

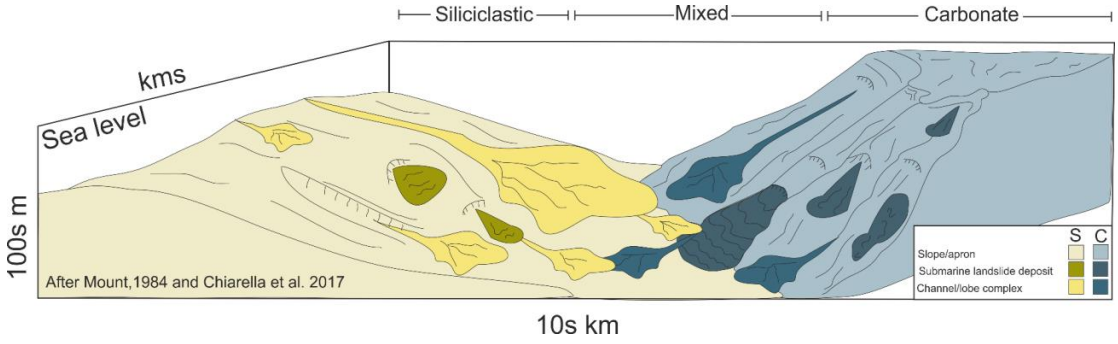

Figure 6.1: Simplified conceptual model showing how siliciclastic and carbonate systems may interact at a basin-scale in a deep-marine mixed siliciclastic-carbonate system. Carbonate material is shed from a shallower carbonate-producing platform that periodically received siliciclastic material; this is then redeposited in the deep-marine by of gravity flows (After Mount 1984, Chiarella et al. 2017).

Mixed lobes

Sediment-gravity-flows that lose confinement on the slope or basin-floor build lobate depositional bodies, known as lobes, which form important archives of palaeoclimatic and palaeogeographic information (e.g. Hessler & Fildani, 2019). Exhumed deep-marine lobes have been studied in great detail, and a wide variety of stacking patterns, depositional processes and facies distributions have been described and interpreted (e.g. Mutti, 1983; Postma et al. 1993; Prélat et al. 2009; Terlaky et al. 2016; Kane et al. 2017; Bell et al. 2018; Fildani et al. 2018; Fonnesu et al. 2018; Soutter et al. 2019, Cumberpatch et al. in prep.). These studies typically focus on siliciclastic systems, with few studies investigating the characteristics of lobes formed in mixed-systems (Fig. 6.1). This study aims to address this by describing exhumed Cretaceous submarine lobes from the Eastern Greater Caucasus (EGC), Azerbaijan (Fig. 6.2) which were built by contemporaneous deposition of calcareous and siliciclastic sediment gravity flows. The characteristics of these mixed lobes and the processes that govern their deposition are then compared with siliciclastic lobes. This study will also describe the sedimentological evolution of the basin throughout the Cretaceous, providing insights into the stratigraphic evolution of a basin characterised by unstable margins.

6.3 ***Geological Setting and Basin Structure***

Evolution of the Eastern Greater Caucasus

The Eastern Greater Caucasus forms the easternmost extent of the NW-SE trending Greater Caucasus orogenic belt, which runs from the Black Sea in the west to the Caspian Sea in the east (Fig. 6.2) (e.g. Bochud 2011). The EGC sits on the southern-edge of the Scythian Platform, which represents the southern margin of the Eastern European continent (Saintot et al. 2006). The exposed EGC is mainly composed of Mesozoic-aged sediments that accumulated during multiple phases of extension and convergence related to sequential closure of the Tethys toward the south (Golonka, 2004; Vincent et al. 2007). Most of these Mesozoic tectonic events occurred in the Jurassic, with Upper Triassic-Lower Jurassic compression followed by Lower- to Mid-Jurassic rifting and compression, and Upper Jurassic rifting and compression (Bochud 2011). These tectonic events are recorded by major thickness variations across the Middle Jurassic interval (Fig. 6.3).

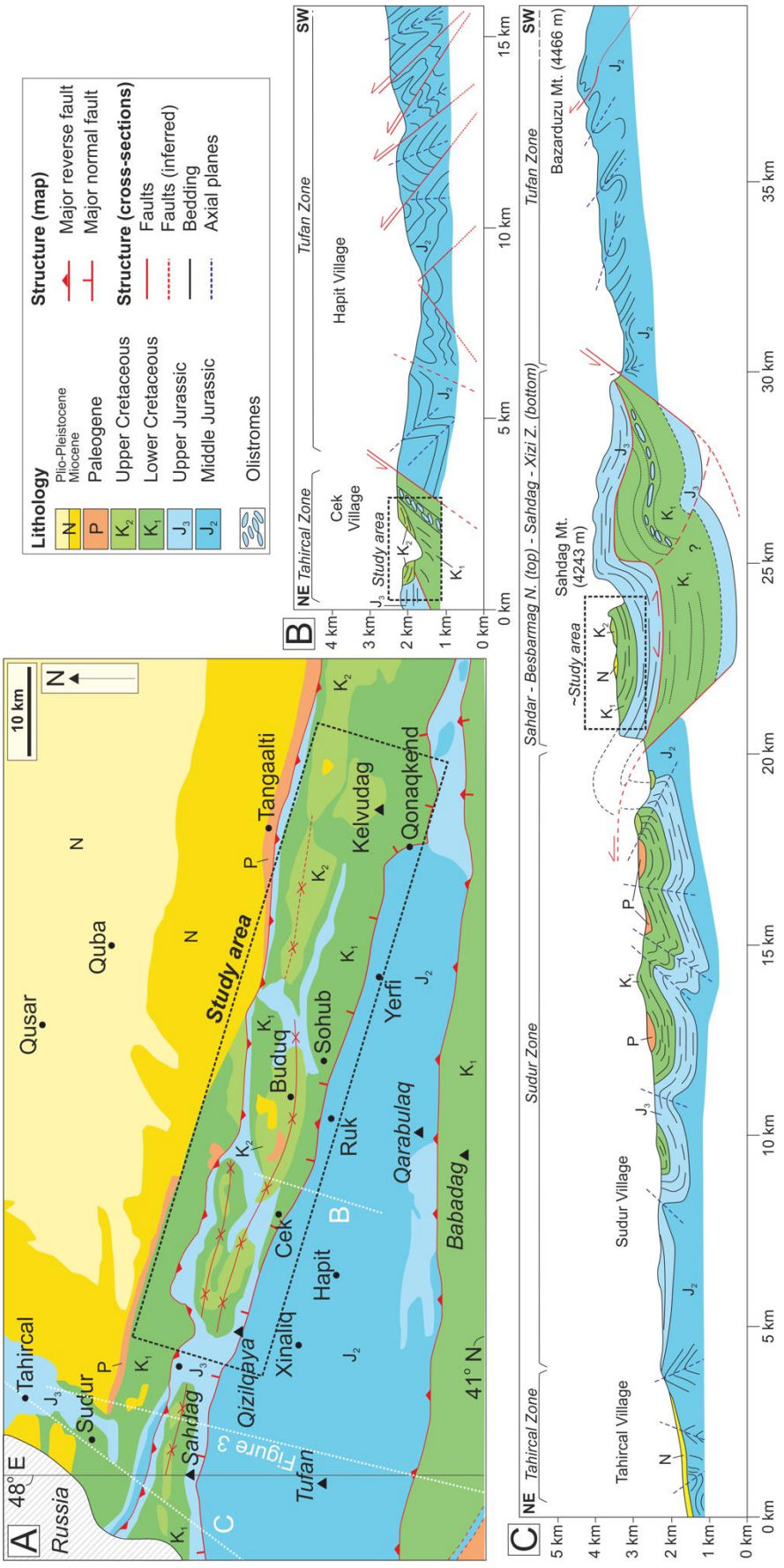

Figure 6.2: Structural and stratigraphic framework of the Eastern Greater Caucasus (EGC) of Azerbaijan. A) Simplified geological map, black box locates study area, lines B and C are located. Schematic location of Figure 3 is shown. B) Cross section across the Cek-Hapit Valley, black box locates study area. C) Cross section from Tahircal-Sabdag Mountain – Bazarduzu Mountain, black box locates equivalent stratigraphy to our studied section (Modified from Bochud, 2011).

The Lower Cretaceous of the EGC was deposited within an unstable marine environment, as recorded by frequent mass-wasting events and major thickness changes across the interval (Egan et al. 2009; Bochud 2011). Subsidence increased through the Lower Cretaceous and into the early Upper Cretaceous due to back-arc extension associated with the opening of the West Black Sea Basin to the west (Nikishin et al. 2001), resulting in deep-marine deposition of extensive mudstones interspersed by submarine landslide deposits and terrigenous sediments (e.g. Brunet et al. 2003).

The remainder of the Cretaceous sequence was deposited during a period of thermal subsidence on a southward-dipping slope, with the basin divided into a series of sub-basins (Bochud 2011). One of these sub-basins, the Buduq Trough, encompasses our study area. The Cretaceous stratigraphy is dominated by calcareous and siliciclastic turbidites and conglomerates interbedded with hemipelagic marls and mudstones (e.g. Brunet et al. 2003). A number of intra-Cretaceous unconformities are seen within the basin and are related to periods of compression (Egan et al. 2009) or sea-level fluctuations. The end of the Cretaceous sequence is represented by a Base-Cenozoic unconformity formed during Paleogene compression (Bochud 2011).

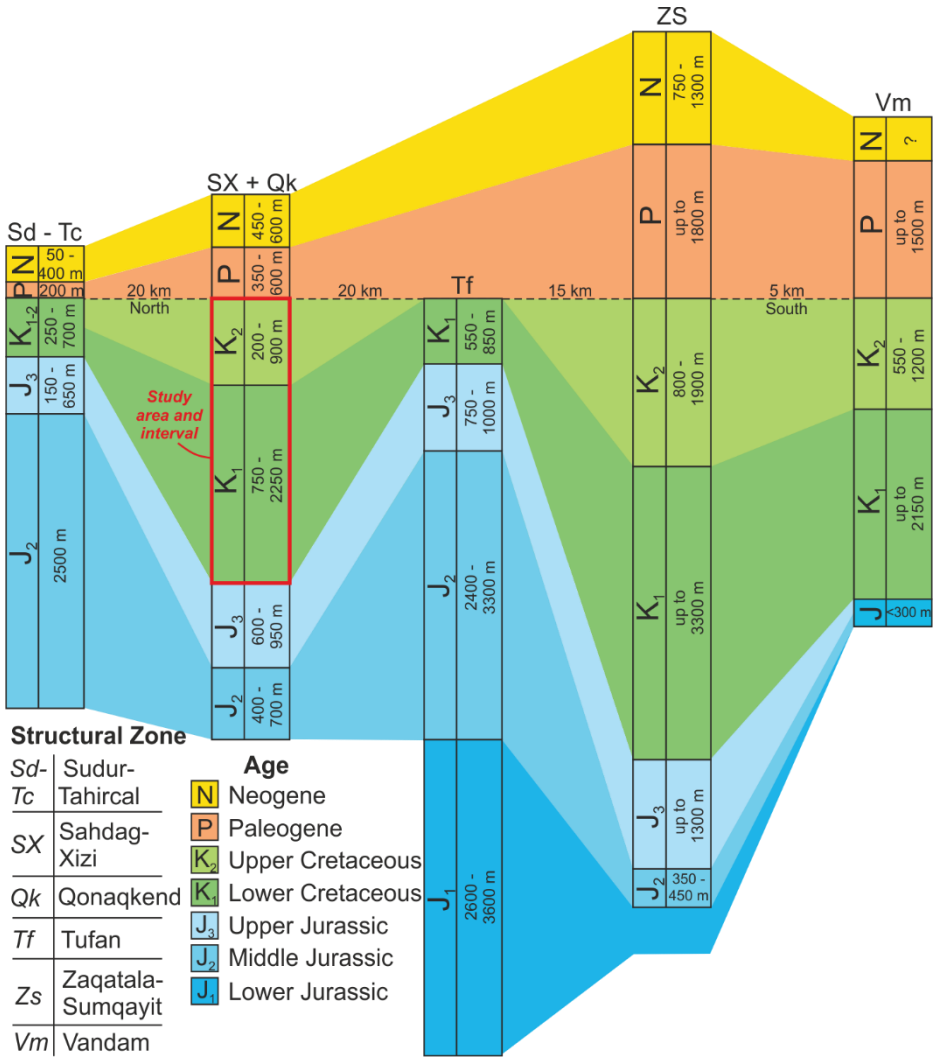

Figure 6.3: Stratigraphic section trending roughly north-south across the five main structural zones (from Bochud 2011) of the EGC. Flattened along the top of the Cretaceous, located on Figure 2.

Collision of the Arabian and Eurasian plates in the Oligocene (Vincent et al. 2007) deformed the Mesozoic and early Cenozoic succession into a series of exhumed synclines bound by major faults. These faults separate distinct structural zones within the EGC (Fig. 6.2; 6.3) (Bochud 2011).

6.4 *The Buduq Trough*

The Buduq Trough is preserved in the east-west trending Qonaqkend structural zone (Fig. 4) and has been interpreted as an Upper Cretaceous 'paleo-valley' incised into Lower Cretaceous deep-marine sediments and Upper Jurassic limestones following a period of compression (Fig. 2B) (Egen et al. 2009; Bochud 2011). It is likely that this compression was related to far-field tectonism in the eastern Black Sea (Sosson et al. 2016),

which overprinted the subsidence that characterised the Cretaceous of the EGC. The earliest fill of the Buduq Trough is preserved in the east and is represented by Cenomanian - Turonian sandstones and conglomerates (Fig. 6.2) (Bochud et al, 2011). The nature of this transition varies across and within the Trough; with the Cenomanian-Turonian conformable with the Aptian-Albian at Mt. Kelevudag (Kopaevich et al. 2015) and sitting directly on Barremian at Khirt (Fig. 6.2; 6.3). The overlying Coniacian-Maastrichtian is represented by mixed siliciclastic-carbonate turbidites and is conformable with the Cenomanian-Turonian in the west. In the east, near Cek, the Cenomanian-Turonian is absent, with the Campanian directly overlying Aptian-Albian thin-bedded mudstones, submarine landslide deposits and predominantly siliciclastic turbidites (Fig. 6.2; 6.3). Upper Cretaceous oceanic red beds (CORBs) are also seen throughout the Upper Cretaceous sequence, particularly in the Coniacian – Campanian turbidites and marls, indicating periodically oxic deep-marine conditions (e.g. Hu et al. 2005).

6.5 ***Data and Methods***

The data set comprises 23 sedimentary logs, totalling 500 m, collected across the Buduq Trough (see supplementary material). Logs were generally collected at 1:25 scale. Bedding and structural data (Fig. 6.4) and palaeocurrent data (Fig. 6.5) were collected to ground truth the geological map and cross sections of Bochud (2011). Palaeocurrent readings were quite rare and were taken only where sedimentary structures were clear enough to permit unambiguous data collection. Sparse biostratigraphic data (Bochud 2011) hinders precise correlation across the study area. Chrono-stratigraphic subdivision of the Buduq Trough are still being refined (cf. Bochud 2011; Bragina & Bragin, 2015; Kopaevich et al. 2015), possibly due to the litho-stratigraphic similarities between the units and the complex paleo-topography in which they were deposited (Egan et al. 2009). Therefore we use mapped stratigraphic units (J_1, J_2, K_1, K_2 etc.) and lithostratigraphy to suggest associated ages (Bochud 2011). Sedimentary logs were used to develop a lithofacies scheme (Fig. 6.6, Table 1) and facies associations (Fig. 6.7).

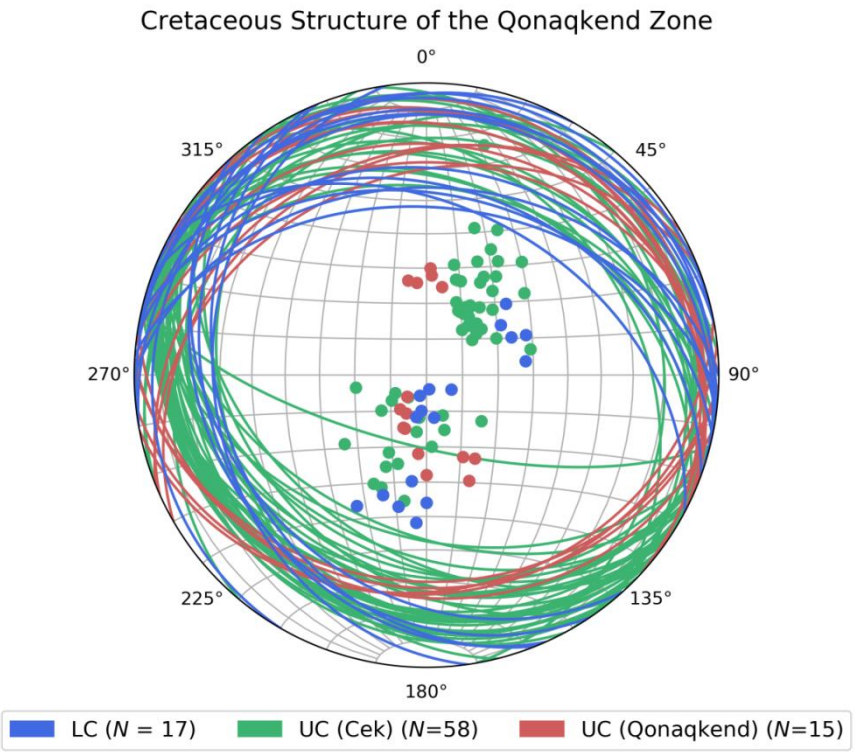

Figure 6.5: Equal area stereographic projection showing bedding readings for Cretaceous stratigraphy across Qonaqkend Zone. Bedding planes shown as lines and poles to bedding shown as dots. Coloured by stratigraphy and location; LC- Lower Cretaceous, UC- Upper Cretaceous. Structural data reveals a shallow-moderate structural dip to the north and south, in agreement with the east-west trending structural zones of the EGC.

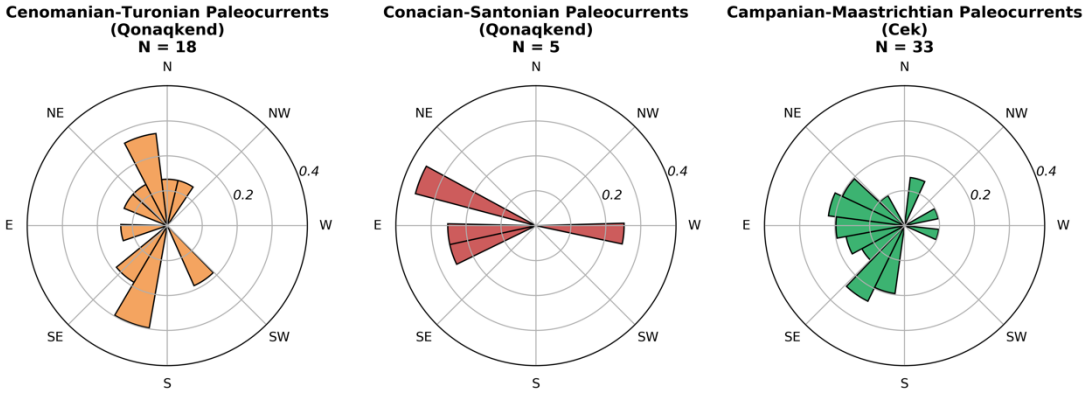

Figure 6.4: Rose diagrams from palaeocurrent indicators (ripples, sole marks, cross-stratification) from the Cretaceous stratigraphy of the Qonaqkend Zone. Readings have been corrected for tectonic tilt and are subdivided by stratigraphy and location (see Figure 6.2).

Over 10,000 sedimentological measurements (e.g. bed thickness, grain size, facies) were collected and quantitatively analysed (Appendix D). Stratigraphic logs were assigned

one of seven facies associations (Fig. 6.7) in order to quantitively compare bed statistics across deep-marine sub-environments (Fig. 6.8; 9; 10; 11).

6.6 ***Results***

Lithofacies

Carbonate and siliciclastic lithofacies presented in Table 1 and Fig. 6 represent beds deposited by individual events (event beds) and are classified based on outcrop observations. 'Mud' is used here as a general term, for mixtures of clay, silt and organic fragments.

Facies Associations

Facies associations have been interpreted based on the dominant lithofacies (Fig. 6, Table 1) and architecture of a given succession and are subdivided into siliciclastic and mixed (carbonate and siliciclastic) associations (Fig. 6.7). Facies associations FA1, FA2 and FA3 are Cenomanian-Turonian and FA 4, FA 5, FA 6 and FA 7 are Coniacian-Maastrichitan (Bochud 2011). Facies associations commonly used for lobes (Prélat et al. 2009; Spychala et al. 2017) and channels (Kane & Hodgson, 2011; Hubbard et al. 2014) best fit our observations.

Table 6.1: Summary of observations and interpretations of lithofacies, used to create facies associations

Facies	Description	Interpretation
Conglomerates (A)	0.1 to 3 + m thick beds of poorly-sorted, disorganised conglomerates. Most commonly clast-supported consisting of sub-angular to sub-rounded boulder-, cobble- and pebble-sized clasts of limestone and sandstone. Matrix comprises a poorly-sorted mix of all finer size fractions. Cm – 10s cm scale mud-clasts occur sporadically throughout the beds. Bed bases are often erosive, and can be amalgamated. This facies often grades into thick bedded sandstones (C).	The characteristics of this facies suggest deposition from debris flows having cohesive as well as frictional strength (Fisher, 1971; Nemeck & Steel, 1984). The grading of conglomerates into thick-bedded sandstones reflects the transition of hyperconcentrated submarine debris flows into highly-concentrated turbulent flows (Mulder & Alexander, 2001; Sohn et al. 2002), due to the entrainment of ambient water (Postma et al. 1988).
Poorly sorted clast rich deposit (B)	0.1 – 1+ m thick poorly sorted deformed, matrix-supported units. Matrix can range from mudstone to coarse sandstone, and is often poorly-sorted and sheared. Clasts include cm-m scale limestone and sandstone blocks, rafts of remobilised folded thin-bedded sandstones, sporadic pebbles and granules and frequent mud-clasts. These deposits are commonly non-graded, but can show weak normal-grading.	The poorly-sorted matrix and large clast sizes are suggestive of 'flow freezing' of a flow with yield strength (Inverson et al. 2010), indicating 'en masse' deposition from a laminar flow (Nardin et al. 1979; Inverson 1997; Sohn 2000). Remobilised thin-bedded sandstones and intra-basinal clasts indicate localised mass failure and reworking.
Thick-bedded sandstones (C)	0.5 – 1+ m brown siliciclastic fine-granular sandstones. Normally-graded or non-graded and typically lacking in primary depositional structures. Bases are often sharp and erosive. Parallel laminations are sometimes present at bed tops and mud-clasts can be observed throughout. Weak cross-lamination is infrequently observed.	The general massive structuration of these deposits suggests that they represent rapid aggradation beneath a highly concentrated but dominantly turbulent flow, and are thus interpreted as high density turbidites (Lowe, 1982; Mutti 1992; Kneller & Branney 1995).

Mixed siliciclastic and calcareous sandstones (D)	0.1-1m beds of medium-bedded calcareous sandstones with punctuated interbeds of cm-scale thin-bedded siliciclastic sandstone, either as continuous beds or lenses. The medium-bedded calcareous sandstones are massive and the siliciclastic beds are often erosively-based and show tractional structures (ripple and planar lamination). Siliciclastic beds can be amalgamated with each other or isolated between calcareous siltstones or sandstones.	Medium-bedded calcareous sandstones are interpreted to represent deposition from a slowly aggrading dilute turbidity current. Periodic, thin-bedded siliciclastic sandstones represent deposition from a relatively quickly aggrading dilute turbidity current, which interacted with a much slower aggrading calcareous turbidity current.
Medium-bedded calcareous sandstones (E)	0.1-1 m thick beige beds of calcareous siltstone -fine sandstone. Normally-graded or non-graded. Planar lamination may be present, but other tractional structures are rare. Beds can be amalgamated.	Based on their tractional structures and normal-grading, beds are interpreted as having being deposited from dilute turbidity currents. These beds are interpreted as medium-density turbidites, due to larger bed thickness and infrequent tractional structures, than thin-bedded calcareous sandstones (G). Thicker beds and fine grain size indicate a slowly aggrading dilute turbidity current.
Medium-bedded siliciclastic sandstones (F)	0.1 -0.5 m thick brown beds of very fine – granular grained, commonly normally-graded, sandstones. Inverse-grading is infrequently observed. Basal parts of the bed are often structureless containing infrequent cm-scale mud-clasts while tops are rich in tractional structures including parallel, ripple and hummock-like laminations. Bed bases are often erosive, and can be amalgamated.	Based on their tractional structures and normal-grading, beds of this lithofacies are interpreted as deposition from a dilute turbidity current. These beds are interpreted as medium-density turbidites due to their bed thickness and common lack of structures in the lower part of the bed (e.g. Soutter et al. 2019).

Thin-bedded calcareous sandstones (G)	0.01 – 0.1 m thick beige beds of calcareous siltstone-fine sandstones. Can be normally-graded, often into silty-mudstones, or not graded. Planar laminations are observed but other tractional structures are typically absent. Individual beds are often amalgamated.	Thin-beds, fine grain size and weak planar laminations represent deposition from a low-concentration turbidity current (Mutti 1992; Jobe et al. 2012; Talling et al. 2012), indicating these beds are low-density turbidites. Fine grain size, thicker beds compared to thin-bedded siliciclastic sandstone (H) and absence of ripple laminations suggest slowly aggrading, dilute remnants of a turbulent flow, (Remacha & Fernández 2003; Bell et al. 2018), which did not reach significant velocity to generate ripple laminations (Baas et al. 2016).
Thin-bedded siliciclastic sandstones (H)	0.005 – 0.1 m thick brown beds of siliciclastic very fine- granular sandstones. Commonly normally-graded, occasional inverse-graded. Tractional structures (planar, ripple, hummock-like and convolute laminations) and sporadic mud-clasts are observed. Bases can be flat or weakly erosive and sometimes contain granules. Bed tops are often flat. Where present, ripples can show opposing palaeoflow.	Thin-bedded, structured sandstones are interpreted to be deposited from low-concentration turbidity currents (Mutti 1992; Jobe et al. 2012; Talling et al. 2012) and are therefore interpreted as low-density turbidites. Ripples with opposing palaeoflow suggests topographic interference.
Bi or tri-partite beds (I)	0.05-0.5 m thick beds that contain multiple parts. Typically consisting of a lower fine-coarse sandstone (division 1) overlain by a poorly-sorted muddy siltstone – medium sandstone (division 2). Division 3 is sometimes present consisting of a siltstone-fine grained sandstone loaded into division 2. Divisions 1 and 3 sometimes contain planar laminations and sporadic cm scale mud-clasts. Division 2 is often highly deformed and rich in mud-clasts and very coarse sandstone to pebble-grade clasts.	Tractional structures in division 1 and 3 indicate formation under turbulent flows. Poor-sorting and mud content suggest division 2 was deposited under a transitional-laminar flow regime. These bi-tri partite beds are hybrid beds (Haughton et al. 2009), generated by flow transformation from turbulent to laminar. Such transformation occurs through flow deceleration (Barker et al. 2008; Patacci et al. 2014) and by an increase in concentration of fines during flow run-out (Kane et al. 2017).

Mudstone (J)	0.005 – 8 m thick pale grey or red mudstone – fine siltstone beds, which are friable and often inferred in areas of missing section. Planar laminations, discontinuous drapes and lenses of siltstone may be present. Commonly calcareous in composition. Red beds are common at the base of the Campanian.	Low energy conditions, representative of background sedimentation via suspension fallout. Laminations may be present below the scale visible in outcrop, representing deposition from a dilute turbidity current (Boulesteix et al. 2019). Pale colour indicates low total organic carbon (TOC). Red beds are similar to Cretaceous Oceanic Red Beds (CORBS) described across Europe (Wang et al. 2005; Hu et al. 2005; Wagreich & Krenmayr, 2005) and represent deposition below the carbonate compensation depth (CCD) in a deep oceanic basin.

Siliciclastic Facies Associations

FA 1: Lobe Fringe

Observations: FA 1 is dominated by metre-scale packages of thin-bedded siliciclastic siltstones to fine-grained sandstones with subordinate mudstones and medium-bedded siliciclastic sandstones (Fig. 6.7A). Beds are laterally extensive for 100's of metres and are commonly flat based and flat topped, often showing normal-grading from fine sandstone to siltstone. Planar and convolute laminations are observed in the upper part of many beds. Debrites, hybrid beds, conglomerates and thick-bedded sandstones are absent.

Interpretations: Thin-bedded, structured sandstones are interpreted to be deposited from low-concentration turbidity currents (Mutti et al. 1992; Jobe et al. 2012; Talling et al. 2012). The lack of hybrid beds and the thin-bedded nature, lateral-extent, fine-grain size and lack of ripple-stratification indicate deposition in a distal lobe fringe (Fig. 6.9) (Mutti 1977; Prélat et al. 2009; Marini et al. 2015; Spychala et al, 2017).

FA 2: Channel Axis

Observations: FA 2 is composed of metre-scale thick-bedded medium-pebbly sandstones and conglomerates with lesser medium-bedded sandstones and rare thin-bedded sandstones, mudstones, debrites and hybrid beds (Fig. 6.7B). Within the Cenomanian-Turonian succession, FA 2 has the highest frequency of thick-bedded

sandstones, conglomerates and bi-tripartite beds (Fig. 6.9). Conglomerates often grade normally into thick-bedded sandstones, commonly associated with a grain size break, with coarse-granular sandstone grade often missing. Where conglomerates do not grade into thick-bedded sandstones they are amalgamated or are less commonly separated by thin beds of mudstone. Conglomerates are poorly-sorted, clast-supported and contain sub-angular – sub-rounded clasts of limestone, sandstone and mudstone that often crudely grade from cobbles to pebbles upwards (Fig. 6.11). Conglomerates also often contain disarticulated shelly fragments. Sandstone and conglomerate bases are almost always erosional.

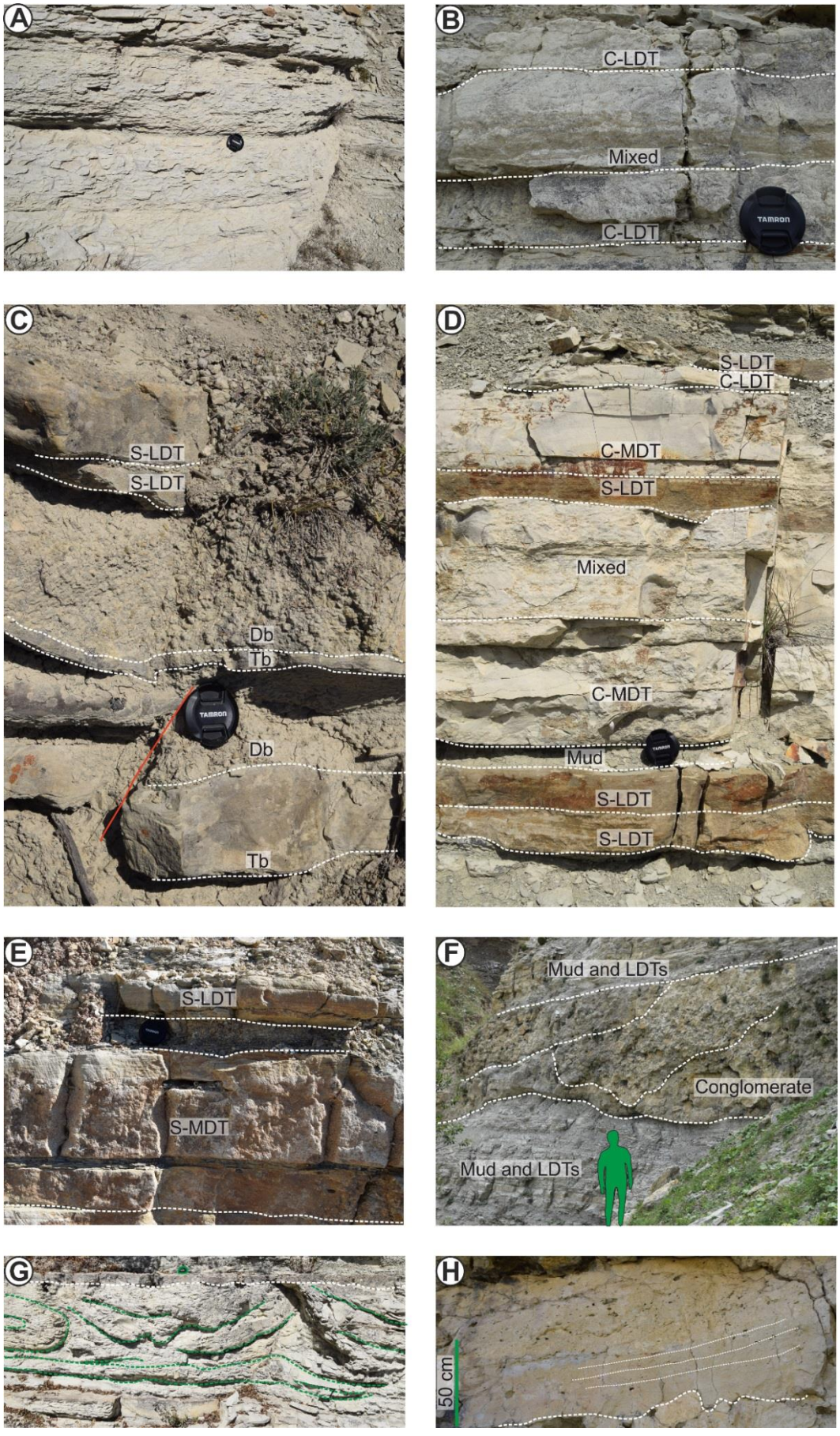
A
B
C-LDT
Mixed
C-LDT
C
S-LDT
S-LDT
Db
Tb
Db
Tb
D
S-LDT
C-LDT
C-MDT
S-LDT
Mixed
C-MDT
Mud
S-LDT
S-LDT
E
S-LDT
S-MDT
F
Mud and LDTs
Conglomerate
Mud and LDTs
G
H
50 cm

Figure 6.6: Facies photographs. Facies described in detail in Table 1. Scale is either lens cap (52 mm), person (1.74 m) or indicated. LDT; low density turbidite, MDT; medium density turbidite, Db; debrite (poorly sorted clast rich deposit); Tb; Turbidite, S; Siliciclastic, C; Calcareous. A) Calcareous mudstone B) Calcareous low density turbidite and mixed beds (of siliciclastic and calcareous low density turbidites). C) Two bi-partite beds consisting of a lower turbidite and an upper debrite, in this case both siliciclastic, overlain by two siliciclastic low density turbidites. D) Evidence for facies scale mixing (sensu Chiarella et al. 2017); calcareous turbidites were recognised in the field by their pale cream colour, while siliciclastic turbidites were brown-orange in colour and contained visual quartz granules. Calcareous turbidite probably accumulated slowly based on their grain size, and were punctuated by siliciclastic gravity flows, forming mixed beds. E) Siliciclastic low and medium density turbidites with cm-scale mud clasts weathered out. F) Mudstone and low density turbidites (both calcareous and siliciclastic) punctuated by metre-scale amalgamated conglomerates. G) Chaotic, clast rich-deposit with deformed, non-extensive bedding. Camera lens cap circled in green. H) Erosionally-based, crudely cross-laminated siliciclastic high density turbidite rich in mud clasts.

Thick-bedded sandstones are often normally-graded but can be non-graded or inversely-graded. Decimetre scale mud-clasts are common throughout thick-bedded sandstones and low angle cross-stratification is infrequently observed. Thin- to medium-bedded sandstones often have erosional bases and contain convolute, hummock-like and planar laminations and are normally-graded, with rare examples of inverse- or non- grading. These sandstones are either amalgamated or separated by 10 cm thick mudstone layers, and often contain mud-clasts throughout the bed with granules concentrated at the bed base. Sporadic debrites are also seen within FA 2; these have a deformed mudstone matrix and contain clasts of limestone and sandstone. Hybrid beds are amalgamated into 30-50 cm packages, with individual beds commonly consisting of a thin 2-4 cm fine-medium grained sandstone overlain by a clast and shelly fragment rich 8-12 cm muddy very fine sandstone debrite.

'Off-axis' successions have fewer thick-bedded sandstones and conglomerates than FA 2, but more than FA 3, and fewer thin-medium, thick-bedded sandstones than FA 3, but more than FA 2 (Fig. 6.9).

Interpretations: The thick-bedded nature, coarse grain size, amalgamation, erosion and entrainment of clasts within the sandstones suggests that the parent flows were highly energetic and capable of eroding and bypassing sediment (Mutti 1992; Stevenson et al.

2015) and are thus these beds are interpreted as high density turbidites (Lowe 1982). The poorly-sorted nature of the conglomerates suggests that they were initially deposited by laminar flows (Sohn 2000), however apparent grading of conglomerates into thick-bedded sandstones could reflect the transition of hyper-concentrated submarine debris flows into highly-concentrated turbulent flows (Mulder and Alexander, 2001) due to entrainment of ambient water (Postma et al. 1988; Kane et al. 2009).

The transition from conglomerates to medium-very coarse sandstone is associated with a grain size break, often missing the granule fraction, suggesting bypass of flow (Stevenson et al. 2015). The coarse-grain size and basal location of the conglomerates with respect to thick-bedded sandstones suggests these beds could have been deposited as channel-base lags (Hubbard et al. 2014). Erosionally-based lenticular sandstones grading from cobble- to fine-sandstones are interpreted to represent submarine channel fill (Jobe et al. 2017; Bell et al. 2018). This facies association is consistent with gravelly-conglomeratic deposits reported elsewhere to represent submarine channel axis deposition (Postma, 1984; Nemec & Steel 1984; Surlyk 1984; Dickie & Hein, 1995; Kane et al. 2009; Li et al. 2018; McArthur et al. 2019; Kneller et al. 2020).

While typically related to storm deposits (e.g. Hunter & Clifton, 1982), hummock-like cross-lamination have been interpreted in deep marine environments elsewhere as anti-dune stratification (Mulder et al. 2009), bottom current deposits (Basilici et al. 2012) and reworking of an initial deposit by a subsequent flow (Mutti 1992; Tinterri et al. 2017). The channel axis interpretation of FA 2 speculatively suggests anti-dunes formed by supercritical flows are the most probable interpretation of these hummock-like structures (Araya & Masuda, 2001; Alexander, 2008).

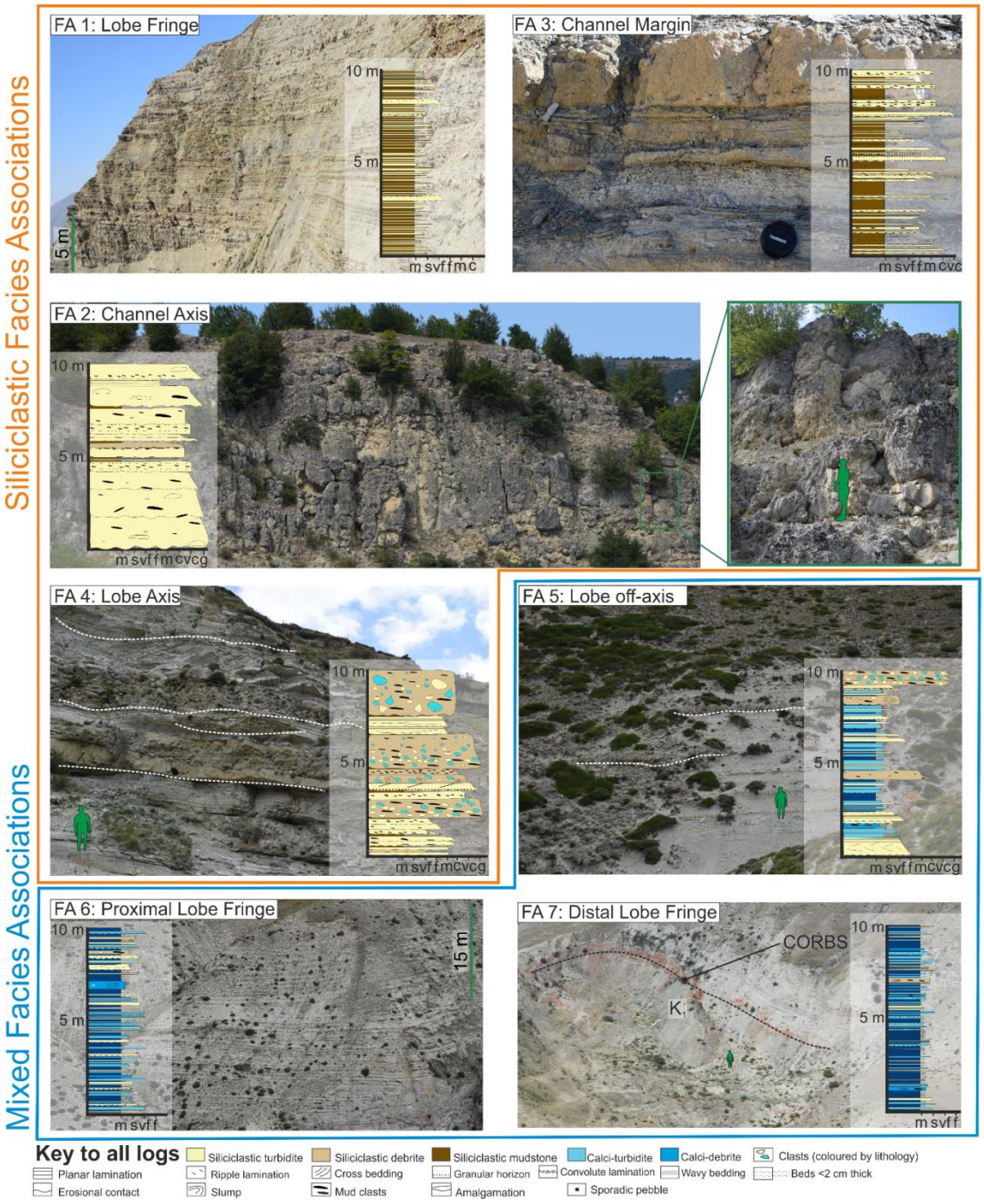

Figure 6.7: Type examples of the seven recognised facies associations, divided into siliciclastic and mixed (siliciclastic and calcareous) associations, by orange and blue boxes respectively. Scale either lens cap (52 mm), person (1.74 m) or indicated. 10 m type log is taken from representative logged section of each facies association. Cretaceous Oceanic Red Beds; CORBS.

FA 3: Channel Margin

Observations: FA 3 comprises thin-medium bedded fine-granular sandstones in 30-80 cm packages interbedded with 10-90 cm dark mudstones (Fig. 7C). Within the siliciclastic Cenomanian-Turonian succession FA 3 has the highest frequency of thin-medium bedded sandstones (Fig. 6.9). Conglomerates and thick-bedded sandstones are rare in FA 3 (Fig. 6.9). Thin-bedded sandstones and the upper part of medium-bedded sandstones can be argillaceous, with visible micaceous grains and are often planar, ripple and convolute laminated, with rarer hummock-like laminations. Sandstones are often normally-graded but inverse-grading is also observed. Beds of medium thickness are rich in mud-clasts and commonly amalgamated along mud-clast laden surfaces, bases can be highly erosive and scour-like, removing a significant proportion of the underlying bed. Thin-bedded sandstones can be flat or erosively-based, commonly scoured; where bases are erosional the lowermost part of the bed is commonly rich in granule-grade material (Fig. 6.7C). Granules and coarser fragments are composed of limestone and sandstone. Infrequent hybrid beds are composed of medium-coarse grained siliciclastic sandstone, overlain by a muddy, occasionally marly fine sandstone debrite.

Interpretations: The thin-bedded nature and presence of tractional structures indicate that this facies association was deposited by a low-density turbidity current (Lowe 1982). Presence of hummock-like laminations could indicate storm-wave influenced deposition (Harms et al. 1975), however their presence within a succession containing thick, dark mudstones and frequent sediment gravity flows suggests a deep-marine origin. Anti-dune formation (Mulder et al. 2009) and tractional reworking of an aggrading deposit (Mutti 1992; Tinterri et al. 2017; Bell et al. 2018) have both been interpreted to form similar hummock-like lamination in deep marine environments. Clean sandstones which grade into argillaceous, micaceous sandstones could indicate transitional flow deposits (Sylvester & Lowe 2004; Baas et al. 2009; Kane & Pontén 2012). The thin-bedded, coarse grain size and erosive nature of these deposits, along with the presence of supercritical bedforms, is similar to the overbank deposits seen adjacent to bypass-dominated channels (Kane & Hodgson 2011; Hubbard et al. 2014; Jobe et al. 2017; Lin et al. 2018; McArthur et al. 2019). These similarities, coupled with the along strike location of FA 3 adjacent to FA 2 (channel axis), has led to the interpretation of FA 3 as a channel overbank (Fig. 6.9). The lateral

transition of FA 2 and 3 is indicative of 'on-axis' to 'off-axis' channel-belt facies (Kane et al. 2009).

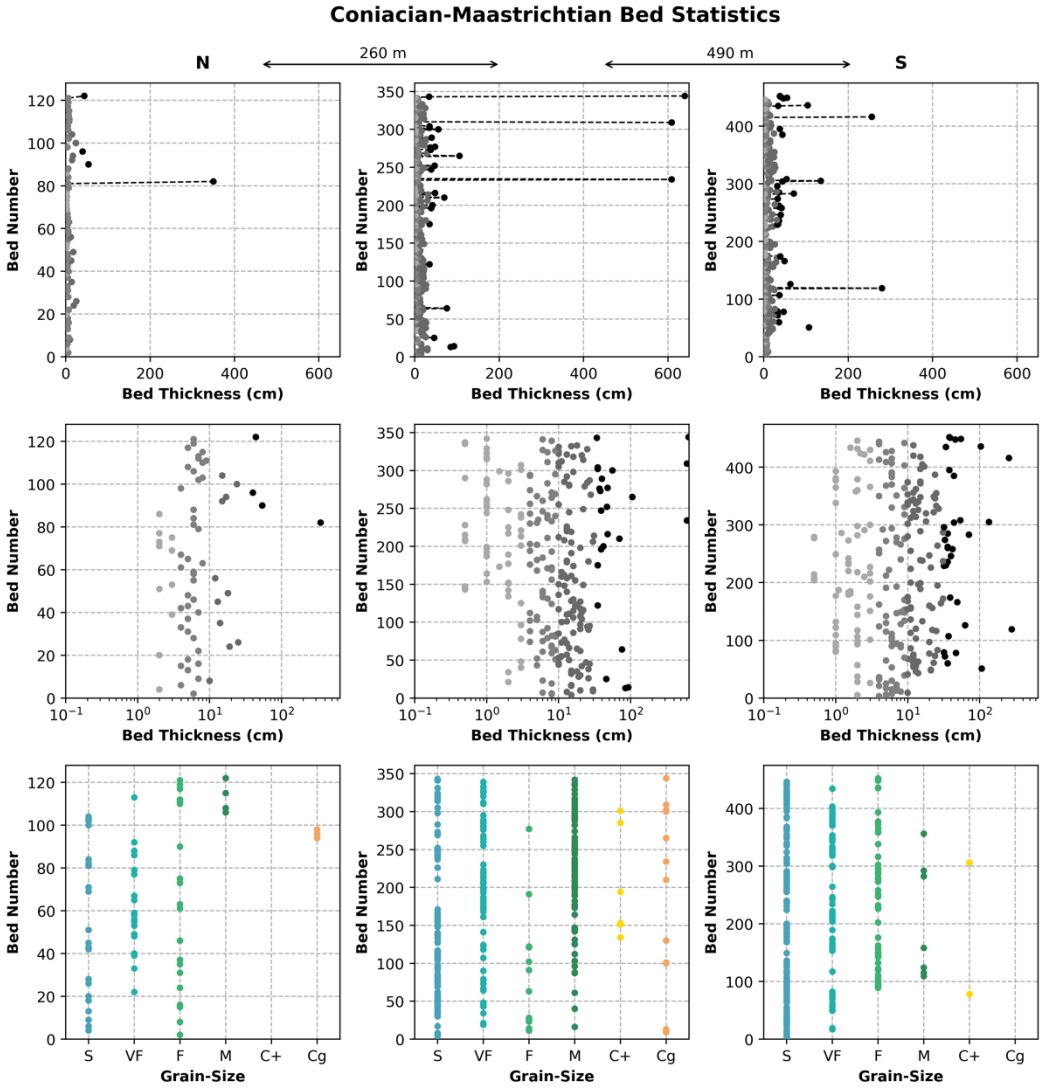

Figure 6.8: Quantitive facies analysis for Coniacian-Maastrichtian stratigraphy. The three columns represent three different logged sections from north to south that are representative of northern margin, axis and southern margin of the basin respectively. Charts compare bed number (with 1 being at the base of the log and 200 at the top) to bed thickness (linearly in the top column and logarithmically in the middle column) and logged grain size (in the basal column). Where grain size varies within the bed average grain size is used. In the top column thick beds are highlighted with a dashed line. Colours are for visual separation of data, and meaning changes per column, blue are thin/fine beds/grain-size, oranges are thick/coarse beds/grain-sizes. Scales for bed number vary across the rows.

FA 4: Lobe Axis

Observations: FA 4 is dominated by > 1 m thick packages of amalgamated conglomerates (Fig. 6.7D; 6.9) interbedded with thin-thick bedded very fine - very coarse sandstones. Within the Coniacian-Maastrichtian succession, the thickest conglomerates are found within FA4 (Fig. 6.8). The conglomerates are laterally discontinuous, erosionally-based, and are either flat-topped when onlapping, or convex-up when downlapping, the slope (Fig. 6.7; 6.12). Conglomerates increase in frequency, clast size (up to cobble-grade) and thickness, up stratigraphy (Fig. 6.8) and contain sub-angular to rounded clasts of limestone, sandstone and mudstone (Fig. 6.11). Within the Coniacian-Maastrichtian stratigraphy the greatest number of amalgamated beds is in FA4 (Fig. 6.10) and the largest grain size range (majority of beds between very-fine sandstone to medium grained sandstone) is observed (Fig. 6.8). Within FA 4, a coarser grain size class (of coarse grained sandstone or above) is observed which is almost absent in other Coniacian-Maastrichtian facies associations (FA 5, FA 6, FA 7) (Fig. 6.8).

Interpretations: Amalgamation of event beds suggests parent flows were energetic and capable of eroding sediment into the flow (Lowe 1982; Stevenson et al. 2015) and amalgamation of conglomerates indicates deposition in a debris-flow dominated environment (Surlyk 1984; Postma 1984; Dickie & Hein, 1995), similar to the debris flow dominated lobes described by McHargue et al. (2019). These conglomerates could also represent sediment bypass within lobe axes (e.g. Kane et al. 2009) or channel fill conglomerates (e.g. Knaust et al. 2014), however their thickness, stacking and geometry are most likely to represent deposition in the axis of a debris-flow dominated lobe.

Mixed Facies Associations

FA 5: Lobe Off-Axis

Observations: FA 5 is represented by erosively-based thin- to medium-bedded, fine-coarse grained siliciclastic sandstones and thin- to medium-bedded fine-grained calcareous siltstones, conglomerates and fine sandstones (Fig. 6.7E, Fig. 6.8). Sandstones with siliciclastic bases and calcareous tops are present throughout and are often amalgamated with siliciclastic and calcareous sandstones, forming packages separated by mudstones and silty-mudstones. Calcareous beds are typically flat-based when overlying mudstones, whilst siliciclastic beds are commonly erosive. Calcareous siltstones and

sandstones are massive, whilst siliciclastic sandstones show planar, convolute and ripple laminations, but can also be structureless. Debrites are interspersed, often incorporating thin-bedded calcareous siltstones and sandstones. Hybrid beds are rare (Fig. 6.9).

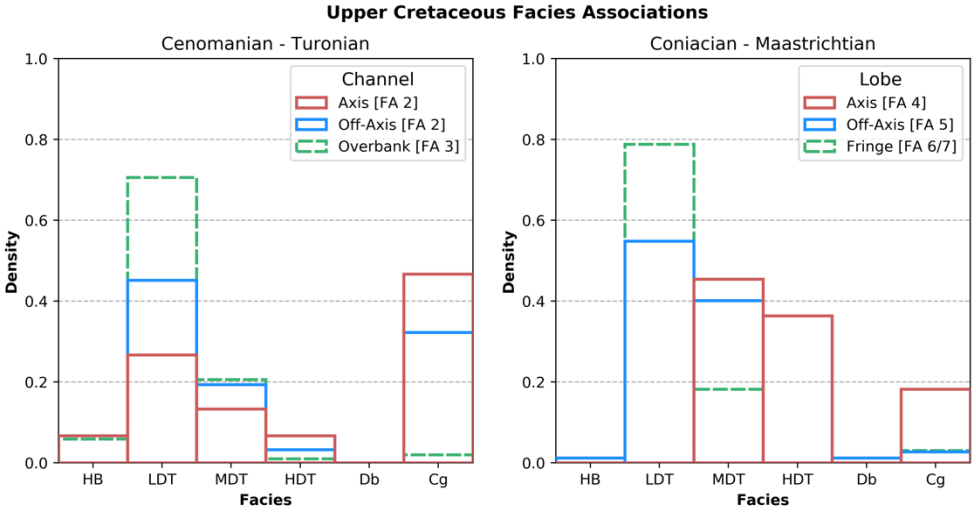

Figure 6.9: Quantitive facies analysis for Upper Cretaceous stratigraphy, divided into Cenomanian-Turonian channelised siliciclastic deposition and Coniacian – Maastrichtian mixed lobe deposition. Facies refer to HB: hybrid bed (bi and tri-partite beds); LDT: low density turbidite; MDT: medium density turbidite; HDT: high density turbidite; Db: debrite (poorly sorted clast rich deposit) and Cg: conglomerate. Coloured by type log for different sub-environment. Density is a probability density function.

Interpretations: The presence of both calcareous and siliciclastic sandstones suggests deposition in a mixed system (Fig. 6.1; 6.10) (Al-Mashaikie & Mohammed, 2017; Chiarella et al. 2017; Walker et al. 2019). Structureless medium-bedded calcareous siltstones and sandstones are interpreted to represent deposition from medium density turbidity currents (Kneller & Branney 1995; Talling et al. 2012; Soutter et al. 2019) aggrading quickly enough to prevent tractional sedimentary structure development in their basal divisions (Kneller & Branney 1995; Sumner et al. 2008). This depositional process is complicated within the calcareous medium-bedded deposits, which appear to have aggraded much more slowly than their siliciclastic counterparts, as evidenced by thin-bedded and medium-grained siliciclastic beds being deposited within medium-bedded and fine-grained calcareous beds. The presence of medium-density turbidites, relatively coarse grain size and common amalgamation suggests lobe off axis deposition (Prélat et al. 2009; Spychala et al. 2017).

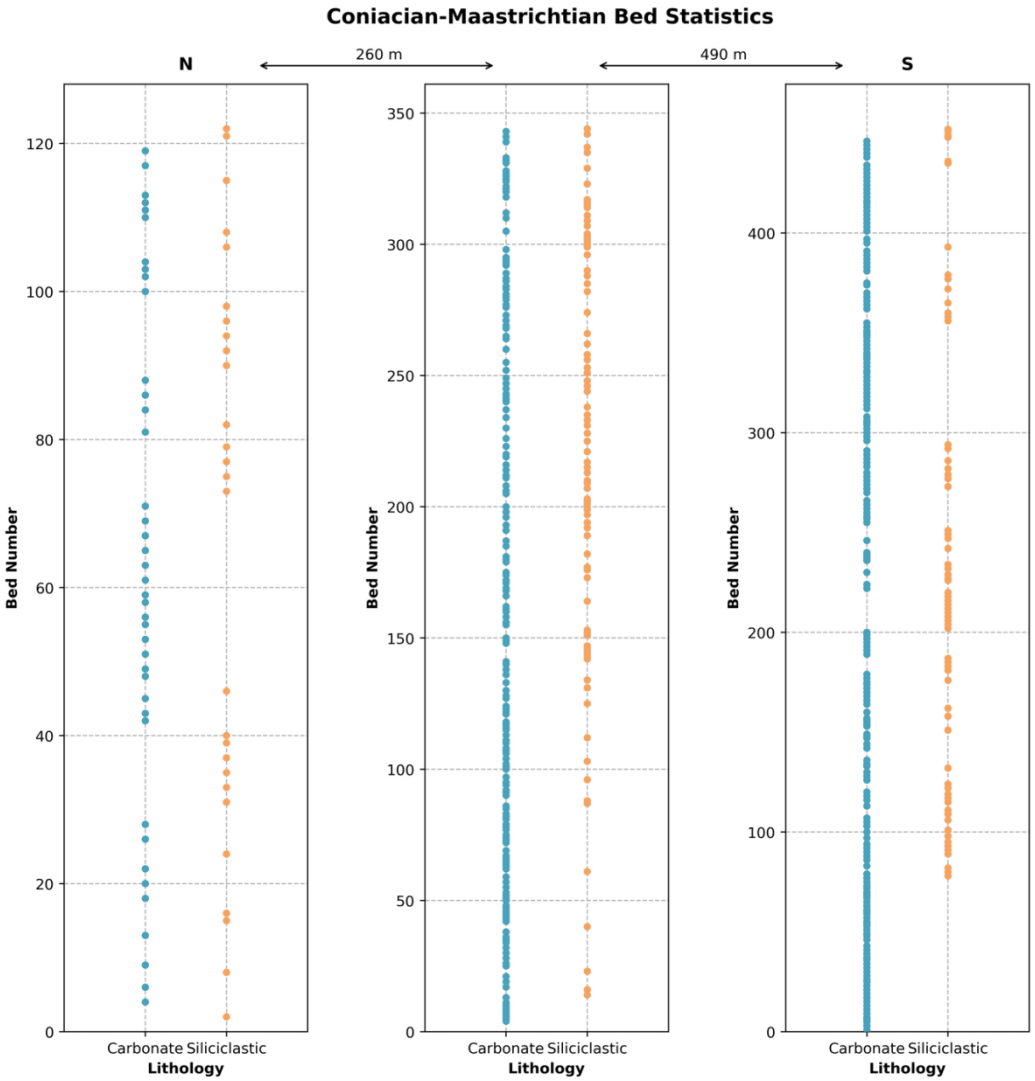

Figure 6.10: Quantitative analysis of Coniacian-Maastrichtian mixed stratigraphy comparing bed composition (carbonate or siliciclastic) against bed number. Using the same logged sections as Figure 8, and thus a different number of beds per log resulting in variable bed number scale.

FA 6: Proximal Fringe

Observations: Primarily composed of normally-graded, thin-medium bedded calcareous very-fine to fine-grained sandstones and siltstones, with subordinate thin-bedded siliciclastic fine-medium sandstones and mixed siliciclastic and calcareous sandstones (Fig. 6.7F; 6.8; 6.9). Calcareous siltstones and sandstones are flat based when overlying mudstones, but are often erosive at amalgamation surfaces (Fig. 6.10). Siliciclastic sandstones, either isolated or within mixed beds, are frequently < 3 cm thick, with flat to weakly erosive bases (Fig. 6.6). Debrites are interspersed within FA 6 and often rework the thin-bedded calcareous siltstones and sandstones. Planar laminations are common within the thin-bedded siliciclastic and calcareous sandstones. Less common

ripple laminations show multiple and opposing palaeocurrent orientations. Hybrid beds are rare (Fig. 6.9).

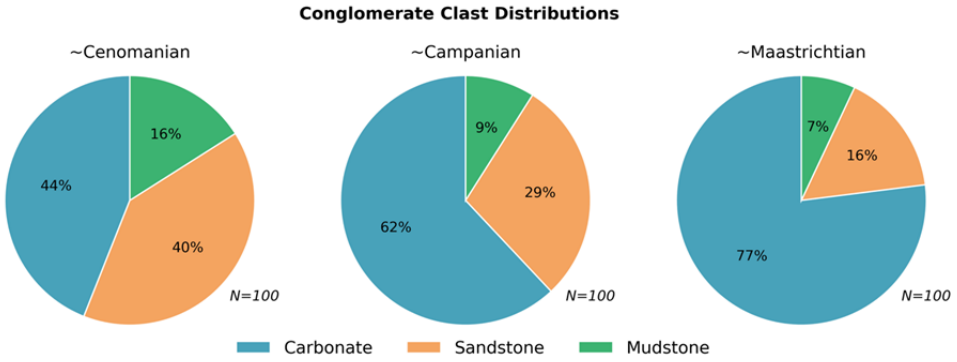

Figure 6.11: Pie charts showing composition of clasts within conglomerates per stratigraphic age, taken from 100 clasts from representative conglomeratic beds of over 1 metre thick. Percentage equates to absolute number of clasts, as 100 are sampled. Carbonate clast content increases through time, discussed in text.

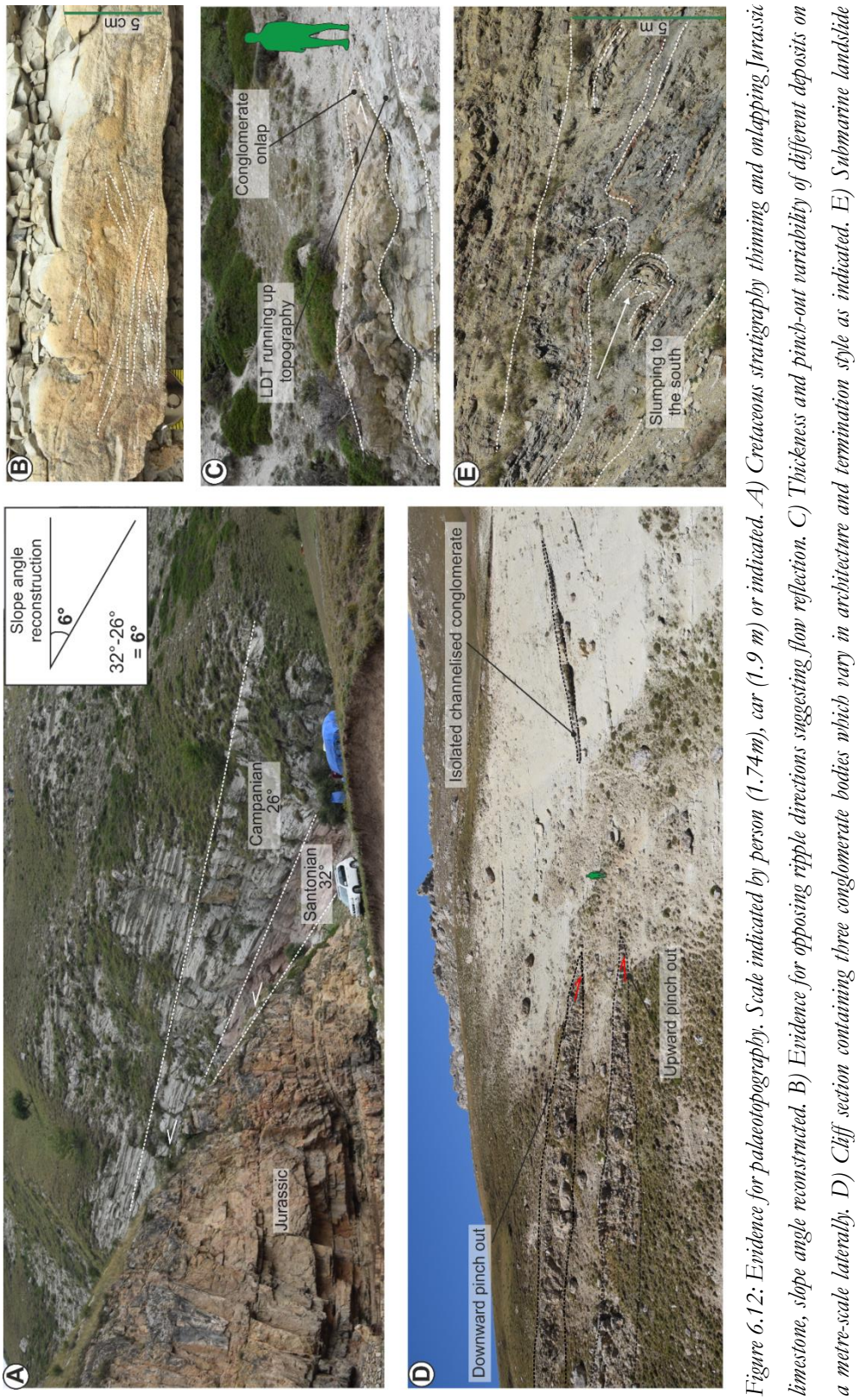

Figure 6.12: Evidence for palaeotopography. Scale indicated by person (1.74m), car (1.9 m) or indicated. A) Cretaceous stratigraphy thinning and onlapping Jurassic limestone, slope angle reconstructed. B) Evidence for opposing ripple directions suggesting flow reflection. C) Thickness and pinch-out variability of different deposits on a metre-scale laterally. D) Cliff section containing three conglomerate bodies which vary in architecture and termination style as indicated. E) Submarine landslide deposit showing evidence for slumping towards the south.

Interpretations: The presence of both calcareous and siliciclastic sandstones suggests deposition in a mixed system (Fig. 6.1; 6.10) (Al-Mashaikie & Mohammed, 2017; Chiarella et al. 2017; Walker et al. 2019). Calcareous sandstones are interpreted to represent

deposition from low- (Lowe 1982; Mutti 1992) to medium-density turbidity currents based on their bed thickness, fine grain size and structuration (Fig. 6.9) The thin-bedded siliciclastic sandstones could represent the depositional products of flow transformation from up-dip debris flows (i.e. the up-dip conglomerates) to turbulent flows following the entrainment of ambient water (Potsma 1988; Haughton et al. 2009), which punctuate slowly aggrading calcareous turbidites, interpreted to represent the remnants of dilute flows (Remacha & Fernández, 2003).

The preservation of both structured and structureless sandstones suggests an off-axis location of deposition; similar preservation of both deposit types has been interpreted in the proximal lobe fringe elsewhere (Prélat et al. 2009; Spychala et al. 2017; Soutter et al. 2019). FA 6 is differentiated from FA 5 based on its thinner beds and less frequent erosional events, and is therefore interpreted as being more distal and deposited within the proximal fringe. Hybrid beds are rare throughout the system therefore a distinction between frontal fringe and lateral fringe is difficult to decipher (e.g. Spychala et al. 2017).

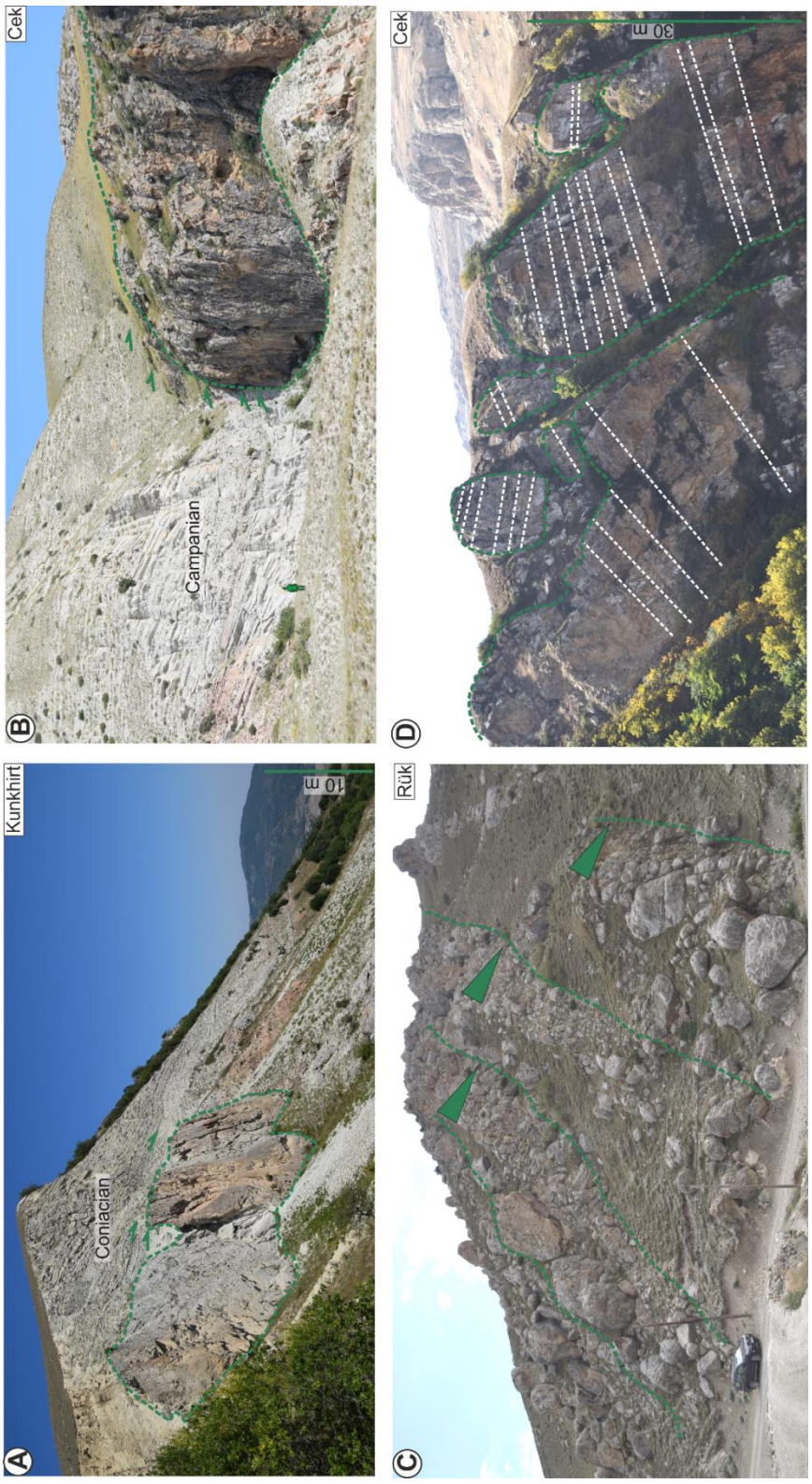

Figure 6.13: Evidence for collapse of the Jurassic carbonate platform. Scale is shown by person (1.74 m), car (1.9 m) or indicated. Onlap indicated by green arrows, extent of clast or bedding surface shown in green dashed line. A) Metre-scale limestone clasts within Coniacian mixed stratigraphy at Kunkhirt. B) Campanian calcareous low density turbidites abutting against a decametre-scale Jurassic limestone block at Cek. C) Stacked, inversely-graded submarine landslide deposits primarily composed of reworked Jurassic limestone blocks at Rük, upwards widening triangles indicate coarsening upwards (inverse-grading). D) In situ break-up of the Jurassic platform at Cek. Clasts are fractured and separated but bedding planes (indicated in white) are still visible showing minimal displacement.

FA 7: Distal Fringe

Observations: Dominated by laterally extensive, metre-scale packages of thin-bedded amalgamated calcareous sandstones which are normally-graded from very fine – fine sandstone to siltstone and are interbedded with metre-scale mudstones and silty-mudstones (Fig. 6.7G; 6.8; 6.9). Beds are flat-based, flat-topped and frequently contain both parallel and convolute laminations. Medium-bedded calcareous siltstones-fine sandstones are present, and may reflect amalgamated thinner-beds which are difficult to decipher. Debrites, siliciclastic thin-bedded sandstones and hybrid beds are rare (Fig. 6.9). The smallest grain size range (between siltstone and very-fine sandstone) is observed in FA6 and FA7 (Fig. 6.8) and amalgamation is infrequent (Fig. 6.10). More thin beds are seen in FA7 than elsewhere in stratigraphy (Fig. 6.7C; 6.8; 6.9).

Interpretations: Thin-bedded, structured sandstones are interpreted to be deposited from low-concentration turbidity currents (Mutti et al. 1992; Jobe et al. 2012; Talling et al. 2012). The presence of medium-bedded calcareous siltstones-fine sandstones and lack of ripple laminations suggest slow aggradation from a turbulent flow (Remacha & Fernández 2003; Bell et al. 2018). Lack of ripple lamination suggests flows did not reach significant velocity to generate ripple laminations (Baas et al. 2016), or turbulence was suppressed near the bed due to high aggradation rates. The infrequency of hybrid beds and siliciclastic beds within this facies association supports deposition within a carbonate dominated environment and the thin-bedded nature, lateral-extent, fine-grain size and lack of ripple-stratification suggests deposition in a distal lobe fringe (Mutti 1977; Prélat et al. 2009; Marini et al. 2015; Spychala et al, 2017).

6.7 ***Discussion***

Nature of the Upper Cretaceous Topography

Toward the west of the Qonaqkend Zone, Upper Cretaceous deep-marine sandstones and limestones can be seen to thin towards, and onlap, Upper Jurassic limestones (Fig. 6.12; 6.13; 6.14). These Upper Jurassic limestones must therefore have formed 100s of metres of relief on the Cretaceous seafloor. The most likely mechanism for the generation of seafloor topography is an allochtonous block (Fig. 6.13; 6.14; 6.15). The presence of decametre-scale allochtonous blocks (mega-clasts of Blair & McPherson 1999) and submarine landslide deposits throughout the Cretaceous stratigraphy indicates a highly

unstable margin, supporting this view (Fig. 6.13; 6.15). The identification of a basin-scale submarine landslide deposit, which forms the Qizilqaya and Shagdag mountains toward the west, further validates this interpretation (Bochud 2011) (Fig. 6.15) with the mega-clasts in the west possibly forming part of this deposit (Fig. 6.14; 6.15; 6.16). The contact is therefore formed as the Cretaceous stratigraphy infilled the accommodation present on the irregular surface of the deposit. Such relationships have been observed at outcrop (e.g.

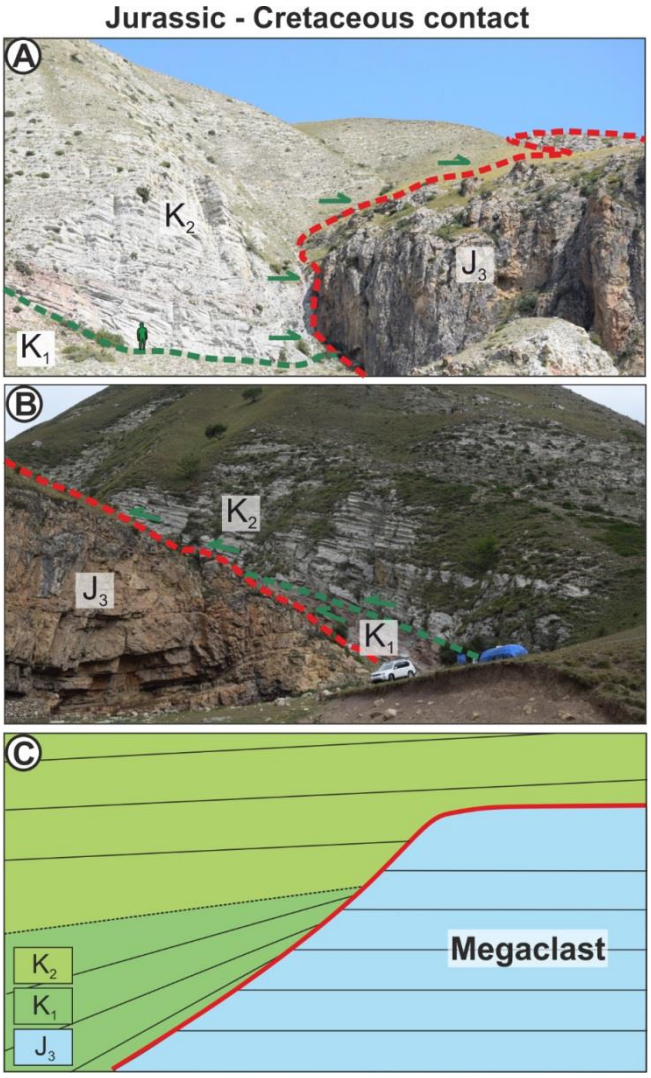

Figure 6.14: Evidence and model for the generation of topography by an allochtonous block throughout the Cretaceous. A&B) field examples of Jurassic stratigraphy forming topography throughout the Cretaceous influencing sediment routing. C) Schematic model showing formation of topography.

Burbank et al. 1992; Armitage et al. 2009, Kneller et al. 2018) and in the subsurface (Fig. 17) (e.g. Soutter et al. 2018, Casson et al. 2020). Differential compaction around these rigid blocks will have resulted in steepening of strata adjacent to the block, which may

contribute to the gradual steepening identified (Fig. 6.12; 6.14), which has been reported elsewhere (e.g. Burbank et al. 1992).

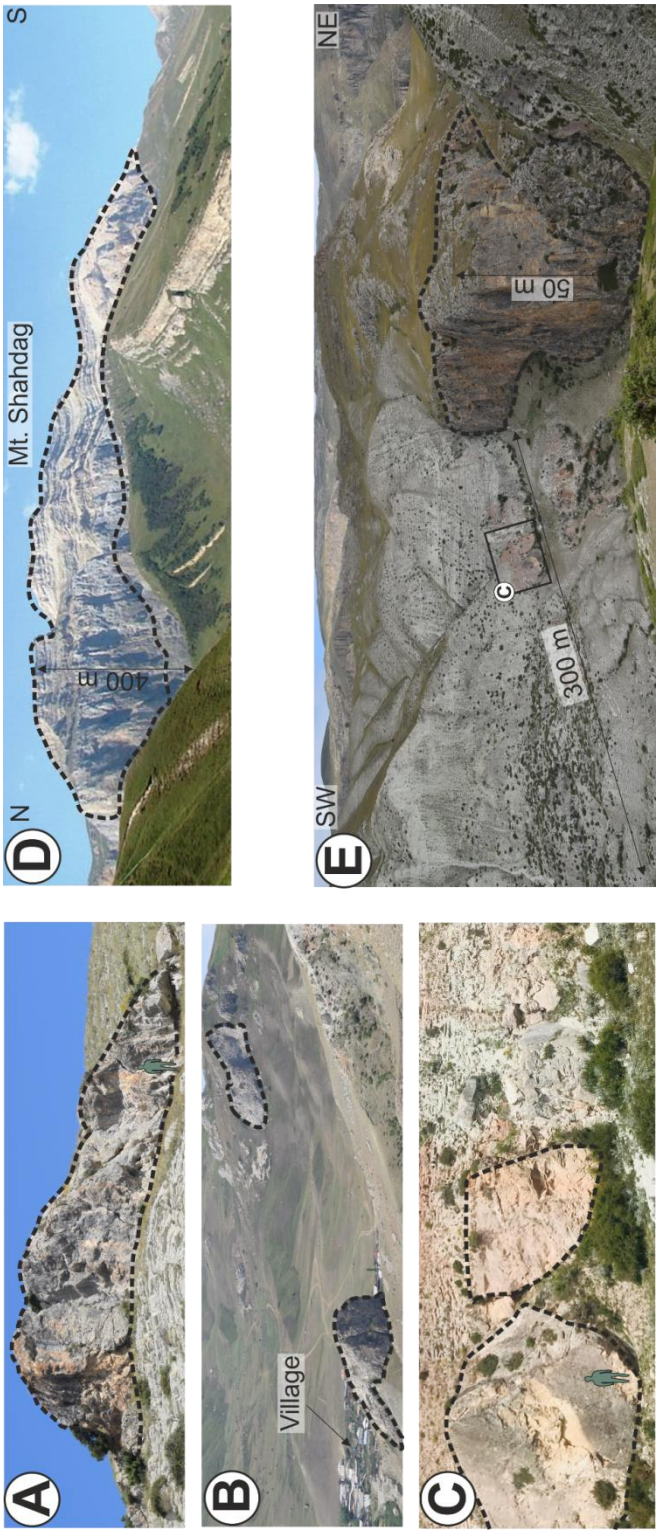

Figure 6.15: Evidence for allochtonous block model as the most likely for the generation of Cretaceous topography. Scale is shown by person (1.74 m) or indicated. Blocks are drawn around with black dashed line. A-C are examples of metre-decametre scale clasts around Cek. D) Shahdag Mountain, the tallest mountain in Azerbaijan, is interpreted as a kilometre-scale wide olistostrome by Bochud, 2011. E) Block with both margins exposed and onlapped by mixed stratigraphy, black box locates C.

Upper Cretaceous evolution of the Buduq Trough

Deep-marine deposition within the Buduq Trough began following a period of compression and folding in the mid-Cretaceous (Fig. 6.16) (Egan et al. 2009, Bochud 2011). Evidence of this compression is seen within the earliest fill in the Trough, which is preserved toward the east of the Qonaqkend structural zone. This early fill is represented by Cenomanian - Turonian conglomeratic slope channels that either erode into Barremian deep-marine mudstones or sit conformably on thin-bedded Aptian-Albian siliciclastic turbidites. These basal-Cenomanian stratigraphic relationships are suggested to be caused by channels preferentially infilling lows present on seafloor, forming entrenched channel axes that pinch-out laterally against Barremian mudstones (Fig. 6.16). These lows may have formed during mid-Cretaceous compression and folding (Egan et al. 2009; Sosson et al. 2016) or through submarine slope failure and consequent scour-formation.

It is possible that poorly preserved thin-bedded Aptian-Albian turbidites represent the distal extents of the Cenomanian slope channels that were either eroded by the channels during progradation or deposited within isolated lows on the Barremian slope. These lows may have formed in response to similar processes to those which entrenched the Cenomanian channels. The abrupt nature of the transition from distal fine-grained turbidite deposition to conglomeratic slope channels may correspond to either tectonic rejuvenation during the Mid-Cretaceous compressional event (Fig. 6.16) (Egan et al. 2009) and/or an abrupt relative sea-level fall, such as the eustatic sea-level fall seen in the mid-Cenomanian (Miller et al. 2003).

Evidence for basinal topography is present during deposition of the Cenomanian – Turonian, with the sequence almost entirely absent 10 km to the west at Cek, indicating the presence of a relative high in this location. Submarine landslide thicknesses also increase toward this high in the Barremian, suggesting the high influenced deposition from the Lower Cretaceous until the Turonian. Previous work has shown the presence of a large Lower Cretaceous submarine landslide toward the west (Fig. 6.16) (Bochud 2011), which is likely to form the high and the complex stratigraphic relationships described previously (Fig. 6.13; 6.14; 6.15). It is also likely that this submarine landslide, and other more minor ones in the area, were emplaced during an earlier period of tectonism and instability related to Lower Cretaceous compression (Fig. 6.16). Evidence for topography (Fig. 6.12) in the Late Cretaceous is also evident on a smaller scale through paleocurrent reversals in low-

density turbidites (e.g. Kneller et al. 1991) indicating a northward-dipping slope confining southward-directed flows (Fig. 6.5; 6.12), and through the deposition of Upper Jurassic blocks within the Turonian succession, indicating slope instability during this period (Fig. 6.13; 6.15).

Following the Cenomanian-Turonian regression the Trough begins to deepen again during the Coniacian-Maastrichtian (CM), as represented by the deposition of laterally-extensive, thin- to medium-bedded, mixed-siliciclastic-carbonate turbidites overlying the slope channels (Fig. 6.16). The mixed-lithology of the turbidites contrasts with the dominantly siliciclastic Aptian-Albian turbidites underlying the slope channels, indicating a change in source or paleogeography between the Lower and Upper Cretaceous (Fig. 6.5; 6.16). The presence of thinning and facies changes toward present-day syncline margins, frequent debrites and out-runner blocks, and divergent palaeocurrent distributions indicates that basinal topography had an impact on CM deposition (Fig. 6.5; 6.12; 6.13; 6.15). This topography may have been formed by differential compaction over the rigid limestone mega-clast, or external compression (Fig. 6.14; 6.15; 6.16). Erosional contacts are seen within the CM succession at the base of small, metre-scale channel fills, which occur with increasing frequency through time. These small channel fills are filled by conglomerates and high-density turbidites with similar compositions to the underlying and much more extensive slope channels. The channels are therefore interpreted as small distributary channels in the axes of lobes that formed at the distal ends of the underlying slope channels (e.g. Normark et al. 1979). The increasing frequency and thickness of these conglomerates through the CM (Fig. 6.8) may therefore represent gradual progradation of the slope channels following their abrupt backstep at the end of the Turonian. Clasts within these younger conglomerates are also more limestone-dominated, which fits with the transition to a more carbonate-dominated system through the Upper Cretaceous (Fig. 6.11; 6.16; 6.18).

Mixed-deep-marine deposition continues in the Buduq Trough throughout the remainder of the Cretaceous until Palaeogene compression ceases deposition (Bochud 2011), forming an unconformity between the Upper Cretaceous and overlying Palaeogene and Neogene sediments (Fig. 6.2; 6.3).

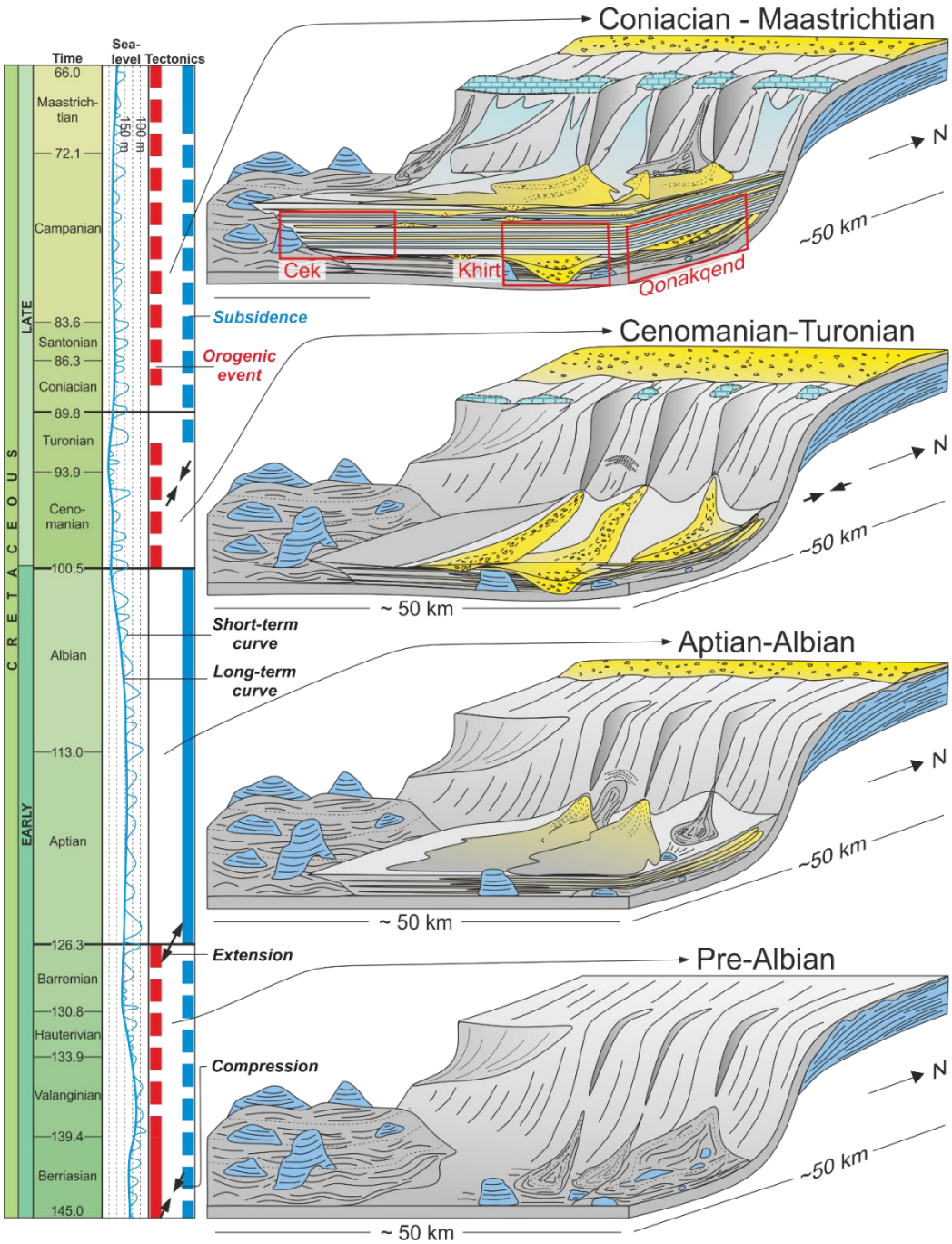

Figure 6.16: Evolutionary model for the Cretaceous of the study area. Studied stratigraphic sections highlighted. Topography, thought to be formed by a mega-clast, is present throughout the Cretaceous and influences deposition, discussed in text. Extract from the geological time column, sea level fluctuations and local tectonic events highlighted on the left. The Pre-Albian was dominated by limestone blocks on a muddy slope. Thin-bedded siliciclastics of a distal lobe were deposited during the Aptian-Albian. Siliciclastic channels are prominent throughout the Cenomanian-Turonian. In the Coniacian-Maastrichtian mixed calcareous and siliciclastic lobes, of different sub-environments interact, and are likely sourced from the same northern margin.

6.8 ***A Subsurface Analogue for the Buduq Trough***

A seismic-scale equivalent of a mixed-system analogous to the Cretaceous Buduq Trough has been identified and is used as a comparison to the outcrop-based model. The continental margin offshore The Gambia, NW Africa, developed through the Late Cretaceous with remarkable similarities in timing and evolution to the Buduq Trough (summarised in Casson et al. 2020 in press; Fig. 6.17). Unconfined mixed-systems developed on the deep-marine basin floor are interpreted to have been line-fed through a heavily canyonised unconformity surface (Fig. 17C). Seismic geomorphology reveals the interfingering of siliciclastic-dominated and carbonate-dominated systems (i.e. at X and Y Fig. 6.19), similar to that observed on facies and facies architecture scale in the EGC (e.g. Fig. 6.6; 6.7).

Sediment gravity flows through the canyons eroded into the underlying carbonate platform redepositing hundreds of metre-scale, seismically-resolvable carbonate mega-clasts 20+ km from the escarpment (Fig. 6.17B, D); our field work suggests that these blocks may be associated with a multitude of different types and sizes of submarine landslides and blocks that are below seismic scale (Fig. 6.13; 6.15). The presence of carbonate blocks and lobe-architecture in the carbonate-dominated systems (*sensu* McHargue et al. 2019) suggests deposition by debris-flows (i.e. FA 4). Hence two stages of mixing occurs, firstly during erosion to form mixed lithology flows, and then through deposition of interfingering systems. Pervasively channelised siliciclastic-systems with single feeder channels show a distinct seismic geomorphological response to their carbonate counterparts (Fig. 17D, E). The lateral location along the margin of siliciclastic-dominated systems is conceivably related to sediment input points (i.e. shelf-incising canyons) capturing an extra-basinal source of siliciclastic sediment from the shallow marine environment, away from shelfal carbonate factories. Basin floor topography is created by early deposits and influences subsequent lobe deposition (Fig. 17), causing stacking and lateral migration of lobes, which cannot be resolved in the Buduq Trough (Fig. 18) probably because the scale of the study area is smaller than the scale at which migration occurred.

Documentation of ancient subsurface mixed-systems has been achieved from the interpretation of seismic reflection data (e.g. Moscardelli et al. 2019, Casson et al. 2020). It may also be possible that transitions from calcareous-dominated to siliciclastic-dominated deep-marine systems, which are commonly associated with the rapid arrival (progradation)

of the siliciclastic system (e.g. Scott et al. 2010; Kilhams et al. 2012; 2015; Soutter et al. 2019; Cumberpatch et al. in prep.), may have been overlooked as 'transition zones', and in fact represent short-lived mixed systems, which are often below the scale of seismic resolution. The role of mixed-system interactions on a petrographic scale, and therefore their reservoir quality, remains unclear until such systems are further studied at outcrop or sampled in the subsurface (Chiarella et al. 2017; Bell et al. 2018; Moscardelli et al. 2019).

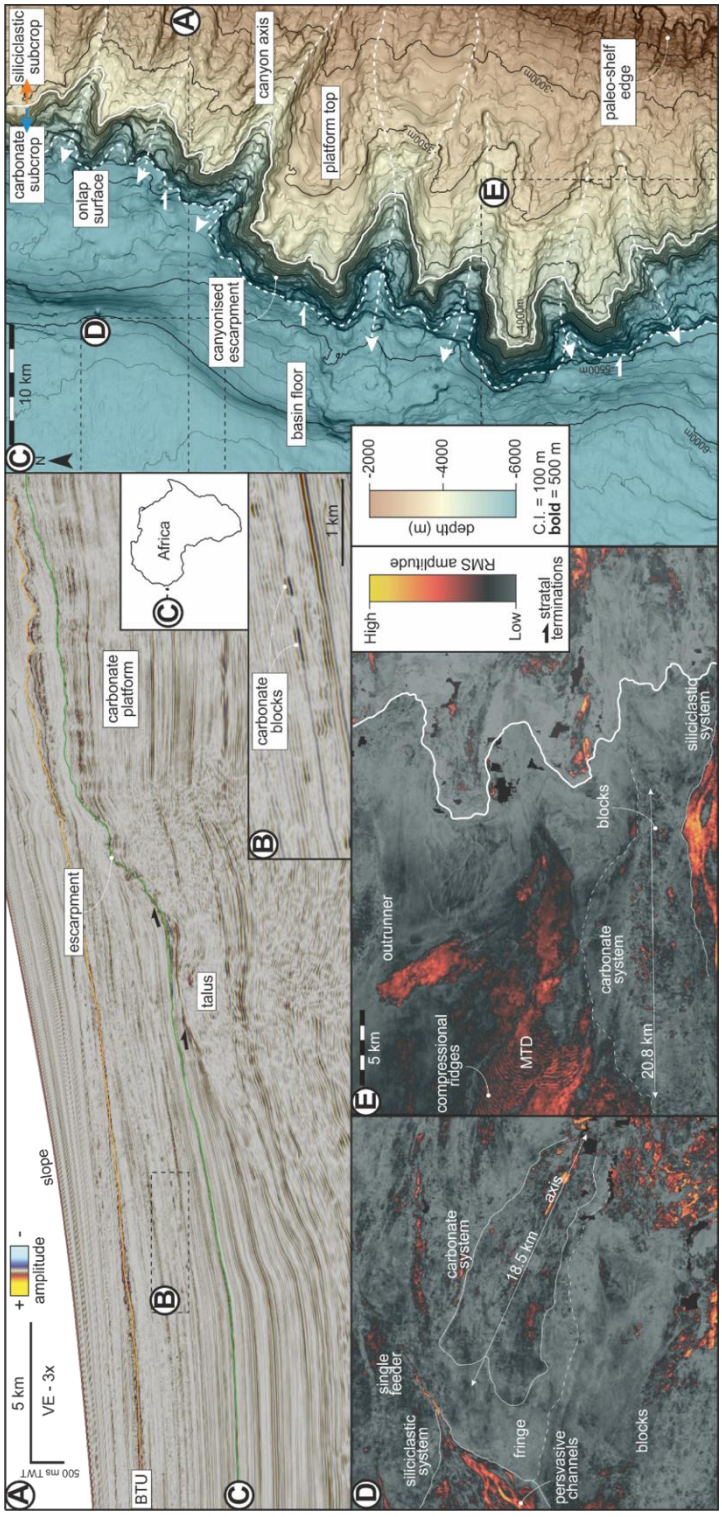

Figure 6.17: Seismic geomorphology of a mixed-system offshore The Gambia, NW Africa. A) East-West two-way time seismic section with key stratigraphic surfaces, location shown in C. B) Enlarged two-way time seismic section of carbonate blocks observed in the deep-marine mixed-system. C) Depth structure map (contoured) with dip magnitude below of the diachronous regional composite unconformity surface displayed on seismic section A, showing the heavily canyonised carbonate escarpment margin, canyon flow pathways (dashed white lines), lithological contact between siliciclastic and carbonate subcrop (solid white line) and onlap surface (dotted white line). D & E) RMS amplitude maps extracted from a +/- 12 ms window around two Late Cretaceous horizons in the basin. Location of maps shown on C.

Mixed lobes

Lobe sub-environments: If individually observed, the siliciclastic system within this mixed succession could be interpreted as stacked lobes, with axial, off-axial and fringe sub-environments identified. The calcareous system, however, would be interpreted as being predominantly lobe fringe deposition (Remacha & Fernández 2003; Bell et al. 2018). Since the two systems are mixed it is difficult to assign a single lobe sub-environment to a sequence of beds as they represent the inter-fingering of two systems (Fig. 6.19). Due to the interaction of these systems, siliciclastic lobe elements are likely to occur within calcareous lobe elements (Fig. 6.1; 6.17; 6.19) (Prélat et al. 2009), forming stacks of mixed event beds (D, Table 1). This is further complicated by often highly erosive siliciclastic turbidity currents which can rework calcareous beds, as evidenced by calcareous rip-up clasts within siliciclastic turbidites. This may remove individual calcareous lobe elements from the rock record, and make stacking interpretations more difficult (Fig. 6.18) (Braga et al. 2001).

Due to these complexities it is perhaps necessary to refer to such systems with a more specific descriptor (e.g. mixed axis-fringe), or broadly refer to them as 'mixed systems' in order to allude to their complexity and contrast them from siliciclastic-dominated systems (Fig. 6.19). Use of the siliciclastic lobe hierarchy of Prélat et al. (2009) is possible in mixed systems, but calcareous and siliciclastic descriptors are required (Fig. 6.19). It is possible to decipher the different systems in our field and subsurface examples, due to their lithological differences being visually resolvable at outcrop (Fig. 6.6; 6.7) and showing different seismic characteristics in the subsurface (Fig. 6.17; 6.19). However, without detailed provenance and geochemical analysis it would be very difficult to decipher the mixing of two siliciclastic systems or two calcareous systems, due to similarity in depositional facies and thus seismic character. Unless an individual system can be followed from source to sink in outcrop or the subsurface we must always consider the possibility of multiple systems interacting, modulating each other and complicating stacking patterns (Fig. 6.19).

Stacking patterns*:* Deep-marine stacking motifs can show either aggradational, progradational, retrogradational or unorganized stacking patterns (Stow & Mayall, 2000;

Deptuck et al. 2007; Straub et al. 2009; Prélat & Hodgson 2013), which can be modulated by both external and internal processes (e.g. Ferguson et al. 2020). Our study shows that in mixed systems it can be difficult to decipher stacking patterns within each individual system due to the convolution of each system by the other (Fig. 6.18; 6.19). Bed thickness trends within the calcareous turbidites are difficult to decipher, possibly due to their narrow grain size range preventing the identification of thinner-beds, and amalgamation within thicker beds (Fig. 6.18).

Siliciclastic conglomerates become more frequent and thicker throughout the Coniacian-Maastrichtian, perhaps reflecting a progradation of the siliciclastic system (Fig. 8; 6.16). However, bed thickness and grain size analysis for the Coniacian-Maastrichtian do not show any thickness trends or stacking patterns within the calcareous or siliciclastic turbidites (Fig. 6.18). This suggests that in mixed systems it may therefore not be possible to describe the progradation or retrogradation of an individual system, and only possible to describe the relative ratio between the two; the apparent dominance of the mixed system (e.g. if siliciclastic (s) > carbonate (c) this could be due to progradation of s or by the retrogradation of c, both of which are controlled by a number of external and internal forcings).

On the scale of the outcrops (100s m), the calcareous turbidites appear to be sheet-like, while the siliciclastic turbidites show thickness variation, representing more typical channel and lobe geometries (e.g. Prélat et al. 2009). Conglomerates observed in the FA4 appear to be confined to isolated depocentres and pinch-out across meters - 10s of meters, indicating the presence of subtle topography (Fig. 6.12). This suggests the deposition of the conglomerates may have been controlled by depositional topography (compensational stacking) and that the underlying calcareous turbidites do exhibit subtle, long-wavelength thickness changes over a greater scale than observed at outcrop, influencing subsequent sediment routing. Alternatively, the thinning of conglomerates was due to the basinal topography present at this time, preventing these highly-concentrated flows running-out over great distances (Fig. 6.12).

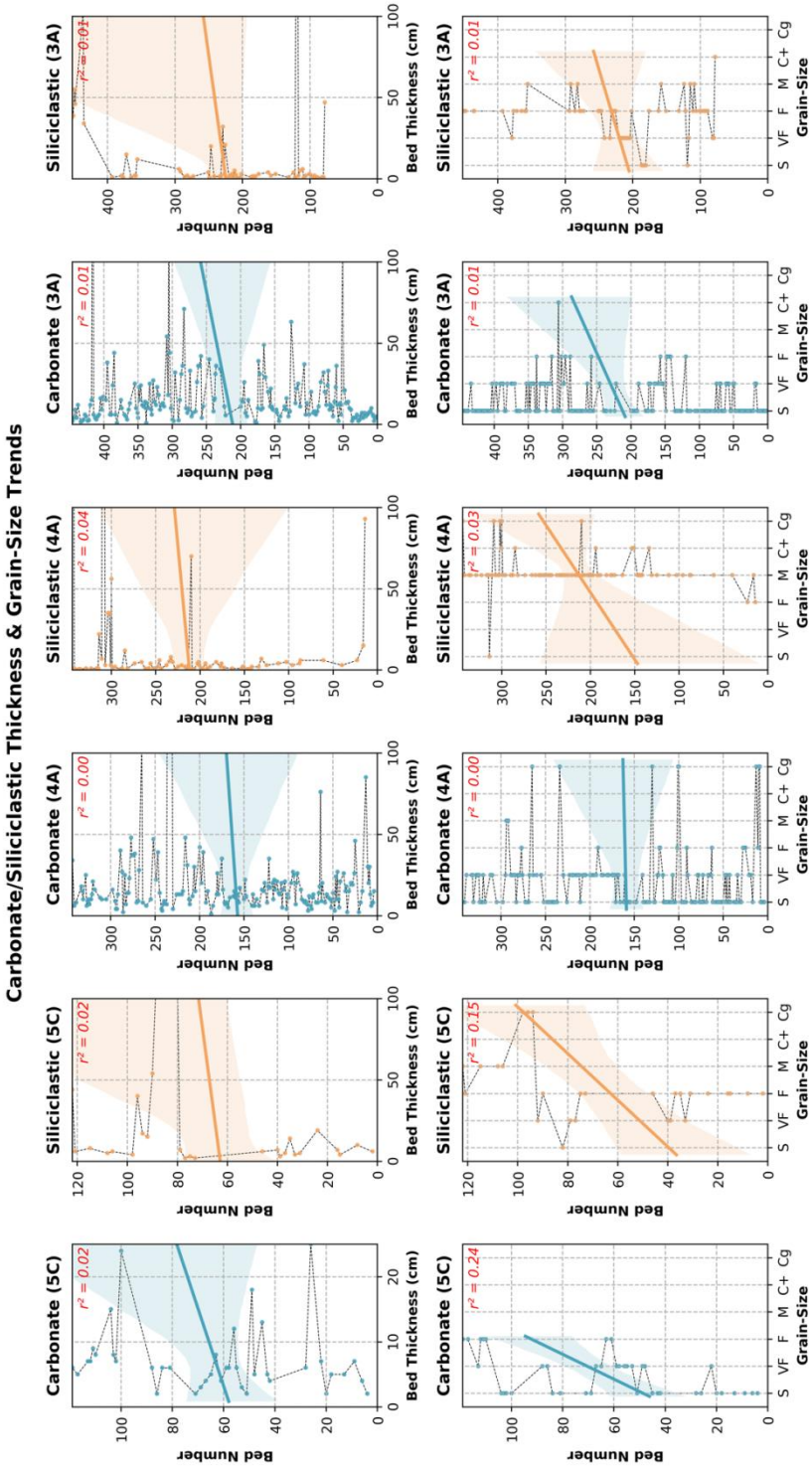

Figure 6.18: Quantitative facies analysis for Coniacian-Maastrichtian stratigraphy around Cek. Logs are the same as Figures 8 and 10. 5C, 4A and 3A represent northern margin, axis and southern margin respectively. Each log is divided into carbonate and siliciclastic beds, and bed number is plotted against bed thickness (upper row) and grain size (bottom row). Lines indicate linear regression, r^2 value is labelled in red, shading either side of the line indicates a 95% confidence interval for the linear regression (trend line). Low-no correlation is observed suggesting no stacking patterns or modulation of any stacking patterns by interaction of both systems, discussed in text.

Mixed-system origin: Previous work on mixed systems has correlated alternations in calcareous and siliciclastic turbidites to 3rd order sea level cycles (Yose & Heller, 1989; Miller & Heller, 1994); the alternations in the Buduq Trough are lower frequency than these cycles but could be interpreted as fifth-sixth order sea level cycles (parasequences) occurring on a 10,000 – 100,000 year cycle (Fig. 6.16) (Van Wagoner et al. 1990), related to Milankovitch orbital cycling (Goldhammer et al. 1990; D'Argenio et al. 1999). Elsewhere mixed systems have been interpreted to represent alternating cool-wet and cold-dry climate cycles driven by precession orbital cycles (García-García et al. 2009). No obvious stacking can be deduced in the study area (Fig. 6.18) preventing a confident interpretation to be made regarding the forcings behind the high-frequency lithological variations.

Rugose carbonate platform margins (e.g. Saller et al. 1989; Grant et al. 2019, Casson et al. 2020), like those observed in the Buduq Trough (Fig. 6.13; 6.16; 6.17), have been proposed as conduits for siliciclastics without requiring a sea level change (Francis et al. 2008; Braga et al. 2008; Puga-Bernabéu et al. 2014; Al-Mashaikie & Mohammed, 2017; Walker et al. 2019). This could indicate that the calcareous deep-marine system in the Buduq Trough is part of a much more extensive and line-fed system derived from shedding of active carbonate factories perched on the shelf (e.g. Fig. 6.17). The contemporaneous siliciclastic system may therefore have been derived from multiple point source conduits along this margin that either 1) periodically punctuated this larger carbonate system or 2) were long-lived conduits permanently bound by carbonate factories (Fig. 6.16) (Mueller et al. 2017; Moscardelli et al. 2019). Two different sources for separate components of a mixed system have been documented elsewhere (Fig. 6.1; 6.17; 6.19A) (Ditty et al. 1997; Riaz Ahmad & Jamil Afzal, 2012; Poprawski et al. 2014; 2016; Chiarella et al. 2017). The presence of Late Jurassic blocks (Fig. 6.13; 6.15) within the Cretaceous complicates this model, with the blocks interpreted as either 1) Late Cretaceous failures from an exposed Jurassic shelf, 2) out-running blocks from Lower Cretaceous failures (e.g. De Blasio et al. 2006) that were subsequently deposited around during the Late Cretaceous, or 3) blocks that were periodically shed through the Late Cretaceous from high-relief Lower Cretaceous slope submarine landslides identified in the west (Fig. 6.14; 6.16).

Palaeoflow indicators are limited for the calcareous system due to lack of ripple lamination developed in its fine-grained, slowly accumulating deposits (Baas et al. 2015). It is therefore difficult to decipher whether these siliciclastic and calcareous systems were

perpendicular, oblique or parallel to each-other. The palaeoflow indicators that were collected, however, are consistent with a provenance to the north (Fig. 6.5; 6.12; 6.15) A northern provenance is also suggested from palaeographic maps for the interval, suggesting a Scythian platform source area (Nikishin et al. 1998).

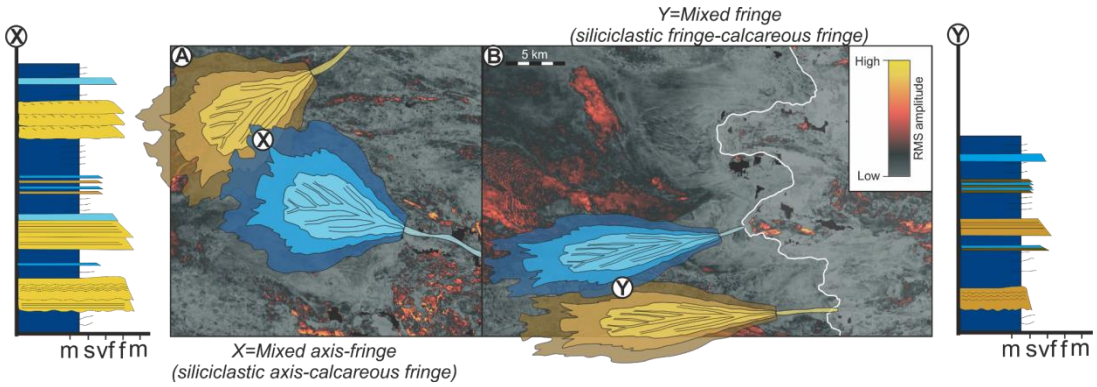

Figure 6.19: Schematic showing potential interactions of calcareous and siliciclastic lobes in mixed systems. A and B are RMS maps from Figure 17, which have been overlain by lobe complex geometries, as an interpretation based on seismic facies analysis and understanding of regional source area (see Casson et al. 2020). X and Y represent log/core through locations where the lobe complexes interact in A and B respectively. X crosses the lobe fringe of the calcareous system and the lobe axis of the siliciclastic system and Y crosses the lobe fringe of both systems resulting in a thinner and finer grained succession when compared to X. This variability highlights difficulties arising from exporting sub-environment terminology developed in siliciclastic systems (e.g. Prélat et al. 2009) into mixed systems

6.9 ***Conclusion***

This study uses the Upper Cretaceous Buduq Trough, Azerbaijan to document the characteristics of an unstable and mixed siliciclastic-carbonate system. Deposition in the Trough is represented by a Cenomanian-Turonian submarine channel complex, which transitions into a Coniacian-Maastrichtian mixed lobe succession. This sequence represents an abrupt Cenomanian regression, probably related to a mid-Cretaceous compressional event and/or an abrupt mid-Cenomanian eustatic sea level fall; followed by a relatively abrupt late Turonian-Coniacian transgression, likely associated with subsidence caused by back-arc extension. Throughout the remainder of the Cretaceous, the mixed-system exhibits weak progradation. A westerly topographic high formed by a Lower Cretaceous submarine landslide complex deposited during earlier compression is interpreted to have prevented deposition of the Cenomanian–Turonian toward the west. This submarine landslide complex may also have provided a lateral source for landslides through secondary

remobilisation perpendicular to the regional palaeflow from the north. Bed pinch-out, thinning, ripple reflections and debrites provide further evidence for the presence of basinal topography during deposition.

The Coniacian-Maastrichtian mixed siliciclastic-calcareous deep marine system contains both siliciclastic and calcareous lobe elements, which represent different lobe sub-environments, requiring modification of terminology developed for siliciclastic lobes. Mixed systems are also shown to have unique facies, both in outcrop and a subsurface analogue from offshore The Gambia, reflecting differing depositional processes between the systems operating contemporaneously. Interaction between the two deep-marine environments characterising the mixed systems has also made stacking patterns difficult to decipher, with each system attenuating the other.

CHAPTER 7: The effect of variable topography on turbidity currents: physical models and geological implications

Euan L. Soutter[1], Daniel Bell[1], Zoë A. Cumberpatch[1], Ross A. Ferguson[1], Yvonne Spychala[2], Ian A. Kane[1], and Joris T. Eggenhuisen[2]

[1]Department of Earth and Environmental Sciences, University of Manchester, Oxford Road, Manchester, M13 9PL, UK

[2]EuroSEDS, Department of Earth Sciences, Utrecht University, Utrecht, 3584 CB, NL

7.1 *Abstract*

The stratigraphic expression of deep-water systems records tectonic or climatic signals from the hinterland, as well as the structural evolution of the basin in which they occur. This expression may be modulated by basin and slope topography, which in deep-marine basins affects turbidity currents and the deposits they generate at the sub-flow to basin scale. Here, Shields-scaled physical models of turbidity currents are used to better understand the processes that govern the architecture of submarine lobe deposits influence by basin topography. The subaqueous topography consists of an erodible barrier orientated 1) parallel, 2) oblique and 3) perpendicular to the incoming flow. An unconfined control run generated a supercritical turbidity current that decelerated across the slope, forming a deposit that thickened basinwards before abruptly thinning. Flow-parallel confinement resulted in erosion of the barrier by the bypassing flow, enhanced axial velocities, and generated a deposit that extended 10% farther into the basin than when unconfined. Oblique confinement caused partial deflection and acceleration of the flow along the barrier, which resulted in a deposit that bifurcated upstream and downstream of the barrier. Forced deceleration at the barrier resulted in thickened deposition on the slope. Frontal confinement resulted in onlap and lateral spreading at the barrier, along with erosion of the barrier and down-dip overspill that formed a deposit deeper in the basin. Acceleration down the back of the barrier by this overspill resulted in the generation of a plunge-pool at the foot of the barrier as the flow impacted the slope substrate. Observations from ancient and modern turbidity current systems can be explained by our physical models, such as: the deposition of thick sandstones upstream of topography, the deposition of thin sandstones high on confining slopes, and the complex variety of potential stacking patterns produced by confinement.

7.2 *Introduction*

Turbidity currents are the primary mechanism by which sediment is transported from shallow to deep water (e.g. Kuenen and Migliorini, 1950), where they build the largest sediment accumulations on Earth (e.g. Curray and Moore, 1971; Ingersoll et al. 2003). Turbidity currents are strongly affected by subaqueous topography (e.g. Ericson et al. 1952; Gorsline and Emery, 1959; van Andel and Komar, 1969) that can be formed by a many processes, such as: compressional folding (e.g. Lucente et al. 2004; Morley and Leong, 2008), extensional faulting (e.g Cullen et al. 2019), contourite drifts (e.g. Fonnesu et al. 2020), or salt diapirism (e.g. Doughty-Jones et al. 2017). Understanding the effects this topography exerts on turbidity currents is crucial for the prediction of turbidity current pathways and deposit character (e.g. Kneller and Buckee, 2000). This has implications for reconstructing ancient sediment routing systems (e.g. Sinclair, 1994; Lomas and Joseph, 2004; Smith, 2004; Bell et al. 2018a; Dodd et al. 2019; Soutter et al. 2019), de-risking subsurface infrastructure placement (e.g. Bruschi et al. 2006; Carter et al. 2014), predicting hydrocarbon or CO2 reservoir quality (e.g. McCaffrey and Kneller, 2001), and for improved understanding of fluid mechanics (e.g. Mulder and Alexander, 2001; Meiburg and Kneller, 2010).

The effect of confining topography orientation has been shown to be influential in the stratigraphic record of turbidity currents, with both centimetre-scale sedimentary structures and kilometre-scale depositional patterns differentially affected (e.g. Sinclair, 1994; Hansen et al. 2019). Lateral confinement, for example, has been used to explain lobe thinning trends (Amy et al. 2004) and stacking patterns (Spychala et al. 2017), oblique confinement has been suggested to cause deflection (Kneller et al, 1991; Haughton, 1994) and acceleration (Jobe et al. 2017) of incoming flows, and frontal confinement has been postulated as the reason for thick deep-marine sandstones deposited up-stream of the confinement (e.g. Bersezio et al, 2005; Stevenson and Peakall, 2010).

Natural turbidity currents are notoriously difficult to observe, with only a few studies collecting direct measurements of their behaviour (e.g. Talling et al. 2013; Clarke, 2016; Azpiroz-Zabala et al. 2017; Symons et al. 2017; Paull et al. 2018). The characteristics of turbidity currents are therefore often inferred from scaled-down physical model analogues (e.g. de Leeuw et al. 2016; Pohl et al. 2019ab) that permit systematical variation of individual parameters and analysis of their effects. The effect of subaqueous topography

on experimental turbidity currents has been studied previously (e.g. Edwards et al. 1994; Alexander and Morris 1994; Kneller, 1995; Kneller and McCaffrey, 1995; Brunt et al. 2004; Bursik and Woods, 2000; Al Ja'aidi et al. 2004; Amy et al. 2004; Kubo, 2004; Stevenson and Peakall, 2010; Oshaghi et al. 2013; Abhari et al., 2018; Farizan et al., 2019). However, almost all of these studies are performed either within narrow flumes, with non-erodable substrate, or using homogenous or synthetic sediment. While these studies are very insightful regarding interaction between turbidity currents and topography, they therefore only representative patterns of erosion and deposition at their particular bounding conditions.

Supercritical turbidity currents and their deposits are becoming increasingly recognised as influential components of modern and ancient deep-water systems (e.g. Postma and Cartigny, 2014). Deposition from supercritical flows can be driven by their transition to a subcritical regime via a hydraulic jump (e.g. Komar, 1971). Hydraulic jumps are most commonly associated with channelised flows (e.g. Hage et al. 2018), flows on levees (Fildani et al. 2006), or flows at slope-breaks (e.g. Kostic and Parker, 2006; Covault et al. 2017; Brooks et al. 2018). The prevalence and character of hydraulic jumps and their associated deposits are less well understood in topographically-complex settings (e.g. Edwards et al. 1994; Lamb et al. 2008; Maier et al. 2018; Howlett et al. 2019).

This study documents scaled physical models of turbidity currents interacting with basin-floor topography and has three main aims: 1) to assess the effect of the incidence angle onto topography (0º, 45º, and 90º) on turbidity currents and their deposits, 2) to explore the effect of topography on flow criticality and associated depositional features; and 3) to use these findings to aid in the stratigraphic interpretation of deep-water basins.

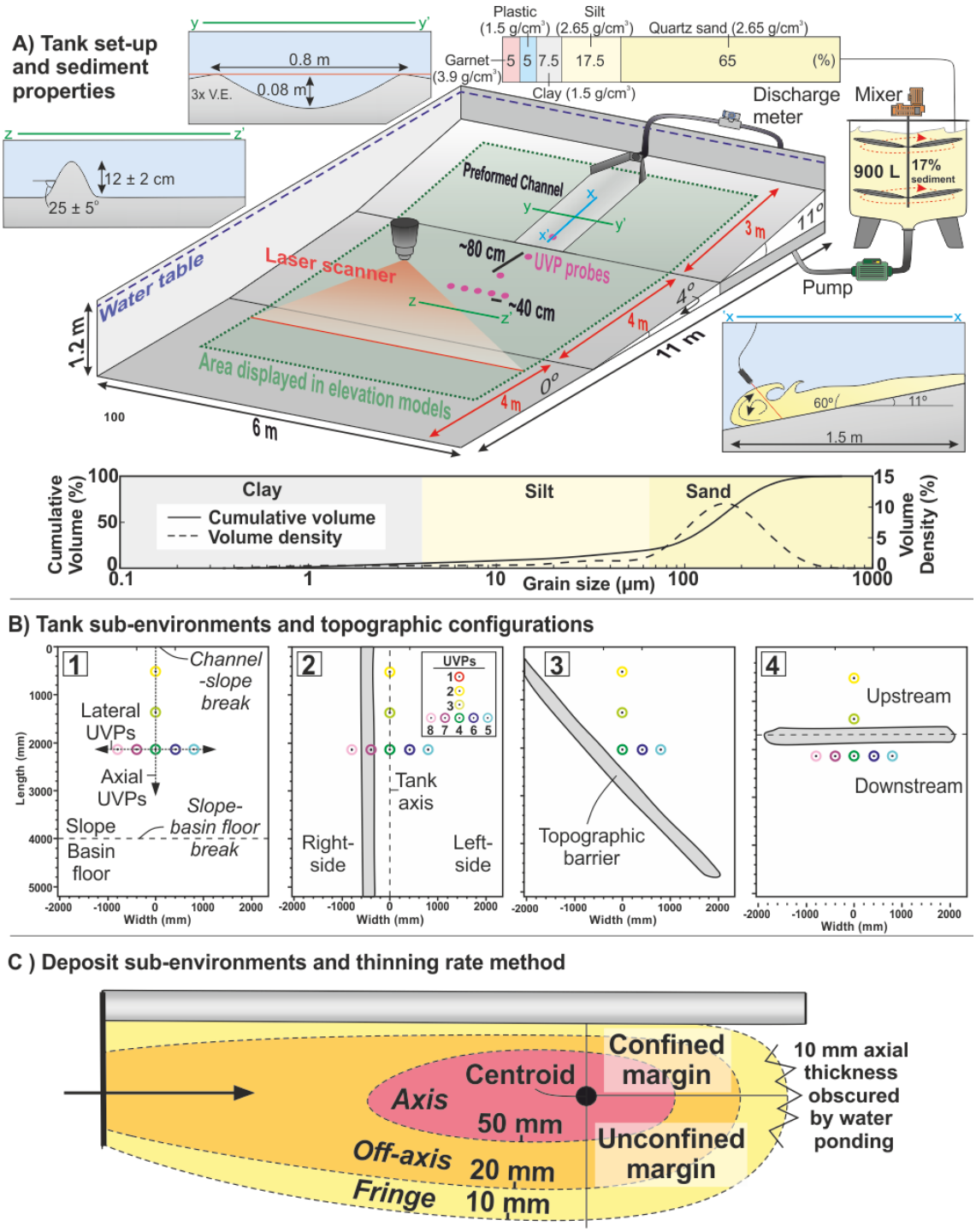

Figure 7.1: A) Key features and dimensions of the experimental method showing the channel, slope, topography ana sediment mixture. UVP probe positions and sediment composition are also indicated (modified from Ferguson et al. 2020). Grain-size distributions are derived from Malvern Mastersizer analysis. B) Tank sub-environments ana topographic configurations discussed in text. The left- and right-sides of the tank are with respect to the flow. C) Schematic lobe deposition adjacent to topography, showing sub-environments and thinning rate method used within this study. Arrow = flow direction.

7.3 *Methodology*

Experimental Set-up and Data Collection

Experiments were carried out in the Eurotank flume tank at Utrecht University. The flume tank configuration used is the similar to that of other studies (e.g. de Leeuw et al. 2018; Ferguson et al. 2020; Pohl et al. 2019a; Spychala et al. 2019). It comprises a 3 m long, 80 cm wide and 8 cm deep channel on a 11° dipping slope, a 4 m long and 4° dipping slope without a channel, and a 4 m long horizontal basin floor (Fig. 7. 1A). The most confining channel-form used by de Leeuw et al. (2018) was used in order to promote bypass along the upper slope and deposition on the topographically-confined lower slope.

The first experiment was run without any basin-floor topography (i.e. unconfined). A linear topographic ridge was created for three subsequent experiments with incidence angles of 0, 45, and 90° relative to the dip-slope (lateral, oblique and frontal confinement respectively (Fig. 7. 1B)). The ridge was a 12 ± 2 cm high, ~40 cm wide triangular prism with a confining surface that dipped at 25° ± 5° on both the upstream- and downstream-facing sides (Fig. 7. 1A). The barrier height was scaled to approximately double the flow thickness in order to fully confine the flow (Fig. 7. 1A). The barrier, channel, slope, and basin floor were formed from fine-sand (Fig. 7. 1B). The use of an erodible substrate allowed both erosion and deposition to be recorded by high-resolution laser scans (2 x 2 mm resolution) of the tank before and after each run (Fig. 7.1A). These difference maps were used to describe the geometry of the deposit, to create cross- and dip-sections and to quantify changes in deposit thickness laterally and longitudinally (thinning rates). Thinning rates were calculated based on three thickness segments or 'sub-environments': 1) thickest point of deposit to 5 cm (axis), 2) 5 cm to 2 cm (off- axis) and 3) 2 cm to 1 cm (fringe) (Fig. 7. 1C). Longitudinal thinning rates (parallel to flow and deposit axis) could not be calculated within the distal fringe due to ponding of water at the base of the drained tank, which obscured the edge of the deposit (Fig. 7. 1C). The edges of deposits, and therefore morphometric descriptions, are also measured based on the 20 mm pinch-out line due to water ponding at the toe of the deposit after draining of the tank prior to laser-scanning.

Ultrasonic Doppler Velocity Profiler (UVP) probes were used to measure flow velocity. Seven UVP probes were located on the slope and one was located in the channel (Fig. 7.1A). Four UVPs were positioned through the axis of the tank and spaced ~80 cm apart (UVP 1, 2, 3, 4), and four UVPs were positioned laterally across at ~20 cm spacing (UVP 5, 6 7, 8), forming a 'T' shaped probe distribution capable of capturing both longitudinal and lateral cross-sections (Fig. 7.2; 7.4). In order to record the entirety of the passing flow and maintain geometric consistency between the steeply dipping channel and shallowly dipping slope the UVPs were orientated facing downward at a 60° angle relative to the local bed. Consequently, the velocities measured reflect the velocity field from the indicated UVP position to ~ 10 cm upstream on the slope and ~ 12 cm in the channel (Fig. 7.2A). The velocity profiles were calculated from the UVP measurements under the assumption that the mean flow is dominantly parallel to the bed (Cartigny et al., 2013) and that bed-perpendicular velocity is negligible. It should be noted that the lateral measurements were collected with the probes aligned straight up-slope, obliquely with respect to the spreading oncoming flow, therefore the measured velocities from these probes may be slightly underestimating the true flow speed. Normalised velocities (by maximum channel velocity for axial velocities and UVP D for lateral velocities) are used to

A) Sediment Properties

Parameter	Grainsize (μm)
Clay D_{50}	7
Plastic D_{50}	331
Silt D_{50}	53
Sand D_{50}	161
Garnet D_{50}	193
Mixed D_{10}	18
Mixed D_{50}	141
Mixed D_{90}	274

B) Unconfined Flow Properties

Parameter	Channel (UVP 1)	Slope (UVP 4)
Flow height (h) (m)	0.07	0.05
Flow density (ρ_c) (kg/m^3)	1290	~1290
Maximum velocity (U_{max}) (m s^{-1})	1.09	0.77
Shear velocity (U^*) (m s^{-1})	0.07	0.05
Densimetric Froude number (Fr_d)	1.78	1.46
Reynolds number (Re)	76278	37348
Particle Reynolds number (Re_p)	9.65	6.88
Shields number	3.09	1.57

Table 7.1: Experimental sediment (A) and flow properties (B).

compare velocities between each run in order to counter the effect of minor variations in discharge that may be present between each run.

Flow Properties

Each flow had a sediment concentration of 17 %, as this value allowed the flows to meet the scaling criteria (next section). The sediment in each experiment consisted of a mixture of materials (Fig. 1; Table 1A). The sediment composition, by weight-percent, was 65% sand (2.65 g/cm^3), 17.5 % silt (2.65 g/cm^3), 7.5 % kaolinite clay (2.65 g/cm^3), 5 % plastic (1.5 g/mm^3) and 5 % garnet (3.9 g/mm^3) (Fig. 7.1A). This sediment mixture was used to investigate in the effect of sediment density on deposit characters. Results relating to these compositional effects will be discussed in a separate manuscript, here we will only discuss the effect of the basin topography on depositional patters. The sediment composition (variable densities) and grain-size is similar to that measured within natural turbidity current deposits (e.g. Stanley, 1963; Bell et al. 2018b). Grain size distributions were collected using a Malvern Mastersizer laser diffraction particle size analyser (Fig. 7.1A; Table 7.1). The sediment-laden water was pumped at a discharge rate of 30 m^3/s into the flume tank and flowed down the channel and onto the slope as a turbidity current.

Scaling

Froude scaling: Froude scale modelling uses the dimensionless Froude and Reynolds numbers to scale natural turbidity currents to experimental turbidity currents (Peakall et al. 1996; Kneller and Buckee, 2000), with the Reynolds number relaxed compared to natural systems and the Froude number held as similar (e.g. Graf, 1971). The Reynolds number (Re) describes the ratio of inertial to viscous forces, where Re values greater than 2000 represent a fully turbulent flow:

$$(1) \quad Re = \frac{\rho_c U h_{max}}{\mu}$$

where ρc = the density of the current, U = the average velocity below the flow height (h), h_{max} = flow height at the velocity maximum, and μ = dynamic viscosity. Flow height is calculated as the height of the flow at ½ of the U_{max} (Launder and Rodi, 1983; Pohl, 2020). The viscosity of water was used assuming that the low-concentration of weakly cohesive kaolinite clay had little effect on the flow viscosity (Baker et al. 2017). The experimental flows used by this study have Reynolds numbers of 76,000 within the channel and 37,000 at the most distal axial probe on the slope (~200 cm), and are therefore fully turbulent (Table 1) (e.g. Leeder, 1982).

The Froude number (Fr) describes the ratio of inertial to gravitational forces acting on a turbidity current, and for scaling purposes it should be held as comparable to natural turbidity currents. Flows with Froude numbers greater than 1 are termed supercritical, while flow with Froude numbers less than 1 are termed subcritical (e.g. Komar, 1971). The transition from supercritical to subcritical flow is marked by a discontinuity known as a hydraulic jump, and is manifested by thickening and deceleration of the flow through the jump (e.g. Komar, 1971; Garcia and Parker, 1989). The ratio between Fr upstream of the jump (Fr_1) and Froude number downstream of the jump (Fr_2) controls the strength of the jump (velocity decrease and thickness increase), with low ratios resulting in weaker jumps and high ratios resulting in stronger jumps (e.g. Cartigny et al. 2014). The densimetric Froude number (Fr_d) further accounts for gravity acting on the density difference between the flow and ambient fluid (i.e. the reduced gravity (g')), and is thus used for describing turbidity currents (Kneller and Buckee, 2000):

$$(2) \quad Fr_d = \frac{U_{max}}{(hg')^{1/2}}$$

where

$$(3) \quad g' = g\left(\frac{\rho_c - \rho_a}{\rho_a}\right)$$

where g = acceleration due to gravity and ϱa= the density of the ambient fluid. The modelled turbidity currents (based on the unconfined control experiment) were supercritical (Fr_d = > 1) within the channel axis (Fr_d = 1.78) and on the mid-slope (Fr_d = 1.46) (Table 1). These Fr_d numbers are consistent with those estimated for natural turbidity currents (cf. Sequerios, 2012), and thus scalable to natural systems. It should be noted that Froude number calculations assume a constant flow density; however, it is likely that flow density decreased and Fr_d increased distally as the flow became more dilute, making the Fr_d numbers a minimum estimation.

Shields scaling: Recent experimental studies (e.g. Fernandes et al. 2019; Pohl, 2019b; Ferguson et al. 2020) have adopted the scaling approach of de Leeuw et al. (2016), which emphasises the importance of scalable turbulence-sediment interactions. This approach depends on the relationship between the Shield's number (τ*) (Shields, 1936), and the

particle Reynolds numbers (Re_p), which governs how sediment is transported (e.g. van Rijn, 1984; de Leeuw et al. 2016) (Table 7.1; Fig. 7.4):

$$\tau^* = \frac{U^{*2}}{(\rho_s/\rho_f - 1)gD_{50}} \quad (4)$$

$$Re_p = \frac{U^* D_{50}}{v} \quad (5)$$

where ϱs is the sediment density (1290 kg/m3), D50 is the median grain size (141 μm), v is kinematic viscosity of fresh water at 20°C, and U^* is the shear velocity (m s^{-1}) as described by Middleton and Southard, 1984; van Rijn, 1993):

$$U^* = U_{max} k \left[\ln\left({}^{h_{max}}/_{0.1D_{90}}\right)\right]^{-1} \quad (6)$$

where k is von Kármán's constant (0.40), and D90 is the 90th percentile of grain size (274 μm). If the Shields number is too low, then the experimental current is below the initiation of suspension and is therefore not representative of natural turbidity currents (Fig. 7.4). Relaxation of the Re_p compared to natural systems is permitted as long as the boundary layer is rough, or transitionally rough, and thus dominated by turbulent, and not viscous, forces (Fig. 7.2) (Garcia, 2008). The experimental turbidity currents in this study plot above the initiation of suspension and developed a suspended sediment profile throughout the flow (e.g. Bagnold, 1966; van Rijn, 1984) (Fig. 7.4). The currents also had a transitionally rough boundary layer, which causes both turbulent and viscous forces to interact with the bed and prevents the flow being overly depositional (de Leeuw, 2016), or 'depletive' (e.g. Kneller, 1995) This means that, when characterised with the Shields parameter and the particle Reynolds number, these flows are in the same dynamic regime as natural turbidity currents (Fig. 7.4). Both of these scaling criteria hold true for flows within the channel, and flows at the point of topographic interaction on the slope (Fig. 7.4). The sediment mobility of these physical models therefore scales to natural turbidity currents using the most current scaling approaches.

Hierarchical scaling: The deposits generated by the individual experimental flows have been suggested to represent lobe elements (sensu Prélat et al. 2009) by other studies (Spychala et al. 2019; Ferguson et al. 2020). This is due to the way in which an individual experimental deposit shows little to no compensation and instead aggrades vertically, while multiple experimental deposits are heavily influenced by the relief of previous deposits and stack compensationally (Spychala et al. 2019; Ferguson et al. 2020). This same pattern of poorly-developed compensational stacking between successive event beds to the well-developed compensational stacking between successive lobe elements (that build lobes) has been observed in the subsurface (e.g. Deptuck et al. 2008) and at outcrop (e.g. Prélat et al. 2009), leading to the interpretation that the deposits formed in these models are most representative of lobe elements.

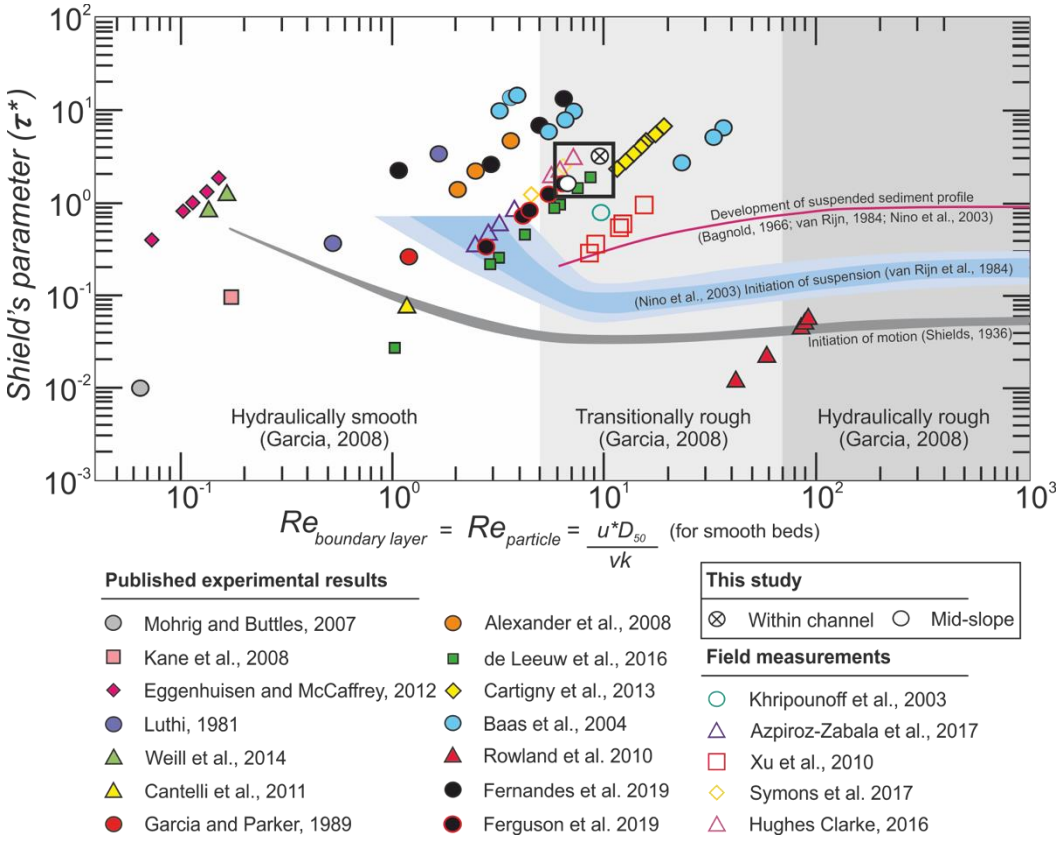

Figure 7.2: Shields-scaled experimental and field-measured flows. (modified from Fernandes et al. 2019). The flows produced by these experiments are Shields-scaled within the channel (UVP 1) and on the slope (UVP 4) to promote both sediment entrainment and transport, making the experimental flows similar to natural flows.

7.4 *Physical modelling results*

Channel and channel-slope transition: All experiments

Observations: The input flow parameters and channel-form dimensions were uniform across all runs so the following description applies to all flows. Flows were highly erosional within a 15 cm zone around the mouth of the inlet pipe, becoming partly depositional down the axis of the channel (Fig. 7.2). Channel deposits thin distally and laterally, reaching maximum thicknesses of 5.1 cm ~7 cm away from the inlet pipe and thinning to < 2 cm at the channel-mouth and channel-margin. Channel margins were eroded asymmetrically, with erosion of up to 4 cm into the inside channel margin measured (Fig. 7.2). Thin (< 1 cm) overbank deposits were observed across the runs.

Loss of channel confinement and reduction in slope angle at the channel-slope transition was characterized by < 2 cm of deposition, or non-deposition, through the axis for a distance of 1 m (Fig. 7.2). This axial zone initially thins at the mouth of the channel toward a depositional minimum at ~20 – 60 cm down-dip, before thickening again ~160 cm down-dip of channel mouth. This results in an up to ~40 cm wide and ~90 – 130 cm long oval-shaped area of bypass on the slope. This area of bypass was flanked by up to 3 cm of deposition that thickens down-dip from the margins of the channel.

Interpretation: Excessive erosion at the channel head is caused by the turbidity current suspension exiting the inlet pipe and transitioning from un-erodible to erodible substrate, and is therefore an experimental artefact. Deposition immediately down-dip of this zone is driven by capacity-driven deposition (sensu Hiscott, 1994), with thicker deposits in the channel axis than the channel margins due to higher sediment concentrations within the axis. The channel was predominantly a bypass zone but the deposit gradually aggraded due to the initial high concentration of the flows, eventually filling by sedimentation of the slower and more depositional tail of the flow (e.g. Barton et al. 2010). Lateral confinement of the flow caused erosion along the length of the channel margins. This asymmetrical channel-margin erosion is attributed to either variation within turbulent flows exiting the inlet pipe at slightly offset directions, or small irregularities in the pre-formed channel topography. Deposition on the outsides of the channel-form margins was driven by overspill of the upper parts of the turbidity current that were able to

surmount the channel relief (e.g. de Leeuw et al. 2016; 2018), forming levees (e.g. Normark et al. 1983; Kane & Hodgson, 2011).

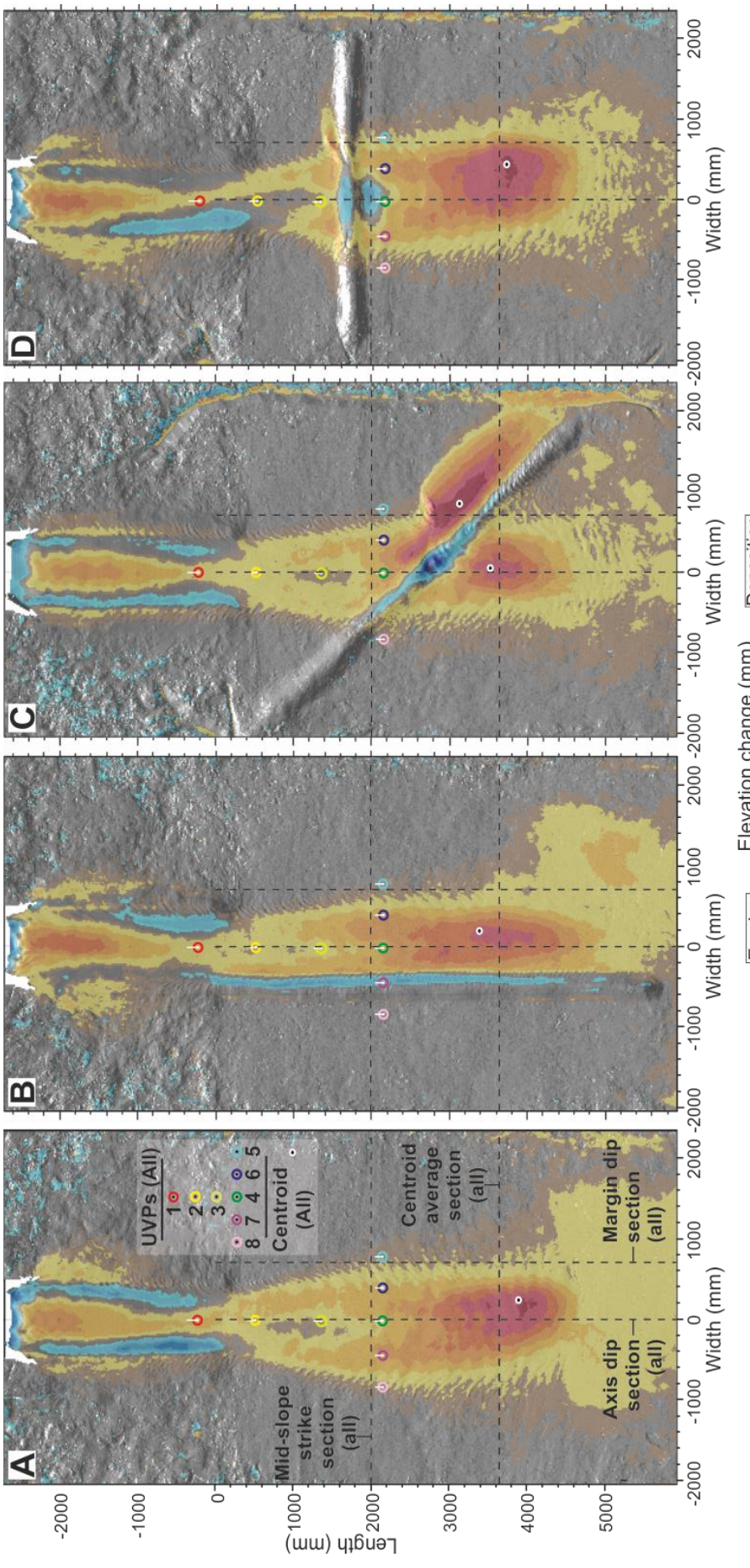

Figure 7.3: Difference maps for the experimental runs discussed in this study. The maps are made by subtracting the laser scan derived elevation of the pre-experiment tank surface from the post-experiment tank surface. A) Unconfined, B) laterally confined, C) obliquely confined and D) frontally confined. Erosion is shown in blue and deposition is shown in yellow, orange and red. White tick on UVP represents the approximate limit of upstream velocities captured by that UVP.

Flow relaxation, coupled with a relatively high slope angle, counteracted the effects of flow expansion and deceleration at the channel mouth, developing the broad bypass region (Pohl et al. 2019a). Deposition occurred at the margins of this non-depositional zone due to lower velocities at the margins of the flow (e.g. de Leeuw et al. 2016). The marginal deposits acted to further confine the flow, enhancing bypass and creating a constructional channel-form evident in strike cross-sections (Fig. 7.7A1) (e.g. Hamilton et al. 2015; de Leeuw et al. 2016).

Channel-slope transition – basin floor

The following sections will describe deposition solely on the topographically-varied portions of the slope and basin floor (> 1.5 m down-dip from the channel-slope break), except within the laterally confined run, which is affected by topography from the mouth of the channel to the basin floor.

Unconfined

Observations: The unconfined experiment produced a 12.8 cm wide and 46 cm long deposit, with a length-width ratio (L/W) of 3.6. The deposit thickened from 1 - 2 cm to a maximum between 20 cm - 32 cm down-dip (Fig. 7.2A), with the thickest point of the deposit (centroid) reaching 6.5 cm near the slope-floor break at 390 cm (Fig. 7. 2A). From 43 to 320 cm the deposit maintained a 5 - < 6 cm thickness, forming a 90 cm long and 60 cm wide axial zone. The deposit thinned to < 2 cm thick over 30 cm before the thickness became obscured by ponded water on the flat basin floor (Fig. 7.5A). The deposit also thinned laterally, reaching its maximum width of 128 cm, 240 cm down-dip of the channel mouth (Fig. 7.7A; B; 8A; B).

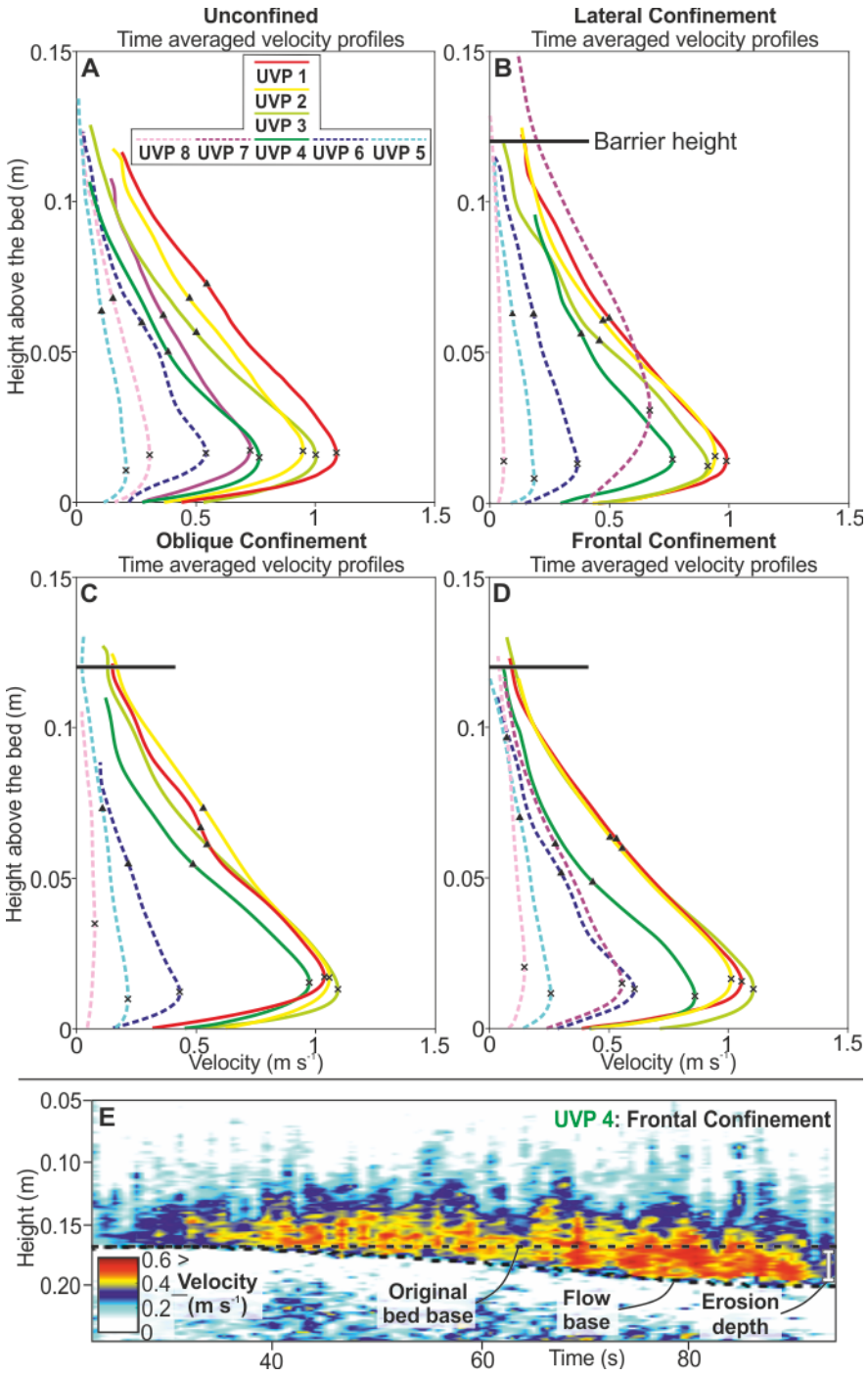

Figure 7.4: A-D) Time-averaged velocity profiles for each experimental run. Dashed lines indicate lateral velocity measurements. The head (first 5 s) and tail (final 15 s) have been cropped to exclude noise from the depth averaging process. The cross on the time-averaged velocity profiles = U_{max}, and the triangle = the flow height. E) Velocity field through the passage of frontally confined turbidity current immediately downstream of the barrier. Acceleration through time and erosion is indicated by the UVP data.

Flow velocity decreased with distance away from the inlet pipe and through time (Fig 4A). The maximum velocity of 1.09 m s^{-1} was recorded by the most proximal probe in the channel. The velocity decreased down-dip to 0.77 m s^{-1} at the most distal axial probe (UVP 4) over a distance of 240 cm. Velocity decay was more rapid laterally within the flow, from 0.77 m s^{-1} to 0.21 - 0.31 m s^{-1} over 80 cm, away from the flow axis (UVPs 5 and 8). Velocity decay laterally was not symmetrical. Velocity initially decayed slower toward the left of the flow between the axis and first lateral probe (UVP 6), before decelerating more-rapidly between the first and second left-lateral probe. Comparatively, the right-lateral probe measurements showed more linear velocity decay from axis to margin (Fig. 7.3A; Fig. 7.8C).

Interpretations: Distal thickening of the unconfined deposit is attributed to the gradual waning of flow velocity as the flow expanded across the slope (Fig. 7.3A; 5A), with velocities likely decreasing and deposition increasing throughout the run in this zone as the deposit gradually aggrades and generates topography (Hamilton et al., 2015). The centroid located near the slope to basin floor transition suggests that the reduction in slope angle at this point enhanced deposition. Thinning of the deposit down-dip of the centroid is attributed to waning and competency-driven deposition of the less dense components of the flow (clay, silt and plastic) (Table 1) on the basin floor. Lateral thinning is attributed to flow expansion, deceleration and deposition on the margins (e.g. de Leeuw et al. 2016). The variation in lateral thinning rates is possibly due subtle lateral-dip variations on the constructed slope.

Lateral Confinement

Observations: Lateral confinement parallel to the right-hand channel margin resulted in a deposit 34 % narrower (58.5 cm) than the unconfined deposit and 10 % longer (50.6 cm) (L/W = 6) (Fig. 7. 1B; 3B; 8D). Lateral thinning rates differed between the confined and unconfined sides of the deposit; on the confined margin the deposit thinned 74 % less from the centroid (5.6 cm) to 5 cm, 29 % less in the off-axis, and ~8x more in the fringe when compared with the unconfined deposit (Fig. 7.8B). On the unconfined margin the deposit thinned 8 – 17 % less initially, before thinning 72 % more at the fringe (Fig. 7. 1C). Thinning rates were also reduced by 78 % down-dip of the centroid (Fig. 7.2B; 8A). Up to 3 cm of erosion was seen along the barrier margin confining

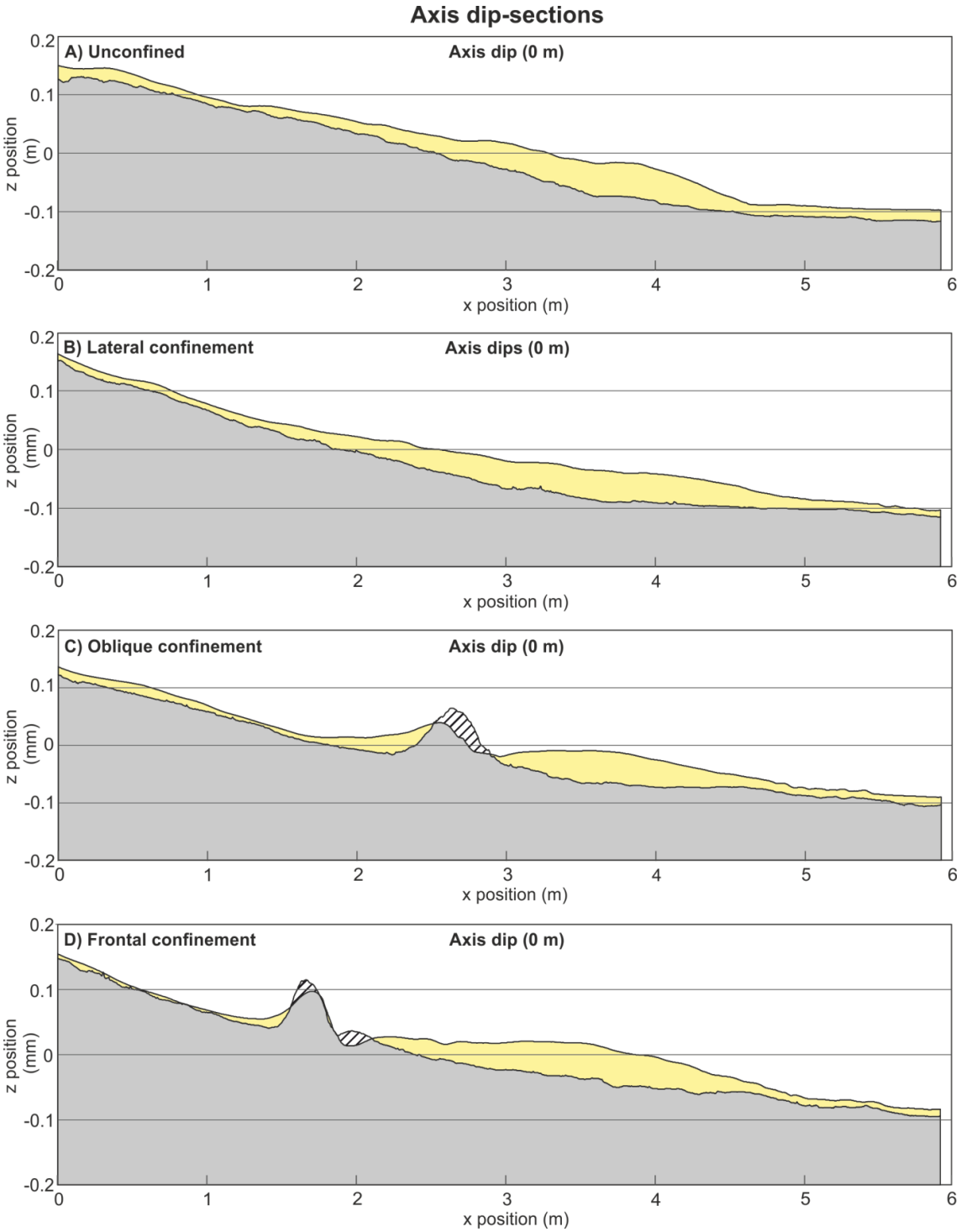

Figure 7.5: Dip sections along the axis of the deposits. Section locations on Fig. 3. Hatched fill represents erosion.

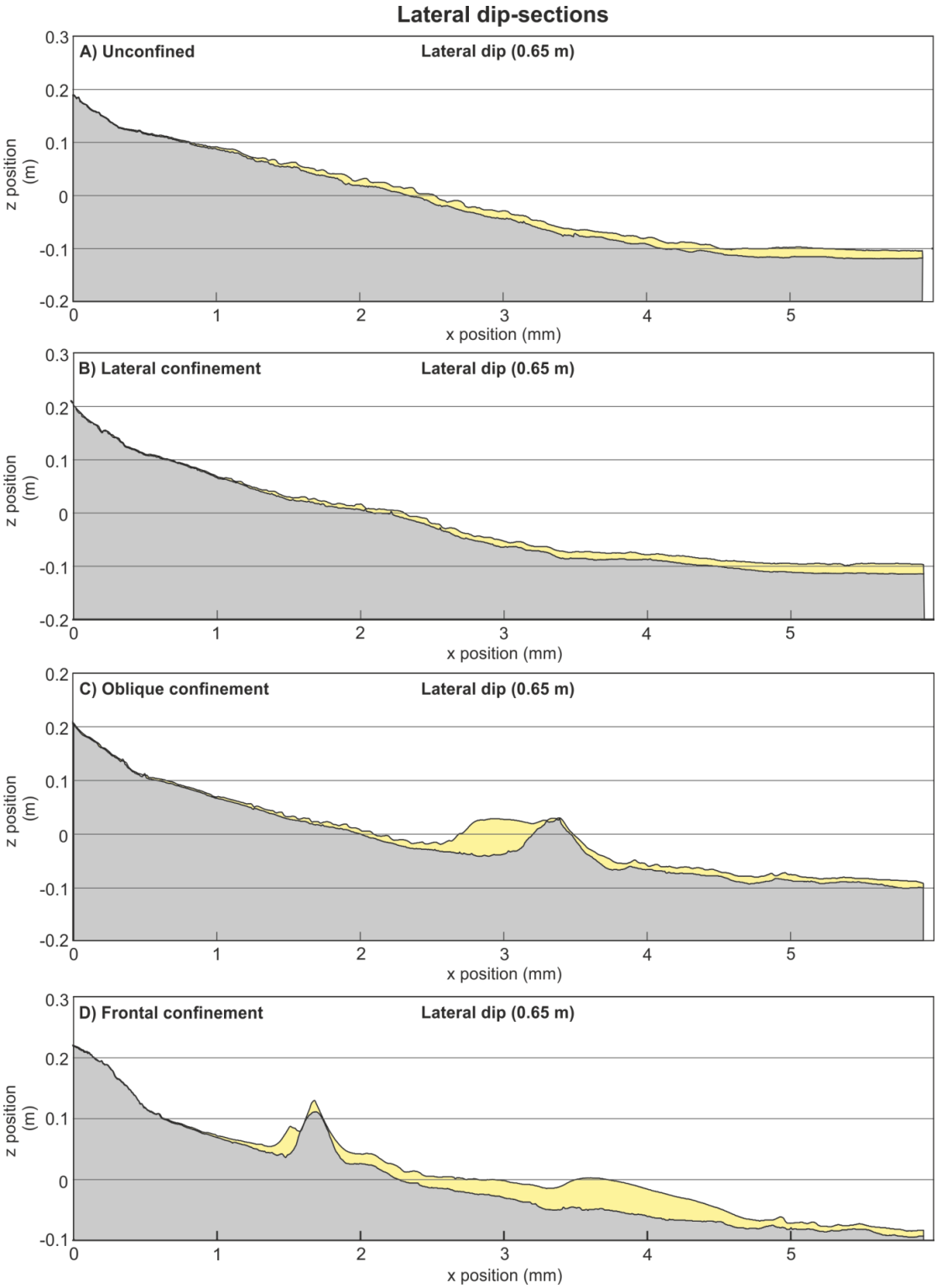

Figure 7.6: Dip sections through the margin of the deposits. Section location on Fig. 3. Hatched fill represents erosion.

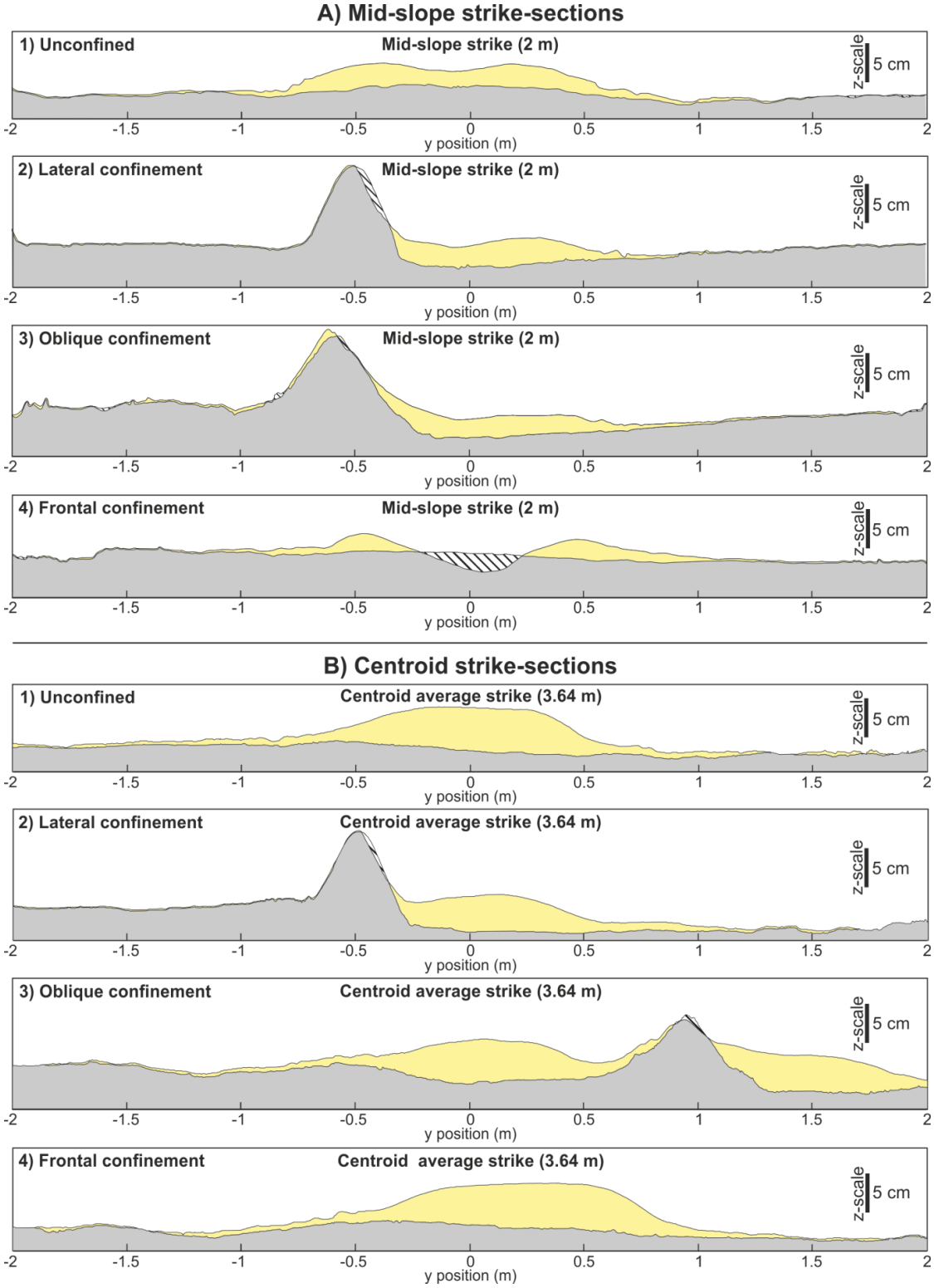

Figure 7.7: A) Strike sections through the deposits mid-way down the slope. Section locations on Fig. 3. B) Strike sections through the average position of the centroid across the runs. Section locations on Fig. 3. Hatched fill represents erosion.

the flow (Fig 7A). This erosion extends for ~440 cm down-dip from the channel-mouth, adjacent to the main deposit.

The normalized axial velocity (UVP 4) of the laterally confined run was 20% faster (0.76 m/s) compared with the unconfined run (Fig. 7.3B). Lateral velocities were also affected by confinement, with the velocity profile measured by the UVP adjacent to the barrier having an U_{max} ~50% higher than the equivalent point in the unconfined run. On the outside of the topography (UVP 8) the velocity was 81 % slower than the unconfined run (Fig. 7.3B). The velocity at the equivalent probe on the unconfined side of the laterally confined flow was 10 % slower than the unconfined run.

Interpretations: Erosion of the lateral barrier was caused by confinement of the flow and consequent shear stresses exerted on the barrier substrate (Cossu and Wells, 2012). Erosion decreased down-dip as the flow waned. Non-deposition on the right-hand 'shielded' side of the barrier was caused by this confinement, which prevented lateral spreading of the flow and deposition on the right-hand side of the tank (Fig. 7.10). This is supported by the reduced velocities measured on the right-hand side of the barrier (Fig. 7.3B). The velocity measurement collected adjacent to the barrier with a vertically higher Umax is attributed to a more well-mixed, homogenous and slower upper part of the flow that was able to run-up the topographic barrier (Al Ja'aidi, 2000; Al Ja'aidi et al. 2004).

Enhanced thinning rates in the fringe adjacent to the barrier are suggested to be caused by the barrier (Fig. 7.8B), with the barrier slope causing flow deceleration, resulting in faster rates of deposition in lateral positions (e.g. Barker et al. 2008), and consequent onlap of the deposit against the barrier (Fig. 7.7A2, B2). Reduced thinning rates through the axis and on the unconfined margin of the flow are also attributed to this confinement. The axis of the flow was confined laterally between the barrier and marginal deposition, thus allowing the maintenance of high velocities along its length and decreased rates of deposition down-dip and laterally, resulting in an elongation of axial deposition. This interpretation is slightly complicated by the 14% faster velocity decay measured from axis to margin on the unconfined side of the flow compared with the unconfined run (Fig. 7.8C). This indicates that proximally (0 – 200 cm) the flow was focused axially through the basin due to confinement by the barrier and marginal deposition, resulting in rapid velocity drop-off laterally within the flow. The rate of marginal deposit aggradation will have exceeded the rate of axial aggradation throughout the passage of the experiment, further

confining the flow (e.g. de Leeuw et al. 2016), enhancing sediment bypass, and causing elongation of axial deposition. At more distal positions (200 - 400 cm) this effect had been reduced as the flow began to spread laterally over the slope. Amy et al (2004) reported similar patterns based on outcrop and experimental observations, with enhanced bypass adjacent to a laterally-confining barrier and enhanced deposition away from the barrier during the passage of a high-velocity flow.

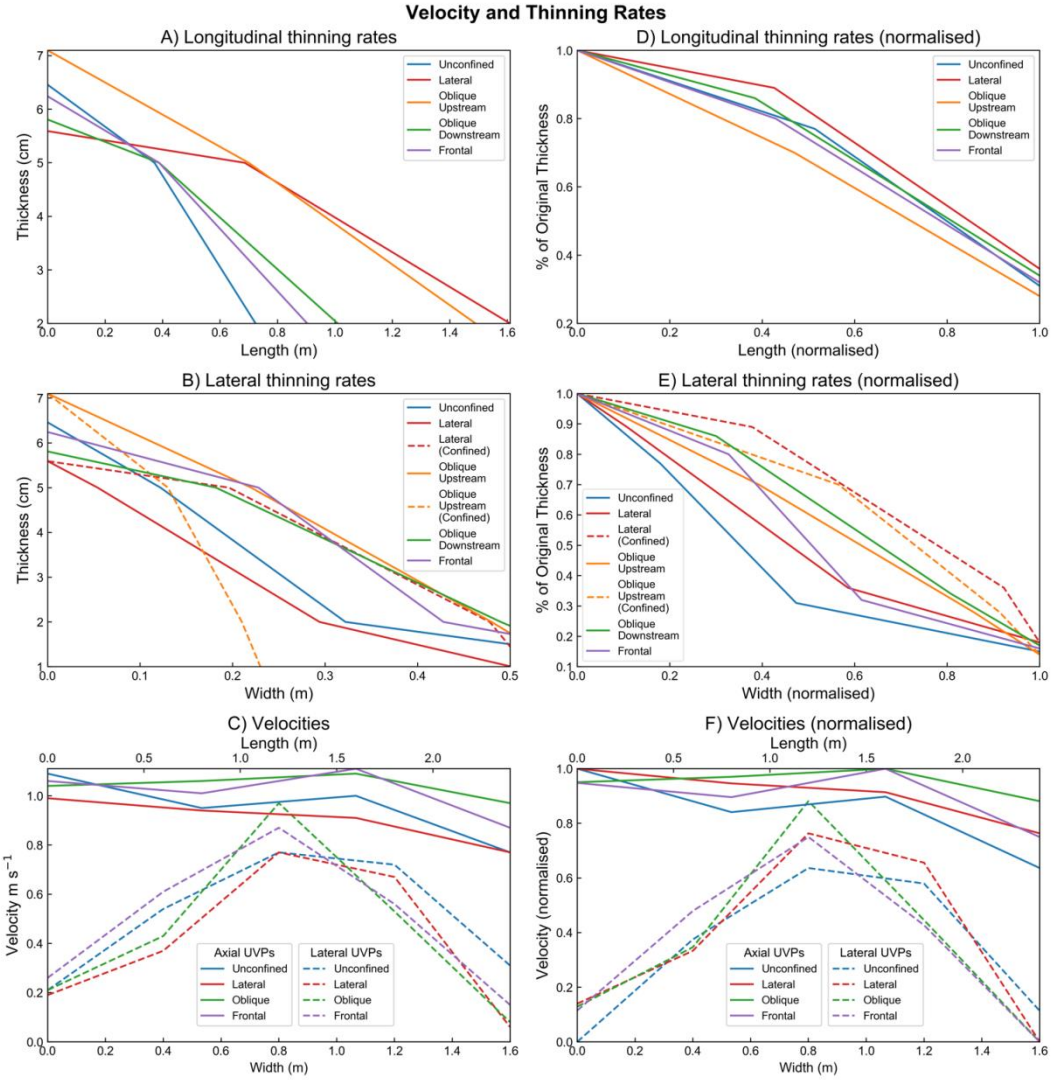

Figure 7.8: Actual (A, B, C) and normalised (D, E, F) thinning and velocities recorded by these experiments. The deposits have been divided into their depositional components, i.e. in the oblique experiment the upstream confined deposit is treated as a separate to the downstream unconfined deposit.

Oblique Confinement

Observations: Oblique confinement of the flow resulted in a bifurcated deposit, with one 'axis' of the deposit positioned upstream of the barrier, and the other 'axis' downstream of the barrier (Fig. 7.2C), resulting in two distinct centroids. The upstream centroid was 20 % thicker than the downstream centroid (7 cm compared with 5.8 cm). The upstream deposit was also more elongate (L/W 5.3) and extended over a longer distance than the downstream deposit (L/W 1.5), having a similar geometry to the laterally confined deposit described previously (Fig. 7.2B; 8D). The upstream deposit was different, however, in that it displayed an arcuate surface on its upstream side that dipped steeply towards the channel, forming a wedge or ridge like geometry. (Fig. 7.2C; 6C). Thickening across this surface was rapid, increasing down-dip from ~10 cm to ~70 cm over ~20 cm, forming a ridge with a steeply dipping upstream face and a shallow downstream face. The ridge caused a discontinuity within the axis of the upstream deposit, with the axis ~50% narrower than would be expected if continuous along the barrier. Thinning from centroid to 5 cm thick down-axis within this upstream deposit was 78 % less, and 62 % less in the off-axis, when compared with the unconfined deposit (Fig. 7.8A). Thinning rates on the confined margin of the upstream oblique deposit were also much greater than those measured within the laterally confined deposit; the oblique deposit thinned 451 % greater within the axis, 257 % greater with the off-axis, and 100 % greater within the fringe (Fig. 7.8B).

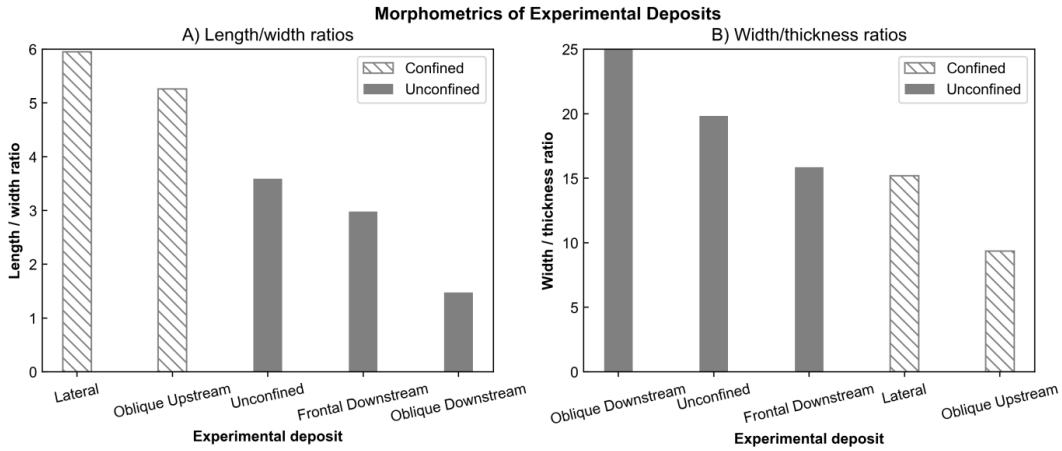

Figure 7.9: A) L/W ratios from experimental deposit. Lateral confinement results in the highest L/W ratios, while up-dip confinement results in the lowest L/W ratios. B) Width-thickness ratios for each experimental deposit. Laterally confined deposits have the greatest thickness-width ratios.

Up to 7.8 cm of erosion was recorded down the axis, removing a substantial amount of material from the topographic barrier (Fig. 7.2C; 5C). Erosion decreased laterally and was confined to an erosional zone approximately the same width as the channel (~ 8 cm). Deposition initially thinned across the barrier, before thickening again down-dip, forming the same downstream depositional geometry as seen in the unconfined experiment, but with a thinner centroid (5.6 cm). Thinning rates were slower within this downstream deposit compared to the unconfined deposit, with down-dip thinning rates 47 % slower in the axis, and 43 % slower in the off-axis. Marginal thinning rates were also slower, with thinning rates 63 % slower in the axis, and 35 % slower from in the off-axis. This resulted in a more equant, and less lobate, deposit down dip (L/W 1.5).

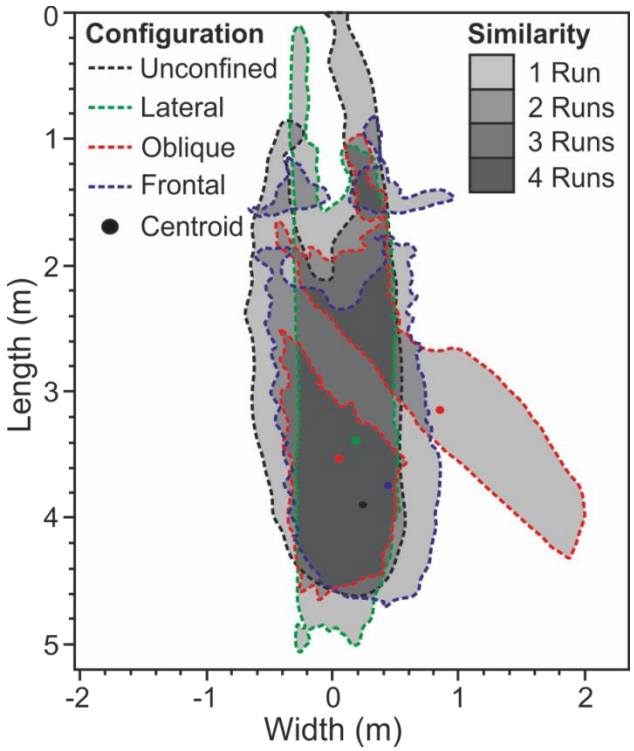

Figure 7.10: Overlayed deposit extent maps showing the similarity between each deposit. The pinch-out line is at 2 cm due to the difficulty in tracing accurately around the 2 cm line because of water-ponding in the drained tank.

The measured velocity field of this flow was similar to that of the unconfined run due to most of the UVP probes being located upstream of topography (Fig. 7.2C). The only anomalous upstream velocity measurement was collected by the UVP closest to the topography (UVP 4), which was located within the axis of the flow 20 cm upstream of the topography. When normalized the velocities at this axial position were 36 % higher than

the same relative position within the unconfined run and 20 % higher than the laterally confined run (Fig. 7.8C). This velocity anomaly was present throughout the experiment and was maintained even when more proximal velocities began to wane. Velocities from the 'shielded' UVP 8 on the downstream side of the topography were also affected, being 74 % slower than the equivalent position on the unconfined experiment and 2.5x higher Umax (Fig. 7.2C). Velocities were not able to be analyzed from UVP 7 due to incomplete data collection.

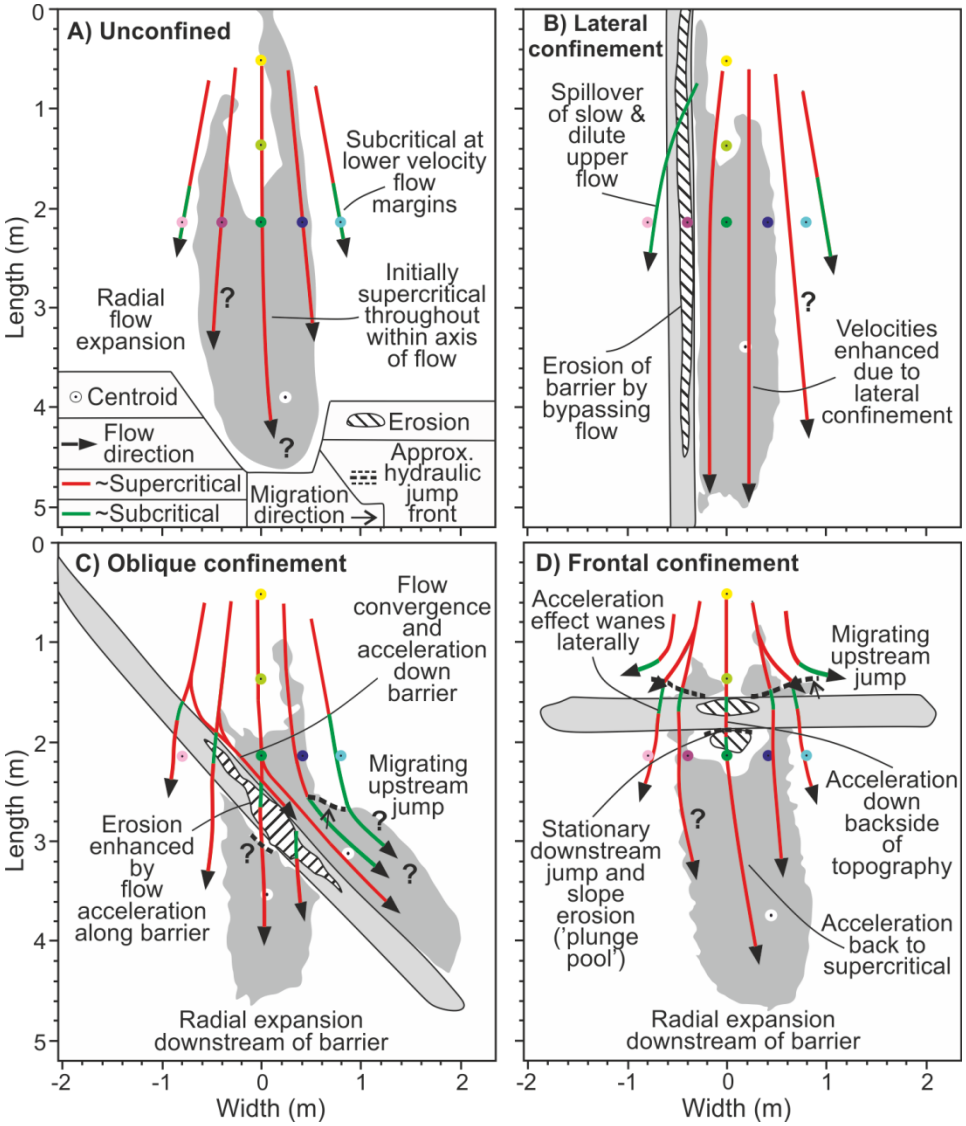

Figure 7.11: Flow pathways and criticality for each of the runs. Criticality is based on UVP measurements. Criticality down-dip of UVPs is inferred based on sedimentary structures.

Interpretations: The increased thickness of the upstream bifurcated deposit indicates that it formed immediately upon turbidity current interaction with the barrier and

that left-lateral deflection was the primary route taken by the incoming flow throughout the experiment. The downstream deposit may have formed concurrently with the upstream deposit, with the deposit representing the lower concentration upper regions of the flow that were able to surmount the topographic relief (e.g. Sinclair and Tomasso, 2002) (Fig. 7. 13). This may explain the equant shape of the deposit, which is a characteristic of deposition from lower-concentration flows (Al-Ja'aidi et al. 2004). Alternatively, the downstream deposit formed after the upstream deposit as erosion of the barrier decreased the degree of confinement, allowing the flow to overtop it. A combination of both of these processes is likely to have contributed to the deposition of the downstream deposit. The similarity in geometry between the unconfined deposit and this downstream deposit is as expected due to their relative lack of confinement.

The higher flow-velocities upstream of the barrier are suggested to be caused by the axis of the flow impacting with the barrier. Flow convergence and acceleration down the barrier will have enhanced this erosion, with deposition extending obliquely down-dip along the barrier (Fig. 7.10C). Flow convergence is attributed to similar features seen at oblique onlap surfaces in field investigations (see 'accumulative flow' of Kneller and McCaffrey, 1999). It is also possible that flow reflection may have interfered with the velocity measurement; however this should have resulted in deceleration, and not acceleration, so is not deemed to be significant. Erosion of the barrier may have been enhanced by flow convergence as the flow became increasingly laterally confined by the margins of the barrier incision (Gee et al. 2001). Erosion may also have been enhanced through time as the deposit aggraded decreasing the relative height of the barrier. The low-velocities and higher U_{max} measured on the UVP 8 downstream of the barrier are interpreted to have been caused by shielding of this UVP by the barrier, with only the well-mixed and lower velocity upper parts of the flow able to surmount the topography and be detected by the UVP. This is an analogous process as interpreted to have occurred at UVPs 7 and 8 over the crest of the barrier and on the shielded side of the tank. The velocity measured in the oblique run is slightly higher (0.08 m s^{-1} compared with 0.06 m s^{-1}), possibly due acceleration of the flow down the backside of the oblique topographic barrier.

The steep-sided ridge deposited adjacent to the barrier and to the left (looking downstream) of the flow axis is suggested to be formed through rapid flow deceleration and thickening upon interaction with the barrier (e.g. Rottman et al. 1984). Similar

geometries have been formed within both topographically-affected experimental and numerical turbidity currents and has been attributed to the flow thickening and decelerating at the barrier and forming a hydraulic jump or reflective bore (Edwards et al. 1994; Kneller and Buckee, 2000; Lamb et al. 2004; Howlett et al. 2018), resulting in the deposition of a thick 'sediment ridge' at the barrier (Alexander and Morris, 1994). Similar sttrctures were also produced in granular pyroclastic flows through the formation of a 'granular jump' (Smith et al. 2006). Flow 'lofting' has also been described within subcritical flows encountering frontal barriers (Stevenson and Peakall, 2010). While there are no UVP measurements in the correct position to record a jump, it can be inferred based on the supercriticality of the incoming flow, the geometry of the ridge and its similarity to other examples where Fr numbers were more constrained (e.g. Hamilton et al. 2015; 2017) The aggrading sediment ridge, along with increased flux from deflected flow upstream (Alexander and Morris, 1994), will have caused the jump front and associated deposition to migrate and back-step through time (Fig. 7.10C). The formation of the ridge laterally within the flow, and not within the axis, is attributed to lateral flow velocities and being sufficiently low to allow hydraulic jump formation upon deceleration at the barrier. The axial velocities were high enough to maintain supercritical conditions upon deceleration at the barrier, therefore deposition was concentrated downstream of the barrier, forming an essentially unconfined deposit (Fig. 7.10C; 11).

Frontal Confinement

Observations: Frontal confinement resulted in onlap and perpendicular spreading of the deposit against the barrier (Fig. 7.2D). Spreading was greater on the left-hand side of the flow axis. Deposition was not significantly thicker upstream of the barrier, and compared with the unconfined deposit, the perpendicular geometry of the deposition on the left hand-side was the only variation. The ridge seen at the up-dip extent of the deflected deposit within the obliquely confined run was also observed at the up-dip reaches of the deflected deposits within this run, albeit at a smaller scale (Fig. 7.6) The same thickening pattern was observed, although the deposit only thickens to ~ 4 cm compared to 7 cm in the obliquely confined run.

Erosion of the middle of the barrier was again observed, although not as deep as the erosion in the obliquely confining run (Fig 3D; 5). Erosion (up to 2.5 cm) was also focused on the upstream side of the barrier and failed to fully breach the barrier, while

erosion was more focused on the downstream side of the oblique barrier, breaching it with up to 7.8 cm of erosion (Fig. 7.2C; D). Erosion was also observed at the downstream foot of the barrier (Fig. 7.2D), forming a 2.5 cm deep scour into the slope substrate that shallowed down-dip over 40 cm before the flow became depositional (Fig. 7.7A4). This down-dip deposition had a similar depositional pattern to the unconfined run, with thickening and thinning occurring at broadly the same points on the slope. However, the frontally confined deposit had more linear frontal and lateral margins (L/W = 3) than the unconfined deposit (L/W = 3.6), which was more lobate and had more curvilinear margins (Fig. 7.9). The frontally-confined deposit thinned from its centroid (6.2 cm) to 5 cm down-dip, 18 % less than the unconfined deposit (Fig. 7.8A). Marginal thinning rates were similar to the unconfined deposit (Fig. 7.8B).

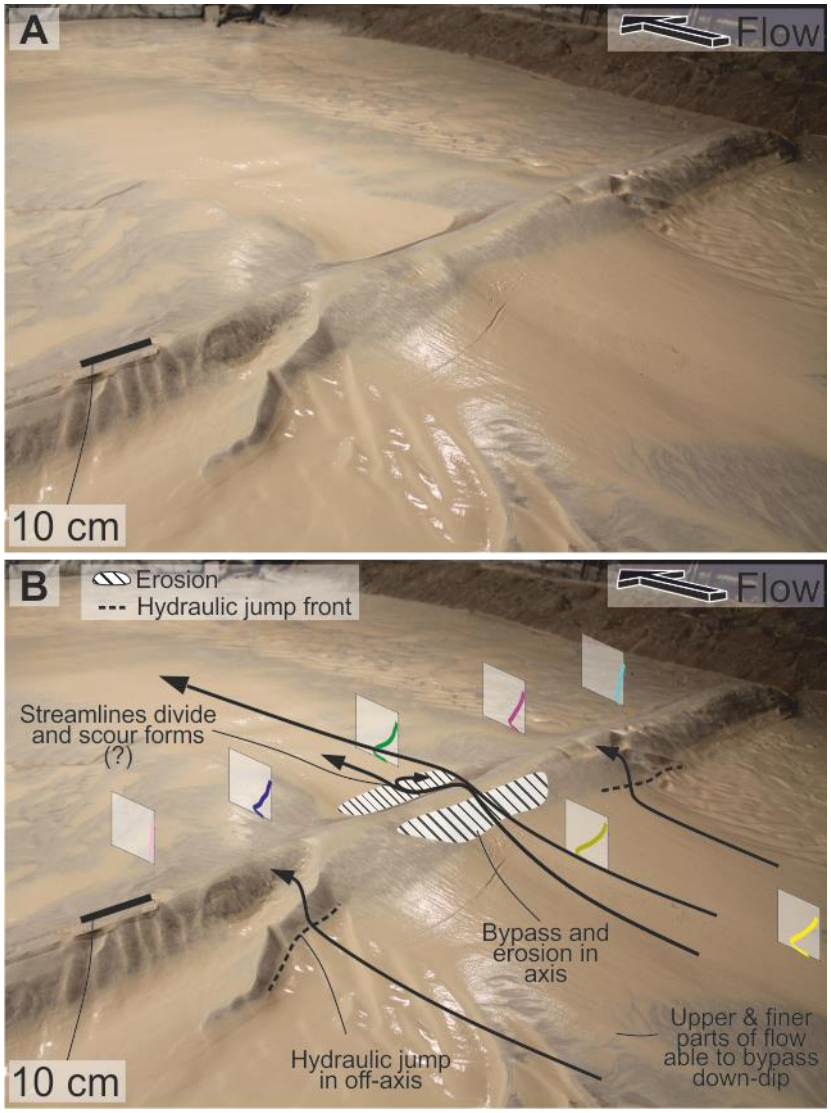

Figure 7.12: A) Photograph of frontally-confined deposit. B) Interpreted photograph of the flow processes occurring during the initial experiment. The ridge-like deposits on the upstream margin of the deposit are suggested to be formed by hydraulic jumps within the lower-velocity margin of the flow. The flow margins had lower-velocities than the axis, so were able to decelerate below unity upon encountering the barrier, while the axis was able to stay about unity due to its higher velocity.

Velocities up-dip of the topography were similar to those observed in the unconfined control run (Fig. 7.3D). The axial velocity measurement (UVP 4) when averaged between 10 and 40s is similar to those seen in the unconfined run. The velocity at UVP 4 was not constant, however, and accelerated throughout the run, reaching a normalized velocity 36 % higher than the unconfined run by ~ 55s (Fig. 7.3E). Lateral

UVPs show the opposite pattern, however, with the flow initially up to 16 % faster than the unconfined run, before decelerating through the run and becoming up to 33 % slower.

Interpretations: The downstream velocity increase toward the end of this experiment indicates that more of the flow was able to surmount the topography and deposit down-dip through time (Fig. 7.3E), compared to the obliquely-confined experiment. This suggests that the upstream deflected 'wing' was deposited initially as the flow decelerated at the barrier. Similar spreading at frontally confining barriers has been reproduced in numerically-modelled turbidity currents (Howlett et al. 2019). Aggradation upstream of the barrier gradually reduced the degree of confinement, allowing bypass and deposition downdip, i.e. 'fill-and-spill' deposition (e.g. Sinclair and Tomasso, 2002). This loss of relative frontal confinement was enhanced by axial erosion of the barrier, which also has been observed in subsurface fold-thrust belts (Morley and Leeong, 2008). The axial deposition that allowed the topography to be surmounted is interpreted to have been subsequently eroded, leaving the upstream right-hand margin 'wing' (Fig. 7.2D) and left-hand margin onlap (Fig. 7.13) as the erosional remnants of this early deposition (Fig. 7.2D). The opposite pattern observed by the lateral probes (deceleration through time) is suggested to be caused by the upstream deposition preventing overspill in lateral position through time, thus limiting the flow's ability to reach the lateral probes downstream through time. Alternatively, the velocity decrease is due to increasing confinement axially within the downstream scour, which allowed only the upper and lower-velocity parts of the flow to reach the lateral UVPs.

The ridge present on the upstream right-hand side of the deposit are suggested to be formed in the same way as those formed in the same relative position on the obliquely confined deposit, with the flow decelerating and thickening at the barrier and subsequently undergoing a localized hydraulic jump on the slope (Fig. 7.10) (e.g. Alexander and Morris, 1994). The axial erosion seen on the slope at the downstream base of the topographic barrier is attributed to either deceleration at the foot of the slope, hydraulic jump formation and scouring (e.g. Sumner et al. 2013) or excavation by flows that accelerated down the backside of the barrier and impacted the slope (e.g. Lee et al. 2002). Erosion may have been enhanced by entrainment of the early onlapping garnet, which increased the flow density and velocity (Fig. 7.13). As more of the flow was able to surmount and flow down the barrier the velocity gradually increased, which would have deepened the scour, and may

have gradually prevented deposition downstream through entrenchment (Fig. 7.3E; 10). Deposition dowstream of this scour, possibly analogous to deposition on the stoss-side of a cyclic step (e.g. Postma et al. 2014), resulted in an unconfined lobate deposit at the slope to slope-basin floor transition. If a jump was absent at the foot of the slope then it is likely that the flow re-accelerated and deposited in the same manner as in the unconfined experiment.

It is also possible that the barrier acted essentially as a defect on the bed, with the incoming flow attempting to equilibrate the slope. This process would be analogous to a waxing flow that has formed bedforms (i.e. the barrier) that were stable at a low velocity, but which are now unstable at higher velocities and are therefore re-worked by the flow (e.g. Cartigny et al. 2014). The scour at the foot of the barrier in this case may therefore be formed by streamline separation and erosion at the foot of the lee-slope, much in the same way erosion occurs at the foot of a lee-slope during ripple formation (e.g. Allen, 1969).

Summary and comparison of results

Morphometrics: The laterally confined deposits have the highest length-width (L/W) ratios (5.3 – 6) (Fig. 7.9A). The lowest L/W ratios are seen in the deposits downstream of slope confinement (1.5 – 3). Complete unconfinement produces the median L/W ratio (3.6) (Fig. 7.2A). These differences in L/W ratios between confined and unconfined deposits are consistent with those seen in natural systems (Prélat et al. 2010), with the unconfined deposit having the same L/W as the average of unconfined lobes on the Amazon Fan, for example (Fig. 7.9A). The experimentally confined deposits when taken in isolation, however, have much higher L/W ratios than the average for natural generically-confined systems (5.3 – 6 and 1.7 – 2 respectively), further indicating that lateral confinement in particular causes extension and/or narrowing of deposits. Ratios of width-to-thickness show similar trends, with unconfined deposits tending to be more laterally extensive but thinner, and confined deposits tending to be less laterally extensive but thicker (Fig. 7.9B).

Thinning rates: Across the experiments the unconfined deposits show lateral thinning rates that are higher than longitudinal thinning rates, giving all of the deposits a lobate shape elongate in the dip or flow-parallel direction (Fig. 7.8B). The unconfined deposit shows the greatest longitudinal thinning rate, with laterally confined deposits

having the lowest rates (Fig. 7.8A, D). The opposite relationship describes the outer margins of the deposits, with thinning rates enhanced at the fringe when confined (Fig. 7. 8B; E). It should be noted, however, that in the axis and off-axis lateral thinning rates are lower when confined than when unconfined, and that elevated thinning rates associated with confinement are only seen in the fringe (Fig. 7.8B, E).

Velocities: Normalised axial velocities (UVP 4) are lowest in the purely unconfined experiment (0.64 m s^{-1}), and greatest during the obliquely confined experiment (0.86 m s^{-1}), with confinement (at any orientation) always causing an acceleration of axial velocities (Fig. 7.8F). The lowest velocities measured (0.06 – 0.08 m s^{-1}) were in the furthest lateral positions on the shielded sides of the parallel and oblique topography (Fig. 7.8C). Lateral velocities (UVP 4 to 6/7) decayed fastest from the axis during frontal and oblique confinement and decayed slowest from the axis on the confined margin of the laterally confined experiment (Fig. 7.8F). Lateral confinement had the fastest velocity decay from the axis on the unconfined margin, however. Lateral confinement also showed the greatest velocity decay on the furthest lateral margins (UVP 7 to 8) within the 'shadow' zone on the backside of the barrier.

7.5 *Discussion*

Topographically-forced hydraulic jumps

Two styles of topographically-forced transition between supercritical and subcritical flow and consequent hydraulic jump may be inferred from the depositional products of these experiments. One jump style is formed upstream of topography and the other is formed downstream of topography (Fig. 7.12; 13).

Upstream jumps are forced by sudden flow deceleration and thickening upstream of confining topography (Fig. 7.10C, D; 11; 12) (e.g. Alexander and Morris, 1994; Howlett et al. 2019), forming a thick ridge of sediment upstream of the barrier (Fig. 7.6C). Experimental granular pyroclastic density currents exhibit the same depositional pattern, depositing increasingly steep backsets until the topography of the backset is such that a 'granular jump' forms, forming an upstream-thickened deposit that is remarkably similar to that produced by this study (Smith et al. 2019). This 'granular jump' occurs in the absence

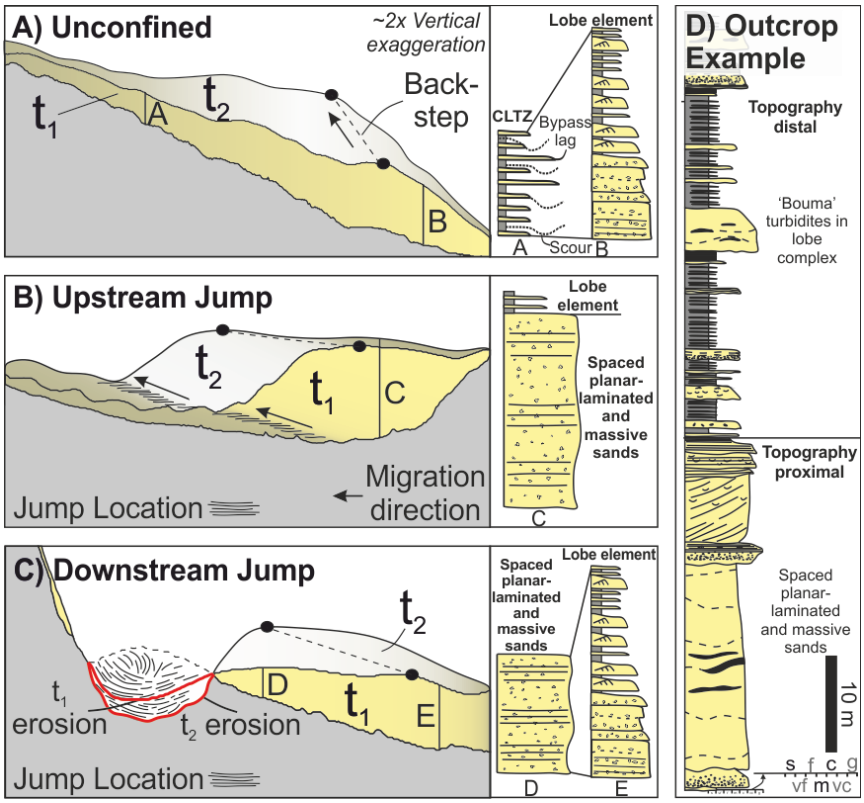

Figure 7.13: Schematic diagram showing the likely stacking pattern and outcrop representation induced by different styles of hydraulic jump seen across the runs. Facies downstream of jumps modified from Postma and Cartigny (2014). A) Back-stepping of lobes caused by the depositional relief of the underling deposit. B, C) Major back-stepping caused by an upstream hydraulic jump (B) or downstream (C) hydraulic jumps and erosion. These jumps form due to rapid deceleration at counter-slopes. The second deposit (t_2) in A, B and C is hypothetical. D) Logged section from the Annot Basin, SE France showing the potential field expression of hydraulic jump proximal deposition passing into hydraulic distal lobe deposition.

of topography, indicating that this style of jump may arise should flow be sustained for long enough to allow backsets to sufficiently steepen and decrease Fr_d of the incoming flow below unity. This was demonstrated within turbidity currents by Hamilton et al. (2017), who showed that as unconfined supercritical deposits aggrade their topography, eventually this forces deceleration and hydraulic jump formation within the incoming flow, resulting

in backset development and eventually avulsion. Pohl et al. (2019b) also experimentally demonstrated that such a jump was generated if the depositional topography become high enough to create an adverse slope (with an up-flow dip). These experiments show that this effect can be enhanced by the presence of pre-existing slope topography.

This hydraulic jump generation and migration process may be recorded stratigraphically as thick sandstones overlain by more 'typical' heterolithic lobe deposits (e.g. Prélat et al. 2009; Kane et al. 2017; Fig. 13B; D) where ancient incoming flows encountered topography, thickened and decelerated, and the overlying thinner-sandstones representing the down-dip expression of younger thick sandstones deposited upstream as the jump migrated landwards (Fig. 13B, C). Backsets may be present within the thick sandstone, indicating upstream aggradation. Such a stratigraphic relationship is seen at outcrop in the deep-marine Grès d'Annot of the bathymetrically-complex Cenozoic Alpine foreland basin (see Joseph and Lomas, 2004 for review), and may be attributed to oblique confinement and rapid deposition. There, thick amalgamated sandstones that appear to have aggraded rapidly adjacent to fault topography are overlain by heterolithic sandstones and mudstones that appear to be less confined and stack compensationally (Fig. 13D). Evidence for flow reflection, such as opposing paleocurrent values (e.g. Kneller et al. 1991), may also form upstream of the confining barrier should the reflected bore tractionally-rework the aggraded sediment (e.g. Edwards et al. 1994). Opposing paleocurrents are present at the base of the outcrop example presented in Fig. 13D, as predicted by Edwards et al. (1994).

Downstream jumps are formed downstream of topography when either: 1) supercritical flows descend and rapidly decelerate at the foot of an intra-basinal slope or 2) subcritical flows descend, accelerate and become supercritical down the slope, before decelerating at the foot of the slope and passing through a hydraulic jump (Fig. 7.11; 13C). Scouring of the slope (Fig. 7.13C) may occur in response to the development of strong vertical velocities within the hydraulic jump (Sumner et al. 2013), or, in the absence of a jump, as the flow impacts the slope and erodes the substrate, much like plunge-pools seen at the foot of slopes in seafloor bathymetry data ('impact pool' of Lee et al. 2002; Schnyder et al. 2018). Deposition downstream of the jump in nature may form a thick sequence of amalgamated sandstones that may correlate with more organised lobe deposits further down-dip (Amy et al. 2007; Lee et al, 2004) (Fig. 7.13C). Downstream hydraulic jumps may

be important in settings with steep intra-basinal slopes, such as fold-thrust belts (e.g. Amy et al. 2007; Vinnels et al. 2010), salt provinces (e.g Prather et al. 1998) or active margins (e.g. Harris and Whiteway, 2011). Due to the relatively high slope angle in these experiments it is possible that the flow accelerated and became supercritical once again downstream of the jump, or did not undergo a hydraulic jump and instead excavated the slope (Lee et al. 2002) and re-accelerated, before expanding across the slope and decelerating (Fig. 7.11D). The presence of steep slopes and topography may therefore allow the formation of multiple types of hydraulic jump upstream and downstream of

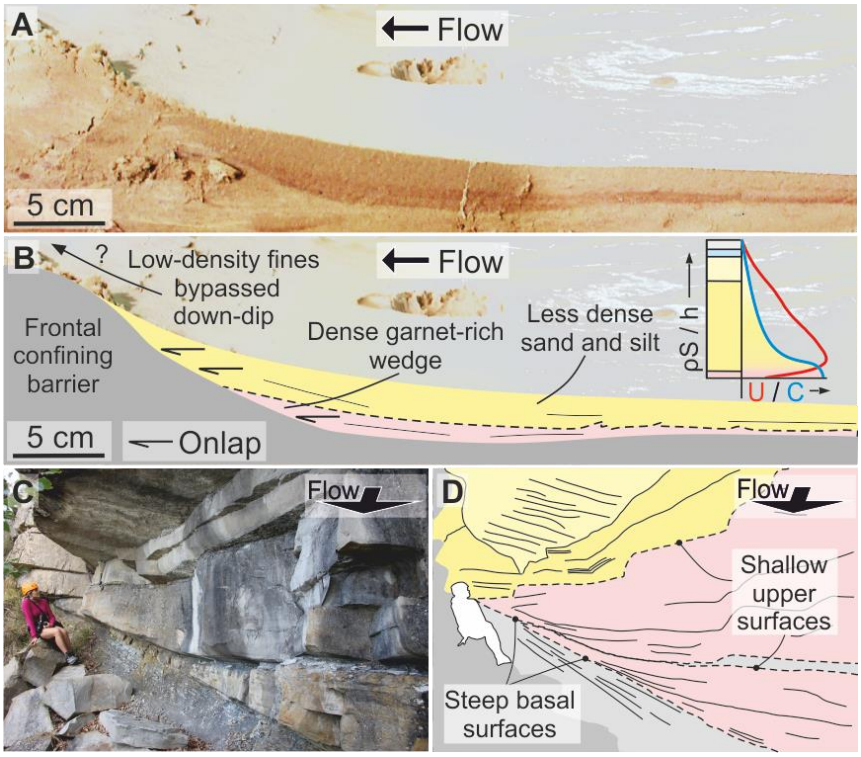

Figure 7.14: A) Uninterpreted and B) interpreted cross-section photographs from the upstream side of the frontally confining run. This section is taken ~20 cm off-axis. The image shows onlap of a red garnet-rich layer and layer onlap of a more sand-silt dominated layer. A schematic concentration-velocity profile is also indicated on B) based on the relative densities of the sediment that comprises the flow and from measured concentration profiles within supercritical flows (Sequerios, 2012) C) Uninterpreted and D) interpreted field expression of the onlap geometries seen on A and B from the Eocene- Oligocene Annot Basin, SE Frnace. The red shading highlights the wedged onlapping flows.

topography, and associated depositional heterogeneities.

Run-up of confined turbidity currents

Run-up, or 'superelevation', of turbidity currents and consequent deposition of turbidites high on counter-slopes has been noted in geophysical (e.g. Muck and

Underwood, 1990; Lamb et al. 2008), theoretical (e.g. Dorrell et al. 2018) and field (e.g. Soutter et al. 2019) investigations. Run-up has also been recognised in these experiments (Fig. 7.6C; 7A2, 3, 4; 7B2, 3, 4), with the dense and higher-concentration garnet-rich axis of the flow less able to run up the topography than the less dense sand-silt on the flow fringes, forming an onlapping red wedge against the barrier (Fig. 7.14A).

An example of this stratigraphic relationship can be seen in the Grès d'Annot turbidites of SE France, where distal low-density turbidites form a thin-bedded drape that healed the original tectonically-formed basin margin onlap surface (Soutter et al. 2019). This drape was subsequently onlapped by later turbidites, and is thus termed an intra-formational onlap surface (Fig. 7.15B). In the experiments of this study, the downstream deposit adjacent to the oblique barrier was thickest 90 cm away from the ridge, which it thinned towards (Fig. 7.7B). The lateral fringe of the deposit thinned and onlapped the slope of the topography, creating a relative low between the deposit centroid and the deposit onlapping the topography (Fig. 7.15A). A hypothetical subsequent turbidity current (t_2) would fill this relative bathymetric low, and onlap directly against the slope drape of the early deposit, and not the topographic barrier (Fig. 7.15A). These experiments provide evidence for this stacking pattern being a common feature of confined basins, and provide a mechanism for explaining abrupt coarsening-upward trends adjacent to basin margins (Fig. 7. 15B).

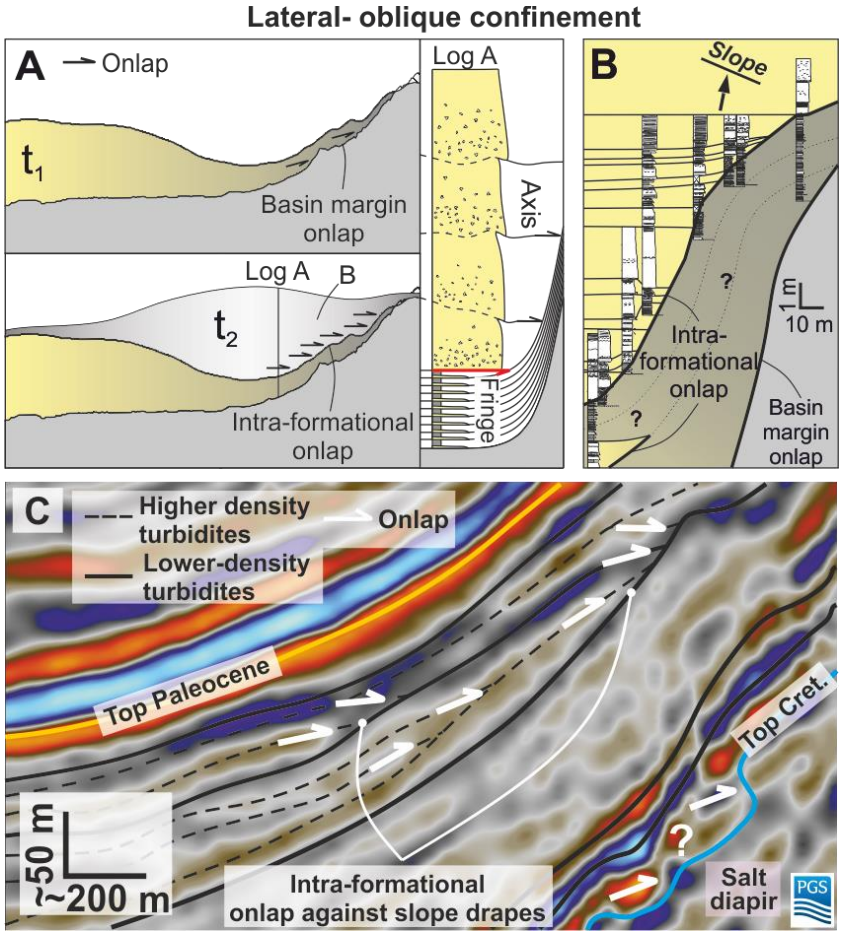

Figure 7.15: A) Schematic diagram showing the predicted deposition if another current (t_2) was able to deposit over the obliquely confined t_1, and the sedimentary log representation of that geometry. Allogenic onlap surfaces are generated by basinal tectonics, while autogenic onlap surfaces are generated by the depositional system, e.g. run-up of a low-density fringe. B) A field example from the Cenozoic Annot Basin (SE France) showing an onlap geometry that may have been formed in the same manner as A. Question marks indicate uncertainty in thin-bed correlation. C) Seismic example from a Paleocene deep-marine system of the North Sea. Sedimentary lobe deposits are interpreted to onlap topography created by a salt-diapir. More continuous reflections, which may represent thin-bedded turbidites, are offlaped and onlapped by subsequent reflections, which may represent the deposits of higher-density flows. Downward increase in acoustic impedance represented by a trough (blue reflection).

Seismic data from the Paleocene deep-marine system of the North Sea (see Mudge, 2015 for review) shows that this stacking pattern may be resolvable on relatively deep geophysical datasets (~25 m resolution), with reflections that appear to drape topography onlapped by subsequent reflections (Fig. 7.15C). This may represent lower-density turbidites forming a slope drape, with higher-density turbidites pinching-out against the drape. It should be noted that such a pattern could also be interpreted as being formed through subsidence or sediment supply variations (Sylvester et al. 2015) and the example in Fig. 7.15C is purely for visualisation purposes.

Implications for the interpretation of variably confined deep-water systems

These experiments highlight the morphological variation possible simply by changing the orientation of confining basin topography. This is synthesized on Figure 16, where a hypothetical active margin receives two consecutive periods of sustained sediment delivery (t_1 and t_2). Assuming no external or allogenic signature is recorded in the deposits, lobe elements in unconfined settings are expected to avulse and back-step (Hamilton et al. 2015, 2017; Ferguson et al. 2020) as each successive flow is influenced by depositional relief created by previous flows (Fig. 7.13A). This process is enhanced where flows are frontally or obliquely confined, as successive flows have to surmount both the barrier and the underlying thick sandstones (t1) that were deposited by previous flows at the barrier, thus trapping coarse-grains on the slope (Fig. 7.14) (Brunt et al. 2004) and causing a topographically-forced back-step (Fig. 7.16) that could be mis-interpreted as an external signal, such as decreasing sediment supply or sea-level rise.

Topographic orientation also affects the spatial distribution of individual flows. This is best seen where an individual flow is obliquely confined, resulting in two separate axial zones from one sediment input into the basin (Fig. 7.2D; 15). These disparate areas of positive relief will act to complicate compensational stacking patterns and therefore the correlation of units that are spatially distinct but time-equivalent. Bifurcation of deposits will also affect paleocurrent measurements, with two separate populations of paleocurrents in spatially separate areas (e.g. two separate exposures) representing deflection of turbidity currents and not a migrating sediment input point (Fig. 7.16). Lateral and oblique confinement may also affect lobe morphologies by preventing lateral expansion of turbidity currents and enhancing their ability to transport sediment basinward. This would cause a topographically-forced progradation that again could be mis-interpreted as an external signal, such as an increasing sediment supply or sea-level fall.

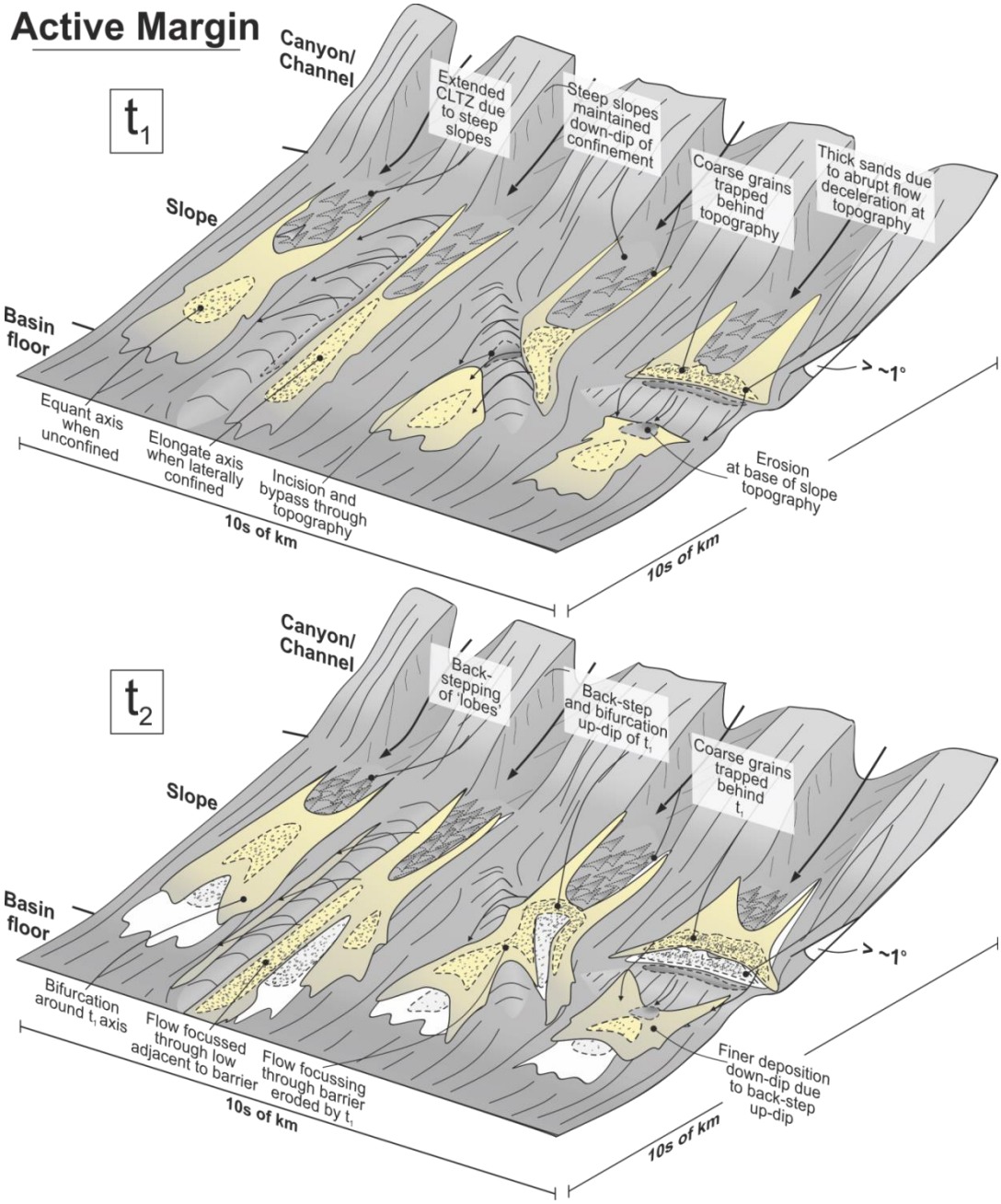

Figure 7.16: Summary schematic diagram showing the depositional features and stacking patterns that can be expected within steep and active margins based on these experiments. Initial deposition (t_1) is based on the experiments, while t_2 is hypothetical. Initial deposition (t_1) indicated by white fill on t_2.

Implications for resolving external signals

Recent subsurface investigations have highlighted the role transfer-zone topography may play in the manifestation of external signals in deep-water settings, and the implications of this for source-to-sink studies (Prather et al. 2017). This study further highlights the role of slope topography in the propagation of external signals. Deep-water systems characterised by flows moving parallel to basin structure will be expected to

maintain deposition farther into the basin than flows moving perpendicular to basin structure (Fig. 7.16; 17). This will result in more source-representative signals in sinks down-dip from transfer zones dominated by lateral confinement, such as axially sourced foreland basins (e.g. Salles, 2014), and more attenuated and delayed signals in sinks down-dip from transfer zones dominated by frontal confinement, such as fold-thrust belts (e.g. Vinnels et al. 2010) (Fig. 7.17). Frontal confinement may also effect signal detection by trapping signals on the slope (Fig. 7.17). These older signals (e.g. provenance mineralogy/isotopic signatures) may then be eroded and incorporated within later sediment pulses giving a false representation of the relative signal strength and age. Flows unconfined by basin margins may be the mid-case source-to-sink scenario, with part of the signal diluted through radial spreading of the flows and part of the signal delayed through flow deceleration (Fig. 7.17).

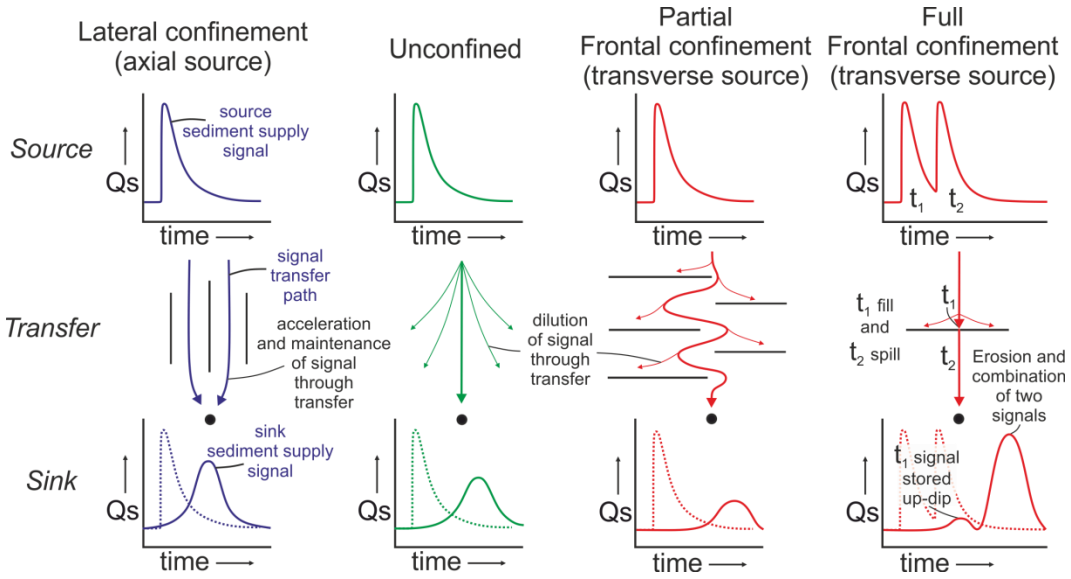

Figure 7.17: Rates of signal propagation and attenuation across bathymetrically-complex deep-marine margins (modified from Romans et al. 2016).

7.6 ***Conclusions***

Physical models of turbidity currents interacting with topographic barriers at incidence angles of 0°, 45° and 90° have been created in order to better understand the effect topography has on natural turbidity currents and their deposits. Unconfined turbidity currents are able to spread radially over the slope, forming a lobate deposit that thickens, then thins distally. Laterally confined turbidity currents are prevented from spreading on one side, forming an asymmetric deposit. Down-dip thinning rates are also reduced in a laterally confined setting, allowing flows to deposit farther into the basin. Oblique confinement resulted in an upstream deflected deposit and a downstream deposit, which

has implications for deposit correlation in deep-water subsurface and outcrop datasets. Frontal confinement caused lateral spreading, with inferred trapping of coarse grains higher on the slope, compared to unconfined deposits.

Two styles of topographically-forced hydraulic jump are inferred from these experiments. Upstream jumps are formed when flows rapidly decelerate upstream of slope topography, resulting in the deposition of thick sandstones up-dip of topography. Downstream jumps are formed downstream of topography and are caused by rapid deceleration of flows at the foot of the barrier, with slope erosion occurring at the foot of the barrier as the flow impacts the slope. The prevalence of these jump styles will be greater in deep-water environments capable of producing local and steep slopes e.g. fold and thrust belts and salt-influenced basins. The wide variation of depositional patterns produced by changing confinement highlights the need to appreciate the structural orientation of the confining margin with respect to sediment input, which will affect the prediction of sediment distribution and character adjacent to topography, the interpretation of stacking patterns in topographically-complex basins, and the propagation of external signals through deep-water transfer-zones.

CHAPTER 8: Synthesis

This chapter aims to address the research questions that were posed in Chapter 2 within the context of the results presented in Chapters 3 – 7. Future research questions and directions generated by this study are also proposed.

8.1 *What is the stratigraphic evolution of onlap in a confined deep-water basin?*

Different styles of pinchout and onlap have been described in exhumed and subsurface confined deep-water basins (e.g. Bakke et al. 2013). The generic models for onlap produced by these studies are often dualistic, with only two end-member styles described and little discussion of the stratigraphic evolution of onlap through the fill of a confined basin (e.g. Smith and Joseph, 2004). Numerical modelling has shown that the stratigraphic evolution of onlap can be used to infer the sediment supply and subsidence history of a confined basin (Sylvester et al. 2015), however internal factors, such as longitudinal flow evolution, are not incorporated into the model. Chapter 3 used the well-exposed onlap surfaces from the Annot Basin to show that internal factors have a major effect on onlap patterns, and that this effect is stratigraphically predictable.

External and internal controls on deep-water onlap

The results of Chapter 3 suggest that the stratigraphic evolution of flow-type and resultant deposit identified in confined lobes of Grès d'Annot records the progradation of a siliciclastic deep-water system, with the Annot Basin fill transitioning from predominantly distal lobe deposition, characterised by low-density turbidite deposition, to proximal lobe deposition, characterised by high-density turbidite deposition, through time. This progradation is suggested to have been driven by the external forces of sea-level and tectonism (Callec, 2004; Euzen et al. 2004; Puigdefàbregas et al. 2004), and is characterised in the Annot Basin by a coarsening-upward sequence of stacked lobes that each display similar vertical facies transitions as unconfined exhumed lobes (e.g. Hodgson et al, 2009). These vertical facies transitions record the building of lobes, and are interpreted to represent different lobe sub-environments. These sub-environments are broadly differentiated by a prevalence of flows of increasing concentrations as flows longitudinally evolve from proximal to distal parts of the basin. Internal topographic interaction and pinchout of each of these sub-environments against the Annot Basin margin forms a concentration-controlled onlap pattern that is stratigraphically predictable. A simple numerical model shows that the observations made in this study can be reproduced, with the low concentration flows able to run-up and deposit high on basin margins, and higher-

density flows less able to run-up the basin margin. Chapter 3 therefore proposed a numerical and field-supported stratigraphic evolution of onlap.

A predictable stratigraphic evolution of onlap

Initial siliciclastic deep-water deposition within a confined basin is represented by low-density turbidites of the distal lobe fringe, which run-up and drape the confining slope due to the low-concentration of their parent flows. Hybrid beds deposited by higher-concentration flows of the proximal lobe fringe will overly these deposits. These flows are less able to run-up topography due to their higher concentration, which will be will be recorded by abrupt onlap against the underlying lobe fringe that draped the slope, forming an intra-formational onlap surface that marks the transition between lobe sub-environments. Medium-density turbidites deposited by lower-concentration flows in the lobe off-axis overly hybrid beds of the proximal fringe, which will be recorded at onlap by flows more able to drape topography than the underlying deposits. High-density turbidites of the lobe axis represent the final stages of deposition which is manifested by their abrupt onlap against the basin margin, or intra-formational onlap against underlying low-density turbidites deposited high on the slope.

Onlap pattern interpretation

This stratigraphic evolution of onlap produces an autogenic onlap pattern characterised by landward and basinward shifts in onlap termination. This mimics onlap patterns formed through changing external controls on deep-water deposition (Sylvester et al. 2015), highlighting the complexity of using onlap patterns alone to reconstruct the history of confined basins. The scale of observation is also shown be important within this onlap model as internal processes will be more influential at smaller temporal scales than external processes, which may result in the onlap pattern described in Chapter 2 being below seismic-resolution or adding internal noise to externally-derived onlap patterns. Similar findings have recently been made by Sweet et al. (2019), who found that allogenic processes in the Quaternary Golo fan controlled system-scale lobe morphologies, while autogenic processes controlled internal lobe geometries.

Tectonism, in the form of progressive tilting of the basin margins, will also add noise to onlap patterns, with intra-formational onlap occurring as older beds are titled and subsequently onlapped. The interplay between both internal factors, such as flow type at

pinchout, and external factors, such as sediment supply and tectonism, therefore needs to be taken account when using onlap patterns to infer basin evolution.

8.2 ***Can you resolve external controls on a deep-water sedimentary system?***

Climate, tectonism and eustasy are the primary external controls on deep-water sedimentary systems. Disentangling the relative impacts of these processes on a given deep-water basin is often difficult due to poor chrono-stratigraphic resolution preventing robust links between tectonic, climatic or eustatic changes. An attempt to disentangle these controls was performed by Castelltort et al. (2017) using the $\delta^{13}C$ record of the Pyrenean foreland basin. The $\delta^{13}C$ record is sensitive to sea-level and climate and allowed Castelltort et al. (2018) show that periods of Pyrenean foreland deep-water deposition were controlled by eustasy and tectonism. Chapter 3 reproduced this methodology to resolve the external controls on deposition of the deep-water Grès d'Annot in the Eocene-Oligocene Alpine foreland basin using the Chalufy locality as an example.

Resolving external controls on deep-water deposition

The $\delta^{13}C$ record of fine-grained intervals at Chalufy, which are interpreted as periods of decreased sediment supply, correlates with time-equivalent sections of North Atlantic eustatic sea-level curves. Coarse-grained intervals between these fine-grained internals are interpreted to represent periods of submarine fan progradation, and correlate with periods of low or falling eustatic sea-level on these curves. Chapter 3 therefore suggests that deep-marine deposition in the Alpine foreland basin was enhanced by eustatic sea-level falls. These sea-levels falls are were caused by cooling events during the stepped transition from Eocene greenhouse conditions to Oligocene icehouse conditions, within the period known as the Eocene-Oligocene Transition (EOT). Climate change may therefore have also supported the growth of submarine fans by reducing hinterland vegetation during the cooling events, thus enhancing run-off into fluvial systems and sediment supply to the deep sea.

Chapter 3 also showed that deposition in the deep-water Alpine foreland was influenced by other external factors, with a period of fan delta aggradation and deep-marine channelization occurring during a eustatic highstand. This is inferred to have been caused by a transient increase in sediment supply during a period of tectonic deformation and uplift in the tectonically-active Corsica-Sardinia hinterland. This inferred sediment

supply increase would have outpaced accommodation creation during the rising sea-level, causing submarine fan advancement.

Can deep-water systems modulate their own external controls?

During the EOT cooling was enhanced by falling atmospheric CO_2 levels. Chapter 4 therefore also proposes that enhanced burial of organic carbon in growing submarine fans during these sea-level falls will have acted as a positive feedback on atmospheric CO_2 levels, with falling CO_2 levels causing cooling and glaciation, which dropped sea-levels and enhanced organic carbon burial in submarine fans, which further deceased CO_2 and cooling. The external controls of eustasy and climate may therefore both modulate, and be modulated by, deep-marine deposition.

8.3 *What is the response of a deep-water sedimentary system to tectonic activity?*

Chapter 4 showed that low eustatic sea-levels and cooler climates caused enhanced sediment supply to the Paleogene Alpine foreland deep-water basin, with deposition during high eustatic sea-levels inferred to have been driven by a period of hinterland uplift and erosion. Deep-water deposition in the Paleogene post-rift North Sea has also been shown to be influenced by hinterland uplift (e.g. White and Lovell, 1997).

Response of a deep-water basin to tectonism

Chapter 5 shows that the initial plume-induced tectonic perturbation at ~63 Ma was associated with widespread mass-transport in the deep-marine North Sea Basin. This is most clearly resolved by the emplacement of a major mass-transport-complex (MTC) in the Central Graben, which was termed the 'Halibut Slide'. The Halibut Slide body is ~200 km long and ~30 km wide, making it the largest MTC discovered in an epicontinental basin. Scours ~1 km wide and ~150 m deep indicate the Slide was derived from the paleoshelf in the Moray Firth, which is located close to major fault zones that were reactivated by both plume-induced tectonic perturbations and the Alpine orogeny. Chapter 5 therefore suggested that this reactivation and associated seismicity caused instability around the North Sea, resulting in the emplacement of the Halibut Slide and other MTCs deep in the basin.

As plume-related dynamic uplift continued during the Paleocene siliciclastic systems were able to establish themselves and prograde across on the shelf, resulting in the deposition of extensive sand-rich submarine fans across the North Sea. The distribution of

these fans was influenced by the topography of the early mass-transport-dominated period for 10 million years and into the early Eocene. Similar patterns have been observed in Paleocene deep-water systems of the eastern North Sea, with sand-dominated channel-fills and lobe complexes prograding over an early mass-transport-dominated interval during a period of tectonic perturbation (Sømme et al. 2019). The results of Chapter 4 are also in line with these findings, with sand-dominated channel fills inferred to form during a period of hinterland tectonism in the Alpine foreland. The lack of a mass-transport-dominated interval in the Alpine foreland may be due to its much smaller size and shorter depositional duration, which would have prevented the build-up of significant thicknesses of sediment on the slope. The North Sea accumulated significant thicknesses of sediment during post-rift tectonic quiescence through the Cretaceous, thus making the basin susceptible to mass-failure when tectonism initiated.

A generic model

Chapter 5 therefore shows that the sedimentary response of a deep-water basin to tectonic activity is characterised initially by intra-basinal mass-transport as the system is brought out of equilibrium by tectonic rejuvenation. As the erosional products of the uplifted hinterland begin to reach the deep-sea sand-rich submarine fans are able to build and prograde. These newly-established deep-water systems will be affected by both the magnitude of the external tectonic processes, e.g. uplift rates, and by internal influences, such as the depositional topography of the initial mass-transport-dominated period. As the hinterland equilibrates to the new tectonic regime sediment supply will decrease and submarine fan deposition will either be reduced or controlled by other external factors.

8.4 *What is the stratigraphic evolution of a mixed deep-water system on an unstable margin?*

Chapters 3 and 4 showed the way in which a deep-water basin may be affected by topography and eustasy, and chapter 5 showed how topography and tectonism may affect a deep-marine basin. Chapter 6 assessed the exportability of these findings by investigating the stratigraphic evolution of the Cretaceous post-rift Buduq Trough, Eastern Greater Caucasus, Azerbaijan. This study also resulted in important contributions to the poorly-understood sedimentology and stratigraphy of mixed-siliciclastic-carbonate deep-water systems, and assessed the applicability of using purely siliciclastic deep-water systems as analogues.

Exhumed evolution of an unstable margin

The stratigraphic evolution of the Buduq Trough is represented by four stages: 1) Early Cretaceous slope instability and mass-transport, 2) Aptian-Albian thin-bedded and fine-grained siliciclastic lobe deposition, 3) Cenomanian-Turonian coarse-grained submarine channel deposition, and 4) Conacian-Maastrichtian mixed siliciclastic-carbonate lobe deposition. Each of these stages records basin-external events related to compression during the opening of the Black Sea to the west, and eustatic sea-level fluctuations. Early Cretaceous mass-transport and Cenomanian-Turonian channel deposition, for example, occur in response to regional compressional events. The reason for the contrasting depositional response to these events may be the same as within the Paleogene North Sea (Chapter 5), with early tectonic perturbations causing mass-transport and later tectonic perturbations causing progradation of now-established siliciclastic systems. The generic model for the response of a deep-water basin to tectonic activity outlined in Chapter 5 therefore informs the understanding of the Buduq Trough in Chapter 6.

The results of Chapter 5 also predict the topographic control seen on deposition in the Buduq Trough, with Early Cretaceous mass-transport in the Trough affecting deep-water depositional patterns throughout the remainder of the Cretaceous period, further indicating that the generic stratigraphic model outlined in the previous section to ongoing tectonism may be commonplace in other deep-water basins, and that the generic model outlined in the previous section is valid.

Mixed systems as a warning for the interpretation of single-lithology systems?

The sedimentological evolution of the Buduq Trough (Chapter 6) is similar to that of the Paleogene North Sea (Chapter 5), with both systems characterised by periods of contemporaneous siliciclastic and carbonate deposition that are inferred to have different provenances. This was shown from Chapter 6 to result in a complex vertical relationship, where the proximal and distal components of each system intersect and interact, thus making stacking pattern interpretations difficult. This complexity was only identifiable due to the obvious difference in the lithology between the two systems.

In systems characterised by a single lithology, e.g. siliciclastics, it would be almost impossible to identify such a complexity at outcrop, with a given succession almost always inferred to be sourced from the same point throughout its depositional duration. This may

lead to erroneous stacking pattern interpretations, with apparently disorganised strata actually reflecting progradation of one system and retrogradation of another in response to changing hinterland drainage, for example. This highlights the need, where possible, to compliment field-based observations with further analytical methods, such as isotope geochemistry (Chapter 4) or provenance analysis (Kilhams et al., 2014), in order to better constrain the external or internal influences on a given system.

8.5 *What effect does topographic orientation have on confined turbidity currents?*

The topographic controls on deep-water sedimentology and stratigraphy discussed in Chapters 3 – 6 were investigated using the deposits of sediment-gravity flows. These deposits were either studied via well-exposed but often incomplete outcrops, or from subsurface data of limited resolution. There is therefore a need to understand how the parent flows responded to topography, and how their deposits may have looked in their entirety. Chapter 7 addressed this by presenting results from experimental models designed to both simplify and mimic the topography that affected deposition in Chapters 3 – 6.

Four experiments were performed: unconfined, parallel confinement, oblique confinement and frontal confinement. Each of these experiments differentially affected flow velocities and deposits, highlighting the potential impact of topographic orientation on deep-water systems.

Application to exhumed and subsurface basins

The results of Chapter 7 recreated some of the topographic controls on deposition discussed in Chapters 3 – 6, and generated new insights for features described in these Chapters. The experimental results, for example, provided insights into the influence of topography on supercritical flows, which are becoming increasingly recognised as important builders of deep-water stratigraphy. The wedged and steep-faced deposits formed up-dip of topography in Chapter 7 have been explained by upstream-migrating hydraulic jumps formed due to rapid deceleration of supercritical flows in this study and others (e.g. Morris and Alexander, 1994). Chapter 7 also expanded on existing facies models for supercritical deposits built on outcrop and modern observations (e.g. Postma and Cartigny, 2014) to hypothesize on the nature of the facies that would be expected in topographically-affected supercritical deposits. Thick sequences of retrogradational massive and planar-laminated sandstones, for example, are expected upstream of topography, while

slope erosion and plunge-pool formation are expected immediately downstream of topography.

This model-based prediction has been used to hypothesize that the formation of thick and coarse sandstones upstream of a fault scarp in Chapter 3 may be attributed to such processes. Chapter 7 also recreated the run-up and onlap described in Chapter 3, further reinforcing the ideas proposed regarding onlap evolution in that chapter. Seismic visualization of this run-up from the Central Graben of the North Sea provided a subsurface analogue for the onlap hypothesized in Chapter 3 and illustrated in Chapter 7, indicating that this stratigraphic pattern may be resolvable in the subsurface and common in deep-water basins.

Topographic influences on external signal transfer

Chapter 4 showed that external factors affecting the Alpine foreland basin were transported efficiently to deep-water, thus allowing a signal to be recorded and resolved. Chapter 7 provides a mechanism to explain why this might be the case, with topographic orientation exerting a control on how much of the external signal (the experiment flow) is transferred to the deep basin (the lower slope of the flume tank). Lateral confinement, much like the confinement that characterizes large sections of the Alpine foreland basin, allows more of the signal to transferred into the basin, while oblique and frontal confinement traps the signal on the slope. A lack of confinement may also act to reduce the signal preservation through flow expansion and dilution, and complications arising through compensational stacking. This indicates that the reason for the effective resolution of external signals in the Chapter 4 may have been due to the regional lateral confinement of the Alpine foreland basin transporting the signal basinwards. The external influence of enhanced sediment supply to deep-water and consequent progradation was therefore enhanced by the influence of basinal topography. The ability for the signal to be resolved by the methods of Chapter 4 was also therefore enhanced.

8.6 *Future research directions*

Stratigraphic evolution of onlap in outcrop and subsurface

The stratigraphic evolution of onlap outlined in Chapter 3 is based on field observations from the Annot Basin coupled with a simple numerical model. Future research should seek to identify the comparative onlap patterns in other exhumed basins or in the subsurface. The Grand Coyer basin, for example, is immediately down-dip of the

Annot Basin, and appears to display many of the features described in Chapter 3 (Stanbrook et al. 2004). There therefore appears to be potential for reappraising the onlap surfaces of this, and other, Grès d'Annot basins in light of the findings in Chapter 3.

Subsurface basins with extensive lithological and seismic data coverage, such as the Gulf of Mexico and North Sea, would be ideal for future subsurface assessments of the model, however they may lack the resolution to accurately trace seismic reflections representing lithological transitions toward onlap. Shallower seismic with higher resolution, such as around the Golo fan in Corsica (Gervais et al. 2004; Sweet et al. 2019), may mitigate against this, however there is less lithological control. Synthetic seismic models (e.g. Bakke et al. 2013) may also allow for both lithological and seismic assessment of the model, and may be tested across different resolutions to see what resolution is required to identify lobe sub-environment transitions and consequent onlap patterns in confined basins.

Tracking external signals

The use of isotope geochemistry as a tool for resolving external controls on deep-water deposition has proven to be successful in the Pyrenean (Castelltort et al. 2018) and the Alpine foreland basin (Chapter 4). Extension of this research is proposed in two directions: 1) detailed geochemical correlation in the Alpine foreland and 2) geochemical investigation of other deep-water basins.

Extensive outcrop belts of the Grès d'Annot have been chrono-stratigraphically correlated around the Alpine foreland basin. These outcrops contain frequent fine-grained hemipelagic intervals that should record the same signals as resolved in the Chalufy outcrop along with greater constraint on controls prior to Chalufy deposition, such as at Peïra Cava, and after Chalufy deposition, such as at Barrême. An integration of all these geochemical records could provide more information on how external controls on Alpine deposition varied across longer time-scales, and if the depositional response to climate and eustasy identified in Chapter 4 was always similar.

Application of the methods outlined in Chapter 4 should also be applied to other deep-water basins where chrono-stratigraphic correlation exists. It would be particularly important to extend the method to basins in different tectonic settings, such as rift and post-rift basins. The Pleistocene Gulf of Corinth rift basin (e.g. Cullen et al. 2019) and

Cretaceous Baja California post-rift basin (e.g. Kneller et al. 2019), for example, are well-studied deep-water basins with excellent chrono-stratigraphic constraint that would greatly benefit from the potential insights derived from this method.

Cretaceous of the Eastern Greater Caucasus

Chapter 6 presented the stratigraphic evolution of the Buduq Trough within the Eastern Greater Caucasus, Azerbaijan. There remains, however, extensive outcrops of Cretaceous-aged sediments in other structural zones within the Greater Caucasus. Future research should focus on extending the sedimentological and stratigraphic findings of Chapter 6 across the entire Cretaceous post-rift basin. This would increase understanding of both the palaeogeographic evolution of the basin, such as sediment input points and lateral-distal facies variations, and the response of the basin to the external controls outlined in Chapter 6, such as whether tectonic activity was a greater influence on the stratigraphic record of the basin closer to the locus of activity in the Black Sea toward the west.

Physical modelling extension

It is suggested that extensions to the physical models described in Chapter 7 should focus on: 1) performing scalable experiments on erodible topographic barriers with different geometries, such as salt-diapir-analogous mounds, 2) performing experiments with multiple confining topographic barriers on one slope, such as two laterally confining barriers, 3) releasing sequential flows into the basin to assess the stacking pattern predictions made in this study, and 4) using barriers of different heights and steepness to compare how flows and their deposits are influenced by varying degrees of confining relief.

These additional experiments would further constrain the findings of Chapter 7 and allow for experimental validation of many hypotheses proposed for deposition in salt-diapir influenced basins. Releasing sequential flows onto topographically-affected slopes would be particularly beneficial as stacking patterns in confined basins remain poorly understood due to 3D control on stacking patterns being rare, as discussed through the Le Ray correlation of Chapter 3. Future experimental models of stacking patterns may therefore be the most suitable method for tackling this research problem. Varying barrier height and steepness would be useful for assessing run-up of turbidity currents, flow stratification and the topographic limits of hydraulic jump formation.

CHAPTER 9: Conclusions

- An outcrop- and numerically-derived model for the stratigraphic evolution of onlap is proposed. During lobe progradation into a confined basin the first flows to reach the basin margin will be of a low-concentration due to longitudinal flow dilution. These low-concentration flows will be less dense and therefore more capable of flowing up counter-slopes, resulting in low-density turbidites deposited high on confining basin margins. Higher-concentration hybrid flows formed in the proximal fringe will follow these lower-concentration flows, resulting in intra-formational onlap against the fringe deposited higher on the slope. Continued progradation will further complicate these onlap patterns as flows lower in concentration and more able to run-up counter-slopes in the off-axis, and higher-concentration and less able to run-up counter-slopes in the axis. The resulting onlap trends will follow a predictable landward and basinward pinchout pattern, which is numerically predicted through the negative correlation between sediment-gravity-flow run-up height and concentration.

  These internally-modulated onlap patterns will obscure the externally-modulated onlap patterns created by sediment supply and subsidence variations. Future use of onlap patterns as indicators of changing external factors should therefore appreciate the effect that internal processes have on onlap patterns.

- External influences on deep-water deposition are shown to be resolved within the sedimentological, stratigraphic and geochemical record of a deep-water system. The $\delta^{13}C$ record of the Grès d'Annot of the Eocene-Oligocene Alpine foreland indicates that periods of submarine fan progradation correlate with cooling events associated with the transition from Eocene greenhouse to Oligocene icehouse conditions (EOT). These cooling events increased hinterland aridity and lowered sea-levels. This is inferred to have increased hinterland erosion rates and sediment supply to fluvio-deltaic systems that were able to quickly prograde across the shallow or exposed shelf and deposit sediment directly in deeper-waters. A period of coarse-grained deep-water deposition also occurred during highstand, indicating sediment supply was able to compete with accommodation creation during this period. This increase in sediment supply is suggested to have been caused by uplift and erosion of the tectonically-active Corsica-Sardinia massif to the south. The relative influence of climate, eustasy and tectonism on the stratigraphic record of the Eocene-Oligocene Alpine foreland therefore changed through time, with tectonism periodically overriding the climatic and eustatic influence.

It is also proposed that the global submarine fan growth and consequent increased burial of terrigenous organic carbon during these EOT cooling steps acted as an important global carbon sink, which helped reduced CO_2 levels in the atmosphere and aid the transition from greenhouse to icehouse conditions. Submarine fans are therefore modulators of the external factors that affect their deposition.

- The stratigraphic evolution of the Paleogene deep-water system within the North Sea Central Graben is shown to be heavily influenced by external tectonism associated with the early phases of mantle plume impingement and North Atlantic formation. Initial tectonic rejuvenation caused widespread slope instability and voluminous mass-transport deposition, such as emplacement of the ~200-km long Halibut Slide. As tectonism and hinterland uplift continued sand-rich deep-marine systems were established in the Central Graben. Deposition in these systems were controlled by both external tectonism and internal topography that was formed by the early mass-transport relief, remnant Mesozoic rift topography, and salt diapirism.

  This stratigraphic evolution is shown to be repeated in the Cretaceous-aged Buduq Trough of the Easter Greater Caucasus - an analogous post-rift basin. There, tectonic activity associated with opening of the Black Sea caused widespread mass-transport. This mass-transport acted to control the sedimentological and stratigraphic evolution of later siliciclastic systems. The identification of this stratigraphic pattern in two separate basins indicates that such a pattern may be common in analogous deep-water basins affected by external forces, with the initial depositional response to the external response acting as internal influence on subsequent depositional responses.

- Deep-water systems characterised by contemporaneous siliciclastic and carbonate sediment-gravity-flow deposition are shown to display facies, facies associations and stacking patterns that vary from their siliciclastic counterparts. Mixing of the two systems results in 1) mixed-event-beds that record differing aggradation rates between finer-grained carbonate and coarser-grained siliciclastic flows, 2) the need to interpret a given vertical section with separate carbonate, siliciclastic and mixed facies associations, and 3) internal modulation of each system by the other resulting in a loss of identifiable stacking patterns.

- Experimental turbulent flows and their deposits are shown to be heavily influenced by the orientation of topography they interact with. Laterally-confined flows are accelerated relative to unconfined flows, and deposit farther into the basin. Obliquely-confined flows form two separate areas of thickened deposition, with part of the deposit deflected upstream of topography and part of the deposit able to surmount the topography and deposit downstream. Oblique confinement also causes significant velocity increases upstream of topography and consequently significant erosion of the confining topography. Frontal-confinement causes deflection and deposition upstream of topography and erosion downstream of topography. Flow criticality is also shown to be important, with thickened deposition upstream of topography inferred to be caused by sudden deceleration and hydraulic jump formation. These experimental observations are also inferred to explain some of the bedforms observed in the Grès d'Annot.

  These experiments highlight the control that variable basin-internal topography has on 1) the erosive capabilities of flows, 2) the distribution of the deposits of these flows, 3) the potential complexity of stacking patterns produced by variable topography, and 4) the effect that topographic orientation will have on the ability of a deep-water system to record external signals affecting deposition, with lateral confinement aiding signal transfer and oblique frontal confinement potentially slowing or complicating signal transfer.

CHAPTER 10: References

Abhari, M.N., Iranshahi, M., Ghodsian, M. and Firoozabadi, B., 2018, Experimental study of obstacle effect on sediment transport of turbidity currents: Journal of Hydraulic Research, p. 1-12.

Abreu, V., Sullivan, M., Pirmez, C., and Mohrig, D., 2003, Lateral accretion packages (LAPs): An important reservoir element in deep water sinuous channels: Marine and Petroleum Geology, v. 20, p. 631–648, doi: 10.1016/j.marpetgeo.2003.08.003.

Ahmad, R., and Afzal, J., 2012, Sequence Stratigraphy of the Mixed Carbonate-Siliciclastic System of the Eocene Nisai Formation, Pishin Basin: Distribution of Source Rocks and Reservoir Facies

Ahmadi, Z.M., Sawyers, M., Kenyon-Roberts, S., Stanworth, C.W., Kugler, K.A., Kristensen, J., and Fugelli, E.M.G., 2003, Paleocene, in Evans, D., ed., The Millennium Atlas: Petroleum Geology of the Central and Northern North Sea: Geological Society of London, p. 235–259.

Advokaat, E.L., van Hinsbergen, D.J., Maffione, M., Langereis, C.G., Vissers, R.L., Cherchi, A., Schroeder, R., Madani, H. and Columbu, S., 2014, Eocene rotation of Sardinia, and the paleogeography of the western Mediterranean region: Earth and Planetary Science Letters, v. 401, p. 183-195.

Aehnelt, M., Worden, R.H., Canham, A.C., Hill, S.J., Hodgson, D.M., and Flint, S.S., 2013, Geochemical correlation in an exhumed submarine channel complex (Tabernas Basin, SE Spain): Comparison to sedimentological correlation at various length scales: Journal of Sedimentary Research, v. 83, p. 669–690, doi: 10.2110/jsr.2013.41.

Al Ja'Aidi, O.S., 2000, The influence of topography and flow efficiency on the deposition of turbidites. Unpublished PhD thesis. University of Leeds, UK, 162 p.

Al Ja'Aidi, O.S., McCaffrey, W.D., and Kneller, B.C, 2004, Factors influencing the deposit geometry of experimental turbidity currents: implications for sand-body architecture in confined basins, in Lomas, S., and Joseph, P., eds., Confined Turbidite Basins: Geological Society of London, Special Publication 222, p. 45–58.

Al-Mashaikie, S., and Mohammed, Y., 2017, Anatomy of carbonate breccias, turbidite facies and depositional systems of Gercus Formation, in Donkan Area, Northern Iraq.

Alexander, J., 2008, Bedforms in Froude-supercritical flow: Marine and River Dune Dynamics, Leeds, p. 1-5.

Alexander, J and Morris, S., 1994, Observations on experimental, nonchannelized, high-concentration turbidity currents and variations in deposits around obstacles. Journal of Sedimentary Research, v. 64, p. 899-909.

Allen, J.R.L., 1985, Principles of Physical Sedimentology: London, George Allen & Unwin, 272 p.

Allen, P. A. 1997. Earth surface processes. Oxford, Blackwell Science, 404 p

Allen, P.A., 2008, From landscapes into geological history: Nature, v. 451, p. 274–276.

Allin, J.R., Hunt, J.E., Clare, M.A. and Talling, P.J., 2018, Eustatic sea-level controls on the flushing of a shelf-incising submarine canyon: GSA Bulletin, v. 130, p. 222-237.

Alfaro, E. and Holz, M., 2014, Seismic geomorphological analysis of deepwater gravity-driven deposits on a slope system of the southern Colombian Caribbean margin: Marine and Petroleum Geology, v. 57, p. 294-311.

Allin, J.R., Hunt, J.E., Clare, M.A. and Talling, P.J., 2018. Eustatic sea-level controls on the flushing of a shelf-incising submarine canyon: GSA Bulletin, v. 130, p. 222-237.

Altinakar, M.S., Graf, W.H. and Hopfinger, E.J., 1996, Flow structure in turbidity currents: Journal of Hydraulic Research, v. 34, p. 713-718.

Alves, T.M., 2010, 3D Seismic examples of differential compaction in mass-transport deposits and their effect on post-failure strata: Marine Geology, v. 271, p. 212-224.

Amy, L.A., McCaffrey, W.D., and Kneller, B.C., 2004, The Influence of a lateral basin-slope on the depositional patterns of natural and experimental turbidity currents, in Lomas, S., and Joseph, P., eds., Deep-Water Sedimentation in the Alpine Basin of SE France: New Perspectives on the Grès d'Annot and Related Systems: Geological Society of London, Special Publication 221, p. 311-330.

Amy, L.A., Talling, P.J., Peakall, J., Wynn, R.B. and Thynne, R.A, 2005, Bed geometry used to test recognition criteria of turbidites and (sandy) debrites. Sedimentary Geology, v. 179, p. 163-174.

Amy, L.A., Kneller, B.C. and McCaffrey, W.D., 2007, Facies architecture of the Gres de Peira Cava, SE France: landward stacking patterns in ponded turbiditic basins: Journal of the Geological Society, v. 164, p. 143-162.

Anderson, K.S., Graham, S.A. and Hubbard, S.M., 2006, Facies, architecture, and origin of a reservoir-scale sand-rich succession within submarine canyon fill: insights from Wagon Caves Rock (Paleocene), Santa Lucia Range, California, USA: Journal of Sedimentary Research, v. 76, p. 819-838.

Apps, G, 1987, Evolution of the Grès d'Annot Basin, SW Alps: Ph.D. thesis, University of Liverpool, 434 p.

Apps, G.M., Peel, F.J., Travis, C.J. and Yeilding, C.A., 1994, Structural controls on Tertiary deep water deposition in the northern Gulf of Mexico. In: Submarine Fans and Turbidite Systems: SEPM Foundation, Gulf Coast Section, p. 1-7.

Apps, G., Peel, F., and Elliott, T., 2004, The structural setting and palaeogeographical evolution of the Grès d'Annot basin. in Lomas, S., and Joseph, P., eds., Deep-Water Sedimentation in the Alpine Basin of SE France: New Perspectives on the Grès d'Annot and Related Systems: Geological Society of London, Special Publication 221, p. 65-96.

Araya, T., and Masuda, F., 2001, Sedimentary structures of antidunes: An overview; Journal of the Sedimentological Society of Japan, v. 53, p. 1-15.

Armitage, D.A., Romans, B.W., Covault, J.A. and Graham, S.A., 2009, The influence of mass-transport-deposit surface topography on the evolution of turbidite architecture: The Sierra Contreras, Tres Pasos Formation (Cretaceous), southern Chile: Journal of Sedimentary Research, v. 79, p. 287-301.

Azpiroz-Zabala, M., Cartigny, M.J., Sumner, E.J., Clare, M.A., Talling, P.J., Parsons, D.R. and Cooper, C., 2017a. A general model for the helical structure of geophysical flows in channel bends: Geophysical Research Letters, v. 44, p. 11-932.

Azpiroz-Zabala, M., Cartigny, M.J., Talling, P.J., Parsons, D.R., Sumner, E.J., Clare, M.A., Simmons, S.M., Cooper, C., and Pope, E.L., 2017b, Newly recognized turbidity current structure can explain prolonged flushing of submarine canyons: Science Advances, v. 3, e1700200.

Baas, J.H., 2004, Conditions for formation of massive turbiditic sandstones by primary depositional processes: Sedimentary Geology, v. 166, p. 293-310.

Baas, J.H., Van Kesteren, W. and Postma, G., 2004, Deposits of depletive high-density turbidity currents: a flume analogue of bed geometry, structure and texture: Sedimentology, v, 51, p. 1053-1088.

Baas, J.H., and Best, J.L., 2002, Turbulence modulation in clay-rich sediment-laden fl ows and some implications for sediment deposition: Journal of Sedimentary Research, v. 72, p. 336–340,

Baas, J.H. and Best, J.L., 2008, The dynamics of turbulent, transitional and laminar clay-laden flow over a fixed current ripple: Sedimentology, v. 55,p. 635–666.

Baas, J.H., Best, J.L., Peakall, J. and Wang, M., 2009, A phase diagram for turbulent, transitional and laminar clay suspension flows: Journal of Sedimentary Research, v. 79, p. 162-183.

Baas, J.H., Best, J.L., and Peakall, J., 2011, Depositional processes, bedform development and hybrid bed formation in rapidly decelerated cohesive (mud-sand) sediment flows: Sedimentology, v. 58, p. 1953-1987.

Baas, J., Best, J. and Peakall, J., 2016, Predicting bedforms and primary current stratification in cohesive mixtures of mud and sand: Journal of the Geological Society, v. 173, p. 12-45.

Baas, J.H., McCaffrey, W.D., Haughton, P.D.W. and Choux, C., 2005, Coupling between suspended sediment distribution and turbulence structure in a laboratory turbidity current: Journal of Geophysical Research: Oceans, v. 110, p. 1–20.

Bagnold, R., 1966, An approach to the sediment transport problem from general physics: U.S. Geological. Survey Professional Paper, v. 422, p. I1–I37.

Baker, M.L., Baas, J.H., Malarkey, J., Jacinto, R.S., Craig, M.J., Kane, I.A. and Barker, S., 2017, The Effect of Clay Type On the Properties of Cohesive Sediment Gravity Flows and Their Deposits: Journal of Sedimentary Research, v. 87, p. 1176-1195.

Bakke, K., Kane, I.A., Martinsen, O.J., Petersen, S.A., Johansen, T.A., Hustoft, S., Jacobsen F.H., and GrotH, A., 2013, Seismic modeling in the analysis of deep-water sandstone termination styles: American Association of Petroleum Geologists, Bulletin, v. 97, p. 1395-1419.

Bao, R., Strasser, M., McNichol, A.P., Haghipour, N., McIntyre, C., Wefer, G. and Eglinton, T.I., 2018, Tectonically-triggered sediment and carbon export to the Hadal zone. Nature communications, v. 9, p. 121.

Barker, S.P., Haughton, P.D.W., McCaffrey, W.D., Archer, S.G., and Hakes, B, 2008, Development of rheological heterogeneity in clay-rich high-density turbidity currents: Aptian Britannia Sandstone Member, UK continental shelf: Journal of Sedimentary Research, v. 78, p. 45–68.

Basilici, G., Vieira de Luca, P. H. and Poiré, D. G., 2012, Hummocky cross-stratification-like structures and combined-flow reipples in the Punta Negra Formation (Lower-Middle Devonian, Argentine Precordillera): A turbiditic deep-water or storm-dominated prodelta inner-shelf systems?: Sedimentary Geology, v. 267-268, p. 73-92.

Barton, M., O'Byrne, C., Pirmez, C., Prather, B., Van der Vlugt, F., Alpak, F.O. and Sylvester, Z., 2010, Turbidite channel architecture: Recognizing and quantifying the distribution of channel-base drapes using core and dipmeter data: AAPG Memoir, v. 92, p. 195-210.

Beaubouef, R.T., and Friedmann, S.J., 2000, High resolution seismic/sequence stratigraphic framework for the evolution of Pleistocene intra slope basins, western Gulf of Mexico: depositional models and reservoir analogs, in: Deep-Water Reservoirs of the World: Gulf Coast Section SEPM 20th Annual Research Conference, p. 40-60.

Berggren, W. A., Kent, D. V., Swisher, C. C. & Aubry, M.-P, 1995, Geochronology, Time Scales and Global Stratigraphic Correlations: A Unified Temporal Framework for an Historical Geology, eds Berggren, W. A., Kent, D. V. & Hardenbol, J.: SEPM, p. 129–212.

Bell, D., Kane, I.A., Pontén, A.S., Flint, S.S., Hodgson, D.M., and Barrett, B.J., 2018a, Spatial variability in depositional reservoir quality of deep-water channel-fill and lobe deposits: Marine and Petroleum Geology, v. 98, p. 97-115.

Bell, D., Stevenson, C.J., Kane, I.A., Hodgson, D.M. and Poyatos-Moré, M., 2018b, Topographic controls on the development of contemporaneous but contrasting basin-floor depositional architectures: Journal of Sedimentary Research, v. 88, p. 1166-1189.

Bell, H.S., 1942, Density currents as agents for transporting sediments: The Journal of Geology, v. 50, p. 512-547.

Bersezio, R., Felletti, F. and Micucci, L., 2005, Statistical analysis of stratal patterns and facies changes at the terminations of "turbiditic" sandstone bodies: the Oligocene Cengio Unit (Tertiary Piedmont Basin): GeoActa, v. 4, p. 83-104.

Blair, T.C. & McPherson J.G., 1999, Grain-size and textural classification of coarse sedimentary particles: Journal of Sedimentary Research, v. 69, p. 6-19.

Bochud, M., 2011, Tectonics of the Eastern Greater Caucasus in Azerbaijan (Doctoral Dissertation, University of Freiburg). p. 202.

Boulesteix, K., Poyatos-More, M., Flint, S.S., Taylor, K., Hodgson, D.M., and Hasiotis, T. M., 2019a, Transport and deposition of mud in deep-water environments: processes and stratigraphic implications: Sedimentology, v. 66, p. 2894-2925.

Boulesteix, K., Poyatos-Moré, M., Flint, S., Hodgson, D.M., Taylor, K.G., and Parry, G.R. 2019b, Sedimentary facies and stratigraphic architecture of deep-water mudstones beyond the basin-floor fan sandstone pinchout: EarthArXiv: https://eartharxiv.org/3qrew/.

Bourget, J., Zaragosi, S., Ellouz-Zimmermann, S., Ducassou, E., Prins, M.A., Garlan, T., Lanfumey, V., Schneider, J.L., Rouillard, P. and Giraudeau, J., 2010, Highstand vs. lowstand turbidite system growth in the Makran active margin: Imprints of high-frequency external controls on sediment delivery mechanisms to deep water systems: Marine Geology, v. 274, p. v187-208.

Bourget, J., Zaragosi, S., Ellouz-zimmermann, N., Mouchot, N., Garlan, T., Schneider, J.L., Lanfumey, V. and Lallemant, S., 2011, Turbidite system architecture and sedimentary

processes along topographically complex slopes: the Makran convergent margin: Sedimentology, v. 58, p. 376-406.

Bourget, J., Zaragosi, S., Rodriguez, M., Fournier, M., Garlan, T. and Chamot-Rooke, N., 2013, Late Quaternary megaturbidites of the Indus Fan: Origin and stratigraphic significance. Marine Geology, v. 336, p. 10-23.

Bouma, A.H., 1962, Sedimentology of Some Flysch Deposits; A Graphic Approach to Facies Interpretation: New York, Elsevier, 168 p.

Bouma, A. H, 1964, Turbidites. Developments in sedimentology, v. **3**, p. 247-256.

Braga, J., Martin, J. and Wood, J., 2001, Submarine lobes and feeder channels of redeposited, temperate carbonate and mixed siliciclastic-carbonate platform deposits (Vera Basin, Almeria, southern Spain): Sedimentology, v. 48, p. 99-116.

Bragina, L. G., and N. Yu Bragin., 2015, New data on Albian-Coniacian radiolarians from the Kelevudag section (northeastern Azerbaijan): Stratigraphy and Geological Correlation v. 23, p. 45-56.

Bramlette, M . N. , and Bradley, W. H., 1940, Geology and Biology of North Atlantic Deep-Sea Cores between Newfoundland and Ireland, U.S. Geological Survey Professional Paper, p 1 – 34.

Brooks, H.L., Hodgson, D.M., Brunt, R.L., Peakall, J. and Flint, S.S., 2018, Exhumed lateral margins and increasing flow confinement of a submarine landslide complex: Sedimentology, v. 65, p. 1067-1096.

Brooks, H.L., Hodgson, D.M., Brunt, R.L., Peakall, J., Hofstra, M. and Flint, S.S., 2018, Deep-water channel-lobe transition zone dynamics: Processes and depositional architecture, an example from the Karoo Basin, South Africa: GSA Bulletin, v. 130, p. 1723-1746.

Brunet M. F., Korotaev M.V., Ershov A.V. and Nikishin A.M., 2003, The South Caspian Basin: a review of its evolution from subsidence modelling: Sedimentary Geology v.156 (1-4), pp. 119-148.

Brunner, C.A., Normark, W.R., Zuffa, G.G. and Serra, F., 1999, Deep-sea sedimentary record of the late Wisconsin cataclysmic floods from the Columbia River: Geology, v. 27, p. 463-466.

Brunt, R.L., McCaffrey, W.D., and Kneller, B.C., 2004, Experimental modeling of the spatial distribution of grain size developed in a fill-and-spill mini-basin setting: Journal of Sedimentary Research, v. 74, p. 438-446.

Bruschi, R., Bughi, S., Spinazzè, M., Torselletti, E. and Vitali, L., 2006, Impact of debris flows and turbidity currents on seafloor structures: Norwegian Journal of Geology/Norsk Geologisk Forening, v. 86, p. 317 – 336.

Bryn, P., Berg, K., Forsberg, C.F., Solheim, A. and Kvalstad, T.J., 2005, Explaining the Storegga slide. Marine and Petroleum Geology, v. 22, p. 11-19.

Buchanan, J. Y., 1887, On the land slopes separating continents and ocean basins, especially those on the West Coast of Africa: Scot. Geograph. Mag., v. III, p. 217-238.

Buchanan, J. Y., 1888, The exploration of the Gulf of Guinea: Scot. Geograph. Mag., v. IV. p. 177-200, p. 233-251.

Bull, S., Cartwright, J. and Huuse, M., 2009, A review of kinematic indicators from mass-transport complexes using 3D seismic data: Marine and Petroleum Geology, v. 26, p. 1132-1151.

Burbank, D.W., Vergés, J., Munoz, A. & Bentham, P., 1992, Coeval hindward- and forward-imbricating thrusting in the south-central Pyrenees, Spain: Timing and rates of shortening and deposition: Geological Society of America Bulletin, v. 104, p. 3-17.

Bursik, M.I. and Woods, A.W., 2000, The effects of topography on sedimentation from particle-laden turbulent density currents: Journal of Sedimentary Research, v. 70, p. 53-63.

Callec, Y., 2004, The turbidite fill of the Annot sub-basin (SE France): a sequence-stratigraphy approach, in Lomas, S., and Joseph, P., eds., Deep-Water Sedimentation in the Alpine Basin of SE France: New Perspectives on the Grès d'Annot and Related Systems: Geological Society of London, Special Publication 221, p. 111-135.

Calvès, G., Huuse, M., Clift, P.D., and Brusset, S., 2015, Giant fossil mass wasting off the coast of West India: The Nataraja submarine slide: Earth and Planetary Science Letters, v. 432, p. 265–272.

Campion, K.M., Sprague, A.R., Mohrig, D., Lovell, R.W., Drzewiecki, P.A., Sullivan, M.D., Ardill, J.A., Jensen, G.N. and Sickafoose, D.K., 2003, Outcrop expression of confined channel complexes: Bulletin of South Texas Geological Society, v. 44. P. 13-37.

Cande, S.C. and Kent, D.V., 1995, Revised calibration of the geomagnetic polarity timescale for the Late Cretaceous and Cenozoic: Journal of Geophysical Research: Solid Earth, v. 100, p. 6093-6095.

Cantelli, A., Pirmez, C., Johnson, S., and Parker, G., 2011, Morphodynamic and Stratigraphic Evolution of Self-Channelized Subaqueous Fans Emplaced by Turbidity Currents: Journal of Sedimentary Research, v. 81, p. 233–247.

Cantero, M.I., Balachandar, S., Cantelli, A., Pirmez, C. and Parker, G. 2009. Turbidity current with a roof: Direct numerical simulation of self-stratified turbulent channel flow driven by suspended sediment: Journal of Geophysical Research: Oceans, v. 114.

Carter, L., Gavey, R., Talling, P., Liu, J., 2014, Insights into submarine geohazards from breaks in subsea telecommunication cables: Oceanography, v. 27, p. 58–67.

Cartigny, M.J., Eggenhisen, J.T., Hansen, E.W. and Postma, G., 2013, Concentration-dependent flow stratification in experimental high-density turbidity currents and their relevance to turbidite facies models: Journal of Sedimentary Research, v. 83, p. 1047-1065.

Cartigny, M.J., Ventra, D., Postma, G. and Van den Berg, J.H., 2014, Morphodynamics and sedimentary structures of bedforms under supercritical-flow conditions: new insights from flume experiments: Sedimentology, v. 61, p. 712-748.

Cartapanis, O., Bianchi, D., Jaccard, S.L. and Galbraith, E.D., 2016, Global pulses of organic carbon burial in deep-sea sediments during glacial maxima: Nature communications, v. 7, p. 10796

Carvajal, C., Paull, C.K., Caress, D.W., Fildani, A., Lundsten, E., Anderson, K., Maier, K.L., McGann, M., Gwiazda, R. and Herguera, J.C., 2017, Unraveling the channel–

lobe transition zone with high-resolution AUV bathymetry: Navy Fan, offshore Baja California, Mexico: Journal of Sedimentary Research, v. 87, p. 1049-1059.

Carvajal, C.R. and Steel, R.J., 2006, Thick turbidite successions from supply-dominated shelves during sea-level highstand. Geology, v. 34, p. 665-668.

Casson, M.A., Calvès, G., Redfern, J., Huuse, M. & Sayers, B., 2020, Cretaceous continental margin evolution from quantitative seismic geomorphology, offshore NW Africa: Basin Research, in press.

Castelltort, S. and Driessche, J.V.D., 2003, How plausible are high-frequency sediment supply-driven cycles in the stratigraphic record? Sedimentary Geology, v. 157, p. 3–13

Castelltort, S., Honegger, L., Adatte, T., Clark, J.D., Puigdefàbregas, C., Spangenberg, J.E., Dykstra, M.L. and Fildani, A., 2017, Detecting eustatic and tectonic signals with carbon isotopes in deep-marine strata, Eocene Ainsa Basin, Spanish Pyrenees: Geology, v. 45, p. 707-710.

Cantalejo, B. and Pickering, K.T., 2014, Climate forcing of fine-grained deep-marine systems in an active tectonic setting: Middle Eocene, Ainsa Basin, Spanish Pyrenees: Palaeogeography, Palaeoclimatology, Palaeoecology, v. 410, p. 351-371.

Catuneanu, O., 2020, Sequence stratigraphy of deep-water systems: Marine and Petroleum Geology, in press.

Caves, J.K., Moragne, D.Y., Ibarra, D.E., Bayshashov, B.U., Gao, Y., Jones, M.M., Zhamangara, A., Arzhannikova, A.V., Arzhannikov, S.G. and Chamberlain, C.P., 2016, The Neogene de-greening of Central Asia: Geology, v. 44, p. 887-890.

Chadwick Jr, W.W., Dziak, R.P., Haxel, J.H., Embley, R.W. and Matsumoto, H., 2012, Submarine landslide triggered by volcanic eruption recorded by in situ hydrophone: Geology, v. 40, p. 51-54.

Chen, C. and Hiscott, R.N., 1999, Statistical analysis of facies clustering in submarine-fan turbidite successions: Journal of Sedimentary Research, v. 69, p. 505-517.

Chiarella, D., Longhitano, S.G. and Tropeano, M., 2017, Types of mixing and heterogeneities in siliciclastic-carbonate sediments: Marine and Petroleum Geology, v. 88, p. 617-627.

Clare, M., Rosenberger, K., Talling, P., Cartigny, M., Parsons, D., Simmons, S., Paull, C., Xu, J., Maier, K., Gwiazda, R. and McGann, M., 2019, New direct measurements explain when and why turbidity current systems are active: Geophysical Research Abstracts, v. 21.

Clare, M.A., Talling, P.J., Challenor, P., Malgesini, G., and Hunt, J., 2014, Distal turbidites reveal a common distribution for large (> 0.1 km^3) submarine landslide recurrence: Geology, v. 42, p. 263-266.

Clark, J.D., and Stanbrook, A., 2001, Formation of large-scale shear structures during deposition from high-density turbidity currents, Grès d'Annot Formation, south-east France: Particulate Gravity Currents, v. 31, p. 219-232.

Clark, J.D. and Pickering, K.T., 1996, Architectural elements and growth patterns of submarine channels: application to hydrocarbon exploration: AAPG bulletin, v. **80**, p. 194-220.

Clark, J.D., Puigdefàbregas, C., Castelltort, S., and Fildani, A., 2017, Propagation of environmental signals within source-to-sink stratigraphy: SEPM, Field Trip Guidebook 13, p. 1–63

Clarke, J.E.H., 2016, First wide-angle view of channelized turbidity currents links migrating cyclic steps to flow characteristics: Nature communications, v. 7, p. 11896.

Clift, P.D., Shimizu, N., Layne, G.D., Blusztajn, J.S., Gaedicke, C., Schluter, H.U., Clark, M.K. and Amjad, S., 2001, Development of the Indus Fan and its significance for the erosional history of the Western Himalaya and Karakoram: Geological Society of America Bulletin, v. 113, p. 1039-1051.

Clift, P., Shimizu, N., Layne, G., Gaedicke, C., Schlter, H.U., Clark, M. and Amjad, S., 2000, Fifty-five million years of Tibetan evolution recorded in the Indus Fan: Eos, Transactions American Geophysical Union, v. 81, p. 277-281.

Cooper, M.R., Anderson, H., Walsh, J.J., Van Dam, C.L., Young, M.E., Earls, G., and Walker, A., 2012, Palaeogene Alpine tectonics and Icelandic plume-related magmatism and deformation in Northern Ireland: Journal of the Geological Society, v. 169, p. 29–36, https://doi.org/10.1144/0016-76492010-182.

Cossu, R. and Wells, M.G., 2012, A comparison of the shear stress distribution in the bottom boundary layer of experimental density and turbidity currents: European Journal of Mechanics-B/Fluids, v. 32, p. 70-79.

Coulthard, T.J. and Van de Wiel, M.J., 2013, Climate, tectonics or morphology: what signals can we see in drainage basin sediment yields?: Earth Surface Dynamics, v. 1, p. 13-27.

Coussot, P. and Meunier, M., 1996, Recognition, classification and mechanical description of debris flows: Earth-Science Reviews, v. 40, p. 209-227.

Covault, J.A. and Graham, S.A., 2010, Submarine fans at all sea-level stands: Tectono-morphologic and climatic controls on terrigenous sediment delivery to the deep sea: Geology, v. 38, p. 939-942.

Covault, J.A., Romans, B.W., Fildani, A., McGann, M. and Graham, S.A., 2010, Rapid climatic signal propagation from source to sink in a southern California sediment-routing system. The Journal of Geology, v. 118, p. 247-259.

Covault, J.A., Fildani, A., Romans, B.W. and McHargue, T., 2011, The natural range of submarine canyon-and-channel longitudinal profiles: Geosphere, v. 7(2), p. 313-332.

Covault, J.A., Kostic, S., Paull, C.K., Sylvester, Z. and Fildani, A., 2017. Cyclic steps and related supercritical bedforms: building blocks of deep-water depositional systems, western North America: Marine Geology, v. 393, p. 4-20.

Covault, J.A., Normark, W.R., Romans, B.W. and Graham, S.A., 2007, Highstand fans in the California borderland: The overlooked deep-water depositional systems: Geology, v. 35, p. 783-786.

Covault, J.A., and Romans, B.W., 2009, Growth patterns of deep-sea fans revisited: Turbidite-system morphology in confined basins, examples from the California Borderland: Marine Geology, v. 265, p. 51-66.

Covault, J.A., Romans, B.W., Fildani, A., McGann, M. and Graham, S.A., 2010. Rapid climatic signal propagation from source to sink in a southern California sediment-routing system. *The Journal of Geology*, *118*(3), pp.247-259.

Covault, J.A., Shelef, E., Traer, M., Hubbard, S.M., Romans, B.W. and Fildani, A., 2012, Deep-water channel run-out length: Insights from seafloor geomorphology: Journal of Sedimentary Research, v. 82, p. 21-36.

Covault, J.A., Sylvester, Z., Hubbard, S.M., Jobe, Z.R. and Sech, R.P., 2016, The stratigraphic record of submarine-channel evolution: The Sedimentary Record, v. 14, p. 4-11.

Cramer, B.S., Toggweiler, J.R., Wright, J.D., Katz, M.E. and Miller, K.G., 2009, Ocean overturning since the Late Cretaceous: Inferences from a new benthic foraminiferal isotope compilation. Paleoceanography, v. 24.

Crevello, P.D. and Schlager, W., 1980, Carbonate debris sheets and turbidites, Exuma Sound, Bahamas: Journal of Sedimentary Research, v. 50, p. 1121-1147.

Cullen, T.M., Collier, R.E.L., Gawthorpe, R.L., Hodgson, D.M. and Barrett, B.J., 2019, Axial and transverse deep-water sediment supply to syn-rift fault terraces: Insights from the West Xylokastro Fault Block, Gulf of Corinth, Greece: Basin Research, v. 00, p. 1 – 35.

Cunha, R.S., Tinterri, R., and Magalhaes, P.M., 2017, Annot Sandstone in the Peïra Cava basin: An example of an asymmetric facies distribution in a confined turbidite system (SE France): Marine and Petroleum Geology, v. 87, p. 60-79.

Curray, J.R. and Moore, D.G., 1971, Growth of the Bengal deep-sea fan and denudation in the Himalayas: Geological Society of America Bulletin, v. 82, p. 563-572.

Dadson, S.J., Hovius, N., Chen, H., Dade, W.B., Hsieh, M.L., Willett, S.D., Hu, J.C., Horng, M.J., Chen, M.C., Stark, C.P. and Lague, D., 2003, Links between erosion, runoff variability and seismicity in the Taiwan orogeny: Nature, v. 426, p. 648.

Dana, J. D., 1863, A Manual of Geology: London, England, Truber, 798 p.

D'Argenio, B., Ferreri, V., Raspini, A., Amodio, S. and Buonocunto, F., 1999, Cyclostratigraphy of a carbonate platform as a tool for high-precision correlation: Tectonophysics, v. 315, p. 357-384.

Dawson, A.G., Long, D., and Smith, D.E., 1988, The Storegga Slides: Evidence from eastern Scotland for a possible tsunami: Marine Geology, v. 82, p. 271–276.

Davis, C., Haughton, P., McCaffrey, W., Scott, E., Hogg, N. and Kitching, D., 2009, Character and distribution of hybrid sediment gravity flow deposits from the outer Forties Fan, Palaeocene Central North Sea, UKCS: Marine and Petroleum Geology, v. 26, p. 1919-1939.

De Blasio, F.V., Engvik, L.E. & Elverhøi, A., 2006, Sliding of outrunner blocks from submarine landslides. Geophysical Research Letters, v. 33.

De Conto, R.M. and Pollard, D., 2003, Rapid Cenozoic glaciation of Antarctica induced by declining atmospheric CO_2: Nature, v. 421, p. 245.

De Leeuw, J., Eggenhuisen, J.T. and Cartigny, M.J., 2016, Morphodynamics of submarine channel inception revealed by new experimental approach: Nature communications, v. 7, p. 10886.

De Leeuw, J., Eggenhuisen, J.T., Spychala, Y.T., Heijnen, M.S., Pohl, F. and Cartigny, M.J., 2018. Sediment Volume and Grain-Size Partitioning Between Submarine Channel–Levee Systems and Lobes: An Experimental Study: Journal of Sedimentary Research, v. 88, p. 777-794.

Den Hartog Jager, D., Giles, M.R., and Griffiths, G.R., 1993, Evolution of Paleogene fans of the North Sea in space and time: Geological Society, London, Petroleum Geology Conference series, v. 4, p. 59–71.

Deptuck, M.E., Sylvester, Z., Pirmez, C. and O'Byrne, C., 2007, Migration-aggradation history and 3-D seismic geomorphology of submarine channels in the Pleistocene Benin-major Canyon, western Niger Delta slope: Marine and Petroleum Geology, v. 24, p. 406-433

Deptuck, M.E., Piper, D.J., Savoye, B., and Gervais, A., 2008, Dimensions and architecture of late Pleistocene submarine lobes off the northern margin of East Corsica: Sedimentology, v. 55, p. 869-898.

DeVries, M., and Lindholm, R.M., 1994, Internal architecture of a channel– levee complex, Cerro Toro Formation, Southern Chile, in Weimer, P., Bouma, A.H., and Perkins, B.F., eds., Submarine Fans and Turbidite Systems: Gulf Coast Section SEPM Foundation, Houston, p. 105–114.

Dickie, J. and Hein, F., 1995, Conglomeratic fan deltas and submarine fans of the Jurassic Laberge Group, Whitehorse Trough, Yukon Territory, Canada: fore-arc sedimentation and unroofing of a volcanic island arc complex: Sedimentary Geology, v. 98, p. 263-292.

Ditty, P.S., Harmon, C.J., Pilkey, O.H., Ball, M.M. and Richardson, E.S., 1977, Mixed terrigenous—Carbonate sedimentation in the Hispaniola—Caicos turbidite basin: Marine Geology, v. 24, p. 1-20.

Dodd, T.J., McCarthy, D.J. and Richards, P.C., 2018, A depositional model for deep-lacustrine, partially confined, turbidite fans: Early Cretaceous, North Falkland Basin: Sedimentology, v. 66, p. 53 -80.

Dorrell, R.M., Patacci, M., and McCaffrey, W. D., 2019, Inflation of ponded, particulate-laden density currents: Journal of Sedimentary Research, v. 88, p. 1276–1282.

Dorrell, R.M., Peakall, J., Sumner, E.J., Parsons, D.R., Darby, S.E., Wynn, R.B., Özsoy, E. and Tezcan, D., 2016, Flow dynamics and mixing processes in hydraulic jump arrays: Implications for channel-lobe transition zones: Marine Geology, v. 381, p. 181-193.

Dorsey, R.J. and Kidwell, S.M., 1999, Mixed carbonate-siliciclastic sedimentation on a tectonically active margin: Example from the Pliocene of Baja California Sur, Mexico: Geology, v. 27, p. 935-938.

Doughty-Jones, G., Mayall, M., and Lonergan, L., 2017, Stratigraphy, facies, and evolution of deep-water lobe complexes within a salt-controlled intraslope minibasin: American Association of Petroleum Geologists, Bulletin: v. 101, p. 1879-1904.

Droxler, A.W. and Schlager, W., 1985, Glacial versus interglacial sedimentation rates and turbidite frequency in the Bahamas: Geology, v. 13, p. 799-802.

Ducassou, E., Migeon, S., Mulder, T., Murat, A., Capotondi, L., Bernasconi, S.M. and Mascle, J., 2009, Evolution of the Nile deep-sea turbidite system during the Late Quaternary: influence of climate change on fan sedimentation: Sedimentology, v. 56, p. 2061-2090.

Du Fornel, E., 2003, Reconstitution sédimentologique tridimensionnelle et simulation stratigraphique du système turbiditique éocène des Grès d'Annot (Alpes méridionales): PhD thesis, Université de Rennes, p. 243.

Du Fornel, E., Joseph, P., Desaubliaux, G., Eschard, R., Guillocheau, F., Lerat, O., Muller, C., Ravenne, C., and Sztrakos, K., 2004, The southern Grès d'Annot outcrops (French Alps): an attempt at regional correlation, in Lomas, S., and Joseph, P., eds., Deep-Water Sedimentation in the Alpine Basin of SE France: New Perspectives on the Grès d'Annot and Related Systems: Geological Society of London, Special Publication 221, p. 137-160.

Dunbar, G.B. and Dickens, G.R., 2003, Late Quaternary shedding of shallow-marine carbonate along a tropical mixed siliciclastic–carbonate shelf: Great Barrier Reef, Australia. Sedimentology, v. 50, p. 1061-1077.

Dzulynski, S., and Sanders, J.E., 1962, Current marks on firm mud bottoms: Connecticut Academy of Arts and Science, Transactions, v. 42, p. 57–96.

Edwards, D.A., Leeder, M.R., Best, J.L. and Pantin, H.M., 1994, On experimental reflected density currents and the interpretation of certain turbidites: Sedimentology, v. 41, p. 437-461.

Egan, S.S., Mosar, J., Brunet, M.F. and Kangarli, T., 2009, Subsidence and uplift mechanisms within the South Caspian Basin: insights from the onshore and offshore Azerbaijan region: Geological Society, London, Special Publications, v. 312, p. 219-240.

Eggenhuisen, J.T., and McCaffrey, W.D., 2012, The vertical turbulence structure of experimental turbidity currents encountering basal obstructions: implications for

vertical suspended sediment distribution in non-equilibrium currents: Sedimentology, v. 59, p. 1101–1120.

Eggenhuisen, J.T., McCaffrey, W.D., Haughton, P.D., and Butler, R.W., 2011, Shallow erosion beneath turbidity currents and its impact on the architectural development of turbidite sheet systems: Sedimentology, v. 58, p. 936-959.

Eggenhuisen, J.T., Cartigny, M.J., and de Leeuw, J., 2017, Physical theory for near-bed turbulent particle suspension capacity: Earth Surface Dynamics, v. 5, p. 269-281.

Eggenhuisen, J.T., Tilston, M.C., de Leeuw, J., Pohl, F. and Cartigny, M.J., 2019, Turbulent diffusion modelling of sediment in turbidity currents: An experimental validation of the Rouse approach: The Depositional Record.

Einsele, G., Ratschbacher, L. and Wetzel, A., 1996, The Himalaya-Bengal Fan denudation-accumulation system during the past 20 Ma: the Journal of Geology, v. 104, p. 163-184.

Eldrett, J.S., Greenwood, D.R., Harding, I.C. and Huber, M., 2009, Increased seasonality through the Eocene to Oligocene transition in northern high latitudes; Nature, v. 459, p. 969.

Elliott, T., 2000, Megaflute erosion surfaces and the initiation of turbidite channels: Geology, v. 28, p. 119-122.

Elliott, T., Apps, G., Davies, H., Evans, M., Ghibaudo, G., and Graham, R.H., 1985, A structural and sedimentological traverse through the Tertiary foreland basin of the external Alps of south-east France, in Field Excursion Guidebook for the International Association of Sedimentologists Meeting on Foreland Basins in Fribourg, eds., Allen, P.A., and Homewood, P, p. 39-73.

Englert, R.G., Hubbard, S.M., Matthews, W.A., Coutts, D.S., and Covault, J.A., 2019, The evolution of submarine slope-channel systems: Timing of incision, bypass, and aggradation in Late Cretaceous Nanaimo Group channel-system strata, British Columbia, Canada: Geosphere, v. 16, p. 1 - 16.

Ericson, D.B., Ewing, M. and Heezen, B.C., 1952, Turbidity currents and sediments in North Atlantic: AAPG Bulletin, v. 36, p. 489-511.

Euzen, T., Joseph, P., Du Fornel, E., Lesur, S., Granjeon, D., and Guillocheau, F., 2004, Three-dimensional stratigraphic modelling of the Grès d'Annot system, Eocene-Oligocene, SE France, in Lomas, S., and Joseph, P., eds., Deep-Water Sedimentation in the Alpine Basin of SE France: New Perspectives on the Grès d'Annot and Related Systems: Geological Society of London, Special Publication 221, p. 161-180.

Fallgatter, C., Kneller, B., Paim, P.S. and Milana, J.P., 2017, Transformation, partitioning and flow–deposit interactions during the run-out of megaflows: Sedimentology, v. 64, p. 359-387.

Farre, J.A., McGregor, B.A., Ryan, W.B. and Robb, J.M., 1983, Breaching the shelfbreak: passage from youthful to mature phase in submarine canyon evolution: SEPM Special Publication 33, p 25 – 39.

Fan, M., Feng, R., Geissman, J.W. and Poulsen, C.J., 2020, Late Paleogene emergence of a North American loess plateau: Geology, v. 48.

Farizan, A., Yaghoubi, S., Firoozabadi, B. and Afshin, H., 2019, Effect of an obstacle on the depositional behaviour of turbidity currents: Journal of Hydraulic Research, v. 57, p. 75-89.

Farquharson, G.W., Hamer, R.D. and Ineson, J.R., 1984, Proximal volcaniclastic sedimentation in a Cretaceous back-arc basin, northern Antarctic Peninsula: Geological Society, London, Special Publications, v. 16, p. 219-229.

Felletti, F., 2002, Complex bedding geometries and facies associations of the turbiditic fill of a confined basin in a transpressive setting (Castagnola Fm., Tertiary Piedmont Basin, NW Italy): Sedimentology, v. 49, p. 645-667.

Fernandes, A. M., Buttles, J., & Mohrig, D., 2018, Flow-Substrate Interactions in Aggrading and Degrading Submarine Channels: EarthArXiv, https://doi.org/10.31223/osf.io/ceyhk.

Ferguson, R., Kane, I. A., Eggenhuisen, J., Pohl, F., Tilston, M., Spychala, Y., & Brunt, R., 2020, Entangled external and internal controls on submarine fan evolution: an experimental perspective: Depositional Record, in press.

Figueiredo, J.J., Hodgson, D.M., Flint, S.S. and Kavanagh, J.P., 2013, Architecture of a channel complex formed and filled during long-term degradation and entrenchment on the upper submarine slope, Unit F, Fort Brown Fm., SW Karoo Basin, South Africa: Marine and Petroleum Geology, v. 41, p. 104-116.

Fildani, A., Clark, J., Covault, J.A., Power, B., Romans, B. W. & Aiello, I. W., 2018, Muddy sand and sandy mud on the distal Mississippi fan: Implications for lobe depositional processes: Geosphere, v. 14, p. 1051-1066.

Fildani, A., Hubbard, S.M., Covault, J.A., Maier, K.L., Romans, B.W., Traer, M. and Rowland, J.C., 2013, Erosion at inception of deep-sea channels: Marine and Petroleum Geology, v. 41, p.48-61.

Fildani, A., Hessler, A.M., Mason, C.C., McKay, M.P. and Stockli, D.F., 2018, Late Pleistocene glacial transitions in North America altered major river drainages, as revealed by deep-sea sediment: Scientific reports, v. 8, p.13839.

Fildani, A. and Normark, W.R., 2004, Late Quaternary evolution of channel and lobe complexes of Monterey Fan: Marine Geology, v. 206, p. 199-223.

Fisher, R.V. 1971, Features of coarse-grained, high concentration fluids and their deposits: Journal of Sedimentary Petrology, v. 41, p. 916- 927.

Flood, R.D. and Piper, D.J., 1997. Amazon Fan sedimentation: the relationship to equatorial climate change, continental denudation, and sea-level fluctuations. in Proceedings-Ocean Drilling Program Scientific Results: NSF, p. 653 – 675.

Fonnesu, M., Haughton, P., Felletti, F., and McCaffrey, W., 2015, Short length-scale variability of hybrid event beds and its applied significance: Marine and Petroleum Geology, v. 67, p. 583-603.

Fonnesu, M., Felletti, F., Haughton, P.D., Patacci, M., and McCaffrey, W.D., 2018, Hybrid event bed character and distribution linked to turbidite system sub-environments: the North Apennine Gottero Sandstone (north-west Italy): Sedimentology, v. 65, p. 151-190.

Fonnesu, M., Palermo, D., Galbiati, M., Marchesini, M., Bonamini, E. and Bendias, D., 2020, A new world-class deep-water play-type, deposited by the syndepositional

interaction of turbidity flows and bottom currents: The giant Eocene Coral Field in northern Mozambique: Marine and Petroleum Geology, v. 111, p. 179-201.

Ford, M., Lickorish, W., and Kusnir, N., 1999, Tertiary foreland sedimentation in the southern subalpine chains, SE France: a geodynamic appraisal: Basin Research, v. 11, p. 315-336.

Forel, M., 1885, Ravins sous-lacustres des fleuves glaciaires, C.R. Acad. Sci. Paris, v. 101, p. 725 -728.

Fournier, L., Fauquembergue, K., Zaragosi, S., Zorzi, C., Malaizé, B., Bassinot, F., Joussain, R., Colin, C., Moreno, E. and Leparmentier, F., 2017, The Bengal fan: external controls on the Holocene Active Channel turbidite activity: The Holocene, v. 27, p. 900-913.

France-Lanord, C., Derry, L. and Michard, A., 1993, Evolution of the Himalaya since Miocene time: isotopic and sedimentological evidence from the Bengal Fan: Geological Society, London, Special Publications, v. 74, pp.603-621.

Francis, J., Daniell, J., Droxler, A., Dickens, G., Bentley, S., Peterson, L. Bradley, N. and Beaufort, L., 2008, Deep water geomorphology of the mixed siliciclastic-carbonate system, Gulf of Papua: Journal of Geophysical Research: Earth Surface, v. 113, F01S16.

Frey-Martínez, J., Cartwright, J. and James, D., 2006, Frontally confined versus frontally emergent submarine landslides: A 3D seismic characterisation: Marine and Petroleum Geology, v. 23, p. 585-604.

Fukushima, Y., Parker, G. and Pantin, H.M., 1985, Prediction of ignitive turbidity currents in Scripps Submarine Canyon: Marine Geology, v. 67, p. 55-81.

Galloway, W.E., 2001. Cenozoic evolution of sediment accumulation in deltaic and shore-zone depositional systems, northern Gulf of Mexico Basin: Marine and Petroleum Geology, v. 18, p. 1031-1040.

Galy, V., France-Lanord, C., Beyssac, O., Faure, P., Kudrass, H. and Palhol, F., 2007, Efficient organic carbon burial in the Bengal fan sustained by the Himalayan erosional system. Nature, 450, p. 407.

Gardiner, A.R., 2006, The variability of turbidite sandbody pinchout and its impact on hydrocarbon recovery in stratigraphically trapped fields, in The Deliberate Search for the Stratigraphic Trap, eds., Allen, M.R., Goffey, G.P., Morgan, R.K., and Walker, I.M. Geological Society of London, Special Publications 254, p. 267-287.

Garcia, M, 2008, Sedimentation Engineering: Processes, Measurements, Modeling and Practise: American Society of Civil Engineers. p. 21 - 46

Garcia, M., and Parker, G., 1989, Experiments on hydraulic jumps in turbidity currents near a canyon-fan transition: Science, v. 245, p. 393–396.

Garcia, M.H., 1994, Depositional turbidity currents laden with poorly sorted sediment: Journal of Hydraulic Engineering, v. 120, p. 1240–1263.

García-García, F., Soria, J., Sar Viseras, C. and Fernández, J., 2009, High-frequency rhythmicity in a mixed siliciclastic-carbonate shelf (Late Miocene, Guadix Basin, Spain): A model of interplay between climatic oscillations, subsidence and sediment dispersal: Journal of Sedimentary Research, v.79, p. 302-315.

Gawthorpe, R.L., 1986, Sedimentation during carbonate ramp-to-slope evolution in a tectonically active area: Bowland Basin (Dinantian), northern England: Sedimentology, v. 33, p. 185-206.

Gee, M.J., Masson, D.G., Watts, A.B. and Mitchell, N.C., 2001, Passage of debris flows and turbidity currents through a topographic constriction: seafloor erosion and deflection of flow pathways: Sedimentology, v. 48, p. 1389-1409.

Georgiopoulou, A., Masson, D.G., Wynn, R.B. and Krastel, S., 2010, Sahara Slide: Age, initiation, and processes of a giant submarine slide: Geochemistry, Geophysics, Geosystems, v. 11. Q07014,

Gervais, A., Savoye, B., Piper, D.J., Mulder, T., Cremer, M., and Pichevin, L., 2004, Present morphology and depositional architecture of a sandy confined submarine system: the Golo turbidite system (eastern margin of Corsica, in Lomas, S., and Joseph, P., eds., Confined Turbidite Basins: Geological Society of London, Special Publication 222, p. 59-89.

Glennie, K.W., 1963, An interpretation of turbidites whose sole markings show multiple directional trends: The Journal of Geology, v. 71, p. 525-527.

Goldhammer, R.K., Dunn, P.A. and Hardie, L.A., 1990, Depositional cycles, composite sea level changes, cycle stacking patterns, and the hierarchy of stratigraphic forcing - examples from platform carbonates of the Alpine Triassic: Geological Society of America Bulletin, v. 102, p. 535-562.

Golonka, J., 2004, Plate tectonic evolution of the southern margin of Eurasia in the Mesozoic and Cenozoic: Tectonophysics, v. 381, p. 235-273.

Gorsline, D.S. and Emery, K.O., 1959, Turbidity-current deposits in San Pedro and Santa Monica basins off southern California: Geological Society of America Bulletin, v. 70, p. 279-290.

Gorsline, D.S., De Diego, T. and Nava-Sanchez, E.H., 2000, Seismically triggered turbidites in small margin basins: Alfonso Basin, western Gulf of California and Santa Monica Basin, California borderland: Sedimentary Geology, v. 135, p. 21-35.

Gradstein, F.M., Ogg, J.G., and Smith, A.G., 2012, A Geologic Time Scale 2012: Cambridge, Cambridge University Press, p. 1129.

Graf, W.H., 1971, Hydraulics of sediment transport: New York, McGraw-Hill, p. 513.

Grant, R., Underhill, J., Hernández-Casado, J., Barker, S. and Jamieson, R., 2019, Upper Permian Zechstein Supergroup carbonate-evaporite platform palaeomorphology in the UK Southern North Sea: Marine and Petroleum Geology, v. 100, p. 484-518.

Grecula, M., Flint, S., Potts, G., Wickens, D. and Johnson, S., 2003, Partial ponding of turbidite systems in a basin with subtle growth-fold topography: Laingsburg-Karoo, South Africa: Journal of Sedimentary Research, v. 73, p. 603-620.

Groenenberg, R.M., Hodgson, D.M., Prélat, A., Luthi, S.M., and Flint, S.S., 2010, Flow-deposit interaction in submarine lobes: Insights from outcrop observations and realizations of a process-based numerical model: Journal of Sedimentary Research, v. 80, p. 252-267.

Grundvåg, S.A., Johannessen, E.P., Helland-Hansen, W., and Plink-Björklund, P., 2014, Depositional architecture and evolution of progradationally stacked lobe complexes in the Eocene Central Basin of Spitsbergen: Sedimentology, v. 61, p. 535-569.

Gulick, S.P., Jaeger, J.M., Mix, A.C., Asahi, H., Bahlburg, H., Belanger, C.L., Berbel, G.B., Childress, L., Cowan, E., Drab, L. and Forwick, M., 2015, Mid-Pleistocene climate transition drives net mass loss from rapidly uplifting St. Elias Mountains, Alaska: Proceedings of the National Academy of Sciences, v. 112, p.15042-15047.

Hage, S., Cartigny, M.J., Clare, M.A., Sumner, E.J., Vendettuoli, D., Clarke, J.E.H., Hubbard, S.M., Talling, P.J., Lintern, D.G., Stacey, C.D. and Englert, R.G., 2018, How to recognize crescentic bedforms formed by supercritical turbidity currents in the geologic record: Insights from active submarine channels. Geology, v. 46, p. 563-566.

Harms, J., Southard, J., Spearing, D., & Walker, R., 1975, Depositional Environments as Interpreted from Primary Sedimentary and Stratigraphic Sequences. SEPM (Society for Sedimentary Geology). 161 p.

Hamilton P.B, Strom K.B, Hoyal D.C., 2015, Hydraulic and sediment transport properties of autogenic avulsion cycles on submarine fans with supercritical distributaries: Journal of Geophysical Research. v. 120, p. 1369 – 1389.

Hamilton, P., Gaillot, G., Strom, K., Fedele, J. and Hoyal, D., 2017, Linking Hydraulic Properties In Supercritical Submarine Distributary Channels To Depositional-Lobe Geometry: Journal of Sedimentary Research, v. 87, p. 935-950.

Hampton, M.A., 1972. The role of subaqueous debris flow in generating turbidity currents: Journal of Sedimentary Research, v. 42.

Hampton, M.A., Lee, H.J. and Locat, J., 1996, Submarine landslides. Reviews of Geophysics, v. 34, p. 33-59.

Hansen, L.A.S., Callow, R.H.T., Kane, I.A., Gamberi, F., Rovere, M., Cronin, B.T. et al., 2015, Genesis and character of thin-bedded turbidites associated with submarine channels: Marine and Petroleum Geology, v. 67, p. 852–879.

Hansen, L.A.S., Hodgson, D.M., Pontén, A., Bell, D., and Flint, S., 2019, Quantification of basin-floor fan pinchouts: examples from the Karoo Basin, South Africa: Frontiers in Earth Science, v. 7. 12 p.

Harris, P.T. and Whiteway, T, 2011, Global distribution of large submarine canyons: geomorphic differences between active and passive continental margins: Marine Geology, v. 285, p. 69–86.

Hartley, R.A., Roberts, G.G., White, N., and Richardson, C., 2011, Transient convective uplift of an ancient buried landscape: Nature Geoscience, v. 4, p. 562, https://doi.org/10.1038/ngeo1191.

Harms, J. C. and Fahnestock, R. K., 1965, Stratification, bed forms, and flow phenomena (with an example from the Rio Grande): Soc. Econ. Paleontologists and Mineralogists Special Publication 12, p. 84-115.

Haughton, P.D.W., 1994, Deposits of deflected and ponded turbidity currents, Sorbas basin, Southeast Spain: Journal of Sedimentary Petrology, v. B64, p. 233–246.

Haughton, P.D., 2000, Evolving turbidite systems on a deforming basin floor, Tabernas, SE Spain: Sedimentology, v. 47, p. 497-518.

Haughton, P.D., Barker, S.P., and McCaffrey, W.D., 2003, 'Linked' debrites in sand-rich turbidite systems - origin and significance: Sedimentology, v. 50, p. 459-482.

Haughton, P., Davis, C., McCaffrey, W., and Barker, S., 2009, Hybrid sediment gravity flow deposits - classification, origin and significance: Marine and Petroleum Geology, v. 26, p. 1900-1918.

Hay, D.C. and Prather, B.E., 2012, Stratigraphic evolution of a tortuous corridor from the stepped slope of Angola. Application of the principles of seismic geomorphology to continental slope and base-of-slope systems: Case studies from sea floor and near–sea floor analogs: SEPM Special Publication, v. 99, p. 163-180.

Heezen, B. C. and Ewing, M., 1952, Turbidity Currents and Submarine Slumps, and the 1929 Grand Banks Earthquake. American Journal of Science, v. 250, p. 849-873.

Hessler, A.M. and Fildani, A., 2019, Deep-sea fans: tapping into Earth's changing landscapes: Journal of Sedimentary Research, v. 89, p. 1171-1179.

Heerema, C.J., Talling, P.J., Cartigny, M.J., Paull, C.K., Bailey, L., Simmons, S.M., Parsons, D.R., Clare, M.A., Gwiazda, R., Lundsten, E. and Anderson, K., 2020, What determines the downstream evolution of turbidity currents?: Earth and Planetary Science Letters, v. 532, p.116023.

Hiscott, R.N. and Middleton, G.V., 1980, Fabric of coarse deep-water sandstones, Tourelle Formation, Quebec, Canada: Journal of Sedimentary Research, v. 50, p. 703-721.

Hiscott, R.N., Pickering, K.T. and Beeden, D.R., 1986, Progressive filling of a confined Middle Ordovician foreland basin associated with the Taconic Orogeny, Quebec, Canada: Foreland Basins, p.307-325.

Hiscott, R.N., 1994, Loss of capacity, not competence, as the fundamental process governing deposition from turbidity currents: Journal of Sedimentary Petrology, v. 64, p. 209–214.

Hiscott, R.N., Hall, F.R. and Pirmez, C., 1997, Turbidity current overspill from Amazon Channel: texture of silt/sand load, paleoflow from anisotropy of magnetic susceptibility, and implications for flow processes. in: eds R.D. Flood, D.J.W. Piper, A. Klaus and L.C. Peterson), Proc. ODP, v. 155, p. 53–78.

Hodgson, D.M., Brooks, H.L., Ortiz-Karpf, A., Spychala, Y., Lee, D.R. and Jackson, C.L., 2019, Entrainment and abrasion of megaclasts during submarine landsliding and their impact on flow behaviour: Geological Society, London, Special Publications, v. 477, p. 223-240.

Hodgson, D.M., Di Celma, C.N., Brunt, R.L. and Flint, S.S., 2011, Submarine slope degradation and aggradation and the stratigraphic evolution of channel–levee systems: Journal of the Geological Society, v. 168, p. 625-628.

Hodgson, N.A., Farnsworth, J., and Fraser, A.J., 1992, Salt-related tectonics, sedimentation and hydrocarbon plays in the Central Graben, North Sea, UKCS: in Hardman, R.F.P., eds., Exploration Britain: Geological Insights for the Next Decade: Geological Society of London, Special Publication 67, p. 31-63.

Hodgson, D.M., Flint, S.S., Hodgetts, D., Drinkwater, N.J., Johannessen, E.P., and Luthi, S.M., 2006, Stratigraphic evolution of fine-grained submarine fan systems, Tanqua depocenter, Karoo Basin, South Africa: Journal of Sedimentary Research, v. 76, p. 20-40.

Hodgson, D.M., Di Celma, C.N., Brunt, R.L. and Flint, S.S., 2011, Submarine slope degradation and aggradation and the stratigraphic evolution of channel–levee systems: Journal of the Geological Society, v. 168, p. 625-628.

Hodgson, D.M., Kane, I.A., Flint, S.S., Brunt, R.L. and Ortiz-Karpf, A., 2016, Time-transgressive confinement on the slope and the progradation of basin-floor fans: Implications for the sequence stratigraphy of deep-water deposits: Journal of Sedimentary Research, v. 86, p. 73-86.

Hodgson, D.M., 2009, Distribution and origin of hybrid beds in sand-rich submarine fans of the Tanqua depocenter, Karoo Basin, South Africa: Marine and Petroleum Geology, v. 26, p. 1940-1956.

Hodgson, D.M., and Haughton, P.D., 2004, Impact of syndepositional faulting on gravity current behaviour and deep-water stratigraphy: Tabernas-Sorbas Basin, SE Spain, in Lomas, S., and Joseph, P., eds., Confined Turbidite Basins: Geological Society of London, Special Publication 222, p. 135-158.

Hofstra, M., Hodgson, D.M., Peakall, J. and Flint, S.S., 2015, Giant scour-fills in ancient channel-lobe transition zones: Formative processes and depositional architecture: Sedimentary Geology, v. 329, p. 98-114.

Hofstra, M., Peakall, J., Hodgson, D.M. and Stevenson, C.J., 2018, Architecture and morphodynamics of subcritical sediment waves in an ancient channel–lobe transition zone: Sedimentology, v. 65, p. 2339-2367.

Howell, D.G., and Normark, W.R., 1982, Sedimentology of submarine fans: American AAPG Memoir, v. 31, p. 365–404.

Howlett, D. M., Ge, Z., Nemec, W., Gawthorpe, R. L., Rotevatn, A. and Jackson, C. A., 2019, Response of unconfined turbidity current to deep-water fold and thrust belt topography: Orthogonal incidence on solitary and segmented folds: Sedimentology, v. 66, p. 2425-2454.

Hu, X., Jansa, L., Wang, C., Sarti, M., Bak, K., Wagreich, M., Michalik, J. and Sotak, J., 2005, Upper Cretaceous oceanic red beds (CORBs) in the Tethys: occurrences, lithofacies, age, and environments: Cretaceous Research, v. 26, p. 3-20.

Hubbard, S.M., Covault, J.A., Fildani, A. and Romans, B.W., 2014, Sediment transfer and deposition in slope channels: Deciphering the record of enigmatic deep-sea processes from outcrop: Geological Society of America Bulletin, v. 126, p. 857-871.

Hunter, R.E. & Clifton, E.H., 1982, Cyclic deposits and hummocky cross-stratification of probable storm origin in Upper Cretaceous rocks of the Cape Sebastian area, southwestern Oregon: Journal of Sedimentary Research, v. 52, p. 127-143.

Ilstad, T., De Blasio, F.V., Elverhøi, A., Harbitz, C.B., Engvik, L., Longva, O. and Marr, J.G., 2004, On the frontal dynamics and morphology of submarine debris flows: Marine Geology, v. 213, p. 481-497.

Ingersoll, R.V., Dickinson, W.R., Graham, S.A., Chan, M.A. and Archer, A.W., 2003. Remnant-ocean submarine fans: largest sedimentary systems on Earth: Special Papers - Geological Society of America, p. 191-208.

Inverson, R.M., 1997, The physics of debris flows: Reviews of Geophysics, v. 35, p. 245-296.

Inverson, R.M., Logan, M., Lahusen, R.G. and Berti, M., 2010, The perfect debris flow? Aggregated results from 28 largescale experiments: Journal of Geophysical Research: Earth Surface, v. 115, p. 1-29.

Ito, M., 1985, The Ashigara Group: a regressive submarine fan-fan delta sequence in a Quaternary collision boundary, north of Izu Peninsula, central Honshu, Japan: Sedimentary Geology, v. 45, p. 261-292.

Jackson, C.A-L, 2011, Three-dimensional seismic analysis of megaclast deformation within a mass transport deposit; implications for debris flow kinematics: Geology, v. 39, p. 203-206.

Jackson, C.A.L., Barber, G.P., and Martinsen, O.J., 2008, Submarine slope morphology as a control on the development of sand-rich turbidite depositional systems: 3D seismic

analysis of the Kyrre Fm (Upper Cretaceous), Måløy Slope, offshore Norway: Marine and Petroleum Geology, v. 25, p. 663-680.

Jackson, C.A.L., Zakaria, A.A., Johnson, H.D., Tongkul, F., and Crevello, P.D., 2009, Sedimentology, stratigraphic occurrence and origin of linked debrites in the West Crocker Formation (Oligo-Miocene), Sabah, NW Borneo: Marine and Petroleum Geology, v. 26, p. 1957-1973.

Jenkyns, H.C., 1996, Relative sea-level change and carbon isotopes: Data from the upper Jurassic (Oxfordian) of central and Southern Europe. Terra Nova, v. 8, p. 75-85.

Jobe, Z.R., Lowe, D.R. and Morris, W.R., 2012, Climbing-ripple successions in turbidite systems: depositional environments, sedimentation and accumulation times: Sedimentology, v. 59, p. 867-898.

Jobe, Z.R., Sylvester, Z., Howes, N., Pirmez, C., Parker, A., Cantelli, A., Smith, R., Wolinsky, M.A., O'Byrne, C., Slowey, N., and Prather, B., 2017, High-resolution, millennial-scale patterns of bed compensation on a sand-rich intraslope submarine fan, western Niger Delta slope: Geological Society of America, Bulletin, v. 129, p. 23-37.

Jobe, Z., Sylvester, Z., Pittaluga, M.B., Frascati, A., Pirmez, C., Minisini, D., Howes, N. and Cantelli, A., 2017, Facies architecture of submarine channel deposits on the western Niger Delta slope: Implications for grain-size and density stratification in turbidity currents: Journal of Geophysical Research: Earth Surface, v. 122, p. 473-491.

Jobe, Z.R., Howes, N., Romans, B.W. and Covault, J.A., 2018, Volume and recurrence of submarine-fan-building turbidity currents. The Depositional Record, v. 4, p. 160-176.

Johnson, A.M., 1970, Physical Processes in Geology. San Francisco: Freeman, Cooper and Company, 577 p.

Joseph, P., Babonneau, N., Bourgeois, A., Cotteret, G., Eschard, R., Garin, B., Gomes De Souza, O., Granjeon, D., Guillocheau, F., Lerat, O. and Quemener, J.M., 2000, December. The Annot Sandstone outcrops (French Alps): architecture description as input for quantification and 3D reservoir modeling. in P. Weimer, RM Slatt, J. Coleman, NC Rosen, H. Nelson, AH Bouma, MJ Styzen, and DT Lawrence, Deep-

Water Reservoirs of the World: Gulf Coast Section SEPM Foundation 20th Annual Research Conference, SEPM CD Special Publication, v. 28, p. 422-449.

Joseph, P., and Lomas, S.A., 2004, Deep-water sedimentation in the Alpine Foreland Basin of SE France: New perspectives on the Grès d'Annot and related systems—an introduction: Geological Society, London, Special Publications 221, p. 1-16.

Jorry, S.J., Jégou, I., Emmanuel, L., Jacinto, R.S. and Savoye, B., 2011, Turbiditic levee deposition in response to climate changes: the Var Sedimentary Ridge (Ligurian Sea): Marine Geology, v. 279, p. 148-161.

Joy, A.M., 1992, Estimation of Cenozoic water depths in the Western Central Graben, UK North Sea, by subsidence modelling, in Hardman, R.F.P., ed., Exploration Britain: Geological Insights for the Next Decade: Geological Society, London, Special Publication 67, p. 107–125, https://doi.org/10.1144/GSL.SP.1992.067.01.05.

Kane, I.A., Catterall, V., McCaffrey, W.D., and Martinsen, O.J., 2010, Submarine channel response to intrabasinal tectonics: the influence of lateral tilt: American Association of Petroleum Geologists, Bulletin, v. 94, p. 189-219.

Kane, I.A. and Clare, M.A., 2019, Dispersion, accumulation, and the ultimate fate of microplastics in deep-marine environments: a review and future directions: Frontiers in Earth Science, v. 7.

Kane, I.A. and Hodgson, D.M., 2011, Sedimentological criteria to differentiate submarine channel levee subenvironments: exhumed examples from the Rosario Fm.(Upper Cretaceous) of Baja California, Mexico, and the Fort Brown Fm.(Permian), Karoo basin, S. Africa: Marine and Petroleum Geology, v. 28, p. 807-823.

Kane, I.A. and Pontén, A.S., 2012, Submarine transitional flow deposits in the Paleogene Gulf of Mexico: Geology, v. 40, p. 1119-1122.

Kane, I.A., McCaffrey, W.D. and Peakall, J., 2008, Controls on sinuosity evolution within submarine channels: Geology, v. 36, p.287-290.

Kane, I.A., McCaffrey, W.D., and Martinsen, O.J., 2009, Allogenic vs. autogenic controls on megaflute formation: Journal of Sedimentary Research, v. 79, p. 643-651.

Kane, I.A., McGee, D.T., and Jobe, Z.R., 2012, Halokinetic effects on submarine channel equilibrium profiles and implications for facies architecture: conceptual model illustrated with a case study from Magnolia Field, Gulf of Mexico, in Alsop G.I et al., eds., Salt Tectonics, Sediment and Prospectivity: Geological Society of London, Special Publication 363, p. 289-302.

Kane, I.A., Pontén, A.S., Vangdal, B., Eggenhuisen, J.T., Hodgson, D.M., and Spychala, Y.T., 2017, The stratigraphic record and processes of turbidity current transformation across deep-marine lobes: Sedimentology, v. 64, p. 1236-1273.

Katz, M.E., Miller, K.G., Wright, J.D., Wade, B.S., Browning, J.V., Cramer, B.S. and Rosenthal, Y., 2008. Stepwise transition from the Eocene greenhouse to the Oligocene icehouse: Nature Geoscience, v. 1, p. 329.

Kennett, J.P., 1977. Cenozoic evolution of Antarctic glaciation, the circum-Antarctic Ocean, and their impact on global paleoceanography: Journal of Geophysical Research, v. 82, p. 3843-3860.

Kenyon, N.H., and Millington, J., 1995, Contrasting deep sea depositional systems in the Bering Sea, in Pickering, K.T., Hiscott, R.N., Kenyon, N.H., Ricci Lucchi, F., and Smith, R.D.A., eds., Atlas of Deep Water Environments: Architectural Style in Turbidite Systems: London, Chapman and Hall, p. 196–202,

Kenyon, N.H., Millington, J., Droz, L. and Ivanov, M.K., 1995, Scour holes in a channel-lobe transition zone on the Rhône Cone: in Atlas of Deep Water Environments, Springer, Dordrech, p. 212 – 215.

Khripounoff, A., Vangriesheim, A., Babonneau, N., Crassous, P., Dennielou, B., and Savoye, B., 2003, Direct observation of intense turbidity current activity in the Zaire submarine valley at 4000 m water depth: Marine Geology, v. 194, p. 151–158.

Kilhams, B., Hartley, A., Huuse, M., and Davis, C., 2012, Characterizing the Paleocene turbidites of the North Sea: the Mey Sandstone Member, Lista Formation, UK Central Graben. Petroleum Geoscience, v. 18, p. 337-354.

Kilhams, B., Morton, A., Borella, R., Wilkins, A. and Hurst, A., 2014, Understanding the provenance and reservoir quality of the Sele Formation sandstones of the UK Central

Graben utilizing detrital garnet suites: Geological Society, London, Special Publications, v. 386, p. 129-142.

Kilhams, B., Hartley, A., Huuse, M., and Davis, C., 2015, Characterizing the Paleocene turbidites of the North Sea: Maureen Formation, UK Central Graben, in McKie, T., et al., eds., Tertiary deep-marine reservoirs of the North Sea region: An introduction: Geological Society, London, Special Publication 403, p. 43–62, https://doi.org/10.1144/SP403.1.

Knaust, D., Warchol, M. & Kane, I.A., 2014, Ichnodiversity and ichnoabundance: revealing depositional trends in a confined turbidite system: Sedimentology, v. 61, p. 2218-2267.

Kneller, B., 2003, The influence of flow parameters on turbidite slope channel architecture: Marine and Petroleum Geology, v. 20, p. 901-910.

Kneller, B. C. and Branney, M.J., 1995, Sustained high-density turbidity currents and the deposition of thick massive sands: Sedimentology, v. 42, p. 607-616.

Kneller, B.C., Edwards, D., McCaffrey, W.D., and Moore, R., 1991, Oblique reflection of turbidity currents: Geology, v. 19, p. 250 252.

Kneller, B. C., 1995, Beyond the turbidite paradigm: physical models for deposition of turbidites and their implications for reservoir prediction. in Hartley, A., and Prosser, D.J., eds., Characterisation of Deep Marine Clastic Systems: Geological Society of London, Special Publications 94, p. 29-46.

Kneller, B.C., and McCaffrey, W.D., 1995, Modelling the effects of salt-induced topography on deposition from turbidity currents: SEPM, Gulf Coast Section, p. 137-145.

Kneller, B. C., and McCaffrey, W. D., 1999, Depositional effects of flow non-uniformity and stratification within turbidity currents approaching a bounding slope: deflection, reflection and facies variation: Journal of Sedimentary Research, v. 69, p. 980-991.

Kneller, B., Dykstra, M., Fairweather, L., and Milana, J.P., 2016, Mass-transport and slope accommodation: implications for turbidite sandstone reservoirs: American Association of Petroleum Geologists, Bulletin, v. 100, p. 213-235.

Kneller, B., Bozetti, G., Callow, R., Dykstra, M., Hansen, L., Kane, I., Li, P., McArthur, A., Santa Catharina, A., dos Santos, T. and Thompson, P., 2019, Architecture, process and environmental diversity in a Late Cretaceous slope channel system: Journal of Sedimentary Research, in press.

Kolla, V. and Buffler, R.T., 1983, Morphologic, acoustic, and sedimentologic characteristics of the Magdalena Fan: Geo-Marine Letters, v. 3, p. 85-91.

Kolla, V. and Perlmutter, M.A., 1993, Timing of turbidite sedimentation on the Mississippi Fan: AAPG Bulletin, v. 77, p. 1129-1141.

Komar, P.D., 1971, Hydraulic jumps in turbidity currents: Geological Society of America Bulletin, v. 82, p. 1477-1488.

Kominz, M.A., Browning, J.V., Miller, K.G., Sugarman, P.J., Mizintseva, S. and Scotese, C.R., 2008, Late Cretaceous to Miocene sea-level estimates from the New Jersey and Delaware coastal plain coreholes: An error analysis: Basin Research, v. 20, p. 211-226

Kopaevich, L.F., Beniamovskii, V.N. and Bragina, L.G., 2015, Upper Albian-Turonian foraminifers and radiolarians from the Kelevudag section, northeastern Azerbaijan: Stratigraphy and Geological Correlation, v. 23, p. 580-599.

Krastel, S., Schmincke, H.U. and Jacobs, C., 2001, Formation of submarine canyons on the flanks of the Canary Islands: Geo-Marine Letters, v. 20, p. 160-167.

Kubo, Y.S., 2004, Experimental and numerical study of topographic effects on deposition from two-dimensional, particle-driven density currents: Sedimentary Geology, v. 164, p. 311-326.

Kuenen, P.H., 1957, Sole markings of graded graywacke beds: The Journal of Geology, v. 65, p. 231-258.

Kuenen, P.H. and Migliorini, C.I., 1950, Turbidity currents as a cause of graded bedding: The Journal of Geology, v. 58, p. 91-127.

Ladant, J.B., Donnadieu, Y., Lefebvre, V. and Dumas, C., 2014, The respective role of atmospheric carbon dioxide and orbital parameters on ice sheet evolution at the Eocene-Oligocene transition: Paleoceanography, v. 29, p. 810-823.

Lamb, M.P., Hickson, T., Marr, J.G., Sheets, B., Paola, C. and Parker, G., 2004, Surging versus continuous turbidity currents: flow dynamics and deposits in an experimental intraslope minibasin: Journal of Sedimentary Research, v. 74, p. 148-155.

Lamb, M.P., Parsons, J.D., Mullenbach, B.L., Finlayson, D.P., Orange, D.L., and Nittrouer, C.A., 2008, Evidence for superelevation, channel incision, and formation of cyclic steps by turbidity currents in Eel Canyon, California: Geological Society of America Bulletin, v. 120, p. 463-475.

Lee, S.E., Talling, P.J., Ernst, G.G. and Hogg, A.J., 2002, Occurrence and origin of submarine plunge pools at the base of the US continental slope: Marine Geology, v. 185, p. 363-377.

Lee, S.E., Amy, L.A., and Talling, P.J., 2004, The character and origin of thick base-of-slope sandstone units of the Peïra Cava outlier, SE France, in Lomas, S., and Joseph, P., eds., Deep-Water Sedimentation in the Alpine Basin of SE France: New Perspectives on the Grès d'Annot and Related Systems: Geological Society of London, Special Publication 221, p. 331-347.

Leeder, M.R., 1982, Sedimentology, process and product: London, George Allen and Unwin Publishers, p. 344.

Li, P., Kneller, B.C., Thompson, P., Bozetti, G. and Dos Santos, T., 2018, Architectural and facies organisation of slope channel fills: Upper Cretaceous Rosario Formation, Baja California, Mexico: Marine and Petroleum Geology, v. 92, p. 632–649.

Liu, Q., Kneller, B., Fallgatter, C., Valdez Buso, V., and Milana, J.P., 2018, Tabularity of individual turbidite beds controlled by flow efficiency and degree of confinement: Sedimentology, v. 65, p. 2368 - 2387.

Liu, Z., Pagani, M., Zinniker, D., DeConto, R., Huber, M., Brinkhuis, H., Shah, S.R., Leckie, R.M. and Pearson, A., 2009, Global cooling during the Eocene-Oligocene climate transition. Science, v. 323, p. 1187-1190.

Locat, J. and Lee, H.J., 2002, Submarine landslides: advances and challenges: Canadian Geotechnical Journal, v. 39, p. 193-212.

Lomas, S.A., and Joseph, P., 2004, Confined turbidite systems, in Lomas, S., and Joseph, P., eds., Confined Turbidite Basins: Geological Society of London, Special Publication 222, p. 1-7.

Lowe, D.R., 1979, Sediment gravity flows: their classification and some problems of application to natural flows and deposits: SEPM Special Publication 27, p. 75-82.

Lowe, D.R., 1982, Sediment gravity flows: II Depositional models with special reference to the deposits of high-density turbidity currents: Journal of Sedimentary Petrology, v. 52. p. 279-297.

Lowe, D.R., and Guy, M., 2000, Slurry-flow deposits in the Britannia Formation (Lower Cretaceous), North Sea: a new perspective on the turbidity current and debris flow problem: Sedimentology, v. 47, p. 31-70.

Lucente, C.C., 2004, Topography and palaeogeographic evolution of a middle Miocene foredeep basin plain (Northern Apennines, Italy): Sedimentary Geology, v. 170, p. 107-134.

Luchi, R., Balachandar, S., Seminara, G. and Parker, G., 2018, Turbidity currents with equilibrium basal driving layers: A mechanism for long runout: Geophysical Research Letters, v. 45, p. 1518-1526.

Luthi, S., 1981, Experiments on non-channelized turbidity currents and their deposits: Marine Geology, v. 40, p. M59–M68.

Macauley, R.V. and Hubbard, S.M., 2013, Slope channel sedimentary processes and stratigraphic stacking, Cretaceous Tres Pasos Formation slope system, Chilean Patagonia: Marine and Petroleum Geology, v. 41, p.146-162.

Maier, K.L., Fildani, A., Paull, C.K., McHargue, T.R., Graham, S.A. and Caress, D.W., 2013, Deep-sea channel evolution and stratigraphic architecture from inception to abandonment from high-resolution autonomous underwater vehicle surveys offshore central California. Sedimentology, v. 60(4), p. 935-960.

Maier, K.L., Roland, E.C., Walton, M.A., Conrad, J.E., Brothers, D.S., Dartnell, P. and Kluesner, J.W., 2018. The Tectonically Controlled San Gabriel Channel–Lobe

Transition Zone, Catalina Basin, Southern California Borderland: Journal of Sedimentary Research, v. 88, p. 942-959.

Maier, K.L., Gales, J., Paull, C.K., Rosenberger, K., Talling, P.J., Simmons, S.M., Gwiazda, R.H., McGann, M., Cartigny, M.J., Lundsten, E. and Anderson, K., 2019, Linking direct measurements of turbidity currents to submarine canyon-floor deposits: Frontiers in Earth Science, v. 7, p. 144.

Mallon, A.J., and Swarbrick, R.E., 2002, A compaction trend for non-reservoir North Sea Chalk: Marine and Petroleum Geology, v. 19, p. 527–539, https://doi.org/10.1016/S0264-8172(02)00027-2.

Manley, P.L. and Flood, R.D., 1988, Cyclic sediment deposition within Amazon deep-sea fan. AAPG Bulletin, v. 72, p. 912-925.

Marr, J.G., Harff, A.P., Shanmugam, G. and Parker, G., 2001, Experiments on sub aqueous sandy gravity flows: The role of clay and water content in flow dynamics and depositional structures: Geological Society of America Bulletin, v. 113, p. 1377–1386.

Marshall, J.D., 1991, Climatic and oceanographic isotopic signals from the carbonate rock record and their preservation: Geological magazine, v. 129, p. 143-160.

Marini, M., Milli, S., Ravnås, R., and Moscatelli, M., 2015, A comparative study of confined vs. semi-confined turbidite lobes from the Lower Messinian Laga Basin (Central Apennines, Italy): implications for assessment of reservoir architecture: Marine and Petroleum Geology, v. 63, p. 142-165.

Marini, M., Patacci, M., Felletti, F., and McCaffrey, W.D., 2016a, Fill to spill stratigraphic evolution of a confined turbidite mini-basin succession, and its likely well bore expression: The Castagnola Fm, NW Italy: Marine and Petroleum Geology, v. 69, p. 94-111.

Marini, M., Felletti, F., Milli, S. and Patacci, M., 2016b, The thick-bedded tail of turbidite thickness distribution as a proxy for flow confinement: Examples from tertiary basins of central and northern Apennines (Italy): Sedimentary Geology, v. 341, p. 96-118.

Marjanac, T., 1990, Reflected sediment gravity flows and their deposits in flysch of middle Dalmatia, Yugoslavia: Sedimentology, v. 37, p. 921-929.

Marshall, J.D., Tucker, O.D. and Lovelock, C.E., 2016, Goldeneye: modelling a depleted field for carbon capture–how much uncertainty is left?: Petroleum Geoscience, v. 22, p. 37-45.

Mason, C.C., Fildani, A., Gerber, T., Blum, M.D., Clark, J.D. and Dykstra, M., 2017, Climatic and anthropogenic influences on sediment mixing in the Mississippi source-to-sink system using detrital zircons: Late Pleistocene to recent: Earth and Planetary Science Letters, v. 466, p. 70-79.

Masson, D.G., Harbitz, C.B., Wynn, R.B., Pedersen, G. and Løvholt, F., 2006, Submarine landslides: processes, triggers and hazard prediction: Philosophical Transactions of the Royal Society A: Mathematical, Physical and Engineering Sciences, v. 364, p. 2009-2039.

Mayall, M., Lonergan, L., Bowman, A., James, S., Mills, K., Primmer, T., Pope, D., Rogers, L., and Skeene, R., 2010, The response of turbidite slope channels to growth-induced seabed topography: American Association of Petroleum Geologists, Bulletin: v. 94, p. 1011-1030.

Meiburg, E. and Kneller, B., 2010, Turbidity currents and their deposits: Annual Review of Fluid Mechanics, v, 42, p. 135-156.

Melchin, M.J. and Holmden, C., 2006, Carbon isotope chemostratigraphy in Arctic Canada: sea-level forcing of carbonate platform weathering and implications for Hirnantian global correlation: Palaeogeography, Palaeoclimatology, Palaeoecology, v. 234, p. 186-200.

Métivier, F., Gaudemer, Y., Tapponnier, P. and Klein, M., 1999, Mass accumulation rates in Asia during the Cenozoic: Geophysical Journal International, v. 137, p. 280-318.

McArthur, A., Kane, I., Bozetti, G., Hansen, L., and Kneller, B., 2019, Supercritical flows overspilling from bypass-dominated submarine channels and the development of overbank bedforms: The Depositional Record, v. 0, p 1 – 20, doi: https://doi.org/10.1002/dep2.78.

McArthur, A.D., Kneller, B.C., Wakefield, M.I., Souza, P.A. and Kuchle, J., 2016, Palynofacies classification of the depositional elements of confined turbidite systems:

Examples from the Gres d'Annot, SE France: Marine and Petroleum Geology, v. 77, p. 1254-1273.

McCaffrey, W.D., and Kneller, B.C., 2001, Process controls on the development of stratigraphic trap potential on the margins of confined turbidite systems and aids to reservoir evaluation: American Association of Petroleum Geologists, Bulletin, v. 85, p. 971-988.

McCaffrey, W.D., and Kneller, B.C., 2004, Scale effects of non-uniformity on deposition from turbidity currents with reference to the Gres d'Annot of SE France, in Lomas, S., and Joseph, P., eds., Deep-Water Sedimentation in the Alpine Basin of SE France: New Perspectives on the Grès d'Annot and Related Systems: Geological Society of London, Special Publication 221, p. 301-310.

McHargue, T., Pyrcz, M.J., Sullivan, M.D., Clark, J.D., Fildani, A., Romans, B.W., Covault, J.A., Levy, M., Posamentier, H.W. and Drinkwater, N.J., 2011, Architecture of turbidite channel systems on the continental slope: patterns and predictions: Marine and Petroleum Geology, v. 28, p. 728-743.

McHargue, T. R., Hodgson, D. M. and Shelef, E., 2019. Architectural Diversity of Submarine Lobes: EarthArXiv, https://eartharxiv.org/cs8rp/.

McNeill, L.C., Dugan, B., Backman, J., Pickering, K.T., Pouderoux, H.F., Henstock, T.J., Petronotis, K.E., Carter, A., Chemale Jr, F., Milliken, K.L. and Kutterolf, S., 2017, Understanding Himalayan erosion and the significance of the Nicobar Fan: Earth and Planetary Science Letters, v. 475, p. 134-142.

Menard Jr, H.W., 1955, Deep-sea channels, topography, and sedimentation: AAPG Bulletin, v. 39, p. 236-255.

Miall, A., 2014, Allogenic sedimentary controls: in Fluvial Depositional Systems, Springer, Cham. p. 171 -215.

Middleton, G.V., 1967, Experiments on density and turbidity currents: III. Deposition of sediment: Canadian Journal of Earth Sciences, v. 4, p. 475-505.

Middleton, G.V., 1993, Sediment deposition from turbidity currents: Annual Review of Earth and Planetary Sciences, v. 21, p. 89-114.

Middleton, G.V., and Hampton, M.A., 1973, Sediment gravity flows: Mechanics of flow and deposition, in Middleton, G.V., Bouma, A.H., eds., Turbidites and Deep Water Sedimentation: Pacific Section, Society of Economic Paleontologists and Mineralogists Book 2, Short Course Notes, p. 1–38.

Miller, R.P. and Heller, P.L., 1994, Depositional framework and controls on mixed carbonate-siliciclastic gravity flows: Pennsylvanian-Permian shelf to basin transect, south-western Great Basin, USA: Sedimentology, v. 41, p. 1-20.

Middleton, G.V and Southard, J.B., 1984, Mechanics of Sediment Movement: SEPM, Eastern Section Short Course 3 Providence, 401 p.

Miller, K.G., Browning, J.V., Aubry, M.P., Wade, B.S., Katz, M.E., Kulpecz, A.A. and Wright, J.D., 2008, Eocene–Oligocene global climate and sea-level changes: St. Stephens Quarry, Alabama. Geological Society of America Bulletin, v. 120, p. 34-53.

Miller, K.G., Kominz, M.A., Browning, J.V., Wright, J.D., Mountain, G.S., Katz, M.E., Sugarman, P.J., Cramer, B.S., Christie-Blick, N. and Pekar, S.F., 2005, The Phanerozoic record of global sea-level change: Science, v. 310, p. 1293-1298.

Miller, K.G., Sugarman, P.J., Browning, J.V., Kominz, M.A., Hernández, J.C., Olsson, R.K., Wright, J.D., Feigenson, M.D. and Van Sickel, W., 2003, Late Cretaceous chronology of large, rapid sea-level changes: Glacioeustasy during the greenhouse world: Geology, v. 31, p. 585-588.

Milliman, J.D. and Syvitski, J.P., 1992, Geomorphic/tectonic control of sediment discharge to the ocean: the importance of small mountainous rivers: The journal of Geology, v. 100, p. 525-544.

Mitchell, S.F., Paul, C.R.C. and Gale, A.S., 1996, Carbon isotopes and sequence stratigraphy: Geological Society, London, Special Publications, v. 104, p. 11-24.

Mitchell, S.F., Pickerill, R.K. and Stemann, T.A., 2001, The Port Morant Formation (Upper Pleistocene, Jamaica): high resolution sedimentology and paleoenvironmental analysis of a mixed carbonate clastic lagoonal succession: Sedimentary Geology, v. 144, p. 291-306.

Mohrig, D., and Buttles, J., 2007, Deep turbidity currents in shallow channels: Geology, v. 35, p. 155-158.

Marr, J.G., Harff, P.A., Shanmugam, G. and Parker, G., 2001, Experiments on subaqueous sandy gravity flows: The role of clay and water content in flow dynamics and depositional structures: Geological Society of America Bulletin, v. 113, p. 1377-1386.

Marsaglia, K.M., Martin, C.E., Kautz, C.Q., Shapiro, S.A. and Carter, L., 2011, Linking a late Miocene–Pliocene hiatus in the deep-sea Bounty Fan off South Island, New Zealand, to onshore tectonism and lacustrine sediment storage: Geosphere, v. 7, p. 305-312.

Morris, W.R. and Busby-Spera, C.J., 1988, Sedimentologic evolution of a submarine canyon in a forearc basin, Upper Cretaceous Rosario Formation, San Carlos, Mexico: AAPG Bulletin, v. 72, p. 717-737.

Morris, S.A., Kenyon, N.H., Limonov, A.F., and Alexander, J., 1998, Downstream changes of large-scale bedforms in turbidites around the Valencia channel mouth, north-west Mediterranean: Implications for palaeoflow reconstruction: Sedimentology, v. 45, p. 365–377,

Morley, C.K. and Leong, L.C., 2008, Evolution of deep-water synkinematic sedimentation in a piggyback basin, determined from three-dimensional seismic reflection data: Geosphere, v. 4, p. 939-962.

Moscardelli, L., Wood, L. and Mann, P., 2006, Mass-transport complexes and associated processes in the offshore area of Trinidad and Venezuela. AAPG bulletin, v. 90, p. 1059-1088.

Moscardelli, L., Ochoa, J., Lunt, I. and Zahm, L., 2019, Mixed siliciclastic–carbonate systems and their impact for the development of deep-water turbidites in continental margins: A case study from the Late Jurassic to Early Cretaceous Shelburne subbasin in offshore Nova Scotia: AAPG Bulletin, v. 103, p. 2487-2520.

Moscardelli, L. and Wood, L., 2008, New classification system for mass transport complexes in offshore Trinidad: Basin Research, v. 20, p. 73-98.

Mougin, F., 1978, Contribution à l'étude des Sédiments tertiaires de la partie orientale du synclinal d'Annot (Alpes de Haute Provence). Stratigraphie, Grochimie, Micropaldontologie: Unpublished Ph.D. Thesis, Université Scientifique et Médicale de Grenoble, Grenoble. 165 p.

Mountjoy, J.J., Howarth, J.D., Orpin, A.R., Barnes, P.M., Bowden, D.A., Rowden, A.A., Schimel, A.C., Holden, C., Horgan, H.J., Nodder, S.D. and Patton, J.R., 2018, Earthquakes drive large-scale submarine canyon development and sediment supply to deep-ocean basins. Science advances, v. 4, p. 3748.

Muck, M.T., and Underwood, M.B., 1990, Upslope flow of turbidity currents: a comparison among field observations, theory, and laboratory models: Geology, v. 18, p. 54-57

Mudge, D.C., and Jones, S.M., 2004, Palaeocene uplift and subsidence events in the Scotland-Shetland and North Sea region and their relationship to the Iceland Plume: Journal of the Geological Society, v. 161, p. 381–386, https://doi.org/10.1144/0016-764903-038.

Mudge, D.C., 2015, Regional controls on Lower Tertiary sandstone distribution in the North Sea and NE Atlantic margin basins, in McKie, T., et al., eds., Tertiary deep-marine reservoirs of the North Sea region: an introduction: Geological Society, London, Special Publications 403, p. 17–42, https://doi.org/10.1144/SP403.5.

Mueller, P., Patacci, M. and Di Giulio, A., 2017, Hybrid event beds in the proximal to distal extensive lobe domain of the coarse-grained and sand-rich Bordighera turbidite system (NW Italy): Marine and Petroleum Geology, v. 86, p. 908-931.

Mulder, T., and Alexander, J., 2001, The physical character of subaqueous sedimentary density flows and their deposits: Sedimentology, v. 48, p. 269-299.

Mulder, T. and Alexander, J., 2001, Abrupt change in slope causes variation in the deposit thickness of concentrated particle-driven density currents: Marine Geology, v. 175, p. 221-235.

Mulder, T., Tisot, J.P., Cochonat, P., and Bourillet, J.F., 1994, Regional assessment of mass failure events in the Baie des Anges, Mediterranean Sea: Marine Geology, v. 122, p. 29–45, https://doi.org/10.1016/0025-3227(94)90203-8.

Mulder, T., Zaragosi, S., Razin, P., Grelaud, C., Lanfumey, V. and Bavoil, F., 2009, A new conceptual model for the deposition process of homogenite: Application to a cretaceous megaturbidite of the western Pyrenees (Basque region, SW France): Sedimentary Geology, v. 222, p. 263-273.

Muto, T., and Steel, R.J., 1997, Principles of regression and transgression: The nature of the interplay between accommodation and sediment supply: Perspectives: Journal of Sedimentary Research, v. 67, p. 994–1000.

Mutti, E., 1977, Distinctive thin-bedded turbidite facies and related depositional environments in the Eocene Hecho Group (South-central Pyrenees, Spain): Sedimentology, v. 24, p. 107–131.

Mutti, E., 1983, The Hecho Eocene submarine fan system, south-central Pyrenees, Spain: Geo-Marine Letters, v. 3, p. 199-202.

Mutti, E., 1992, Turbidite sandstones: AGIP- Instituto di Geologia, Università di Parma, p. 275.

Mutti, E., Bernoulli, D., Ricci Lucchi, F., and Tinterri, R., 2009, Turbidites and turbidity currents from Alpine 'flysch' to the exploration of continental margins: Sedimentology, v. 56, p. 267-318.

Mutti, E. and Normark, W.R., 1987, Comparing examples of modern and ancient turbidite systems: problems and concepts: in Marine Clastic Sedimentology, Springer Netherlands, p. 1-38.

Mutti, E., Tinterri, R., Benevelli, G., di Biase, D. and Cavanna, G., 2003, Deltaic, mixed and turbidite sedimentation of ancient foreland basins: Marine and Petroleum Geology, v. 20, p. 733-755.

Nadin, P.A., and Kusznir, N.J., 1996, Forward and reverse stratigraphic modelling of Cretaceous-Tertiary post-rift subsidence and Paleogene uplift in the Outer Moray Firth Basin,central North Sea, in Knox, R. O. B., ed., Correlation of the early Paleogene in northwest Europe: an overview: Geological Society, London, Special Publication 101, p. 43–62, https://doi.org/10.1144/GSL.SP.1996.101.01.03.

Nardin, T.R., Hein, F.J., Gorsline, D.S. and Edwards, B.D., 1979, A review of mass movement processes, sediment and acoustic characteristics, and contrasts in slope and base-of-slope systems versus canyon-fan-basin floor systems: SEPM Special Publications, v. 27, p. 61-73.

Natland, M . L., and Kuenen, PH. H., 1951, Sedimentary History of the Ventura Basin, California, and the Action of Turbidity Currents: ibid, p. 78-107.

Navarre, J.C., Claude, D., Liberelle, E., Safa, P., Vallon, G. and Keskes, N., 2002, Deepwater turbidite system analysis, West Africa: Sedimentary model and implications for reservoir model construction: The Leading Edge, v. 21, p. 1132-1139.

Nelson, C.H., Gutierrez Pastor, J., Goldfinger, C., and Escutia, c., 2012, Great earthquakes along the western United States continental margin: implications for hazards, stratigraphy, and turbidite lithology: Natural Hazards and Earth System Sciences, v. 12, p. 3191–3208.

Nemec, W. and Steel, R.J., 1984, Alluvial and Coastal Conglomerates: Their Significant Features and Some Comments on Gravelly Mass-Flow Deposits: CSPG Special Publication, Memoir 10, 1 - 31p.

Nikishin, A.M., Cloetingh, S., Brunet, M-F., Stephenson, R.A., Bolotov, S.N., and Ershov, A.V., 1998, Scythian Platform, Caucasus and Black Sea region: Mesozoic-Cenozoic tectonic history and dynamics. In: Crasquin-Soleau, S. and Barrier, É. (eds.), Peri-Tethys Memoir 3: Stratigraphy and Evolution of Peri-Tethyan platforms. Me□ moires du Muse□ um National d'Histoire Naturelle, Paris, v. 177, p. 163-176.

Nikishin A.M., Ziegler P., Panov, D.I., Nazarevich B.P., Brunet M., F., Stephenson R.A., Bolotov S.N., Korataev M.V. & Tikhomrov P.L., 2001, Mesozoic and Cainozoic evolution of the Scythian Platform - Black Sea - Caucasus domain. In: Ziegler P., Cavazza W., Robertson A.H.F. & Crasquin-Soleau S. (Eds.), Peri-Tethys Memoir 6 - Peri-Tethyan rift/wrench basins and passive margins. Me□ moires du Muse□ um national d'Histoire naturelle, Paris, v. 186, p. 295-346.

Nissen, S.E., Haskell, N.L., Steiner, C.T. and Coterill, K.L., 1999, Debris flow outrunner blocks, glide tracks, and pressure ridges identified on the Nigerian continental slope using 3-D seismic coherency: The Leading Edge, v. 18, p. 595-599.

Noda, A., TuZino, T., Kanai, Y., Furukawa, R. and Uchida, J.I., 2008, Paleoseismicity along the southern Kuril Trench deduced from submarine-fan turbidites: Marine Geology, v. 254, p. 73-90.

Normark, W.R., 1978, Fan valleys, channels, and depositional lobes on modern submarine fans: characters for recognition of sandy turbidite environments: AAPG Bulletin, v. 62, p. 912-931.

Normark, W.R. and Reid, J.A., 2003, Extensive deposits on the Pacific Plate from late Pleistocene North American glacial lake outbursts: The Journal of Geology, v. 111, p. 617-637.

Normark, W.R., Piper, D.J.W. and Hess, G.R., 1979, Distributary channels, sand lobes, and mesotopography of Navy submarine fan, California Borderland, with applications to ancient fan sediments: Sedimentology, v. 26, p. 749-774.

Normark, W.R., Piper, D.J.W., and Stow, D.A.V., 1983, Quaternary Development of channels, levees, and lobes on middle Laurentian Fan: American Association of Petroelum Geologists Bulletin, v. 67, p. 1400-1409.

Oluboyo, A.P., Gawthorpe, R.L., Bakke, K., and Hadler-Jacobsen, F., 2014, Salt tectonic controls on deep-water turbidite depositional systems: Miocene, southwestern Lower Congo Basin, offshore Angola: Basin Research, v. 26, p. 597-620.

Omura, A. and Hoyanagi, K., 2004, Relationships between composition of organic matter, depositional environments, and sea-level changes in backarc basins, central Japan: Journal of Sedimentary Research, v. 74, p. 620-630.

Ortiz-Karpf, A., Hodgson, D.M., and McCaffrey, W.D., 2015, The role of mass-transport complexes in controlling channel avulsion and the subsequent sediment dispersal patterns on an active margin: the Magdalena Fan, offshore Colombia: Marine and Petroleum Geology, v. 64, p. 58-75.

Ortiz-Karpf, A., Hodgson, D.M., Jackson, C.A.L., and McCaffrey, W.D., 2016, Mass-transport complexes as markers of deep-water fold-and-thrust belt evolution: insights from the southern Magdalena Fan, Offshore Colombia: Basin Research, v. 30, p. 65-88.

Oshaghi, M.R., Afshin, H. and Firoozabadi, B., 2013, Experimental investigation of the effect of obstacles on the behavior of turbidity currents: Canadian Journal of Civil Engineering, v. 40, p. 343-352.

Osleger, D.A. and Montañez, I.P., 1996, Cross-platform architecture of a sequence boundary in mixed siliciclastic-carbonate lithofacies, Middle Cambrian, southern Great Basin, USA: Sedimentology, v. 43, p. 197-217.

Palanques, A., Kenyon, N.H., Alonso, B. and Limonov, A., 1995, Erosional and depositional patterns in the Valencia Channel mouth: an example of a modern channel-lobe transition zone. Marine Geophysical Researches, v. 17, p. 503-517.

Pantin, H.M. and Leeder, M.R., 1987, Reverse flow in turbidity currents: the role of internal solitons: Sedimentology, v. 34, p. 1143-1155.

Parker, G., Fukushima, Y. and Pantin, H.M., 1986, Self-accelerating turbidity currents: Journal of Fluid Mechanics, v. 171, p. 145-181.

Patacci, M., Haughton, P.D., and McCaffrey, W.D., 2014, Rheological complexity in sediment gravity flows forced to decelerate against a confining slope, Braux, SE France: Journal of Sedimentary Research, v. 84, p. 270-277.

Paull, C.K., Mitts, P., Ussler III, W., Keaten, R. and Greene, H.G., 2005, Trail of sand in upper Monterey Canyon: offshore California: Geological Society of America Bulletin, v. 117, p. 1134-1145.

Paull, C.K., Talling, P.J., Maier, K.L., Parsons, D., Xu, J., Caress, D.W., Gwiazda, R., Lundsten, E.M., anderson, K., Barry, J.P. and Chaffey, M., 2018, Powerful turbidity currents driven by dense basal layers: Nature communications, v. 9, p. 4114.

Paull, C.K., Ussler III, W., Caress, D.W., Lundsten, E., Covault, J.A., Maier, K.L., Xu, J. and Augenstein, S., 2010, Origins of large crescent-shaped bedforms within the axial channel of Monterey Canyon, offshore California: Geology, v. 6, p. 755-774.

Peakall, J., Ashworth, P. and Best, J., 1996, Physical modelling in fluvial geomorphology: principles, applications and unresolved issues: The Scientific Nature of Geomorphology, p. 221-253.

Peakall, J., McCaffrey, B. and Kneller, B., 2000, A process model for the evolution, morphology, and architecture of sinuous submarine channels: Journal of Sedimentary Research, v. 70, p. 434 - 448.

Pearson, P.N., Foster, G.L. and Wade, B.S., 2009, Atmospheric carbon dioxide through the Eocene–Oligocene climate transition: Nature, V. 461, p. 1110.

Pearson, P.N., McMillan, I.K., Wade, B.S., Jones, T.D., Coxall, H.K., Bown, P.R. and Lear, C.H., 2008, Extinction and environmental change across the Eocene-Oligocene boundary in Tanzania: Geology, v. 36, p. 179-182.

Pemberton, E.A., Hubbard, S.M., Fildani, A., Romans, B. and Stright, L., 2016, The stratigraphic expression of decreasing confinement along a deep-water sediment routing system: Outcrop example from southern Chile: Geosphere, v. 12(1), p. 114-134.

Pickering, K.T. and Corregidor, J., 2005, Mass-transport complexes (MTCs) and tectonic control on basin-floor submarine fans, middle Eocene, south Spanish Pyrenees: Journal of Sedimentary Research, v. 75, p. 761-783.

Pickering, K.T., and Hiscott, R.N., 1985, Contained (reflected) turbidity currents from the Middle Ordovician Cloridorme Formation, Quebec, Canada: an alternative to the antidune hypothesis: Sedimentology, v. 32, p. 373-394.

Pickering, K.T. and Bayliss, N.J., 2009, Deconvolving tectono-climatic signals in deep-marine siliciclastics, Eocene Ainsa basin, Spanish Pyrenees: Seesaw tectonics versus eustasy: Geology, v. 37, p. 203-206.

Pickering, K.T., Pouderoux, H., McNeill, L.C., Backman, J., Chemale, F., Kutterolf, S., Milliken, K.L., Hideki, M., Henstock, T.J., Stevens, D.E. and Parnell, C., 2020, Sedimentology, stratigraphy and architecture of the Nicobar Fan (Bengal–Nicobar Fan System), Indian Ocean: Results from International Ocean Discovery Program Expedition 362: Sedimentology. In press.

Pickering, K.T., Underwood, M.B., Saito, S., Naruse, H., Kutterolf, S., Scudder, R., Park, J.O., Moore, G.F. and Slagle, A., 2013, Depositional architecture, provenance, and tectonic/eustatic modulation of Miocene submarine fans in the Shikoku Basin:

Results from Nankai Trough Seismogenic Zone Experiment: Geochemistry, Geophysics, Geosystems, v. 14(6), p. 1722-1739.

Picot, M., Marsset, T., Droz, L., Dennielou, B., Baudin, F., Hermoso, M., De Rafélis, M., Sionneau, T., Cremer, M., Laurent, D. and Bez, M., 2019, Monsoon control on channel avulsions in the Late Quaternary Congo Fan: Quaternary Science Reviews, v. 204, p. 149-171.

Pierau, R., Hanebuth, T.J., Krastel, S. and Henrich, R., 2010, Late Quaternary climatic events and sea-level changes recorded by turbidite activity, Dakar Canyon, NW Africa: Quaternary Research, v. 73, p. 385-392.

Pinter, P.R., Butler, R.W., Hartley, A.J., Maniscalco, R., Baldassini, N., and Di Stefano, A., 2017, Tracking sand-fairways through a deformed turbidite system: the Numidian (Miocene) of Central Sicily, Italy: Basin Research, v. 30, p. 480-501.

Pitman, W.C., 1978, Relationships between eustasy and stratigraphic sequences of passive margins: Geological Society of America Bulletin, v. 89, p. 1389– 1403.

Piper, D.J., Cochonat, P., and Morrison, M.L., 1999, The sequence of events around the epicentre of the 1929 Grand Banks earthquake: initiation of debris flows and turbidity current inferred from sidescan sonar: Sedimentology, v. 46, p. 79-97.

Pohl, F., 2019, Turbidity currents and their deposits in abrupt morphological transition zones. PhD thesis. 210 p.

Pohl, F., Eggenhuisen, J.T., Tilston, M. and Cartigny, M.J.B., 2019a, New flow relaxation mechanism explains scour fields at the end of submarine channels: Nature Communications, v. 10, p. 1-8.

Pohl, F., Eggenhuisen, J., Cartigny, M., Tilston, M., de Leeuw, J., & Hermidas, N., 2019b, The influence of a slope break on turbidite deposits: an experimental investigation. EarthArXiv, https://doi.org/10.31223/osf.io/v58gm.

Posamentier, H.W., Jervey, M.T. and Vail, P.R., 1988, Eustatic controls on clastic deposition I—conceptual framework. SEPM Special Publication 42, p. 109 – 124.

Postma, G., Hilgen, F.J. and Zachariasse, W.J., 1993, Precession-punctuated growth of a late Miocene submarine-fan lobe on Gavdos (Greece): Terra nova, v. 5, p. 438-444.

Postma, G., 1984, Mass-flow conglomerates in a submarine canyon: Abrioja fan-delta, Pliocene, southeast Spain: CSPG Special Publication, Memoir 10, p. 237 – 258.

Postma, G., 1984, Slumps and their deposits in fan delta front and slope (sedimentation model, Spain): Geology, v. 12, p. 27-30.

Postma, G., 1986, Classification of sediment gravity-flow deposits based on flow conditions during sedimentation: Geology, v. 14, p. 291–294

Postma, G. and Cartigny, M.J., 2014, Supercritical and subcritical turbidity currents and their deposits—A synthesis: Geology, v. 42, p. 987-990.

Postma, G., Hilgen, F.J. and Zachariasse, W.J., 1993, Precession-punctuated growth of a late Miocene submarine-fan lobe on Gavdos (Greece): Terra nova, v. 5, p. 438-444.

Postma, G., Nemec, W. and Kleinspehn, K., 1988, Large floating clasts in turbidites: a mechanism for their emplacement: Sedimentary Geology, v. 58, p. 47-61.

Popescu, I., Lericolais, G., Panin, N., Normand, A., Dinu, C. and Le Drezen, E., 2004. The Danube submarine canyon (Black Sea): morphology and sedimentary processes: Marine Geology, v. 206, p. 249-265.

Popescu, I., Lericolais, G., Panin, N., Wong, H.K. and Droz, L., 2001, Late Quaternary channel avulsions on the Danube deep-sea fan, Black Sea: Marine Geology, v. 179, p. 25-37.

Poprawski, Y., Basile, C., Agirrezabala, L., Jaillard, E., Gaudin, M., and Jacquin, T., 2014, Sedimentary and structural record of the Albian growth of the Bakio salt diapir (the Basque Country, northern Spain): Basin Research, v. 26, p. 746-766.

Poprawski, Y., Basile, C., Jailard, E., Gaudin, M., and Lopez, M., 2016, Halokinetic sequences in carbonate systems: An example from the Middle Albian Bakio Breccias Formation (Basque Country, Spain): Sedimentary Geology, v. 334, pp. 34-52.

Prather, B.E., Booth, J.R., Steffens, G.S., and Craig, P. A., 1998, Classification, lithologic calibration, and stratigraphic succession of seismic facies of intraslope basins, deep-water Gulf of Mexico:. American Association of Petroleum Geologists, Bulletin, v. 82, p. 701-728.

Prather, B.E., 2000, Calibration and visualization of depositional process models for above-grade slopes: a case study from the Gulf of Mexico: Marine and Petroleum Geology, v. 17, p. 619-638.

Prather, B.E., Pirmez, C., and Winker, C.D., 2012, Stratigraphy of linked intraslope basins: Brazos-Trinity system western Gulf of Mexico, in Prather B.E. et al., eds., Application of the Principles of Seismic Geomorphology to Continental-Slope and Base-of-Slope Systems: Case Studies from Seafloor and Near-Seafloor Analogues: SEPM, Special Publication 99, p. 83-109.

Prather, B.E., O'Byrne, C., Pirmez, C., and Sylvester, Z., 2017, Sediment partitioning, continental slopes and base-of-slope systems: Basin Research, v. 29, p. 394-416.

Pratson, L.F. and Coakley, B.J., 1996, A model for the headward erosion of submarine canyons induced by downslope-eroding sediment flows: Geological Society of America Bulletin, v. 108, p. 225-234.

Prélat, A., Hodgson, D.M., and Flint, S.S., 2009, Evolution, architecture and hierarchy of distributary deep-water deposits: a high-resolution outcrop investigation from the Permian Karoo Basin, South Africa: Sedimentology, v. 56, p. 2132-2154.

Prélat, A., Covault, J.A., Hodgson, D.M., Fildani, A., and Flint, S.S., 2010, Intrinsic controls on the range of volumes, morphologies, and dimensions of submarine lobes: Sedimentary Geology, v. 232, p. 66-76.

Prélat, A. and Hodgson, D., 2013, The full range of turbidite bed thickness patterns in Submarine lobes: Controls and implications: Journal of the Geological Society, v. 170, p. 209-214.

Prins, M.A., Postma, G., Cleveringa, J., Cramp, A. and Kenyon, N.H., 2000, Controls on terrigenous sediment supply to the Arabian Sea during the late Quaternary: the Indus Fan: Marine Geology, v. 169(3-4), p. 327-349.

Prothero, Donald R., and William A. Berggren eds., 2014, Eocene-Oligocene climatic and biotic evolution: Princeton University Press, 567 p.

Puigdefàbregas, C. and Souquet, P., 1986, Tecto-sedimentary cycles and depositional sequences of the Mesozoic and Tertiary from the Pyrenees: Tectonophysics, v. 129, p. 173-203.

Puigdefàbregas, C., Gjelberg, J.M., and Vaksdal, M., 2004, The Grès d'Annot in the Annot syncline: outer basin-margin onlap and associated soft-sediment deformation, in Lomas, S., and Joseph, P., eds., Deep-Water Sedimentation in the Alpine Basin of SE France: New Perspectives on the Grès d'Annot and Related Systems: Geological Society of London, Special Publication 221, p. 367-388.

Puga-Bernabéu, Á., Webster, J., Beaman, R., Reimer, P. and Renema, W., 2014, Filling the gap: A 60ky record of mixed carbonate-siliciclastic turbidite deposition from the Great Barrier Reef: Marine and Petroleum Geology, v. 50, pp. 40-50.

Pyles, D.R., Nilsen, T.H., Shew, R.D., Steffens, G.S. and Studlick, J.R.J., 2007, Architectural elements in a ponded submarine fan, Carboniferous Ross Sandstone, western Ireland: Atlas of deep-water outcrops: AAPG Studies in Geology, v. 56, p. 206-209.

Pyles, D.R. and Jennette, D.C., 2009, Geometry and architectural associations of co-genetic debrite–turbidite beds in basin-margin strata, Carboniferous Ross Sandstone (Ireland): Applications to reservoirs located on the margins of structurally confined submarine fans. Marine and Petroleum Geology, v. 26, p. 1974-1996.

Rabouille, C., Dennielou, B., Baudin, F., Raimonet, M., Droz, L., Khripounoff, A., Martinez, P., Mejanelle, L., Michalopoulos, P., Pastor, L. and Pruski, A., 2019, Carbon and silica megasink in deep-sea sediments of the Congo terminal lobes: Quaternary Science Reviews, v. 222, 105854, doi: https://doi.org/10.1016/j.quascirev.2019.07.036.

Ravenne, C., Riche, P., Tremolieres, P., and Vially, R., 1987, Sédimentation et tectonique dans le bassin marin Eocène supérieur-Oligocène des Alpes du Sud: Revue de Institut Français du Pétrole, v. 42, p. 529-553.

Reading, H.G. and Richards, M., 1994, Turbidite systems in deep-water basin margins classified by grain size and feeder system: AAPG Bulletin, v. 78, p. 792-822.

Reece, R.S., Gulick, S.P., Horton, B.K., Christeson, G.L. and Worthington, L.L., 2011. Tectonic and climatic influence on the evolution of the Surveyor Fan and Channel system, Gulf of Alaska: Geosphere, v. 7, p. 830-844.

Remacha, E. and Fernández, L.P., 2003, High-resolution correlation patterns in the turbidite systems of the Hecho Group (South-Central Pyrenees, Spain): Marine and Petroleum Geology, v. 20, p. 711–726.

Ricci Lucchi, F. and Valmori, E., 1980, Basin-wide turbidites in a Miocene, over-supplied deep-sea plain: a geometrical analysis: Sedimentology, v. 27, p. 241-270.

Ricci Lucchi, F., 1967, Recherches stratonomiques et sedi-mentologiques sur le flysch Miocene de la Romagna: Giorn. Geol., v. 35, p. 163–192.

Romans, B.W., Castelltort, S., Covault, J.A., Fildani, A., and Walsh, J.P., 2016, Environmental signal propagation in sedimentary systems across timescales: Earth Science Reviews, v. 153, p. 7–29.

Rottman, J.W., Simpson, J.E., Hunt, J.C.R. and Britter, R.E., 1985, Unsteady gravity current flows over obstacles: Some observations and analysis related to the phase II trials: Journal of Hazardous Materials, v. 11, p. 325-340.

Rowland, J.C., Hilley, G.E., and Fildani, A., 2010, A Test of Initiation of Submarine Leveed Channels by Deposition Alone: Journal of Sedimentary Research, v. 80, p. 710–727

Saint-Ange, F., Savoye, B., Michon, L., Bachelery, P., Deplus, C., De Voogd, B., Dyment, J., Le Drezen, E., Voisset, M., Le Friant, A. and Boudon, G., 2011, A volcaniclastic deep-sea fan off La Réunion Island (Indian Ocean): Gradualism versus catastrophism: Geology, v. 39, p. 271-274.

Saintot, A., Stephenson, R.A., Stovba, S., Brunet, M.F., Yegorova, T. and Starostenko, V., 2006, The evolution of the southern margin of Eastern Europe (Eastern European and Scythian platforms) from the latest Precambrian-Early Palaeozoic to the Early Cretaceous: Geological Society, London, Memoirs, v. 32, p. 481-505.

Salles, L., Ford, M., Joseph, P., De Veslud, C.L.C., and Le Solleuz, A., 2011, Migration of a synclinal depocenter from turbidite growth strata: the Annot syncline, SE France: Bulletin de la Société Géologique de France, v. 182, p. 199-220.

Salles, L., Ford, M., and Joseph, P., 2014, Characteristics of axially-sourced turbidite sedimentation on an active wedge-top basin (Annot Sandstone, SE France): Marine and Petroleum Geology, v. 56, p. 305-323.

Saller, A.H., Barton, J.W. and Barton, R.E., 1989, Slope sedimentation associated with a vertically building shelf, Bone Spring Formation, Mescalero Escarpe field, southeastern New Mexico, in, P.D. Crevello, J.J. Wilson, J.F. Sarg, and J.F. Read, eds., Controls on carbonate platform and basin development: Society of Economic Paleontologists and Mineralogists, p. 275-288.

Saltzman, M.R., and Thomas, E., 2012, Carbon isotope stratigraphy, in Gradstein, F., et al., eds., The geologic time scale: Oxford, UK, Elsevier, p. 207–232.

Schlager, W., Reijmer, J.J. and Droxler, A., 1994, Highstand shedding of carbonate platforms: Journal of Sedimentary Research, v. 64, p. 270-281.

Schlanger, S.O. and Premoli Silva, I., 1986, Oligocene sea-level falls recorded in mid-Pacific atoll and archipelagic apron settings: Geology, v. 14, p. 392-395.

Schlünz, B., Schneider, R.R., Müller, P.J., Showers, W.J. and Wefer, G., 1999, Terrestrial organic carbon accumulation on the Amazon deep sea fan during the last glacial sea level low stand: Chemical Geology, v. 159, p. 263-281.

Schnyder, J.S., Eberli, G.P., Betzler, C., Wunsch, M., Lindhorst, S., Schiebel, L., Mulder, T. and Ducassou, E., 2018, Morphometric analysis of plunge pools and sediment wave fields along western Great Bahama Bank: Marine Geology, v. 397, p. 15-28.

Scott, E., Gelin, F., Jolley, S., Leenaarts, E., Sadler, S. and Elsinger, R., 2010. Sedimentological control of fluid flow in deep marine turbidite reservoirs: Pierce Field, UK Central North Sea: Geological Society Special Publication: v. 347, p. 113-132.

Sequeiros, O.E., 2012, Estimating turbidity current conditions from channel morphology: A Froude number approach: Journal of Geophysical Research: Oceans, v. 117, C04003, doi: 10.1029/2011JC007201.

Shanmugam, G. and Moiola, R.J., 1995, Reinterpretation of depositional processes in a classic flysch sequence (Pennsylvanian Jackfork Group), Ouachita Mountains, Arkansas and Oklahoma: AAPG Bulletin, v. 79, p. 672-695.

Shanmugam, G., 1996, High-Density Turbidity Currents: Are They Sandy Debris Flows?: Perspectives: Journal of Sedimentary Research, v. 66, p. 2-10.

Sharman, G.R., Covault, J.A., Stockli, D.F., Wroblewski, A.F.J. and Bush, M.A., 2017. Early Cenozoic drainage reorganization of the United States Western Interior–Gulf of Mexico sediment routing system: Geology, v. 45, p.187-190.

Shumaker, L.E., Sharman, G.R., King, P.R. and Graham, S.A., 2018, The source is in the sink: Deep-water deposition by a submarine volcanic arc, Taranaki Basin, New Zealand: Sedimentology, v. 65(7), p. 2506-2530.

Sheets, B.A., Hickson, T.A., and Paola, C., 2002, Assembling the stratigraphic record: depositional patterns and time-scales in an experimental alluvial basin: Basin Research, v. 14, p. 287-301.

Shields, A., 1936, Anwendung der Aehnlichkeitsmechanik und der Turbulenzforschung auf die 369 Geschiebebewegung: PhD Thesis Technical University Berlin. 26 p.

Simpson, G. and Castelltort, S., 2012, Model shows that rivers transmit high-frequency climate cycles to the sedimentary record: Geology, v. 40(12), p. 1131-1134.

Sinclair, H.D., 1994, The influence of lateral basin slopes on turbidite sedimentation in the Annot Sandstones of SE France: Journal of Sedimentary Petrology, v. B64, p. 42-54.

Sinclair, H.D., 1997, Tectonostratigraphic model for underfilled peripheral foreland basins: An Alpine perspective: Geological Society of America, Bulletin, v. 109, p. 324-346

Sinclair, H.D., 2000, Delta-fed turbidites infilling topographically complex basins: a new depositional model for the Annot Sandstones, SE France: Journal of Sedimentary Research, v. 70, p. 504–519.

Sinclair, H.D. and Cowie, P.A., 2003. Basin-floor topography and the scaling of turbidites: The Journal of Geology, v. 111(3), p. 277-299.

Sinclair, H.D., and Tomasso, M., 2002, Depositional evolution of confined turbidite basins: Journal of Sedimentary Research, p. 72, v. 451-456.

Skene, K.I., Piper, D.J. and Hill, P.S., 2002, Quantitative analysis of variations in depositional sequence thickness from submarine channel levees: Sedimentology, v. 49, p. 1411-1430.

Sobiesiak, M.S., Kneller, B., Alsop, G.I. and Milana, J.P., 2016, Inclusion of substrate blocks within a mass transport deposit: a case study from Cerro Bola, Argentina. in Submarine Mass Movements and Their Consequences, Springer, Cham. p. 487-496.

Sobiesiak, M.S., Kneller, B., Alsop, G.I. and Milana, J.P., 2016. Internal deformation and kinematic indicators within a tripartite mass transport deposit, NW Argentina: Sedimentary Geology, v. 344, p. 364-381.

Sohn, Y.K., 2000, Depositional processes of submarine debris flows in the Miocene fan deltas, Pohang Basin, SE Korea with special reference to flow transformation: Journal of Sedimentary Research, v. 70, p. 491–503.

Sohn, Y., Choe, M. and Jo, H., 2002, Transition from debris flow to hyperconcentrated flow in a submarine channel (the Cretaceous Cerro Toro Formation, southern Chile): Terra Nova, v. 14, p. 405-415.

Sosson, M., Stephenson, R., Sheremet, Y., Rolland, Y., Adamia, S., Melkonian, R., Kangarli, T., Yegorova, T., Avagyan, A., Galoyan, G. and Danelian, T., 2016, The eastern Black Sea-Caucasus region during the Cretaceous: New evidence to constrain its tectonic evolution: Comptes Rendus Geoscience, v. 348, p. 23-32.

Sømme, T.O., Helland-Hansen, W., Martinsen, O.J. and Thurmond, J.B., 2009a. Relationships between morphological and sedimentological parameters in source-to-sink systems: a basis for predicting semi-quantitative characteristics in subsurface systems. Basin Research, v. 21(4), p. 361-387.

Sømme, T.O., Helland-Hansen, W. and Granjeon, D., 2009b, Impact of eustatic amplitude variations on shelf morphology, sediment dispersal, and sequence stratigraphic interpretation: Icehouse versus greenhouse systems: Geology, v. 37, p. 587-590.

Sømme, T.O., Piper, D.J., Deptuck, M.E., and Helland-Hansen, W., 2011, Linking onshore-offshore sediment dispersal in the Golo source-to-sink system (Corsica, France) during the late Quaternary: Journal of Sedimentary Research, v. 81, p. 118-137.

Sømme, T.O., Skogseid, J., Løseth, H. and Embry, P., 2019, Manifestation of tectonic and climatic perturbations in deep-time stratigraphy–an example from the Paleocene succession offshore western Norway: Frontiers in Earth Science, v. 7, p. 303.

Southern, S.J., Patacci, M., Felletti, F., and McCaffrey, W.D., 2015, Influence of flow containment and substrate entrainment upon sandy hybrid event beds containing a co-genetic mud-clast-rich division: Sedimentary Geology, p. 321, v. 105-122.

Southern, S.J., Kane, I.A., Warchoł, M.J., Porten, K.W. and McCaffrey, W.D., 2017, Hybrid event beds dominated by transitional-flow facies: character, distribution and significance in the Maastrichtian Springar Formation, north-west Vøring Basin, Norwegian Sea: Sedimentology, v. 64, p. 747-776.

Soutter, E.L., Kane, I.A., and Huuse, M., 2018, Giant submarine landslide triggered by Paleocene mantle plume activity in the North Atlantic: Geology, v. 46, p. 511-514.

Soutter, E.L., Kane, I.A., Fuhrmann, A., Cumberpatch, Z.A. and Huuse, M., 2019, The stratigraphic evolution of onlap in siliciclastic deep-water systems: Autogenic modulation of allogenic signals. Journal of Sedimentary Research, v. 89, p. 890-917.

Stanbrook, D.A., and Clark, J.D., 2004, The Marnes Brunes Inférieures in the Grand Coyer remnant: characteristics, structure and relationship to the Grès d'Annot, in Lomas, S., and Joseph, P., eds., Deep-Water Sedimentation in the Alpine Basin of SE France: New Perspectives on the Grès d'Annot and Related Systems: Geological Society of London, Special Publication 221, v. 285-300.

Stanley, D.J., 1986, Turbidity current transport of organic-rich sediments: Alpine and Mediterranean examples: Marine Geology, v. 70, p. 85-101.

Stanley, D.J., 1980, The Saint-Antonin conglomerate in the Maritime Alps: a model for coarse sedimentation on a submarine slope: Smithsonian Contributions to the Marine Sciences, v. 5, p. 1–25.

Stanley, D.J., and Mutti, E., 1968, Sedimentological evidence for an emerged land mass in the Ligurian sea during the Palaeogene: Nature, v. 218, p. 32.

Stetten, E., Baudin, F., Reyss, J.L., Martinez, P., Charlier, K., Schnyder, J., Rabouille, C., Dennielou, B., Coston-Guarini, J. and Pruski, A.M., 2015, Organic matter characterization and distribution in sediments of the terminal lobes of the Congo deep-sea fan: Evidence for the direct influence of the Congo River: Marine Geology, v. 369, p. 182-195.

Stow, D.A.V. and Mayall, M., 2000, Deep-water sedimentary systems: new models for the 21st Century: Marine and Petroleum Geology, v. 17, p. 125-135.

Smith, R.D.A., 1995, Reservoir architecture of syn-rift lacustrine turbidite systems, early Cretaceous, offshore South Gabon: Geological Society, London, Special Publications, v. 80, p. 197-210.

Smith, R.U., 2004a, Silled sub-basins to connected tortuous corridors: sediment distribution systems on topographically complex sub-aqueous slopes, in Lomas, S., and Joseph, P., eds., Confined Turbidite Basins: Geological Society of London, Special Publication 222, p. 23-43.

Smith, R., 2004b, Turbidite systems influenced by structurally induced topography in the multi-sourced Welsh Basin, in Lomas, S., and Joseph, P., eds., Confined Turbidite Basins: Geological Society of London, Special Publication 222, p. 209-228.

Smith, R., and Joseph, P., 2004, Onlap stratal architectures in the Grès d'Annot: Geometric models and controlling factors, in Lomas, S., and Joseph, P., eds., Deep-Water Sedimentation in the Alpine Basin of SE France: New Perspectives on the Grès d'Annot and Related Systems: Geological Society of London, Special Publication 221, p. 389-399.

Smith, G., Rowley, P., Williams, R., Giordano, G., Trolese, M., Silleni, A., Parsons, D.R., Capon, S., 2019, A bedform phase diagram for dense granular currents: EarthArXiv, https://doi.org/10.31223/osf.io/6c4pv

Spencer, J. W., 1889, High elevations preceding the Pleistocene period [in America]: Bulletin of the Geological Society of America, v. 1.

Spencer, J.W., 1903, Submarine valleys off the American coast and in the North Atlantic: Bulletin of the Geological Society of America, v. 14, p. 207-226.

Spinewine, B., Sequeiros, O.E., Garcia, M.H., Beaubouef, R.T., Sun, T., Savoye, B. and Parker, G., 2009, Experiments on wedge-shaped deep sea sedimentary deposits in minibasins and/or on channel levees emplaced by turbidity currents. Part II. Morphodynamic evolution of the wedge and of the associated bedforms: Journal of Sedimentary Research, v. 79, p. 608-628.

Sprague, A. R., Sullivan, M. D., Campion, K. M., Jensen, G. N., Goulding, F. J., Garfield, T. R., Sickafoose, D. K., Rossen, C., and Jennette, D. C., 2002, The physical stratigraphy of deep-water strata: A hierarchical approach to the analysis of genetically-related stratigraphic elements for improved reservoir prediction: National AAPG/SEPM meeting abstracts, Houston, Texas, March 10–13.

Sprague, A.R.G., Garfield, T.R., Goulding, F.J., Beaubouef, R.T., Sullivan, M.D., Rossen, C., Campion, K.M., Sickafoose, D.K., Abreu, V., Schellpeper, M.E. and Jensen, G.N., 2005, Integrated slope channel depositional models: the key to successful prediction of reservoir presence and quality in offshore West Africa. CIPM, 1-13.

Spychala, Y.T., Hodgson, D.M., Flint, S.S., and Mountney, N.P., 2015, Constraining the sedimentology and stratigraphy of submarine intraslope lobe deposits using exhumed examples from the Karoo Basin, South Africa: Sedimentary Geology, v. 322, p. 67-81.

Spychala, Y.T., Hodgson, D.M., Stevenson, C.J., and Flint, S.S., 2016, Aggradational lobe fringes: The influence of subtle intrabasinal seabed topography on sediment gravity flow processes and lobe stacking patterns: Sedimentology, v. 64, p. 582-608.

Spychala, Y.T., Hodgson, D.M., Prélat, A., Kane, I.A., Flint, S.S., and Mountney, N.P., 2017, Frontal and lateral submarine lobe fringes: comparing sedimentary facies, architecture and flow processes: Journal of Sedimentary Research, v. 87, p. 75-96.

Spychala, Y., Eggenhuisen, J., Tilston, M., and Pohl, F., 2019, The influence of basin settings and flow properties on the dimensions of submarine lobe elements: EarthArXiv, https://eartharxiv.org/sk8v3/

Stanley, D.G., 1963, Vertical petrographic variability in Annot sandstone turbidites; some preliminary observations and generalizations: Journal of Sedimentary Research, v. 3, p. 783-788.

Stevenson, C.J., Jackson, C.A.L., Hodgson, D.M., Hubbard, S.M., and Eggenhuisen, J.T., 2015, Deep-water sediment bypass: Journal of Sedimentary Research, v. 85, p. 1058-1081.

Stevenson, C.J., Feldens, P., Georgiopoulou, A., Schönke, M., Krastel, S., Piper, D.J., Lindhorst, K., and Mosher, D., 2018, Reconstructing the sediment concentration of a giant submarine gravity flow: Nature communications, v. 9, p. 2616.

Straub, K.M., Mohrig, D., McElroy, B., Buttles, J., and Pirmez, C., 2008, Interactions between turbidity currents and topography in aggrading sinuous submarine channels: a laboratory study: GSA Bulletin, v. 120, p. 368-385.

Straub, K., Paola, C., Mohrig, D., Wolinsky, M. and George, T., 2009, Compensational stacking of channelized sedimentary deposits: Journal of Sedimentary Research, v. 79, pp. 673-688.

Straub, K.M. and Pyles, D.R., 2012. Quantifying the hierarchical organization of compensation in submarine fans using surface statistics: Journal of Sedimentary Research, v. 82, p. 889-898.

Stevenson, C.J. and Peakall, J., 2010, Effects of topography on lofting gravity flows: Implications for the deposition of deep-water massive sands: Marine and Petroleum Geology, v. 27(7), p. 1366-1378.

Stow, D.A., Howell, D.G. and Nelson, C.H., 1983, Sedimentary, tectonic, and sea-level controls on submarine fan and slope-apron turbidite systems: Geo-Marine Letters, v. 3, p. 57-64.

Sumner, E., Amy, L., and Talling, P., 2008, Deposit structure and processes of sand deposition from decelerating sediment suspensions: Journal of Sedimentary Research, v. 78, p. 529–547,

Sumner, E.J., Peakall, J., Parsons, D.R., Wynn, R.B., Darby, S.E., Dorrell, R.M., McPhail, S.D., Perrett, J., Webb, A. and White, D., 2013, First direct measurements of hydraulic

jumps in an active submarine density current: Geophysical Research Letters, v. 40, p. 5904-5908.

Sumner, E.J., Talling, P.J. and Amy, L.A., 2009, Deposits of flows transitional between turbidity current and debris flow. Geology, v. 37, p. 991-994.

Surlyk, F., 1984, Fan-delta to submarine fan conglomerates of the Volgian-Valanginian Wollaston Forland Group, East Greenland. In E. H. Koster, and R. J. Steel, eds., Sedimentology of Gravels and Conglomerates: Canadian Soc. of Petroleum Geologists, Memoir, v. 10, p. 359-382.

Sweet, M.L., Gaillot, G.T., Jouet, G., Rittenour, T.M., Toucanne, S., Marsset, T. and Blum, M.D., 2019, Sediment routing from shelf to basin floor in the Quaternary Golo System of Eastern Corsica, France, western Mediterranean Sea: Geological Society of America Bulletin, in press.

Sylvester, Z., Cantelli, A., and Pirmez, C., 2015, Stratigraphic evolution of intraslope minibasins: Insights from surface-based model: American Association of Petroleum Geologists, Bulletin, v. 99, p. 1099-1129.

Sylvester, Z. and Lowe, D.R., 2004, Textural trends in turbidites and slurry beds from the Oligocene flysch of the East Carpathians, Romania: Sedimentology, v. 51, p. 945-972.

Sylvester, Z., Pirmez, C. and Cantelli, A., 2011. A model of submarine channel-levee evolution based on channel trajectories: Implications for stratigraphic architecture. Marine and Petroleum Geology, v. 28, p. 716-727.

Symons, W.O., Sumner, E.J., Paull, C.K., Cartigny, M.J., Xu, J.P., Maier, K.L., Lorenson, T.D., and Talling, P.J., 2017, A new model for turbidity current behavior based on integration of flow monitoring and precision coring in a submarine canyon: Geology, v. 45, p. 367-370.

Talling, P.J., 1998. How and where do incised valleys form if sea level remains above the shelf edge?: Geology, v. 26, p. 87-90.

Talling, P.J., 2001, On the frequency distribution of turbidite thickness: Sedimentology, v. 48, p. 1297–1329.

Talling, P.J., Allin, J., Armitage, D.A., Arnott, R.W., Cartigny, M.J., Clare, M.A., Felletti, F., Covault, J.A., Girardclos, S., Hansen, E. and Hill, P.R., 2015, Key future directions for research on turbidity currents and their deposits: Journal of Sedimentary Research, v. 85, p. 153-169.

Talling, P.J., Amy, L.A., and Wynn, R.B., 2007b, New insight into the evolution of large-volume turbidity currents: comparison of turbidite shape and previous modelling results: Sedimentology, v. 54, p. 737-769.

Talling, P., Amy, L., Wynn, R.B., Peakall, J., and Robinson, M., 2004, Beds comprising debrite sandwiched within co-genetic turbidite: Origin and widespread occurrence in distal depositional environments: Sedimentology, v. 51, p. 163–194.

Talling, P.J., Malgesini, G. and Felletti, F., 2013, Can liquefied debris flows deposit clean sand over large areas of sea floor? Field evidence from the Marnoso-arenacea Formation, Italian Apennines: Sedimentology, v. 60, p. 720-762.

Talling, P., Masson, D. Sumner, E. and Malgesini, G., 2012, Subaqueous sediment density flows: Depositional processes and deposit types: Sedimentology, v. 59, p. 1937-2003.

Talling, P.J., Paull, C.K. and Piper, D.J., 2013, How are subaqueous sediment density flows triggered, what is their internal structure and how does it evolve? Direct observations from monitoring of active flows: Earth-Science Reviews, v. 125, p. 244-287.

Talling, P.J., Wynn, R.B., Masson, D.G., Frenz, M., Cronin, B.T., Schiebel, R., Akhmetzhanov, A.M., Dallmeier-Tiessen, S., Benetti, S., Weaver, P.P.E. and Georgiopoulou, A., 2007a, Onset of submarine debris flow deposition far from original giant landslide: Nature, v, 450, p. 541.

Tassy, A., Crouzy, E., Gorini, C., Rubino, J.L., Bouroullec, J.L. and Sapin, F., 2015, Egyptian Tethyan margin in the Mesozoic: Evolution of a mixed carbonate-siliciclastic shelf edge (from Western Desert to Sinai): Marine and petroleum Geology, v. 68, p. 565-581.

Terlaky, V., Rocheleau, J. and Arnott, R.W.C., 2016, Stratal composition and stratigraphic organization of stratal elements in an ancient deep-marine basin-floor succession,

Neoproterozoic Windermere Supergroup, British Columbia, Canada: Sedimentology, v. 63, pp.136-175.

Tinterri, R., Laporta, M. and Ogata, K., 2017, Asymmetrical cross-current turbidite facies tract in a structurally-confined mini-basin (Priabonian–Rupelian, Ranzano Sandstone, northern Apennines, Italy): Sedimentary Geology, v. 352, p. 63–87.

Tinterri, R. and Magalhaes, P.M., 2011, Synsedimentary structural control on foredeep turbidites: an example from Miocene Marnoso-arenacea Formation, Northern Apennines, Italy: Marine and Petroleum Geology, v. 28, p. 629-657.

Tinterri, R., Magalhaes, P.M., Tagliaferri, A., and Cunha, R.S., 2016, Convolute laminations and load structures in turbidites as indicators of flow reflections and decelerations against bounding slopes. Examples from the Marnoso-arenacea Formation (northern Italy) and Annot Sandstones (south eastern France): Sedimentary Geology, v. 344, p. 382-407.

Toby, S.C., Duller, R.A., De Angelis, S. and Straub, K.M., 2019. A stratigraphic framework for the preservation and shredding of environmental signals: Geophysical Research Letters, v. 46, p. 5837-5845.

Tőkés, L., and Patacci, M., 2018, Quantifying tabularity of turbidite beds and its relationship to the inferred degree of basin confinement: Marine and Petroleum Geology, v. 97, p. 659- 671.

Tomasso, M., and Sinclair, H.D., 2004, Deep-water sedimentation on an evolving fault-block: the Braux and St Benoit outcrops of the Grès d'Annot, in Lomas, S., and Joseph, P., eds., Deep-Water Sedimentation in the Alpine Basin of SE France: New Perspectives on the Grès d'Annot and Related Systems: Geological Society of London, Special Publication 221, p. 267-283.

Toniolo, H., Lamb, M. and Parker, G., 2006. Depositional turbidity currents in diapiric minibasins on the continental slope: formulation and theory: Journal of Sedimentary Research, v. 76, p. 783-797.

Trincardi, F., Cattaneo, A., Correggiari, A., Mongardi, S., Breda, A. and Asioli, A., 2003, Submarine slides during relative sea level rise: two examples from the eastern

Tyrrhenian margin: in Submarine mass movements and their consequences, Springer, Dordrecht, p. 469 – 478.

Tucker, M.E., 2003, Mixed clastic–carbonate cycles and sequences: Quaternary of Egypt and Carboniferous of England: Geologia Croatica, v. 56, pp.19-37.

Underhill, J.R., 1991, Implications of Mesozoic - Recent basin development in the western Inner Moray Firth, UK: Marine and Petroleum Geology, v. 8, p. 359–369, https://doi.org/10.1016/0264-8172(91)90089-J.

Urlaub, M., Geersen, J., Krastel, S. and Schwenk, T., 2018, Diatom ooze: Crucial for the generation of submarine mega-slides?. Geology, v. 46, p. 331-334.

Vail, P. R., Mitchum, R. M., AND Thompson, S., Ill, 1977, Seismic stratigraphy and global changes of sea level, Part 3: Relative changes of sea level from coastal onlap, in Payton, C. W., ed., Seismic Stratigraphy—Applications to Hydrocarbon Exploration: American Association of Petroleum Geologists Memoir 26, p. 83-97.

van Andel, T.H. and Komar, P.D., 1969, Ponded sediments of the Mid-Atlantic Ridge between 22 and 23 North latitude: Geological Society of America Bulletin, v. 80, p. 1163-1190.

van Rijn, L., 1984, Sediment transport, part 2: Suspended load transport: Journal of Hydarulic Engineering, v. 110, p. 1613–1641.

van Rijn, L.C., 1993, Principles of Sediment Transport in Rivers, Estuaries and Coastal Seas: Aqua Publications, 1200 p.

van Wagoner, J.C., Mitchum Jr., R.M., Campion, K.M., Rahmanian, V.D., 1990. Siliciclastic sequence stratigraphy in well logs, core, and outcrops: concepts for high-resolution correlation of time and facies. American Association of Petroleum Geologists Methods in Exploration Series, v. 7, 55 p.

Vendettuoli, D., Clare, M.A., Clarke, J.H., Vellinga, A., Hizzet, J., Hage, S., Cartigny, M.J.B., Talling, P.J., Waltham, D., Hubbard, S.M. and Stacey, C., 2019, Daily bathymetric surveys document how stratigraphy is built and its extreme incompleteness in submarine channels. Earth and Planetary Science Letters, v. 515, p.231-247.

Vincent, S.J., Morton, A.C., Carter, A., Gibbs, S. and Barabadze, T.G., 2007, Oligocene uplift of the Western Greater Caucasus: an effect of initial Arabia–Eurasia collision: Terra Nova, v. 19, p. 160-166.

Vinnels, J.S., Butler, R.W., McCaffrey, W.D. and Paton, D.A., 2010, Depositional processes across the Sinú accretionary prism, offshore Colombia: Marine and Petroleum Geology, v. 27, p. 794-809.

Voigt, S. and Hilbrecht, H., 1997, Late Cretaceous carbon isotope stratigraphy in Europe: correlation and relations with sea level and sediment stability: Palaeogeography, Palaeoclimatology, Palaeoecology, v. 134, p. 39-59.

Von der Borch, C.C., Grady, A.E., Aldam, R., Miller, D., Neumann, R., Rovira, A. and Eickhoff, K., 1985, A large-scale meandering submarine canyon: outcrop example from the late Proterozoic Adelaide Geosyncline, South Australia: Sedimentology, v. 32, p. 507-518.

Wade, B.S., Houben, A.J., Quaijtaal, W., Schouten, S., Rosenthal, Y., Miller, K.G., Katz, M.E., Wright, J.D. and Brinkhuis, H., 2012, Multiproxy record of abrupt sea-surface cooling across the Eocene-Oligocene transition in the Gulf of Mexico: Geology, v. 40, p. 159-162.

Wagreich, M. and Krenmayr, H., 2005, Upper Cretaceous oceanic red beds (CORB) in the Northern Calcareous Alps (Nierental Formation, Austria): Slope topography and clastic input as primary controlling factors: Cretaceous Research, v. 26, p. 57-64.

Walker, R.G., 1967, Turbidite sedimentary structures and their relationship to proximal and distal depositional environments: Journal of Sedimentary Research, v. 37, p. 25-43.

Walker, R.G., 1978, Deep-water sandstone facies and ancient submarine fans: Models for exploration for stratigraphic traps: AAPG Bulletin, v. 62, p. 932-966.

Walker, W., Jobe, Z. R., Wood, L. and Sarg, R., 2019, Progradational Slope Architecture and Sediment Partitioning in the Outcropping Mixed Siliciclastic-Carbonate Bone Spring Formation, Permian Basin, west Texas: EarthArXiv, https://eartharxiv.org/zkge8/.

Waltham, D., 2004, Flow transformations in particulate gravity currents: Journal of Sediment. Research , v. 74, p. 129–134.

Walther, J., 1894, Einleitung in die Geologie als historische Wissenschaft, in Lithogenesis der Gegenwart. Jena, G. Fischer, v. 3, p. 535–1055.

Wang, C., Hu, X., Sarti, M., Scott, R. and Li, X., 2005, Upper Cretaceous oceanic red beds in southern Tibet: A major change from anoxic to oxic, deep-sea environments: Cretaceous Research, v. 26, p. 21-32.

Wang, X., Luthi, S.M., Hodgson, D.M., Sokoutis, D., Willingshofer, E. and Groenenberg, R.M., 2017, Turbidite stacking patterns in salt-controlled minibasins: Insights from integrated analogue models and numerical fluid flow simulations: Sedimentology, v. 64, p. 530-552.

Wang, Z.Y. and Larsen, P., 1994, Turbulence structure of flows of water and clay suspensions with bedload: Journal of Hydraulic Engineering, v. 120, p. 577–600.

Wang, Z., and Plate, E.J., 1996, A preliminary study on the turbulence structure of flows on non-Newtonian fluid: Journal of Hydraulic Research, v. 34, p. 345–361.

Weber, M.E., Wiedicke, M.H., Kudrass, H.R., Hübscher, C. and Erlenkeuser, H., 1997, Active growth of the Bengal Fan during sea-level rise and highstand: Geology, v. 25, p. 315-318.

Weber, M.E., Wiedicke-Hombach, M., Kudrass, H.R. and Erlenkeuser, H., 2003, Bengal Fan sediment transport activity and response to climate forcing inferred from sediment physical properties: Sedimentary Geology, v. 155, p. 361-381.

Weill, P., Lajeunesse, E., Devauchelle, O., Me□ tiver, F., Limare, A., Chauveau, B., and Mouaze□ , D., 2014, Experimental investigation on self-channelized erosive gravity currents: Journal of Sedimentary Research, v. 84, p. 487–498.

Weimer, P., and Link, M.H., 1991, Global petroleum occurrences in submarine fans and turbidite systems, in Weimer P., and Link M.H., eds., Seismic Facies and Sedimentary Processes of Submarine Fans and Turbidite Systems: Frontiers in Sedimentary Geology, New York, Springer, p. 9-67.

Weimer, P., & Shipp, C., 2004, Mass Transport Complex: Musing on Past Uses and Suggestions for Future Directions: Offshore Technology Conference, v. 1, p. 1–10.

Wells, D.L., and Coppersmith, K.J., 1994, New empirical relationships among magnitude, rupture length, rupture width, rupture area, and surface displacement: Bulletin of the Seismological Society of America, v. 84, p. 974–1002.

Wescott, W.A. and Ethridge, F.G., 1983, Eocene fan delta-submarine fan deposition in the Wagwater Trough, east-central Jamaica: Sedimentology, v. 30, p. 235-247.

White, N., and Lovell, B., 1997, Measuring the pulse of a plume with the sedimentary record: Nature, v. 4192, p. 1995–1998, 10.1038/43151.

Wilkinson, C.M., Ganerød, M., Hendriks, B.W.H., and Eide, E.A., 2016, Compilation and appraisal of geochronological data from the North Atlantic Igneous Province (NAIP), in Péron-Pinvidic, G., et al., The NE Atlantic region: a reappraisal of crustal structure, tectonostratigraphy and magmatic evolution–an introduction to the NAG-TEC project: Geological Society, London, Special Publication 447, p. 69–103, http://doi.org/10.1144/SP447.10.

Williams, G.E. and Gostin, V.A., 2000, Mantle plume uplift in the sedimentary record: origin of kilometre-deep canyons within late Neoproterozoic successions, South Australia: Journal of the Geological Society, v. 157, p. 759-768.

Wilson, D., Davies, J.R., Waters, R.A., and Zalasiewiczt, J.A., 1992, A fault-controlled depositional model for the Aberystwyth Grits turbidite system: Geological Magazine, v. 129, p. 595-607.

Winker, C.D., 1996, High-resolution seismic stratigraphy of a late Pleistocene submarine fan ponded by salt-withdrawal mini-basins on the Gulf of Mexico continental slope. In *Offshore Technology Conference*. Offshore Technology Conference, p. 619 - 628.

Wu, N., Jackson, C. A., Johnson, H., Hodgson, D. M., & Nugraha, H. D., 2019, Mass-transport complexes (MTCs) document minibasin subsidence patterns and diapir evolution in the northern Gulf of Mexico: EarthArXiv, https://doi.org/10.31223/osf.io/ysgqd

Wynn, R.B., Kenyon, N.H., Masson, D.G., Stow, D.A. and Weaver, P.P., 2002, Characterization and recognition of deep-water channel-lobe transition zones: AAPG Bulletin, v. 86, p. 1441-1462.

Wynn, R.B., Masson, D.G., Stow, D.A., and Weaver, P.P., 2000, The Northwest African slope apron: a modern analogue for deep-water systems with complex seafloor topography: Marine and Petroleum Geology, v. 17, p. 253-265.

Xu, J.P., 2010, Normalized velocity profiles of field-measured turbidity currents: Geology, v. 38, p. 563-566.

Yose, L.A. and Heller, P.L., 1989, Sea-level control of mixed-carbonate-siliciclastic, gravity-flow deposition: Lower part of the Keeler Canyon Formation (Pennsylvanian), southeastern California: Geological Society of America Bulletin, v. 101, p. 427-439.

Zachos, J.C., Quinn, T.M. and Salamy, K.A., 1996, High-resolution (104 years) deep-sea foraminiferal stable isotope records of the Eocene-Oligocene climate transition. Paleoceanography, v. 11, p. 251-266.

Zachos, J.C. and Kump, L.R., 2005, Carbon cycle feedbacks and the initiation of Antarctic glaciation in the earliest Oligocene: Global and Planetary Change, v. 47, p. 51-66.

Zeller, M., Verwer, K., Eberli, G.P., Massaferro, J.L., Schwarz, E. and Spalletti, L., 2015, Depositional controls on mixed carbonate–siliciclastic cycles and sequences on gently inclined shelf profiles: Sedimentology, v. 62, p. 2009-2037.

Zonneveld, J.P., Moslow, T.F. and Henderson, C.M., 1997, Lithofacies associations and depositional environments in a mixed siliciclastic-carbonate coastal depositional system, upper Liard Formation, Triassic, northeastern British Columbia: Bulletin of Canadian Petroleum Geology, v. 45, p. 553-575.

CHAPTER 11: Appendices

11.1 *Appendix A: Annot field data*

All sedimentary logs used in Chapter 3 available for download from the online repository for this thesis at: https://doi.org/10.6084/m9.figshare.12400730.v2

11.2 *Appendix C: Chalufy geochemical data*

Bag_Label	Sample_Number	Lithology	Height_m	Position	TOC	TOC_err	IC	IC_err	XRD_Calc	Calc_err	XRD_Qtz	Qtz_err	d13C	d18O	d18O_vsmow
-8	1	1	0	0.5											
-7	2	1	0.5	0.5									0.21	-4.52	26.25
-6	3	1	1	0.5	0.36	0.025	1.68	0.025	16.48	0.336	27.33	0.401	-0.5	-4.5	26.2
-5	4	1	1.5	0.5									-0.35	-7.73	22.94
-4	5	1	2	0.5									-0.81	-7.07	23.62
-3	6	1	2.5	0.5									0.36	-4.92	25.84
-2	7	1	3	0.5											
-1	8	1	3.5	0.5									-0.8	-6.35	24.37
1	9	2	4	1									-0.52	-4.61	26.15
1B	10	2	4.5	1									-1	-4.5	26.3
2	11	2	5	1											
2B	12	2	5.5	1	0.3	0.025	2.04	0.025	19.15	0.393	26.46	0.442	-0.19	-5.77	24.96
3	13	2	6	1									-0.5	-4.5	26.2
3B	14	2	7	1									-1.01	-5.08	25.67
4	15	2	8.8	1	0.4	0.025	1.61	0.025	17.23	0.442	26.94	0.606	-0.73	-3.14	27.67
4B	16	2	9.5	1									0.22	-8.49	22.16
8	20	2	32.2	2											
9	21	2	32.7	2									-2.03	-3.45	27.35
10	22	2	33.2	2									-1.27	-7.02	23.67
11	23	2	33.7	2									-1.59	-7.06	23.63
12	24	2	34.2	2	0.38	0.025	2.34	0.025	20.33	0.477	29.22	0.569	-0.88	-3.58	27.22
13	25	2	34.7	2									-0.82	-8.58	22.06
14	26	2	35.2	2									-0.7	-6.52	24.19
15	27	2	35.7	2									-0.19	-6.91	23.78
16	28	2	36.2	2									-0.18	-6.89	23.81
17	29	2	36.7	2									-0.11	-6.85	23.84
18	30	2	37.2	2									-0.4	-5.43	25.31
19	31	2	37.7	2									-2.44	-7.88	22.78
20	32	2	38.2	2									-0.94	-9.54	21.07
21	33	2	38.7	2									-0.49	-5.62	25.12
22	34	2	39.2	2									1.41	-4.95	25.81
23	35	2	39.7	2									0.7	-5.3	25.4
24	36	2	40.2	2									-0.62	-6.63	24.07
25	37	2	40.7	2									-0.98	-6.88	23.82
26	38	2	41.2	2									-0.85	-4.24	26.54
27	39	2	41.7	2									-0.7	-5.7	25
28	40	2	42.2	2	0.29	0.025	2.92	0.025	26.37	0.44	25.14	0.409			
29	41	2	42.7	2											
30	42	2	43.2	2									-0.8	-6.6	24.1
31	43	2	43.7	2									-1.12	-6.55	24.15
32	44	2	44.2	2									-0.08	-5.15	25.6
33	45	2	44.7	2									-1.28	-6.22	24.5
34	46	2	45.2	2									1.05	-5.84	24.89
35	47	2	45.7	2											
36	48	2	46.2	2									-0.46	-6.89	23.81
37	49	2	46.7	2									-1.1	-6.11	24.61
38	50	2	47.2	2									-0.95	-7.39	23.29
39	51	2	47.7	2									-0.87	-6.18	24.54
40	52	2	48.2	2									-1.6	-7.1	23.6
41	53	2	48.7	2									-0.51	-6.57	24.14
A	54	2	49.2	2									-2.46	-7.44	23.24
B	55	2	49.7	2									-2.12	-8.29	22.37
C	56	2	50.2	2									-0.18	-9.83	20.77

D	57	2	50.7	2									-0.53	-5.9	24.83
E	58	2	51.2	2									-1.23	-6.07	24.65
F	59	2	51.7	2									-1.07	-6.27	24.45
G	60	2	52.2	2									-0.73	-6.36	24.35
H	61	2	52.7	2									-0.57	-7.5	23.18
I	62	2	53.2	2									0.46	-11.45	19.11
J	63	2	53.7	2									-2.74	-4.99	25.77
K	64	2	54.2	2	0.28	0.025	1.93	0.025	16.47	0.335	32.71	0.511	-0.73	-5.01	25.75
L	65	2	54.7	2									-1.57	-4.97	25.79
M	66	2	55.2	2									-2.24	-6.69	24.01
N	67	2	55.7	2									-1.51	-8.24	22.41
O	68	2	56.2	2									-0.86	-6.01	24.71
57	69	3	70.7	3	0.32	0.025	1.32	0.025	13.91	0.337	29.99	0.483			
58	70	3	71.2	3									-1.92	-7.88	22.79
59	71	3	71.7	3									-0.43	-7.1	23.59
60	72	3	72.2	3									-1.75	-7.4	23.28
61	73	3	72.7	3									-1.12	-7.82	22.85
62	74	3	73.2	3									-1.45	-9.29	21.34
63	75	3	73.7	3									-1.75	-7.26	23.43
64	76	3	74.2	3											
65	77	3	74.7	3									-1.84	-8.81	21.83
66	78	3	75.2	3									-1.89	-9.22	21.4
67	79	3	75.7	3									-1.3	-6.16	24.56
68	80	3	76.2	3	0.39	0.025	1.27	0.025	14.22	0.382	28.8	0.543	-1.08	-6.56	24.14
69	81	3	76.7	3											
70	82	3	77.2	3									-1.6	-6.7	24
71	83	3	77.7	3									-0.46	-10.04	20.56
72	84	3	78.2	3											
73	85	3	78.7	3									-2.7	-2.04	28.81
74	86	3	79.2	3									-2.2	-5.4	25.3
75	87	3	79.7	3									-1.42	-7.36	23.32
76	88	3	80.2	3									-1.7	-7.7	22.97
77	89	3	80.7	3									-0.89	-7.68	23
78	90	3	81.2	3									-2.25	-6.84	23.86
79	91	3	81.7	3									-1.05	-6.89	23.81
80	92	3	82.2	3											
81	93	3	82.7	3									2.39	-14.02	16.45
82	94	3	83.2	3									-1.34	-6.27	24.45
82+1	95	3	83.7	3											
83	96	3	84.2	3	0.48	0.025	1.68	0.025	18.43	0.35	30.96	0.457	-0.98	-3.81	26.98
84	97	3	84.7	3									-0.37	-4.01	26.77
85	98	3	85.2	3									-0.89	-5.85	24.88
86	99	3	85.7	3									-1.51	-7.06	23.63
87	100	3	86.2	3											
88	101	3	86.7	3									-0.99	-3.86	26.93
89	102	3	87.2	3									-0.8	-4	26.8
90	103	3	87.7	3									2.15	-4.69	26.08
91	104	3	88.2	3									-1.64	-4	26.79
A3	105	3	88.7	3									-0.1	-5.6	25.14
B3	106	3	89.2	3									-0.91	-8.42	22.23
C3	107	3	89.7	3									-0.61	-4.5	26.27
D3	108	3	90.2	3									-0.57	-4.95	25.81
A1	109	3	90.7	3									-1.33	-5.53	25.21
B1	110	3	91.2	3									-0.68	-6.56	24.14
C1	111	3	91.7	3									-1.74	-5.01	25.74
D1	112	3	92.2	3									0.1	-5.58	25.15
E1	113	3	92.7	3									-0.81	-5.69	25.04
F1	114	3	93.2	3									0.64	-5.16	25.59
G1	115	3	93.7	3									-0.92	-10.6	19.99
H1	116	3	94.2	3	0.65	0.025	2.17	0.025	18.24	0.326	34.68	0.457			
I1	117	3	94.7	3									-0.29	-4.97	25.78
J1	118	3	95.2	3									-1.09	-6.68	24.02
K1	119	3	95.7	3									0.01	-7.22	23.47
L1	120	3	96.2	3									-0.23	-2.9	27.92
M1	121	3	96.7	3									-1.12	-6.54	24.17
N1	122	3	97.2	3									-0.24	-8.62	22.02
O1	123	3	97.7	3									-1.88	-5.81	24.92
P1	124	3	98.2	3									-0.38	-9.22	21.4
Q1	125	3	98.7	3									0.96	-9.94	20.66
Above Slump 1	126	3	102.5	3									-2.07	-8.25	22.41

Above Slump 2	127	3	103	3	-1.37	-4.56	26.21
Above Slump 3	128	3	103.5	3	-0.9	-5.05	25.7
Above Slump 4	129	3	104	3	-1.85	-8.5	22.15

Table 11.1: TOC, isotopic and XRD data from the Chalufy section.

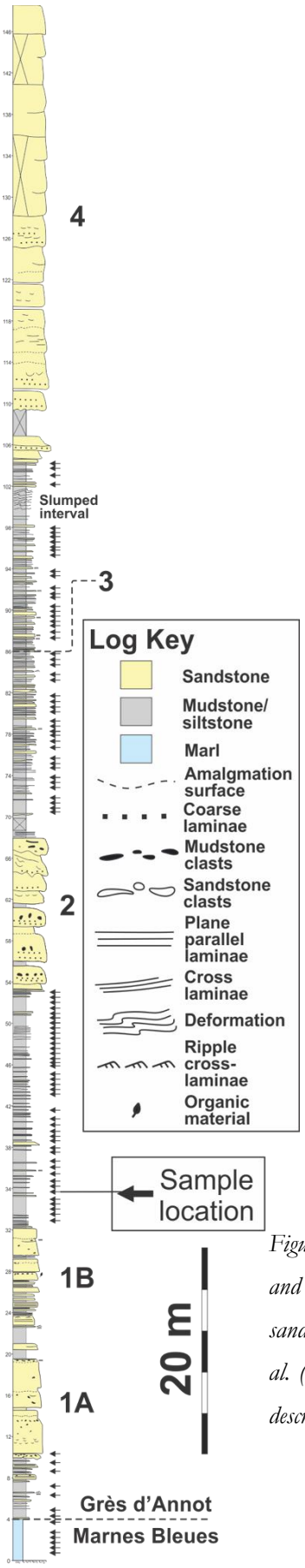

Figure 11.1: Logged section at Chalufy and sample locations. Middle and upper sandstones are from Puigdefàbregas et al. (2004). Number refers to sand unit described in text.

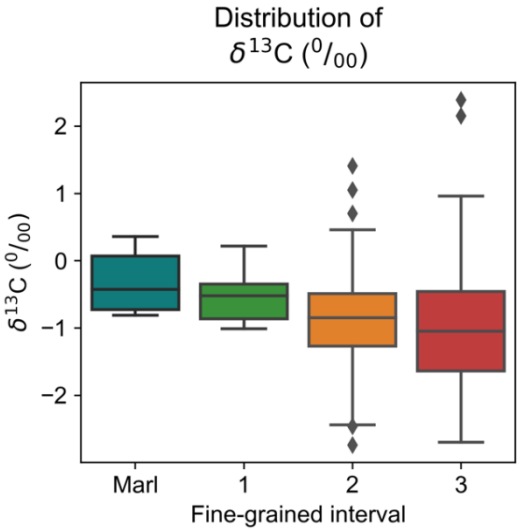

Figure 11.3: Standard deviations of δ13C data.

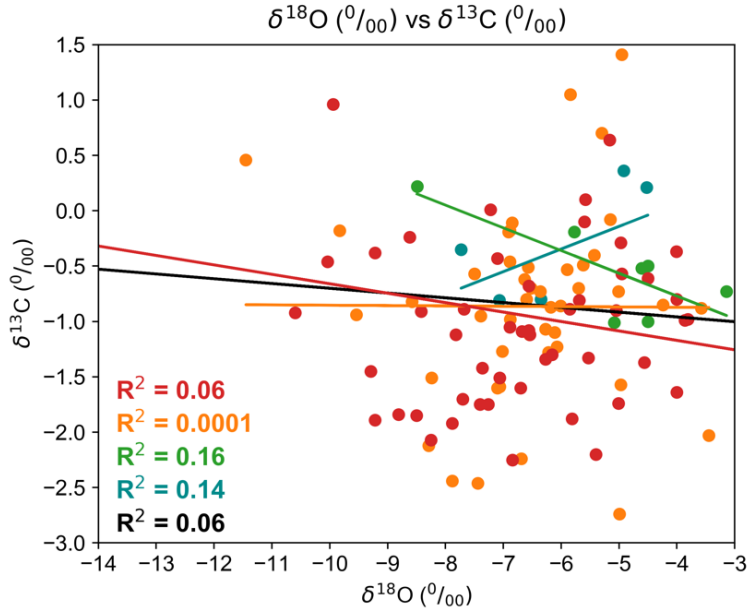

Figure 11.2: Cross-plot of δ18O v δ13C indicates no correlation, and therefore a minimum of diagenetic alteration.

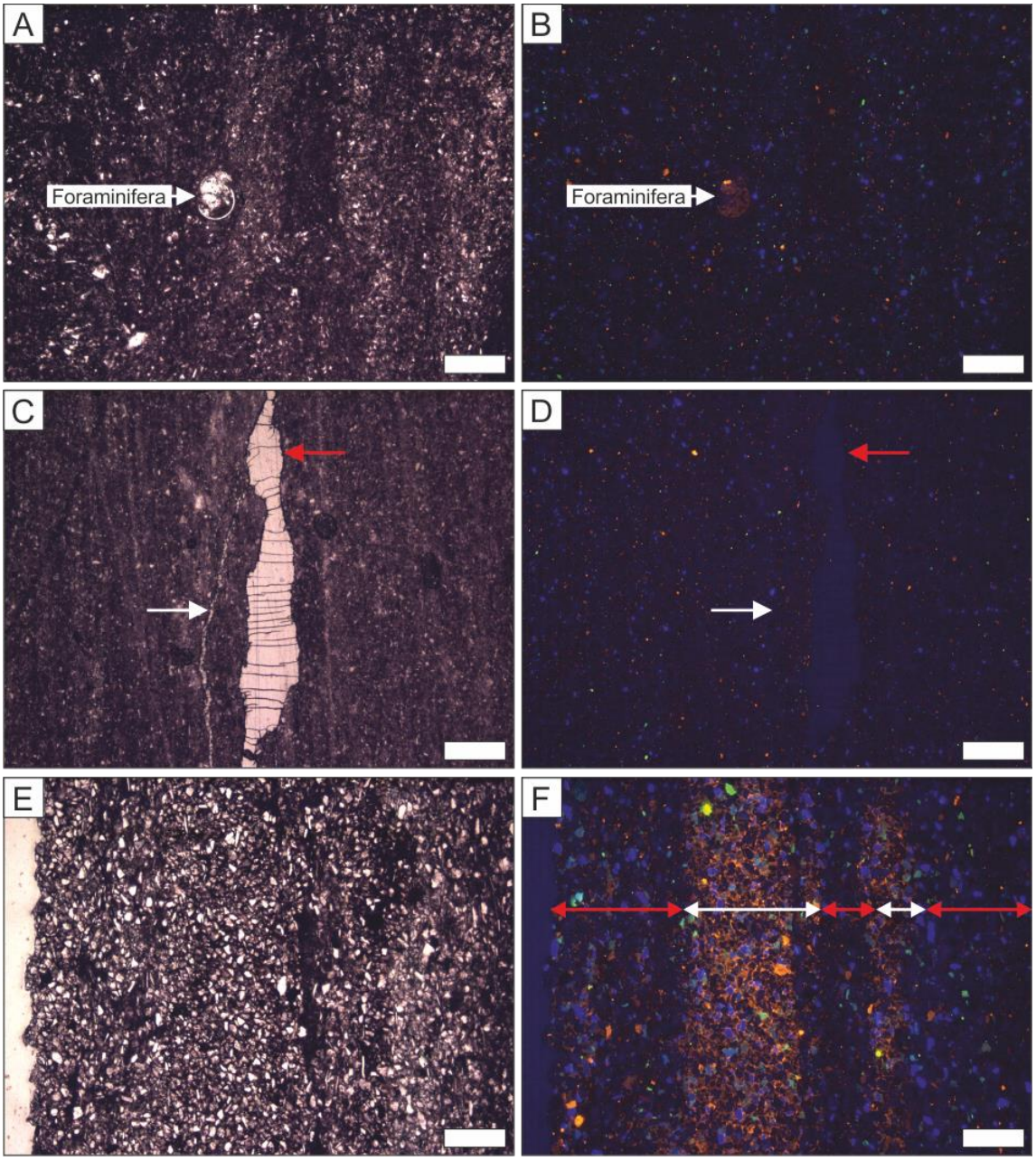

Figure 11.4: Thin-section photomicrographs taken under plane polarized light (PPL) (left) and cathodoluminescence (CL) (right). (A&B) Heterogeneous matrix comprised of mud (light brown in PPL) with silt sized detrital quartz and calcite grains (respectively blue and orange under CL) and foraminifera (arrowed). Stable isotope measurements were derived from this foraminifera-rich material. (B&C) Minor fracture (white arrow) crosscut by a major fracture (red arrow) both cemented by dull blue luminescing calcite. The major fracture is approximately bed parallel, suggesting stylolite cementation. (D&E) Organic matter (dark brown to black in PPL) is bed parallel. Well-developed laminations of quartz-rich (red arrows) and calcite-rich (white arrows) sediment (respectively blue and orange under CL).

11.3 *Appendix D: Supplementary seismic and well data from Central North Sea*

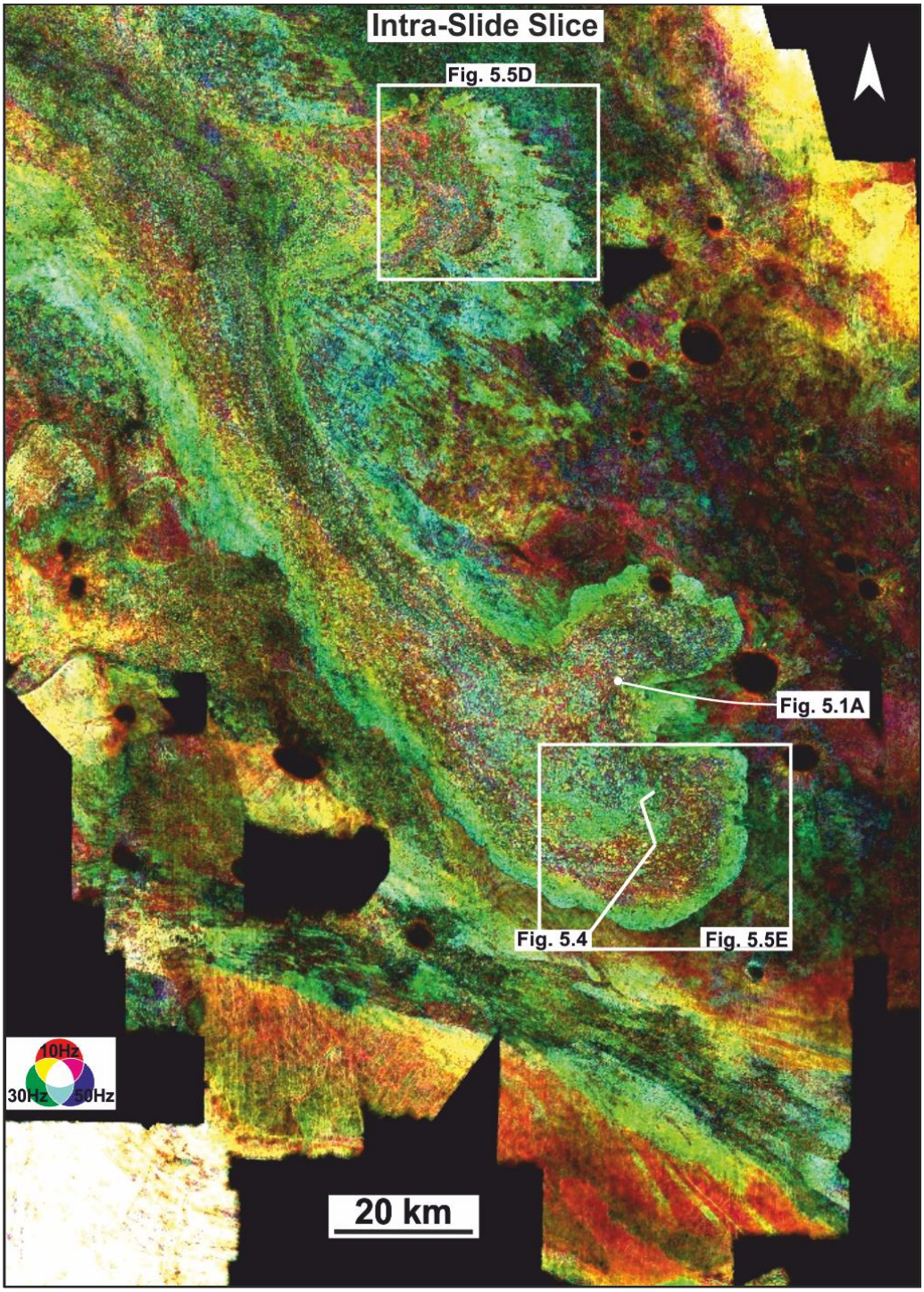

Figure 11.5: Intra-slide spectral deposition of the Halibut Slide interval.

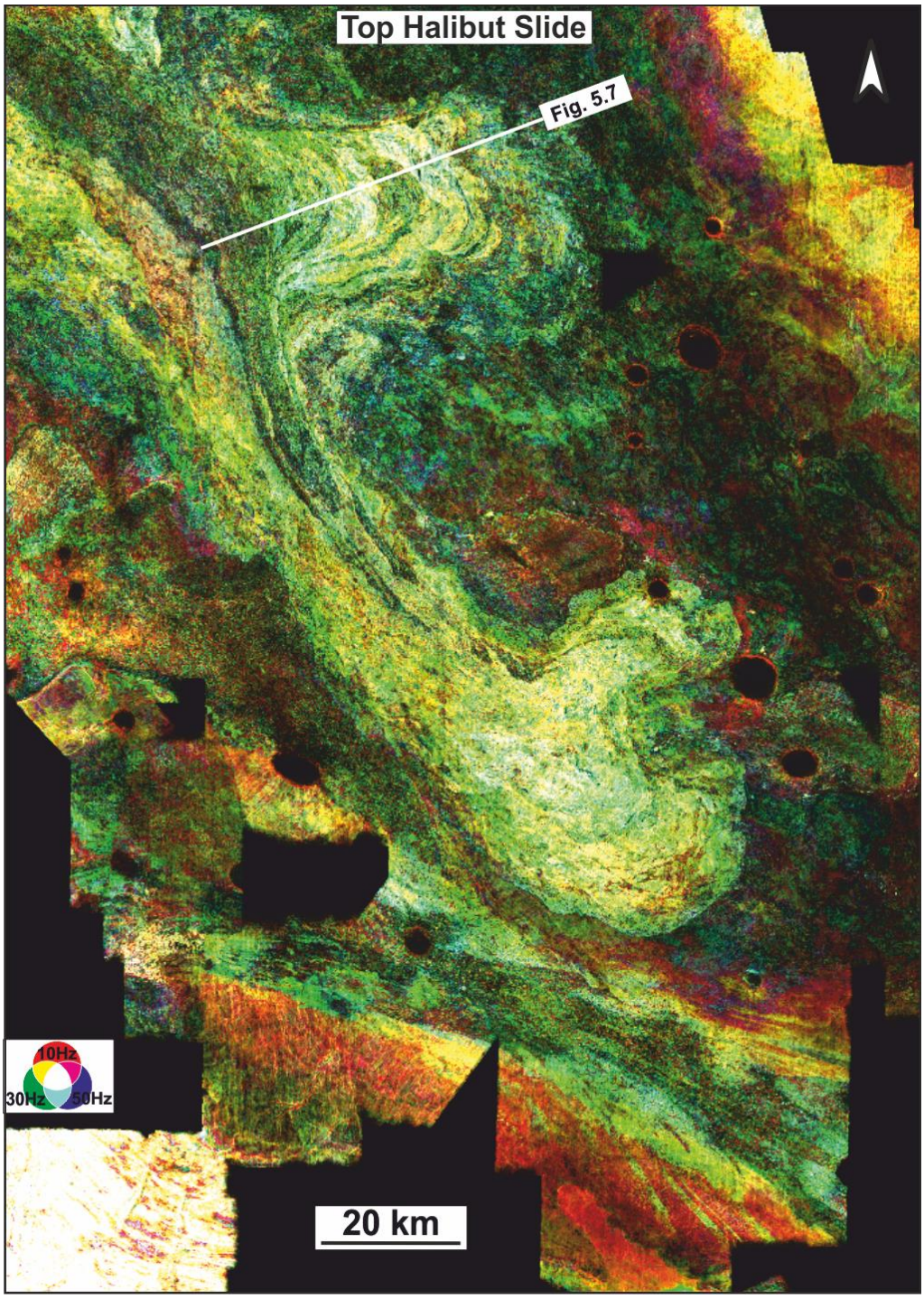

Figure 11.6: Spectral decomposition of the top surface of the Halibut Slide interval.

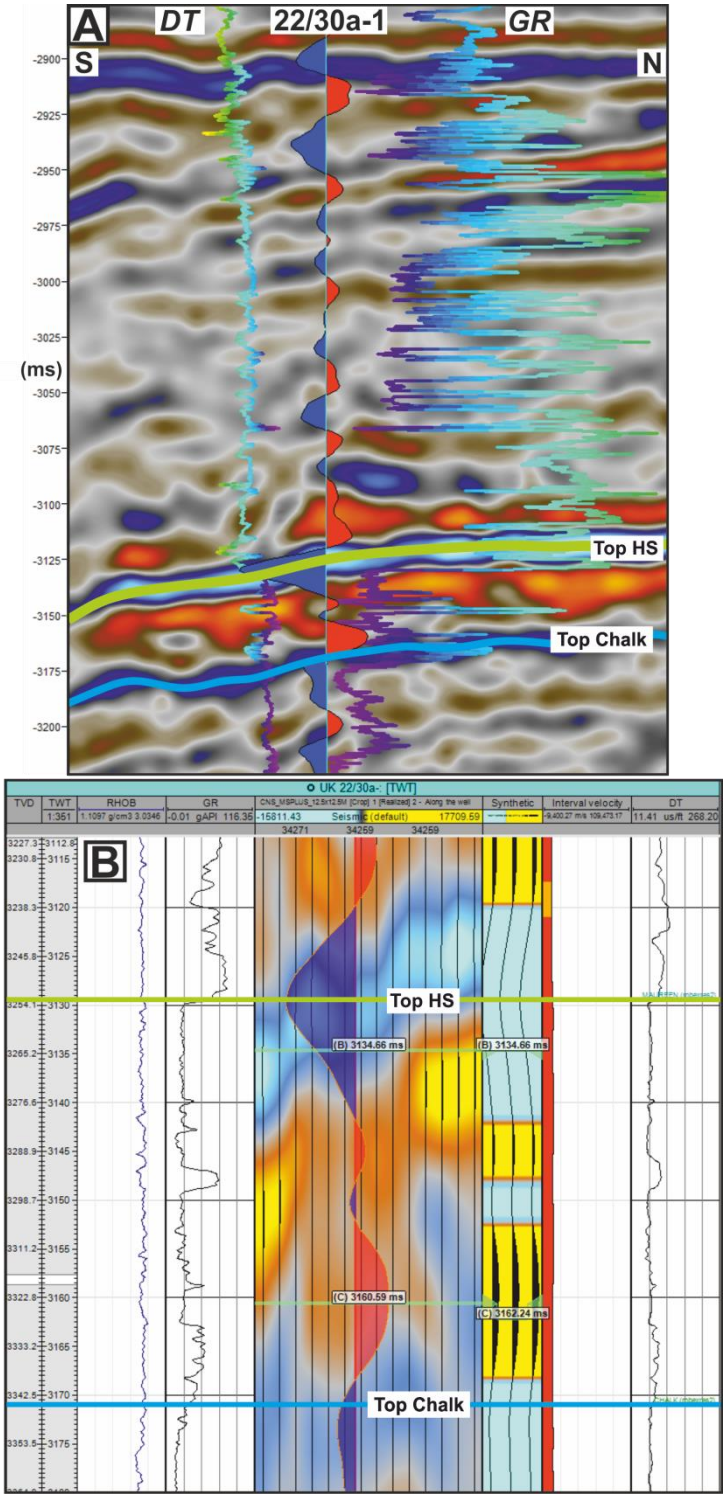

Figure 11.7: A) Sonic, gamma and synthetic seismogram for well 22/30a-1 (Fig. 1). Sonic and gamma values decrease right to left. B) Synthetic generation window and wireline logs for 22/30a-1 showing the petrophysical characteristics of the Halibut Slide.

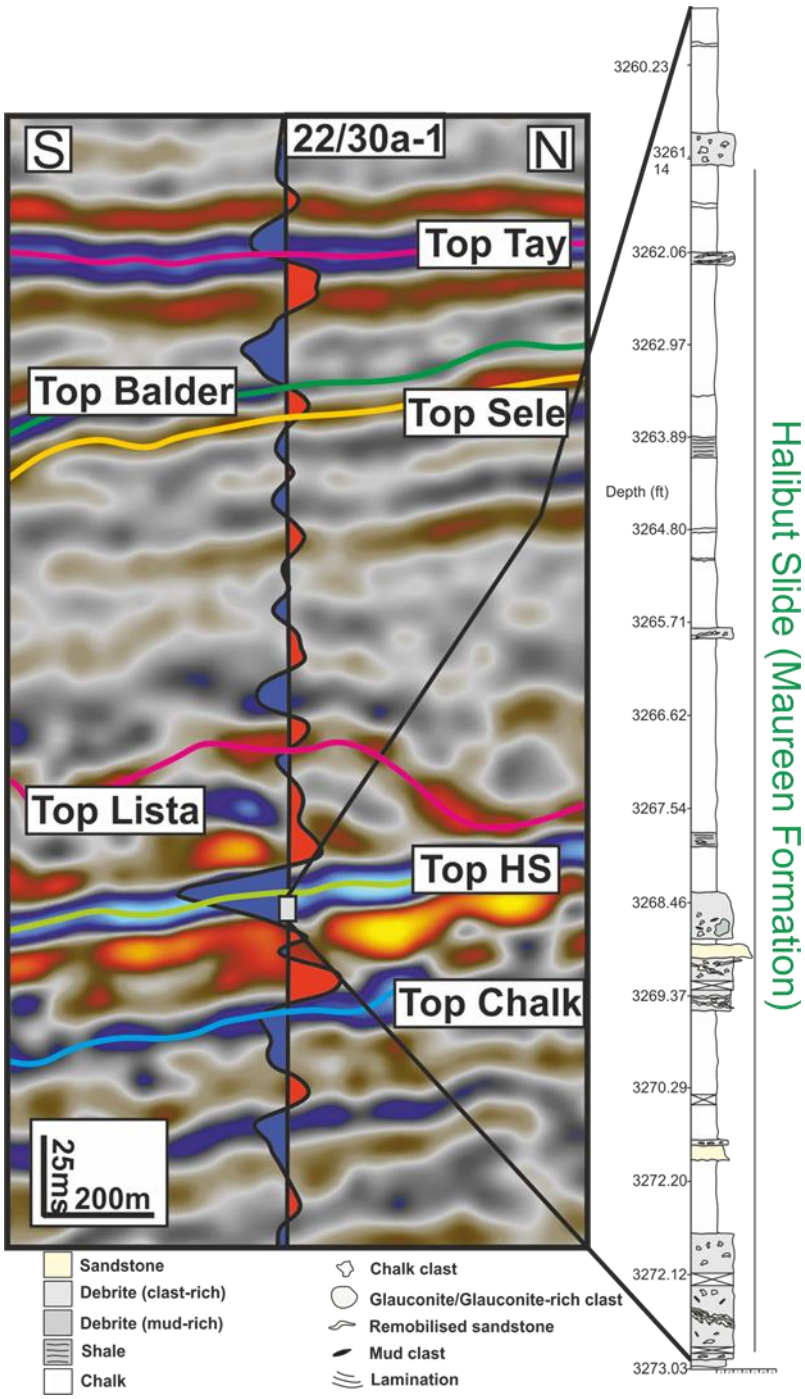

Figure 11.8: Core tied to well log and associated sedimentary log. The cored section forms the lower half of the Top Halibut Slide hard reflector. The reflector is bright because of the density contrast between the clastics of the Paleocene and the chalk of the Halibut Slide.

11.4 ***Appendix E: All logged Cretaceous sections***

All field data and code used in Chapter 6 is available for download from the online repository for this thesis at: https://doi.org/10.6084/m9.figshare.12400730.v2 and https://github.com/eslrgs/azerbaijan_2020

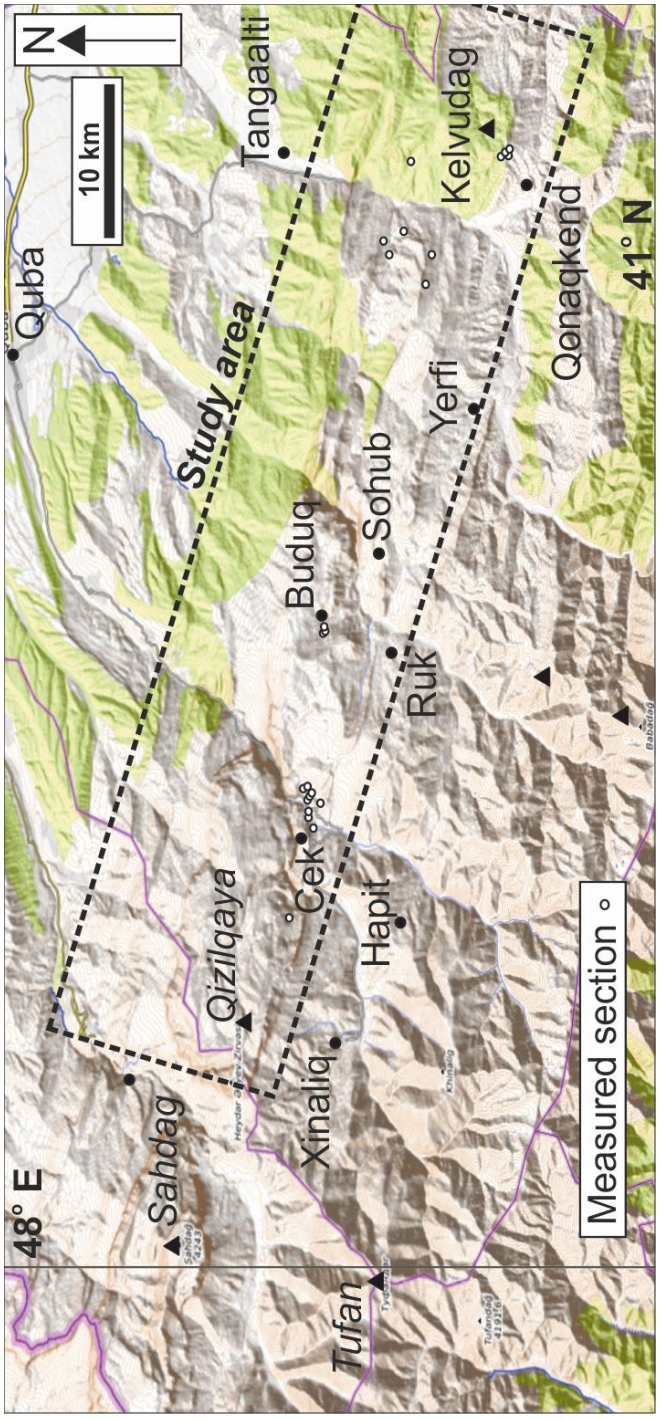

Figure 11.9: Map of logged sections around the Buduq Trough.

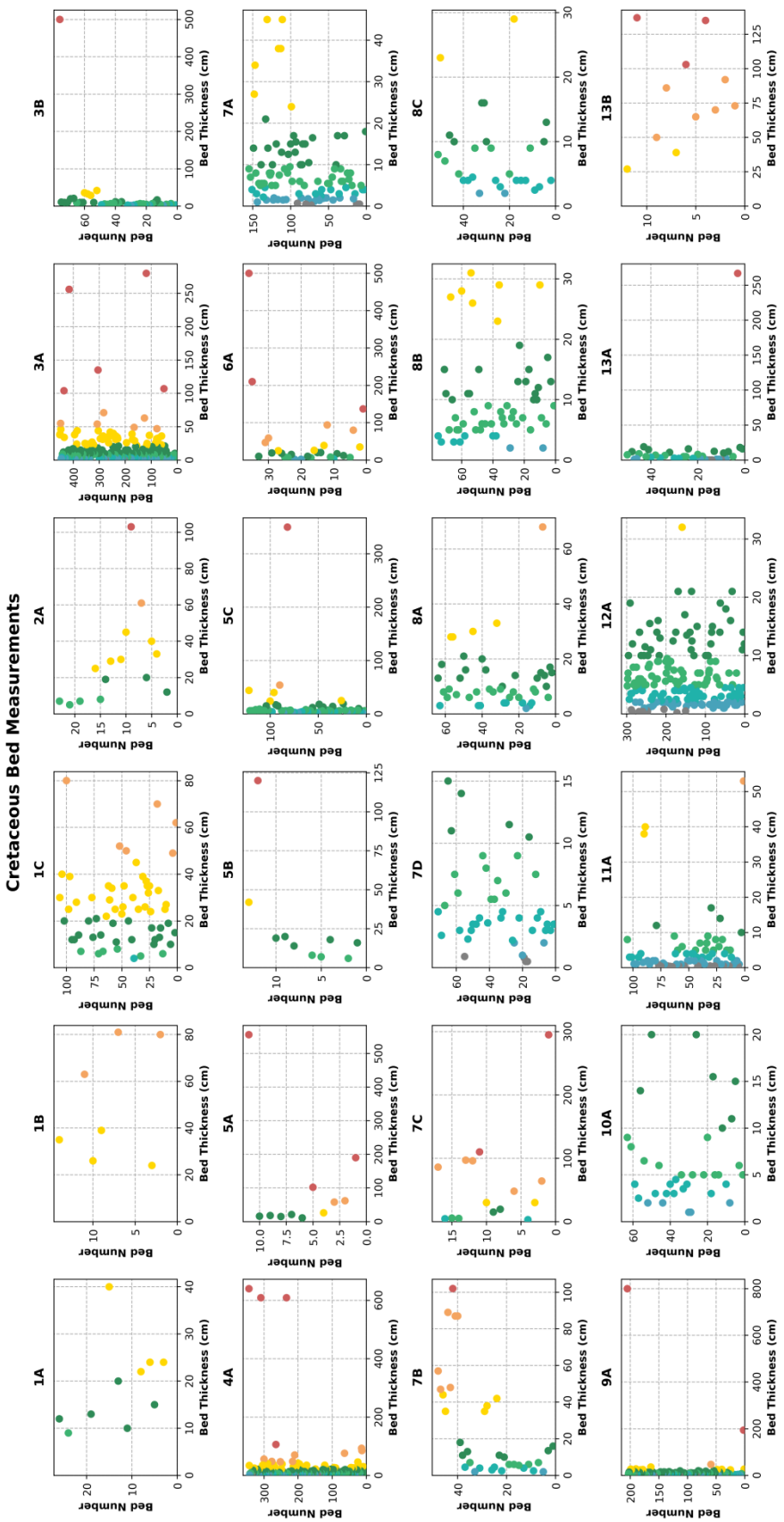

Figure 11.10: Bed number vs bed thickness for all logged Buduq Trough sections.

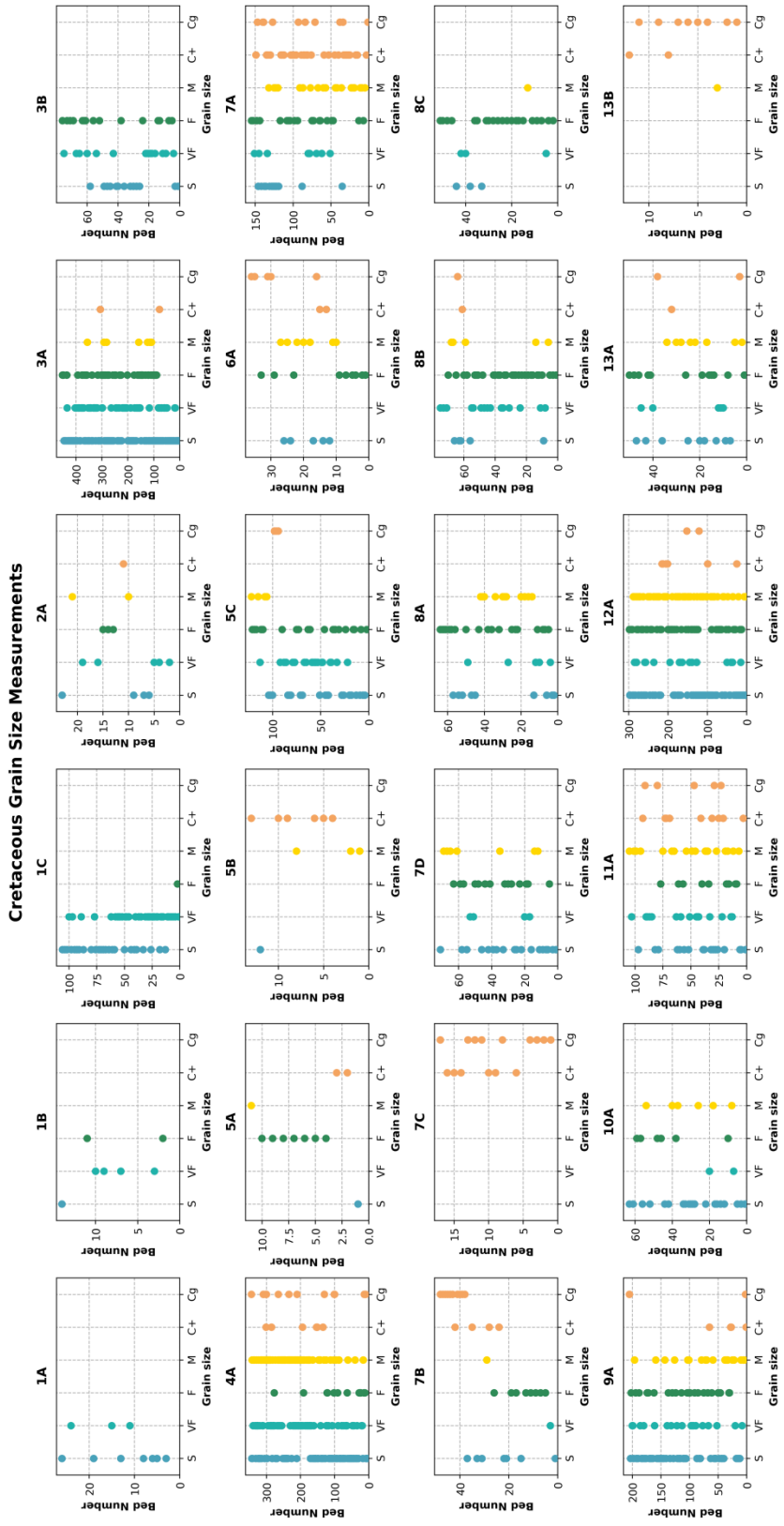

Figure 11.11: Bed number vs grain size for all logged Buduq Trough sections.

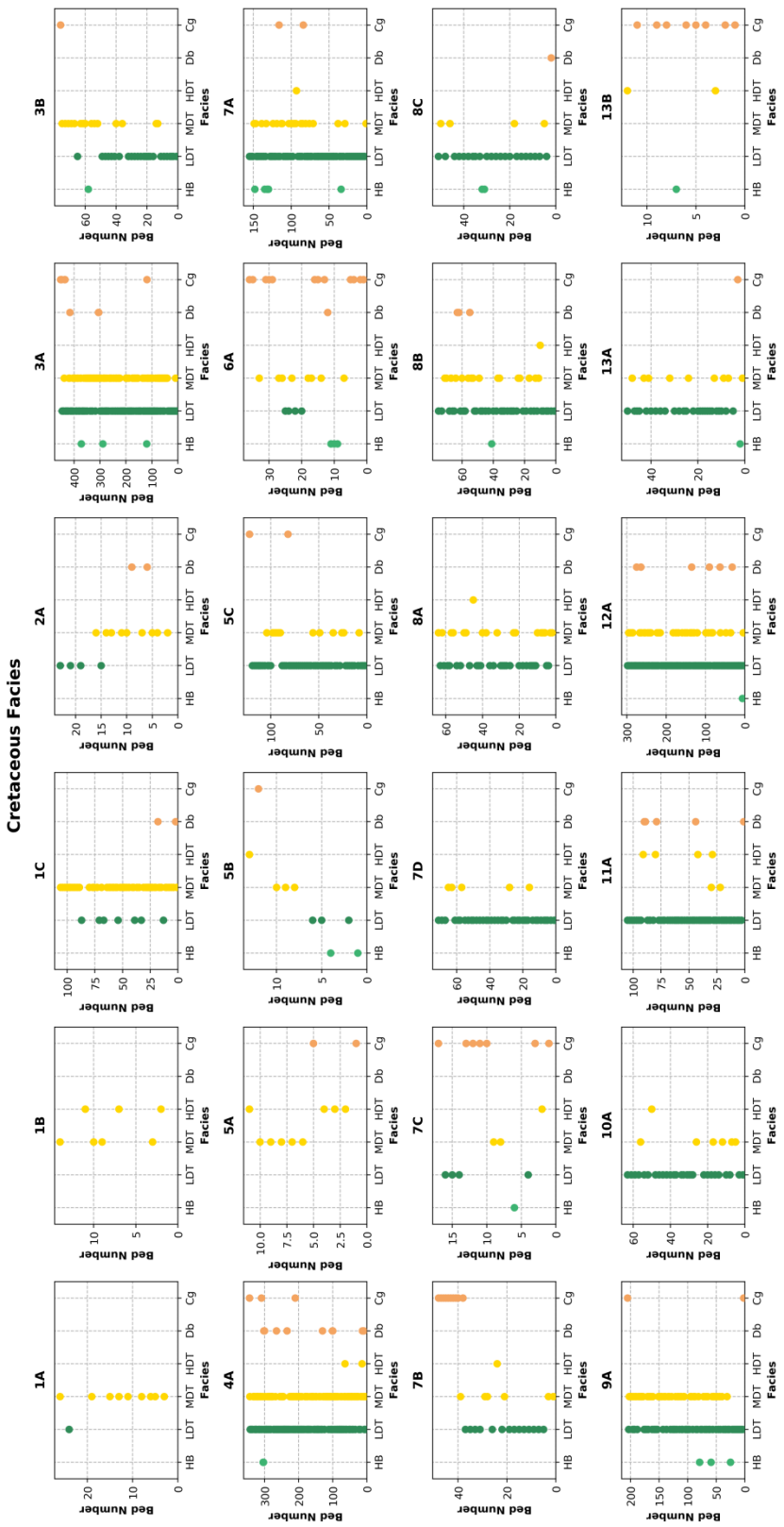

Figure 11.12: Bed number vs facies for all logged Buduq Trough sections.

Log	Latitude	Longitude	Altitude (m)
1A	41.19944	48.24528	1750
1B	41.20167	48.25444	1680
1C	41.20194	48.25167	1530
2B	41.19516	48.25966	1678
3B	41.20219	48.26127	1592
4A	41.20245	48.26867	1656
5A	41.2003	48.26479	1707
5B	41.20069	48.26451	1726
5C	41.20454	48.26743	1598
6A	41.13518	48.57189	1488
7A	41.09737	48.62845	1532
7B	41.09411	48.63032	1613
7C	41.0934	48.63184	1623
7D	41.09359	48.62936	1564
8A	41.19291	48.35996	1887
8B	41.19317	48.35849	1907
8C	41.19345	48.35733	1948
9A	41.21245	48.19414	2485
10A	41.16091	48.58033	1247
11A	41.15792	48.57284	1221
12A	41.13845	48.55533	1777
13A	41.15009	48.58541	1165
13B	41.14625	48.62576	1165

Table 11.10: Location of measured sections in the Buduq Trough.

11.5 *Appendix E: UVP, thickness and morphometric data from physical models*

Measured velocities

UVP	Distance (cm)	Unconfined (m s^{-1})	Lateral (m s^{-1})	Oblique (m s^{-1})	Frontal (m s^{-1})
1	0	1.09	0.99	1.04	1.06
2	80	0.95	0.94	1.06	1.01
3	160	1.00	0.91	1.09	1.11
4	240	0.77	0.77	0.97	0.87
5	0	0.21	0.19	0.21	0.26
6	40	0.54	0.37	0.43	0.61
7	120	0.72	0.67	0.53	0.56
8	160	0.31	0.06	0.08	0.15

All Normalised (vs fastest measurement)

UVP	Distance	Unconfined	Lateral	Oblique	Frontal
1	0.00	1.00	1.00	0.95	0.95
2	0.33	0.84	0.95	0.97	0.90
3	0.67	0.90	0.91	1.00	1.00
4	1.00	0.64	0.76	0.88	0.75
5	0.00	0.00	0.14	0.13	0.11
6	0.17	0.38	0.33	0.35	0.48
7	0.50	0.58	0.66	0.45	0.43
8	0.67	0.11	0.00	0.00	0.00

Lateral Normalised (vs UVP 4)

UVP	Distance	Unconfined	Lateral	Oblique	Frontal
8	0.00	0.00	0.18	0.15	0.15
7	0.25	0.59	0.44	0.39	0.64
4	0.50	1.00	1.00	1.00	1.00
6	0.75	0.91	0.86	0.51	0.57
5	1.00	0.18	0.00	0.00	0.00

Table 11.11: Measured experimental velocities.

Thinning Rates

	Centroid	Axis	Off-Axis	Fringe
Unconfined				
Thickness	64.58	50	20	10
Percent of thickness	1	0.77	0.31	0.15
Width (cm)	0	122	322	680
Width (norm)	0	0.18	0.47	1
Length (cm)	0	372	724	
Length (norm)	0	0.51	1	
Lateral				
Thickness	55.92	50	20	10
Percent of thickness	1	0.89	0.36	0.18
Width (cm)	0	54	294	502
Width (norm)	0	0.11	0.59	1
Width (confined) (cm)	0	196	478	518
Width (confined) (norm)	0	0.39	0.95	1
Length (cm)	0	686	1610	
Length (norm)	0	0.43	1	
Oblique (Upstream)				
Thickness	71	50	20	10
Percent of thickness	1	0.7	0.28	0.14
Width (cm)	0	220	480	560
Width (norm)	0	0.39	0.86	1
Width (confined) (cm)	0	130	210	230
Width (confined) (norm)	0	0.57	0.91	1
Length (cm)	0	700	1490	
Length (norm)	0	0.47	1	
Oblique (Downstream)				
Thickness	58.08	50	20	10
Percent of thickness	1	0.86	0.34	0.17
Width (cm)	0	182	490	606
Width (norm)	0	0.3	0.81	1
Length (cm)	0	388	1010	
Length (norm)	0	0.38	1	
Frontal				
Thickness	62.42	50	20	10
Percent of thickness	1	0.8	0.32	0.16
Width (cm)	0	228	428	696
Width (norm)	0	0.33	0.61	1
Length (cm)	0	388	904	
Length (norm)	0	0.43	1	

Table 11.12: Measured experimental deposit thicknesses and thinning rates.

		Morphometrics				
Run	**Confined**	**Length (mm)**	**Width (mm)**	**Thickness (mm)**	**Length/ Width**	**Width/ Thickness**
Unconfined	0	4600	1280	64.58	3.59	19.82
Lateral	1	5060	850	55.92	5.95	15.20
Oblique Upstream	1	3420	650	69.5	5.26	9.35
Oblique Downstream	0	2140	1450	58.08	1.48	24.97
Frontal Downstream	0	2950	990	62.42	2.98	15.86

Table 11.13: Measured experimental deposit morphometrics.